TREE-NUREG-1130
for U.S. Nuclear Regulatory Commission

IRRADIATION EFFECTS TEST SERIES
TEST IE-5
TEST RESULTS REPORT

DOUGLAS W. CROUCHER TOM R. YACKLE
CHRIS M. ALLISON SCOTT A. PLOGER

January 1978

EG&G Idaho, Inc.

IDAHO NATIONAL ENGINEERING LABORATORY

DEPARTMENT OF ENERGY

IDAHO OPERATIONS OFFICE UNDER CONTRACT EY-76-C-07-1570

DISCLAIMER

Printed in the United States of America
Available from
National Technical Information Service
U.S. Department of Commerce
5285 Port Royal Road
Springfield, Virginia 22161
Price: Printed Copy $9.00; Microfiche $3.00

"The NRC will make available data tapes and operational computer codes on research programs dealing with postulated loss-of-coolant accidents in light water reactors. Persons requesting this information must reimburse the NRC contractors for their expenses in preparing copies of the data tapes and the operational computer codes. Requests should be submitted to the Research Applications Branch, Office of Nuclear Regulatory Research, Nuclear Regulatory Commission, Washington, D.C. 20555."

TREE-NUREG-1130

IRRADIATION EFFECTS TEST SERIES

TEST IE-5

TEST RESULTS REPORT

Approved:

W. J. Quapp, Manager
Program Development and Evaluation Branch

P. E. MacDonald, Manager
Thermal Fuels Behavior Division

L. J. Ybarrondo, Director
Water Reactor Research

TREE-NUREG-1130

Distributed Under Category:
NRC-3
Water Reactor Safety Research
Fuel Behavior

IRRADIATION EFFECTS TEST SERIES

TEST IE-5

TEST RESULTS REPORT

by:

Douglas W. Croucher
Tom R. Yackle
Chris M. Allison
Scott A. Ploger

EG&G IDAHO, INC.

January 1978

PREPARED FOR THE
U.S. NUCLEAR REGULATORY COMMISSION
AND
DEPARTMENT OF ENERGY
IDAHO OPERATIONS OFFICE
UNDER CONTRACT NO. EY-76-C-07-1570

ABSTRACT

Results of Test IE-5 in the Irradiation Effects Test Series administered under the Thermal Fuels Behavior Program of EG&G Idaho, Inc. for the Nuclear Regulatory Commission are presented. The objectives of this test were to evaluate the influence of simulated fission products, cladding irradiation damage, and fuel rod internal pressure on pellet-cladding interaction during a power ramp and on fuel rod behavior during film boiling operation.

Test IE-5, conducted in the Power Burst Facility at the Idaho National Engineering Laboratory, employed three 0.97-m long pressurized water reactor type fuel rods, fabricated from previously irradiated zircaloy-4 cladding and one similar rod fabricated from unirradiated cladding. The four rods were subjected to a preconditioning period, a power ramp to an average fuel rod peak power of 65 kW/m, and steady state operation for one hour at a coolant mass flux of 4880 kg/s-m^2 for each rod. After a flow reduction to 1800 kg/s-m^2, film boiling occurred on one rod. Additional flow reductions to 970 kg/s-m^2 produced film boiling on the three remaining fuel rods. Maximum time in film boiling was 80 s. The rod having the highest initial internal pressure (8.3 MPa) failed 10 s after the onset of film boiling. A second rod failed about 90 s after reactor shutdown.

This report contains a description of the experiment, the test conduct, test results, and results from the preliminary postirradiation examination. Calculations using a transient fuel rod behavior code are compared with the test results.

SUMMARY

Test IE-5 in the Irradiation Effects Test Series was conducted by the Thermal Fuels Behavior Program of EG&G Idaho, Inc. This test series, part of the United States Nuclear Regulatory Commission Fuel Behavior Program to define the behavior of fuel rods during transient operating conditions, is directed toward providing a base of experimental data to aid in the development of verified computer models of irradiated fuel rod behavior. The objectives of this test were to evaluate the influence of simulated fission products, cladding irradiation damage, and fuel rod internal pressure on pellet-cladding interaction during a power ramp and on fuel rod behavior during film boiling operation.

Test IE-5 was conducted in January 1977 in the Power Burst Facility at the Idaho National Engineering Laboratory. Three of the four rods tested, Rods IE-019, IE-020, and IE-021, were fabricated with irradiated zircaloy-4 cladding. The fourth rod, Rod IE-022, was assembled with unirradiated cladding. All rods contained unirradiated UO_2 fuel. The 0.97-m long rods were pressurized with an argon and helium gas mixture which had a thermal conductivity similar to fission gases removed from irradiated Saxton rods. To test the cladding ballooning phenomenon, Rod IE-019 was pressurized to 8.3 MPa, the others were pressurized to 2.6 MPa. To determine whether stresses due to fuel-cladding mechanical interactions in a corrosive environment of fission products might lead to stress-corrosion-cracking of the cladding, chemical compounds to simulate oxygen activity and fission products in fuel with a burnup of about 18 MWd/kgU were added to Rods IE-020, IE-021, and IE-022.

The test was initiated with 28 hours of preconditioning power cycles at maximum fuel rod peak powers of 33 kW/m and included a time period of power oscillation to obtain gap conductance data. To evaluate the potential for pellet-cladding interaction induced cladding failure, the preconditioning phase was followed by a power ramp to an average (of four rods) fuel rod peak power of 65 kW/m at a ramp rate of 3.3 kW/m per minute. Axial elongation during the power ramp was 20 to 25% less for Rod IE-019 than the other rods, as a result of its high internal pressure. Although the diametral gap of Rod IE-021 was 0.046-mm larger than that of the other rods, rod elongation and fuel centerline temperatures were similar to the measured results of the remaining three rods. The rods were operated at high power for about one hour, and then subjected to a flow reduction phase to induce film boiling. Film boiling was first detected on Rod IE-022 at a mass flux for the rod of 1800 kg/s-m^2. The flow reduction was continued to 970 kg/s-m^2 to induce film boiling on the remaining rods for about one minute; afterwards the reactor was rapidly shut down. The maximum time in film boiling was 80 s. Postirradiation examination determined that maximum centerline temperatures in all rods were between 2800 to 3400 K and maximum cladding surface temperatures were about 1600 K.

Two fuel rod failures occurred during the test. Ten seconds after the onset of film boiling, the pressure transducer on Rod IE-019 indicated rod failure. Approximately 90 s after reactor shutdown, the pressure transducer on Rod IE-022 also indicated rod failure. Neither failure location could be visually discerned during postirradiation examination.

Results obtained from the most recent version of the FRAP-T fuel rod behavior computer code were compared with the steady state and transient data from this experiment to aid in understanding the data.

The overall behavior of these rods with irradiated cladding, except for the failure mode of Rod IE-019, was not significantly different from that previously experienced on similarly operated unirradiated fuel rods. The internal pressure of Rod IE-019, 6 MPa above the coolant pressure, produced cladding ballooning and failure during film boiling operation.

CONTENTS

FIGURES

TABLES

IRRADIATION EFFECTS TEST SERIES

TEST IE-5

TEST RESULTS REPORT

I. INTRODUCTION

The Irradiation Effects Test Series is being conducted under the Thermal Fuels Behavior Program by EG&G Idaho, Inc. as part of the Nuclear Regulatory Commission's Fuel Behavior Program[1] to define behavior of irradiated fuel rods during transient reactor conditions. The Irradiation Effects (IE) experiments, performed in conjunction with similar tests on unirradiated fuel rods, are designed to determine the effects of irradiation on fuel rod behavior in abnormal or accident conditions. This test series is directed toward providing a base of experimental data to satisfy one of the major objectives of the Fuel Behavior Program – the development of verified analytical models for calculating the behavior of irradiated fuel rods.

The purpose of this report is to present the results of Test IE-5, the last of the presently scheduled tests in the Irradiation Effects Test Series, which was conducted in the Power Burst Facility (PBF) at the Idaho National Engineering Laboratory. The objectives of this test were to evaluate the influence of simulated fission products, cladding irradiation damage, and fuel rod internal pressure on pellet-cladding interaction (PCI) during a power ramp and on fuel rod behavior during film boiling operation.

Four pressurized water reactor type fuel rods, with differences in simulated fission product content, diametral gap size, internal pressure, and cladding irradiation, were mounted in the central test space of the PBF reactor. These rods, contained in individual circular flow shrouds, were tested simultaneously under the same nominal operating conditions. A complete description of the fuel rods and test train is contained in Section II.

The test consisted of a series of preconditioning power cycles followed by a rapid power ramp, high power steady state period, and a power-cooling-mismatch transient initiated by a flow reduction at high power. A gap conductance test, which used a sinusoidal variation of reactor power to produce gap conductance data, was run early in the preconditioning period. Gap conductance test results, obtained as part of Test IE-5, will be reported separately. Discussion of the test conduct is contained in Section III.

Sections IV and V summarize the test results and the preliminary postirradiation examination results, respectively. Section VI contains detailed experimental results and a comparison of calculated and measured fuel rod behavior data. (Comparison of calculations from a fuel rod behavior computer model with the test results was performed to aid interpretation of the data.) Discussion of the results relative to the test objectives and conclusions regarding the test results are presented in Sections VII and VIII, respectively.

Appendix A contains pretest fuel rod characterization data. An assessment of the instrumentation and data acquisition system uncertainties is presented in Appendix B. Additional test data not presented in the main body of the report and a discussion of the methods used to reduce the test data are contained in Appendix C. Appendix D presents results of a detailed power calibration based on neutron flux wire and self-powered neutron detector data. Discussion of the fuel rod behavior computer model used in conjunction with this test appears in Appendix E.

II. EXPERIMENT DESCRIPTION

The Power Burst Facility consists of an open tank reactor vessel, a driver core region with an active fuel length of 0.91 m, a central flux trap region containing an in-pile tube (IPT), and a loop coolant system providing an environment typical of pressurized water reactor system conditions. The reentrant IPT, which encloses the test space, has inlet and outlet connections for loop coolant flow located at its upper end above the driver core. The coolant enters the top of the IPT and is directed downward on the outside of a flow tube which surrounds the test assembly. At the bottom of the IPT, the coolant flow reverses direction and flows up through the test assembly to the IPT outlet.

A separate flow shroud was used to contain each fuel rod within the IPT. Hence, the fuel rods were hydraulically and thermally isolated from interacting with one another, essentially allowing four single fuel rods to be tested simultaneously. Each fuel rod and flow shroud assembly was instrumented to monitor fuel behavior during nuclear operations. The test train and flow shrouds, fuel rods, and the associated instrumentation are described in this section.

1. TEST TRAIN AND FLOW SHROUDS

The test train symmetrically positioned the four fuel rods in the IPT as shown in Figure 1. A cross-sectional view of the test train assembly presented in Figure 2 defines the relative location of each flow shroud and the self-powered neutron detector (SPND) support tubes.

The flow shrouds, fabricated from zircaloy-4, had a nominal inside diameter of 16.31 mm and a wall thickness of 3.15 mm. Hydraulic and equivalent heated diameters were 6.35 mm and 16.75 mm, respectively, for 9.95 mm diameter fuel rods. The locations of the SPND support tubes relative to the flow shrouds are also shown in Figure 2. A flow shroud with an instrumented fuel rod installed is shown in Figure 3.

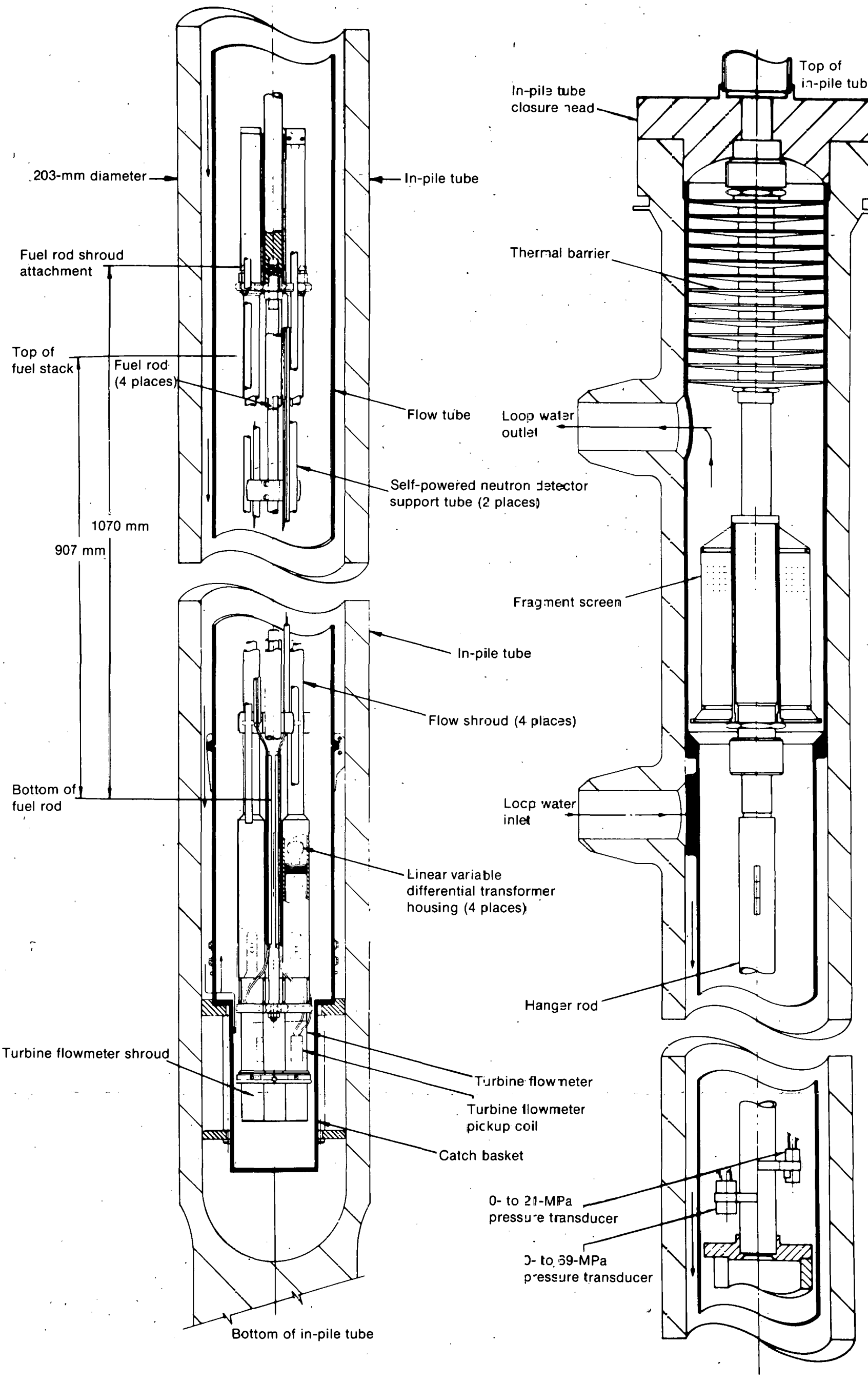

Fig. 1 Test IE-5 four-rod experiment assembly and instrumentation shown installed in the PBF in-pile tube.

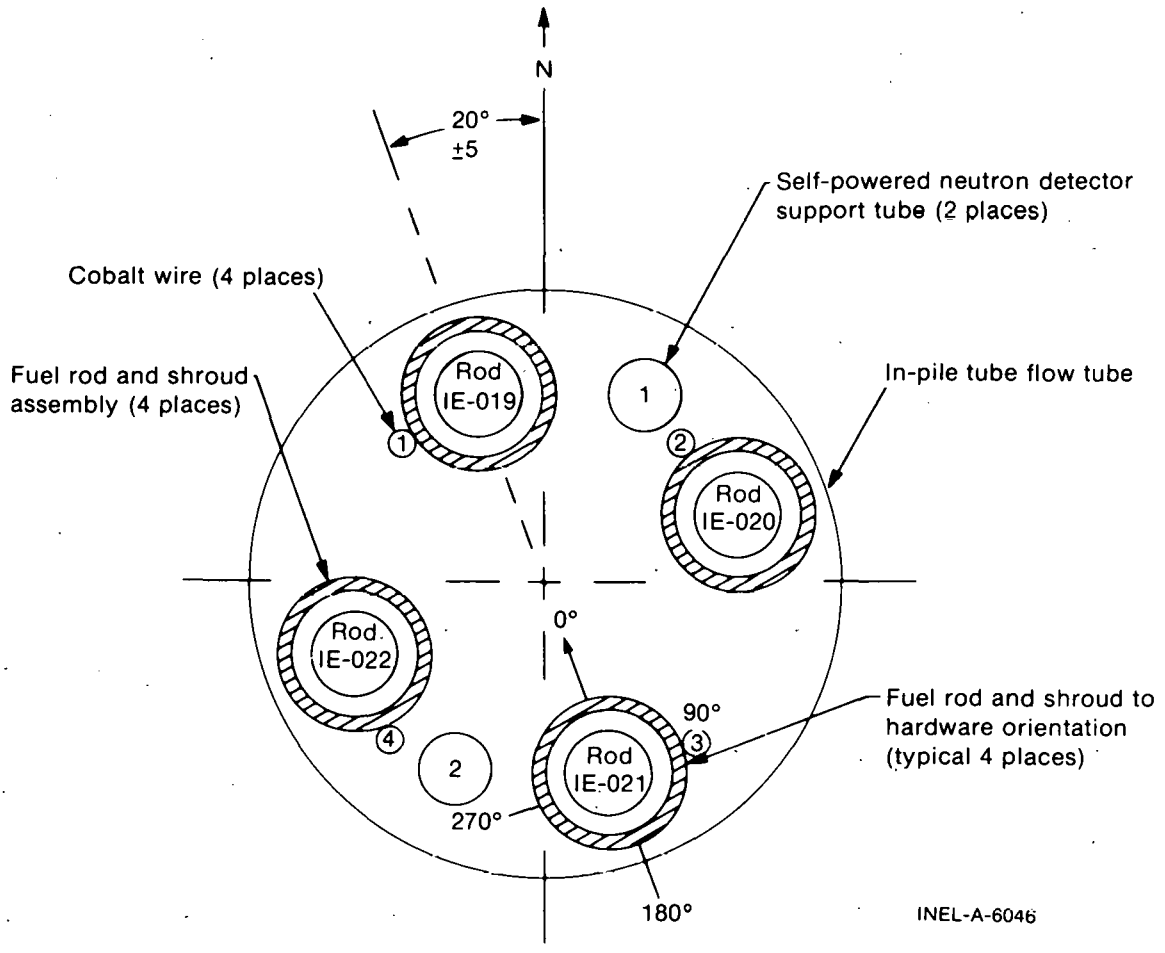

Fig. 2 Top view of Test IE-5 hardware orientation in the PBF in-pile tube.

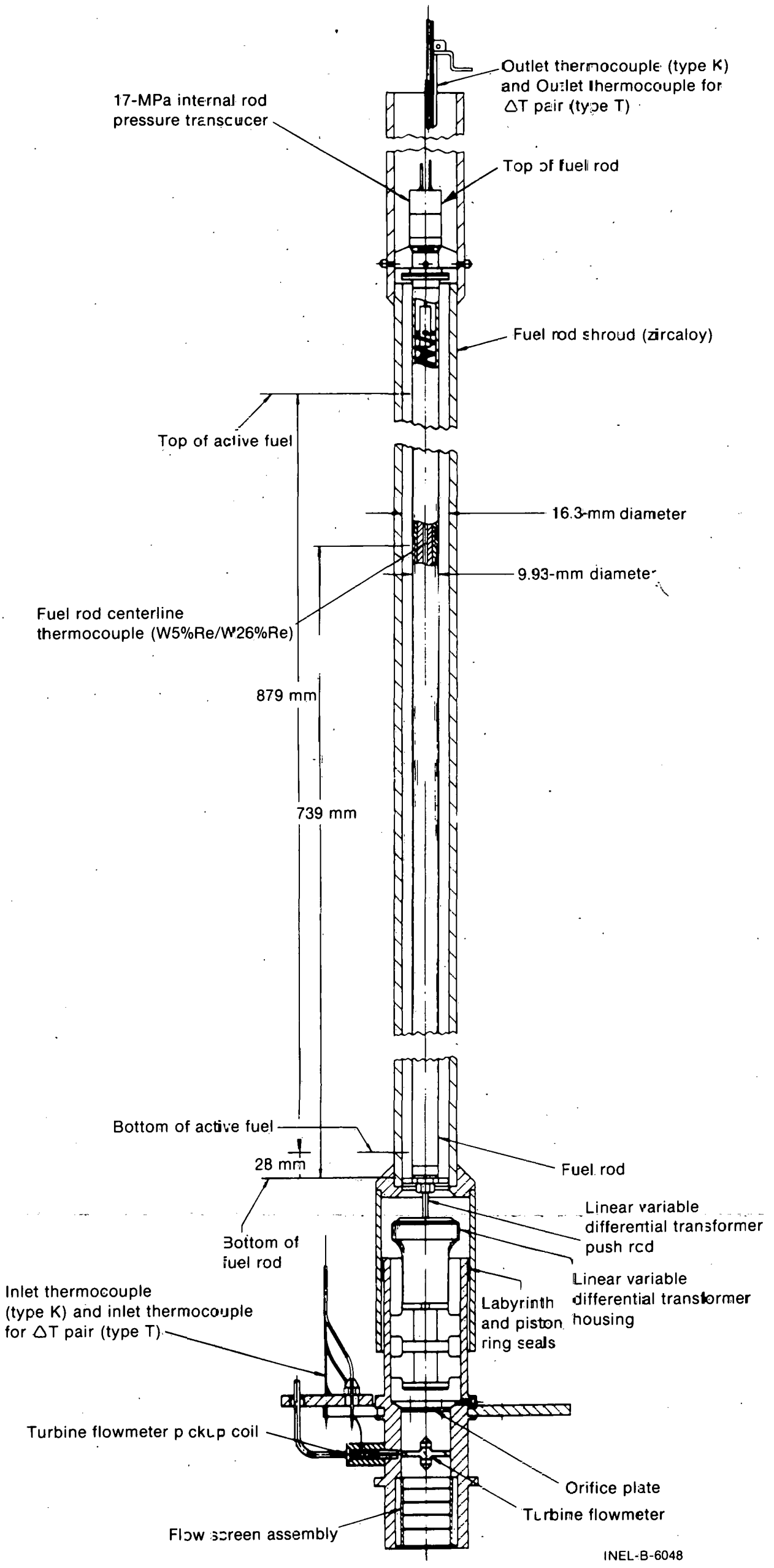

Fig. 3 Typical configuration of flow shroud with instrumented fuel rod for Test IE-5.

2. FUEL RODS

The four fuel rods, Rods IE-019, IE-020, IE-021, and IE-022, contained unirradiated 12.4 wt% $^{235}UO_2$ dished fuel pellets. Rods IE-019, IE-020, and IE-021 were fabricated from irradiated zircaloy-4 cladding and Rod IE-022 was assembled from unirradiated zircaloy-4 cladding. The fuel rods were approximately 0.97-m long (not including the instrumented end cap) and had a nomimal active fuel stack length of 0.879 m. A summary of selected pretest information describing the fuel rods is contained in Table I. Complete pretest cladding and fuel pellet characterization data for each fuel rod are given in Appendix A.

Rods IE-019 and IE-020 were fabricated from irradiated zircaloy-4 cladding tubes W06 and W08 that were used to fill open lattice locations in extended burnup tests in the Saxton reactor[a]. Peak fluences are estimated to be 9.9×10^{20} and 9.3×10^{20} neutrons/cm^2 (> 1 MeV) for tubes W06 and W08, respectively[2]. Scans of both tubes using pulsed-eddy-current inspection equipment[3] indicated a small decrease in cladding wall thickness of 0.01 mm from the bottom to the top of the tubes. The outside diameter of the fuel pellets was ground to produce a nominal 0.09-mm fuel-cladding diametral gap in both rods. The upper pellets in both rods were drilled to accommodate a centerline thermocouple. The upper end of the rod was sealed with an end cap containing a pressure transducer.

Rod IE-021 was fabricated from MAPI[a] Rod M-23, irradiated in the Saxton reactor to an approximate burnup of 3.78 MWd/kgU[2]. The estimated peak cladding fluence received by this rod was 3.05×10^{20} neutrons/cm^2 (> 1 MeV). The rod was filled with air at a pressure of 0.1 MPa during its irradiation in the Saxton reactor. The cladding inside diameter was 0.046-mm larger than the nominal inside diameter of the other rods in this test, thus producing a larger diametral gap of 0.138 mm. Measurements also indicated that the cladding inside diameter between the 0.40- and 0.75-m elevations was approximately 0.02-mm larger than at the ends of the tube. Fuel pellets at the top of the column were drilled to accommodate a centerline ultrasonic thermometer. An upper end cap containing a pressure transducer sealed the top of the rod.

Rod IE-022 was fabricated from the unirradiated cladding of Saxton Rod 930. The fuel-cladding diametral gap was 0.092 mm, similar to that of Rods IE-019 and IE-020. Fuel pellets at the top of the fuel column were drilled to accommodate a centerline ultrasonic thermometer. The rod was sealed with an end cap instrumented with a pressure transducer.

---

[a] The Saxton Reactor was designed by Westinghouse Electric Corporation for the USAEC. The reactor was a small, prototypic, pressurized water reactor.

[b] Mitsubishi Atomic Power Industries of Japan.

TABLE I

CHARACTERISTICS OF FUEL RODS USED IN TEST IE-5

Parameter	Rod			
	IE-019	IE-020	IE-021	IE-022
Cladding Identification	WO6	WO8	M-23	930
Estimated Peak Cladding Fluence (neutrons/cm^2>1MeV)	9.9×10^{20}	9.3×10^{20}	3.1×10^{20}	0
Fuel Density (% TD)	94.0	94.0	94.0	94.0
Smear Density (% TD)	92.0	92.0	91.1	92.0
Fission Product Simulation	No	Yes	Yes	Yes
Cladding Length (m)	0.97	0.97	0.97	0.97
Mean Cladding OD (mm)	9.931	9.931	9.995	9.933
Mean Cladding Thickness (mm)	0.604	0.600	0.609	0.601
Mean Diametral Gap (mm)	0.091	0.092	0.138	0.092
Measured Void Volume (ml)	6.5	6.7	[a]	7.9
Pressure (MPa) (cold, at time of assembly)	8.3	2.5	2.5	2.6

[a] Not measured for this rod.

Chemical compounds were added to every third pellet in the fuel stacks of Rods IE-020, IE-021, and IE-022 to simulate oxygen activity and accumulations of cesium, molybdenum, tellurium, and iodine fission products in fuel with a burnup of about 18 MWd/kgU. The purpose of the added compounds was to determine whether stresses due to pellet-cladding mechanical interactions during a power ramp in a corrosive environment of fission products might lead to stress-corrosion-cracking of the cladding. The simulated fission products, inserted into holes drilled in 17 of the 56 fuel pellets of each fuel stack as shown in Figure 4, were composed of 34 mg of cesium iodide, 453 mg of cesium molybdate, and 37 mg of tellurium. These quantities correspond to the mass of UO_2 fuel expected to release volatile fission products during a power-coolant-mismatch event which melts about 25% of the fuel volume. Thermophysical properties of these materials are contained in Table II. The mass of UO_2 in each stack was approximately 515 g.

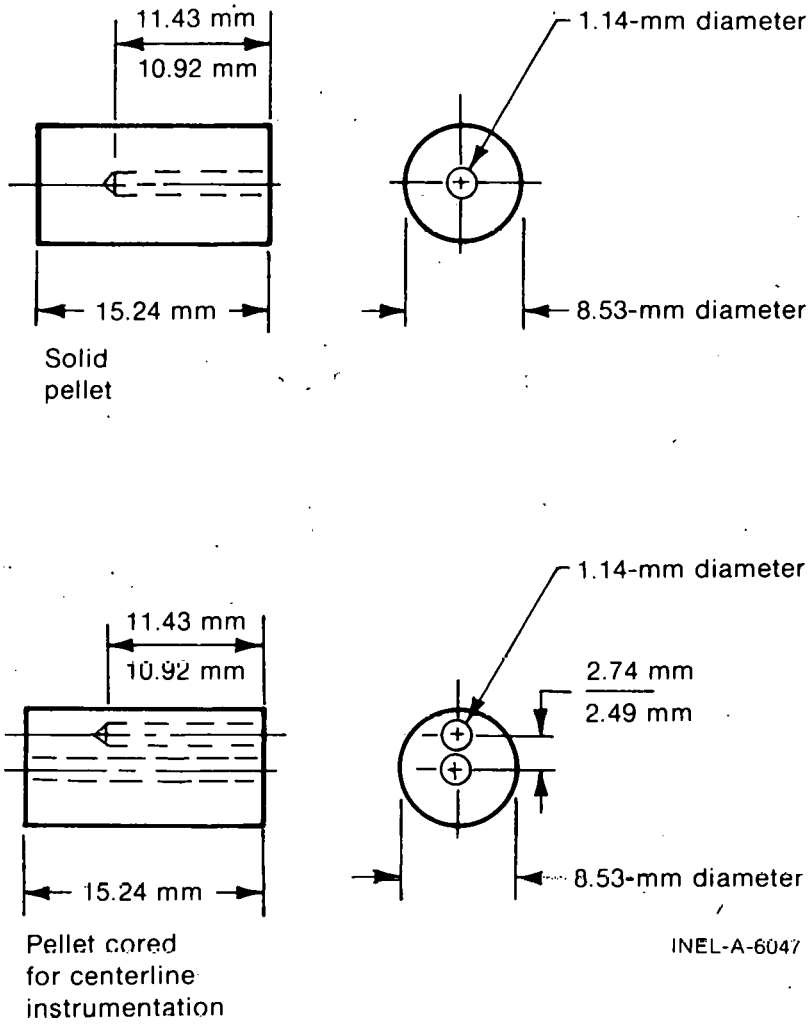

Fig. 4 Illustration of hole within Test IE-5 fuel pellets for accommodating simulated fission products.

TABLE II

THERMOPHYSICAL PROPERTIES OF SIMULATED FISSION PRODUCTS

Material	Melting Point (K)	Boiling Point (K)	Density (g/cm^3)
CsI	894	1553	4.51
Cs_2MoO_4	1200 to 1215	--	--
Te_2	725	1663	6.25

After fabrication, all four fuel rods were backfilled with a 77.7% helium and 22.3% argon gas mixture which has a thermal conductivity similar to the calculated thermal conductivity of the gases removed from irradiated Saxton fuel rods. Rod IE-019 was pressurized to 8.3 MPa (at room temperature) to study the cladding ballooning phenomenon under film boiling conditions. The internal pressure of Rod IE-019 was expected to be approximately 6 MPa above system pressure just prior to the flow reduction transient. The remaining rods were pressurized to approximately 2.5 MPa prior to the test.

3. INSTRUMENTATION

Instrumentation was provided to monitor fuel rod behavior and coolant conditions in each flow shroud during the test. A listing of transducer calibrations and error analyses for the test instruments is given in Appendix B. The test instrumentation was divided into two classifications: test trains instrumentation and fuel rod instrumentation.

3.1 Test Train Instrumentation

The test train instrumentation consisted of the following:

(1) One 0- to 21-MPa and one 0- to 69-MPa strain post type pressure transducer measured the system coolant pressure during the test. Both were positioned in the IPT above the fuel rod assembly as was shown in Figure 1.

(2) A turbine flowmeter was installed on each flow shroud inlet to measure coolant flow. These components were shown in Figure 3.

(3) A calibrated copper-constantan (Type-T) differential thermocouple pair measured the coolant temperature rise across each flow shroud. (The coolant temperature increase, along with the measured coolant flow rate, was used in calculating fuel rod average power for each fuel rod.)

(4) Two magnesium oxide insulated Chromel-Alumel (Type K) thermocouples were positioned near the inlet of the test train assembly to measure the coolant inlet temperature. The coolant outlet temperature of each of the four shrouds was monitored with a similar Type K thermocouple.

(5) One linear variable differential transformer (LVDT), at the bottom of each fuel rod, as was shown in Figure 3, measured changes in fuel rod cladding length. The primary and each of the two secondary coils of the transformer were wound with 500 and 450 turns, respectively, of nickel clad copper wire. The core of the transformer was fabricated from Type 17-4 heat treated stainless steel.

(6) Ten, 0.10-m long, cobalt SPNDS were in two vertical columns of five detectors each, 180 degrees apart in the test train assembly. The locations of these devices relative to the test train are shown in Figure 5. These devices measured the relative axial neutron flux in the IPT during the test. Each column of SPNDs was located with centers at 0.16, 0.31, 0.47, 0.62, and 0.78 m from the bottom of the active core.

(7) A cobalt wire, mounted on the outside of each flow shroud, monitored the axial neutron flux profile in the IPT. The cobalt wire azimuthal locations were shown in Figure 2. The cobalt wires extended beyond the bottom and top of the active core.

3.2 Fuel Rod Instrumentation

The fuel rod instrumentation consisted of the following:

(1) One 0- to 21-MPa strain post type pressure transducer monitored the internal pressure of Rod IE-019. One 0- to 17-MPa pressure transducer was mounted on each of the remaining three rods.

(2) A calibrated thermocouple composed of a 1.57-mm-diameter, tungsten-rhenium (W5%Re/W26%Re) alloy wire with a segmented hard-fired beryllium oxide insulation and a tantalum

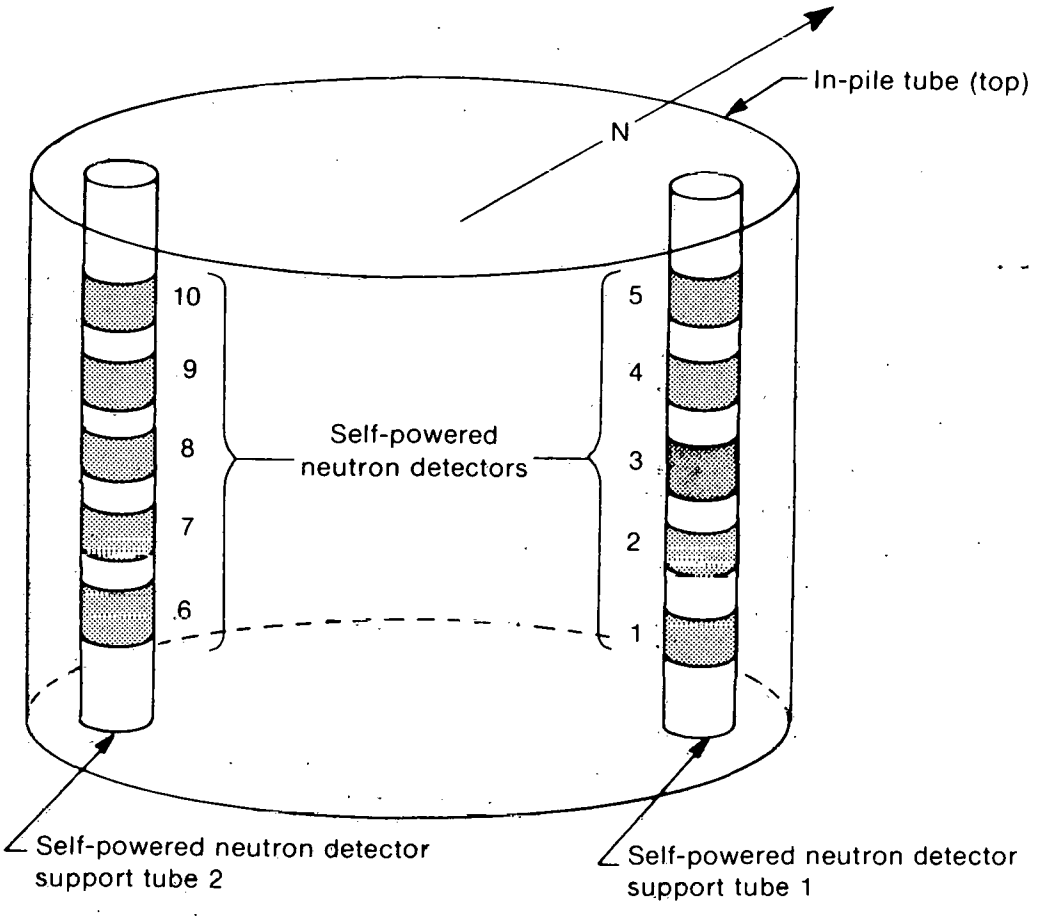

Fig. 5 Orientation of Test IE-5 self-powered neutron detectors.

sheath measured the fuel centerline temperature on Rods IE-019 and IE-020. These thermocouples were inserted into the top of the fuel column through drilled fuel pellets with the junction at the 0.739-m rod elevation[a].

(3) An ultrasonic thermometer (UT) with an active length of 10 cm measured the fuel centerline temperature in each of Rods IE-021 and IE-022. Both UTs used floating sheaths. The devices were inserted into the top of the fuel column through drilled fuel pellets and centered at 0.637 m.

(4) Cladding surface thermocouples were attached on the cladding surface of all rods. Two Chromel-Alumel (Type K) thermocouples were brazed on Rod IE-019 at axial elevations of 0.644 and 0.646 m and azimuthal positions of 45 and

[a] All rod elevations are referenced from the bottom of the fuel rod. The fuel column starts at 27.6 mm above the bottom of the fuel rod.

225 degrees, respectively. Rods IE-020 and IE-021 each had two platinum-10% rhodium/platinum (Type S) thermocouples brazed on the cladding at similar elevations and orientations. The 45- and 225-degree thermocouples on Rod IE-020 were located at 0.641 and 0.646 m, respectively. Both the 45- and 225-degree thermocouples on Rod IE-021 were located at 0.643 m. Four spaded-tip Type S thermocouples were brazed, then laser welded in 0.25-mm deep grooves on Rod IE-022 at elevations of 0.538 m (135 degrees), 0.641 m (45 and 225 degrees), and 0.743 m (315 degrees). The orientations and locations of the thermocouples on Rod IE-022 are shown in Figure 6.

Thermocouple	Orientation	Distance from bottom of fuel rod (m)	Distance from bottom of active fuel (m)
A	45°	0.641	0.613
B	135°	0.538	0.510
C	225°	0.641	0.613
D	315°	0.743	0.715

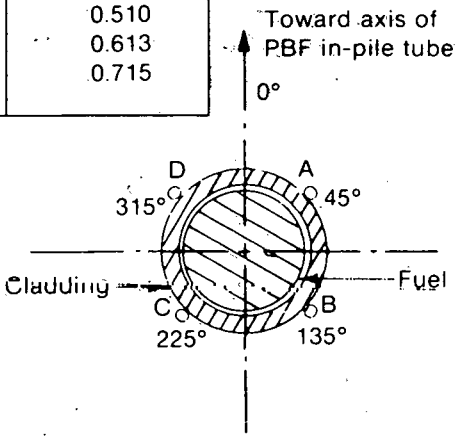

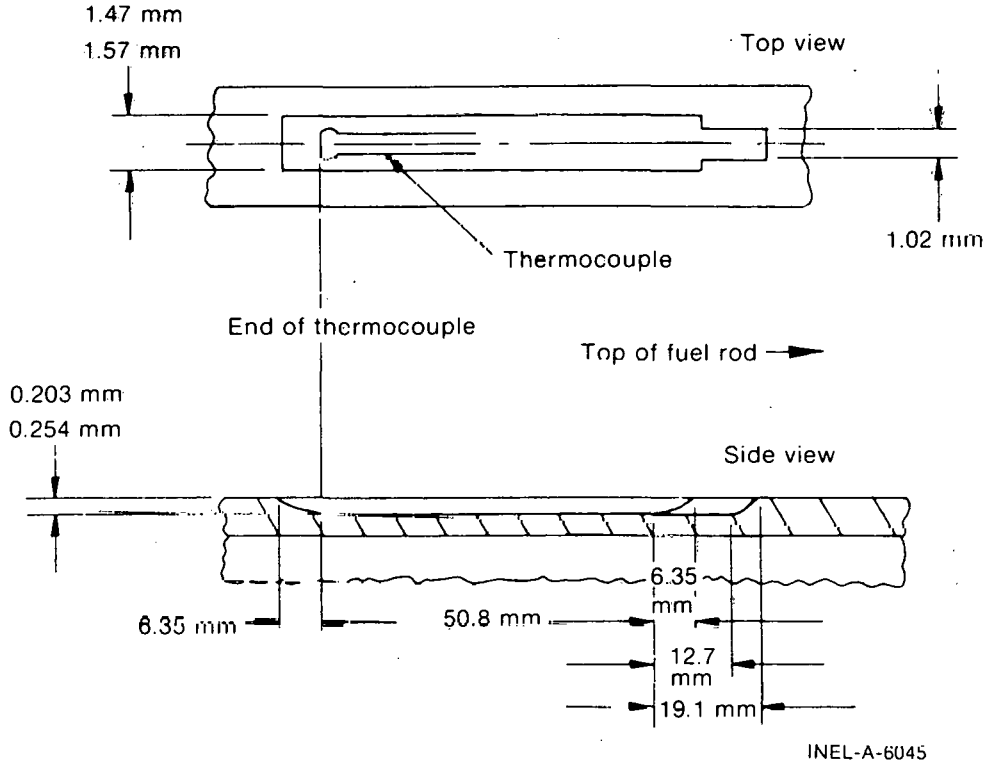

Fig. 6 Orientation and location of Type S thermocouples on Rod IE-022.

III. EXPERIMENT CONDUCT

Test IE-5 consisted of four different operational phases which spanned 29 hours of nuclear operation commencing on January 17, 1977: (a) a preconditioning phase, (b) a rapid ramp to high power, (c) a steady state operation, and (d) a flow reduction which induced film boiling on the rods.

1. PRECONDITIONING

The operating procedure for preconditioning was designed to (a) study the effects of inlet temperature, coolant flow rate, and reactor power and time on fuel rod and test train measurements, and (b) to provide data for a thermal-hydraulic power calibration of each fuel rod. In addition, the preconditioning period was conducted to produce typical fuel pellet crack patterns and fuel relocation.

The preconditioning phase consisted of five cycles, as shown in Figure 7. The first two cycles, with eight steps each, were performed at all possible combinations of coolant flow rate (500 and 750 cm^3/s), inlet temperature (585 and 606 K), and fuel rod average power (23 and 30 kW/m)[a]. The rod average power was slowly increased at a rate of 0.20 kW/m per minute up to the first power step. Subsequent scheduled power changes were completed at ramp rates of 0.50 kW/m per minute.

Cycle 3, testing of the fuel rod gap conductance, consisted of power oscillations of ±20% at nominal fuel rod peak powers of 14 and 23 kW/m. The flow rate was also varied, ranging from 379 to 757 cm^3/s. The inlet temperature remained constant at 555 K. No attempt was made to analyze the gap conductance data for this report. These data were presented only to show the complete sequence of the fuel rod preconditioning phase.

The gap conductance portion of the test was terminated prematurely at 19.4 hours into the test on January 18, 1977, to repair the flow control valve of the PBF in-pile loop. While the reactor was shut down for repairs, amplifier range changes and instrument calibrations were performed. Repair and checkout of the valve required approximately one week and on January 25, 1977, nuclear operation of Test IE-5 resumed. The data shown in Figure 7 and in similar figures spanning the preconditioning phase do not show this lapse in time. The data from the portion of the test that followed the gap conductance testing has been arbitrarily restarted at 21.0 hours for presentation purposes.

---

[a] The combination of flow rate, inlet temperature, and rod linear heat rating was chosen using a 2^3 factorial design with one complete replicate to provide estimates of variances. The steps were randomly arranged in time with a constraint on the inlet temperature as shown in Figure 7. The design was additionally constrained so that the effect of time, electronic drift, . . . , was confounded with the three factor interaction.

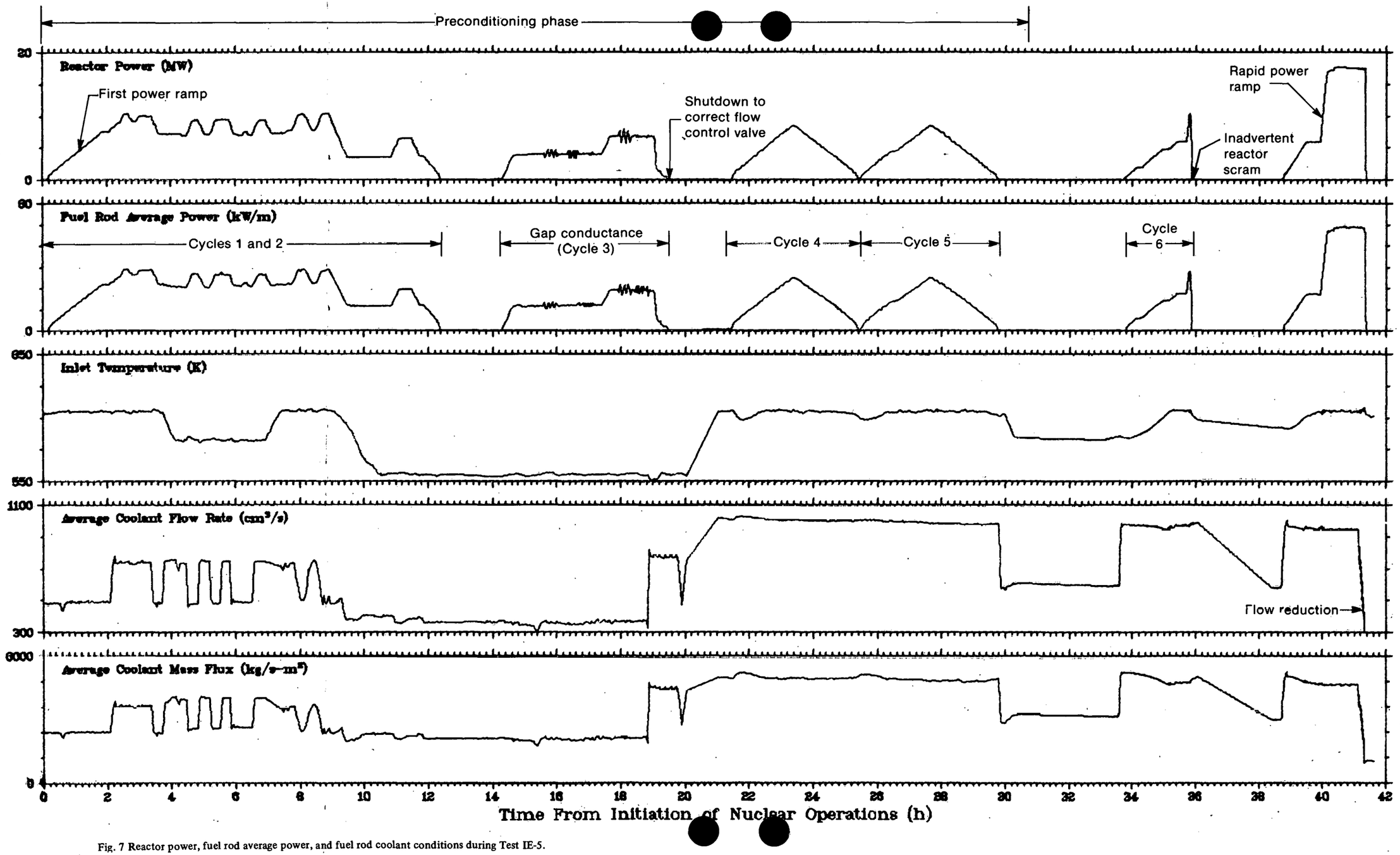

Fig. 7 Reactor power, fuel rod average power, and fuel rod coolant conditions during Test IE-5.

Cycles 4 and 5 consisted of a ramp from zero power to a fuel rod average power of 26 kW/m and a return to zero power at a rate of change of the average power of 0.2 kW/m per minute. Nominal coolant mass flux and inlet temperatures were constant at 4880 kg/s-m^2 (1000 cm^3/s) and 606 K, respectively.

2. POWER RAMP AND STEADY STATE OPERATION

The second and third phases of Test IE-5 consisted of a power ramp and a one-hour period of steady state operation at a high fuel rod power. The power ramp was performed to provide data on pellet-cladding interaction. The steady state operation at high power was conducted to degas the outside surface of the cladding and to evaluate the potential of chemically assisted stress-corrosion-cracking following the power ramp.

Prior to initiating the rapid power ramp the fuel rod peak power was raised to 24 kW/m (Cycle 6). However, after the power ramp was initiated a reactor scram occurred. Afterwards, the fuel rods were returned to a peak power of 24 kW/m. The fuel rod peak power was then increased at a ramp rate of 3.3 kW/m per minute up to an average fuel rod peak power of 63 kW/m.

Following the power ramp, the fuel rods were operated under steady state conditions. The coolant inlet temperature and mass flux remained constant at 605 K and 4880 kg/s-m^2, respectively. During steady state conditions a calculation of fuel rod average power using coolant flow and temperature differential measurements indicated that the fuel rods had peak powers of 60.5, 65.2, 60.7, and 66.7 kW/m for Rods IE-019, IE-020, IE-021, and IE-022, respectively. After about 13 minutes, the reactor power was increased 3% to achieve slightly higher fuel rod peak powers of 62.3, 67.5, 62.8, and 68.6 kW/m in the four rods, respectively. The reactor power and coolant conditions were held constant for an additional 45 minutes to complete the steady state operation.

3. FLOW REDUCTION

After 45 minutes at an average fuel rod peak power of 65 kW/m and a total time of about one hour at nearly constant power and coolant conditions, the flow reduction phase of the test was initiated to sudy integral fuel rod behavior after departure from nucleate boiling (DNB) and during stable film boiling. The fuel rod coolant mass fluxes, nominally the same, 4880 kg/s-m^2 (1000 cm^3/s), for all four rods, were reduced in steps of approximately 240 kg/s-m^2. The mass flux held constant for about one minute after each step. Figure 8 illustrates the test conditions toward the end of the flow reduction phase. At a mass flux of 1800 kg/s-m^2, the LVDT on Rod IE-022 indicated the onset of film boiling. Ten seconds later, the mass flux was reduced to 1154 kg/s-m^2 and film boiling was indicated on the remaining fuel rods. An additional flow reduction to 970 kg/s-m^2 was performed in

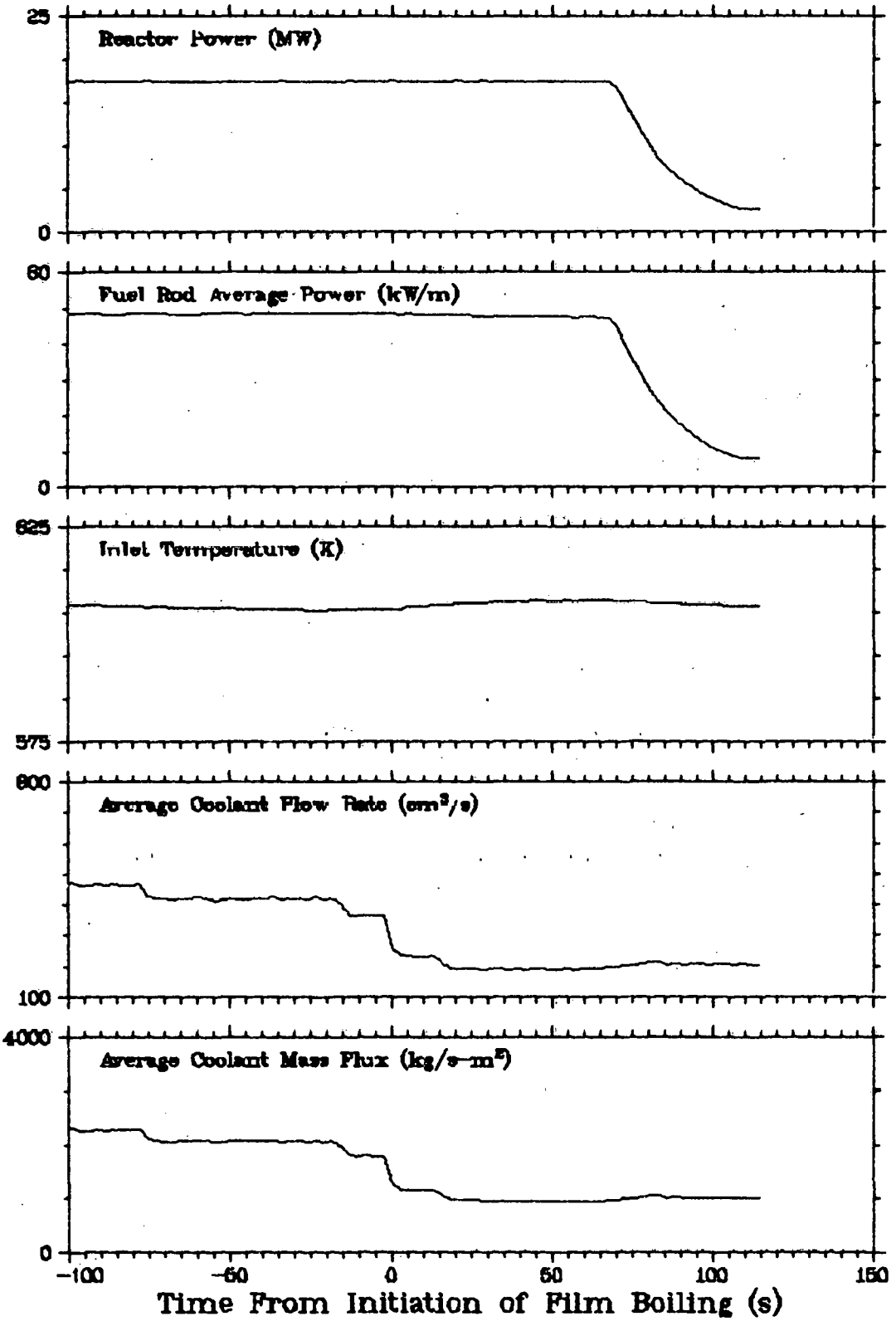

Fig. 8 Reactor power, fuel rod average power, and fuel rod coolant conditions during the flow reduction phase of Test IE-5.

another 10 s. The flow and power were than held constant for about 60 s after which the reactor was shut down. Film boiling on the test fuel rods ceased as the control rods were inserted into the reactor core.

IV. SUMMARY OF TEST RESULTS

The key test results are presented in this section in the form of history plots. Some plots cover the entire test and others cover only the time of the film boiling operation. This format is intended to give the reader an overview of the behavior of each rod during these two time periods. An in-depth discussion of the data is included in Section VI. Minor adjustments and corrections were made for parts of the cladding elongation and rod internal pressure plots in this section and in Section VI. The cladding elongation data were also adjusted to zero at the start of the test. The pressure transducer data were corrected for large zero drifts due to instrument decalibration. These and other aspects of the data reduction process are described in Appendix C.

Test data for the four rods are shown in Figures 9 through 12. Fuel rod average powers were calculated using a thermal balance, and then local and peak powers were calculated using data from two columns of five axially distributed SPNDs and four cobalt flux wires (the specific calculational techniques are discussed in Appendix D). On an average, pellet-cladding interaction occurred at less than 2 kW/m during the first power ramp. After several power cycles, the effective pellet-cladding gap enlarged and the rod peak power at which PCI occurred increased to 20 kW/m. After equilibrium was established, Rod IE-019 experienced the onset of PCI at higher power levels than the remaining three rods, perhaps due to the higher initial internal rod pressure. The occurrence of fuel and cladding creep was evident above rod peak powers of 35 kW/m during the ramp to high power and the one-hour period of steady state operation at 65 kW/m. Fuel centerline temperatures on Rods IE-021 and IE-022 were not recorded during this one-hour period because both ultrasonic thermometers failed.

Data from the four rods during film boiling operation are shown in Figures 13 through 16. Flow reduction steps are illustrated in the plots of coolant mass flux versus time. Rod powers during the flow reduction were determined from the neutron flux normalized to the rod power obtained during steady state operation. Film boiling was characterized by internal pressure variations and increases in cladding elongation, fuel centerline temperature, and cladding surface temperature.

Film boiling was first indicated by a change in cladding elongation on Rod IE-022, the rod with highest power at a mass flux of 1800 kg/s-m^2. The flow was reduced to induce film boiling on Rods IE-019, IE-020, and IE-021 at coolant mass fluxes of 1275, 1315, and 1210 kg/s-m^2, respectively. At the onset of film boiling on Rod IE-019, the internal pressure decreased, indicating possible cladding swelling or ballooning. Ten seconds after the initiation of film boiling on Rod IE-019, the pressure decreased to the coolant pressure, indicating a cladding failure. Rod IE-022 remained in film boiling for approximately 80 s; all other rods, approximately 70 s. Approximately 90 s after reactor shutdown, a pressure increase within Rod IE-022 indicated rod failure. Neither the failure location on Rod IE-019 nor the one on Rod IE-022 were visually discernible during the postirradiation examination discussed in the following section.

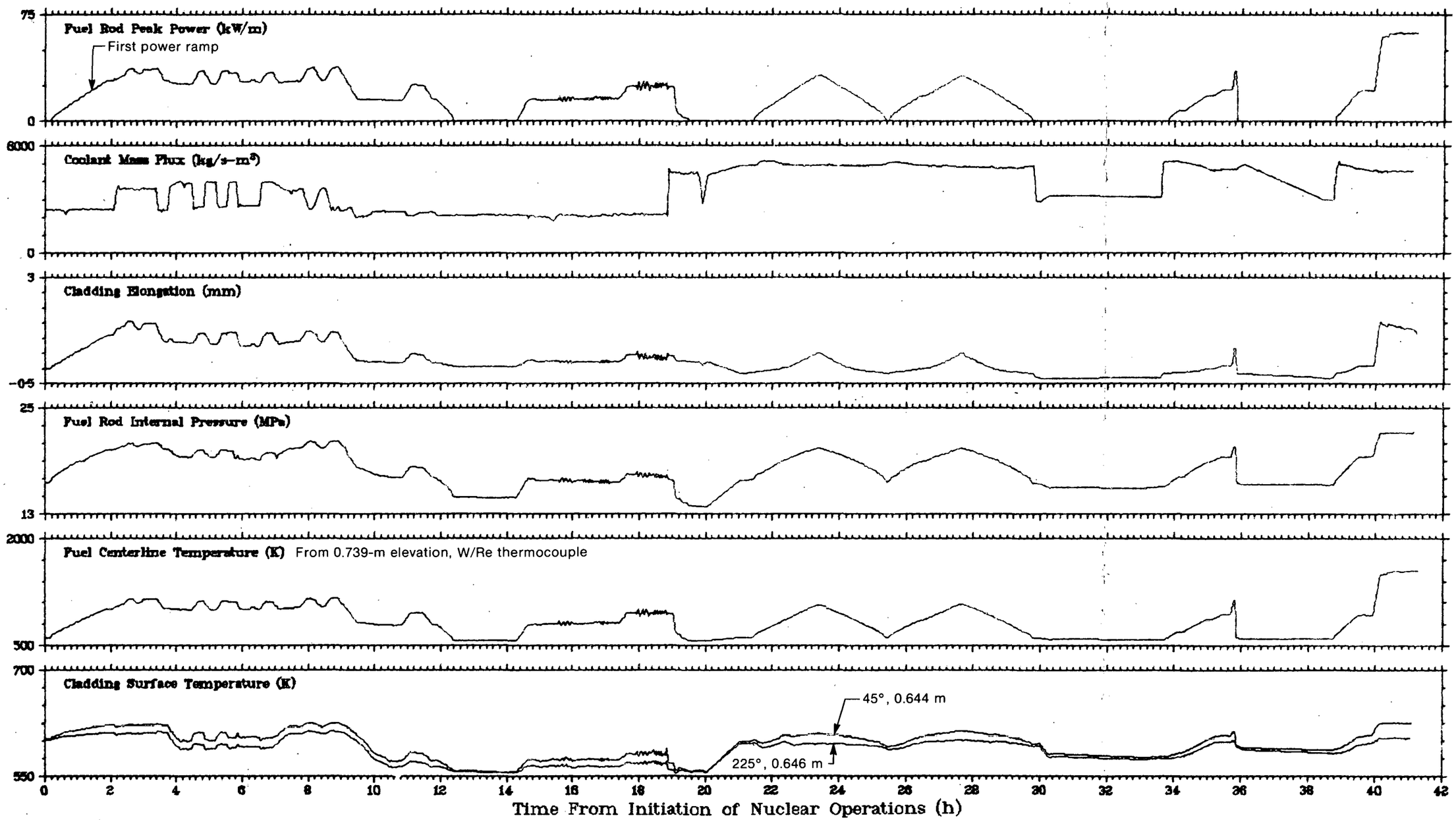

Fig. 9 Rod IE-019 behavior data during Test IE-5.

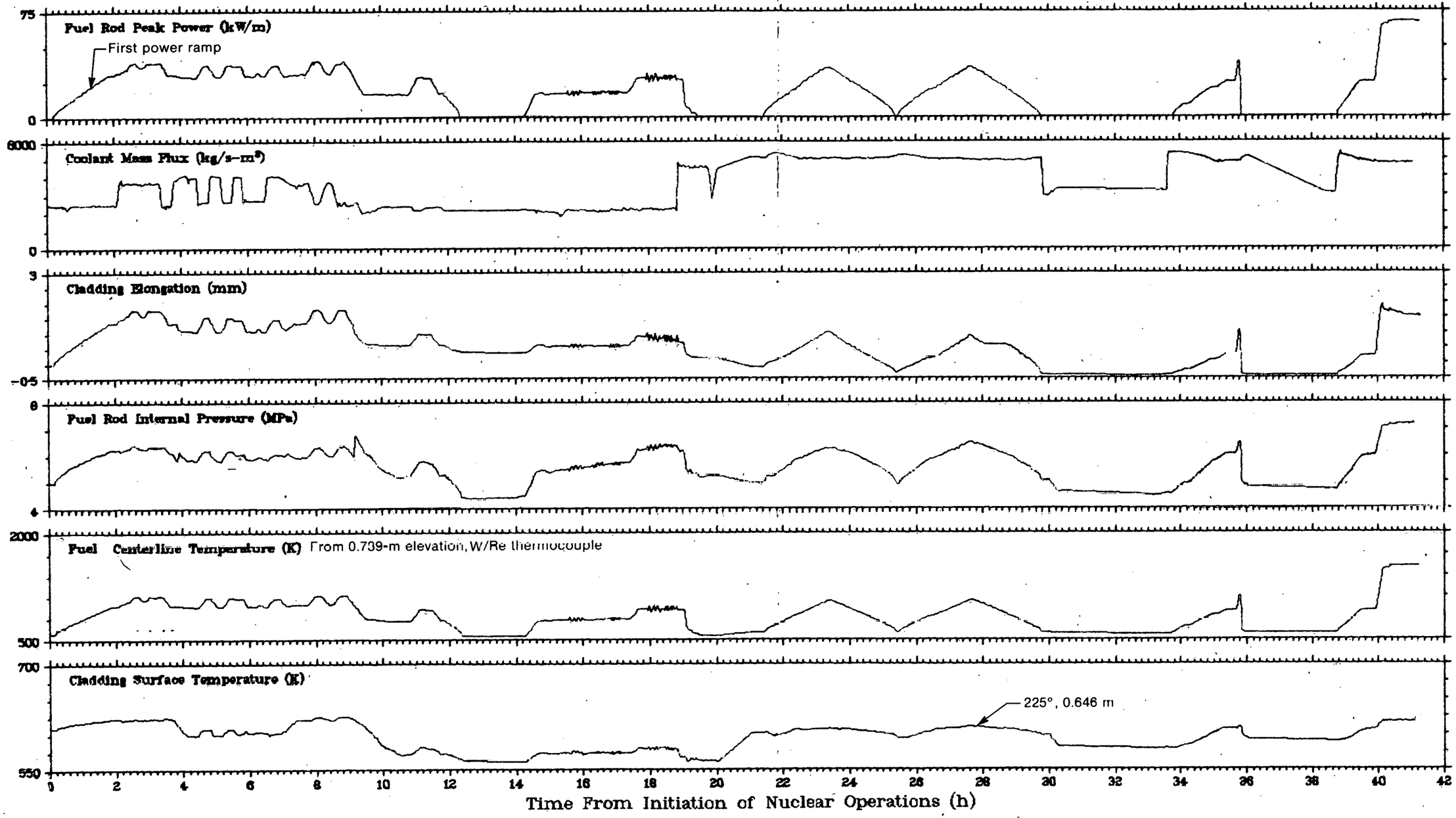

Fig. 10 Rod 1E-020 behavior data during Test IE-5.

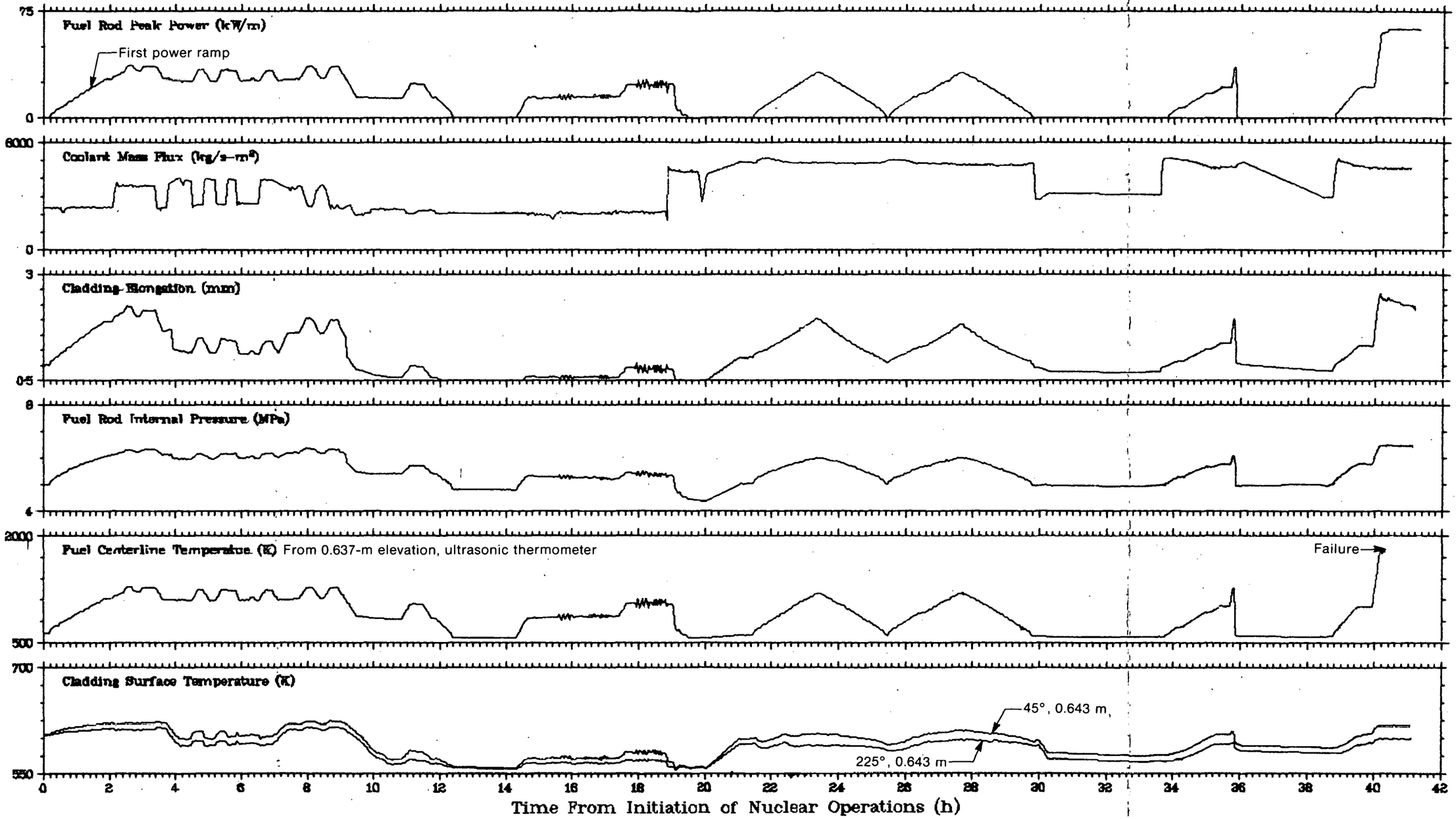

Fig. 11 Rod IE-021 behavior data during Test IE-5.

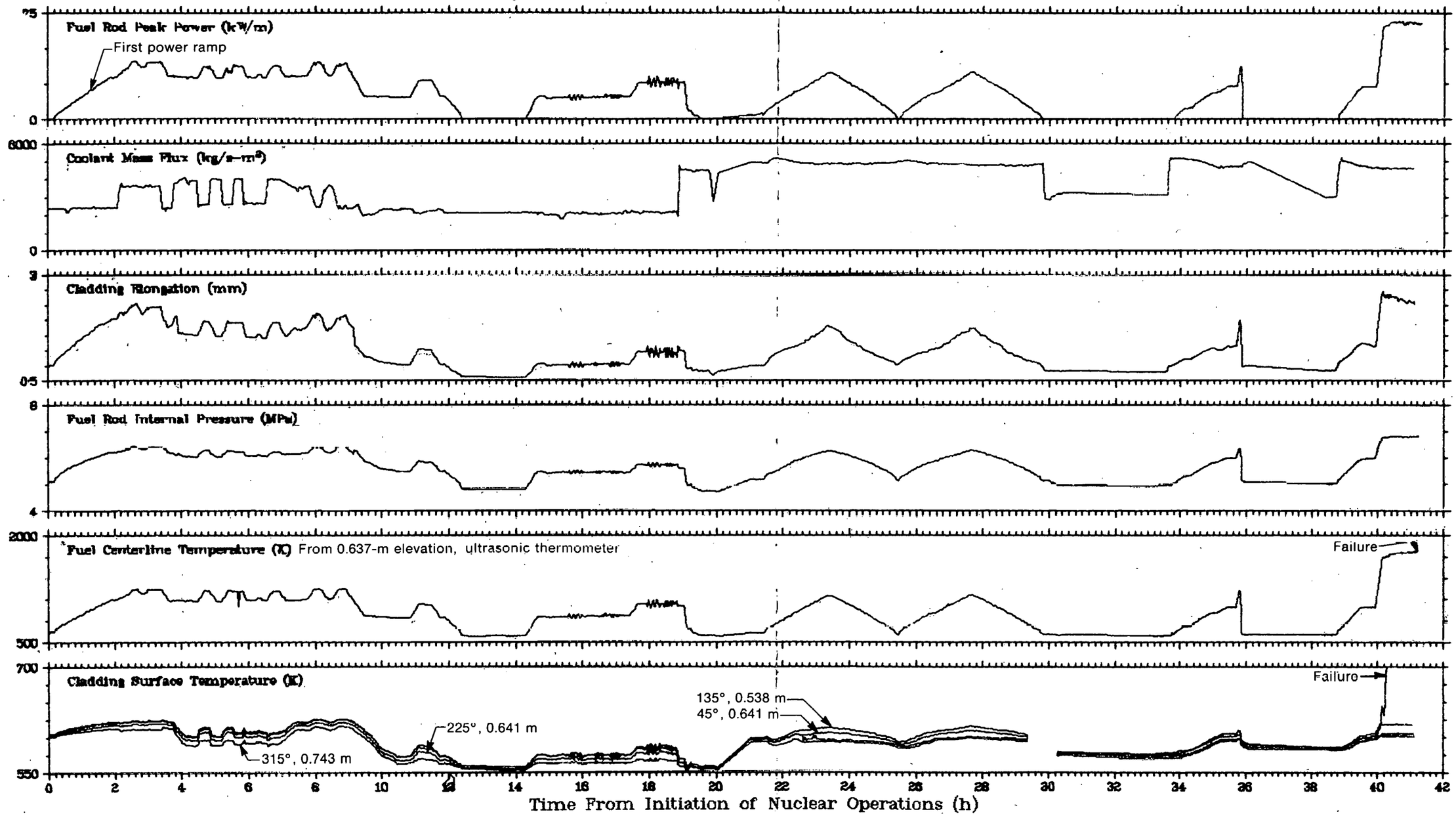

Fig. 12 Rod IE-022 behavior data during Test IE-5.

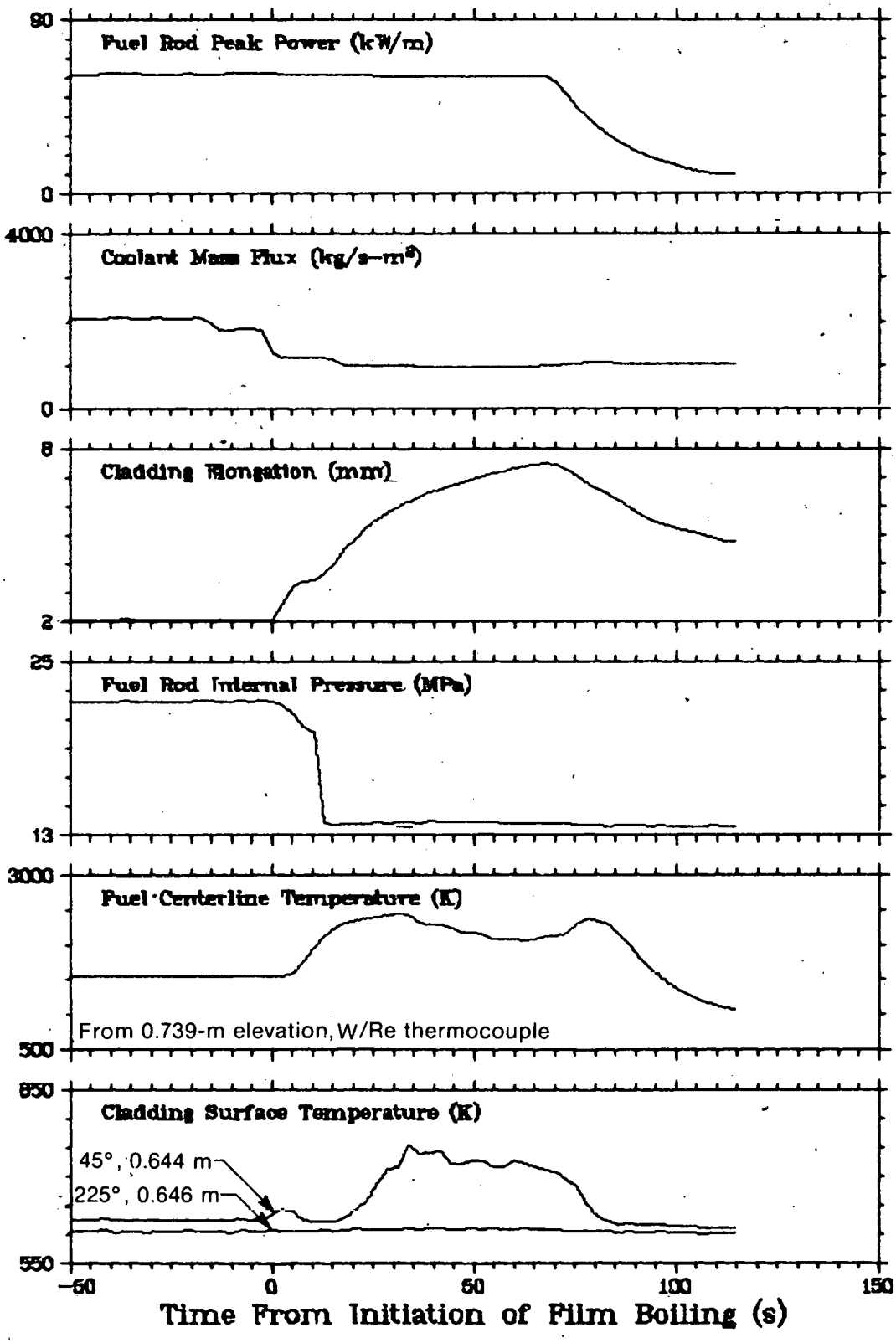

Fig. 13 Rod IE-019 behavior data during film boiling operation.

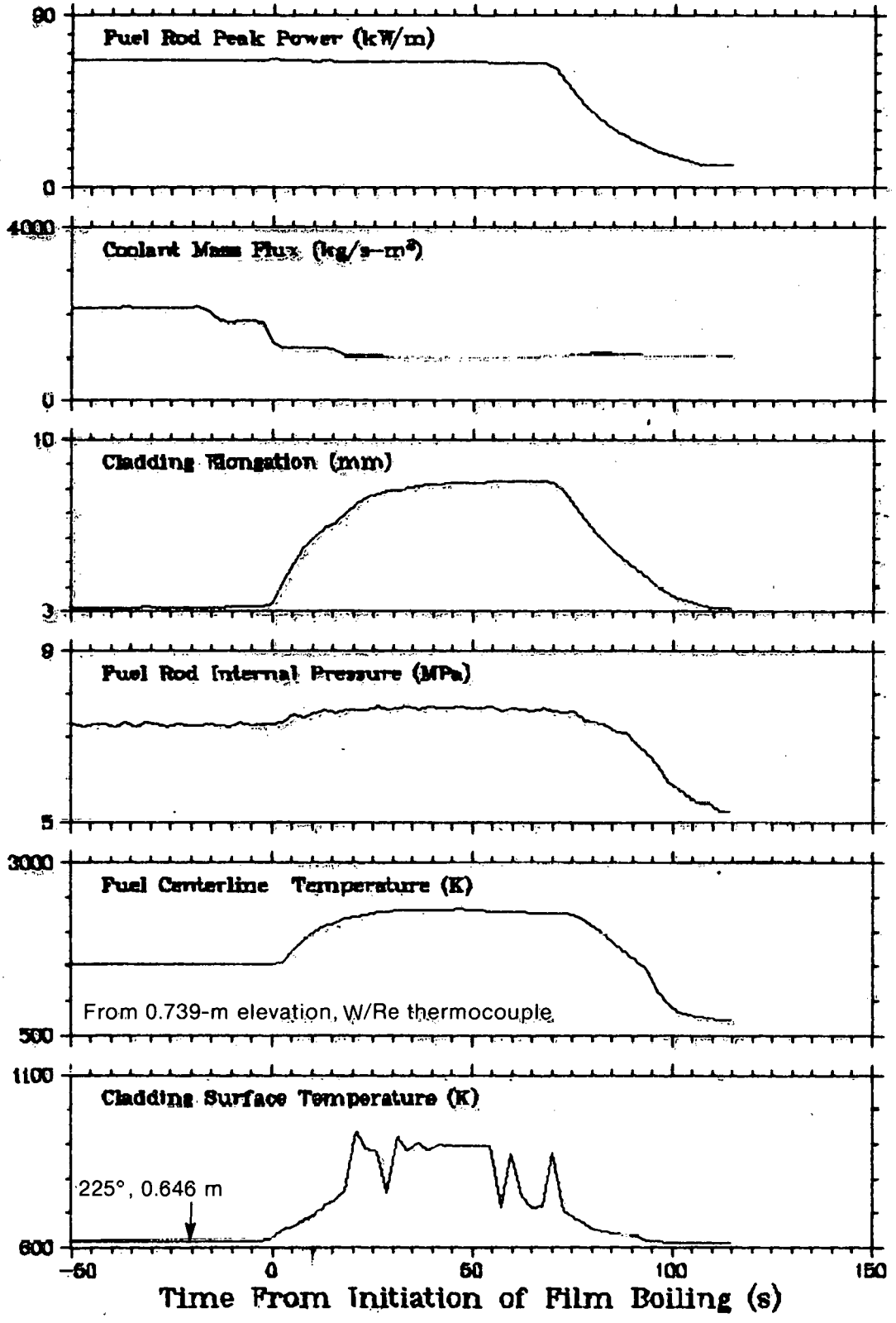

Fig. 14 Rod IE-020 behavior data during film boiling operation.

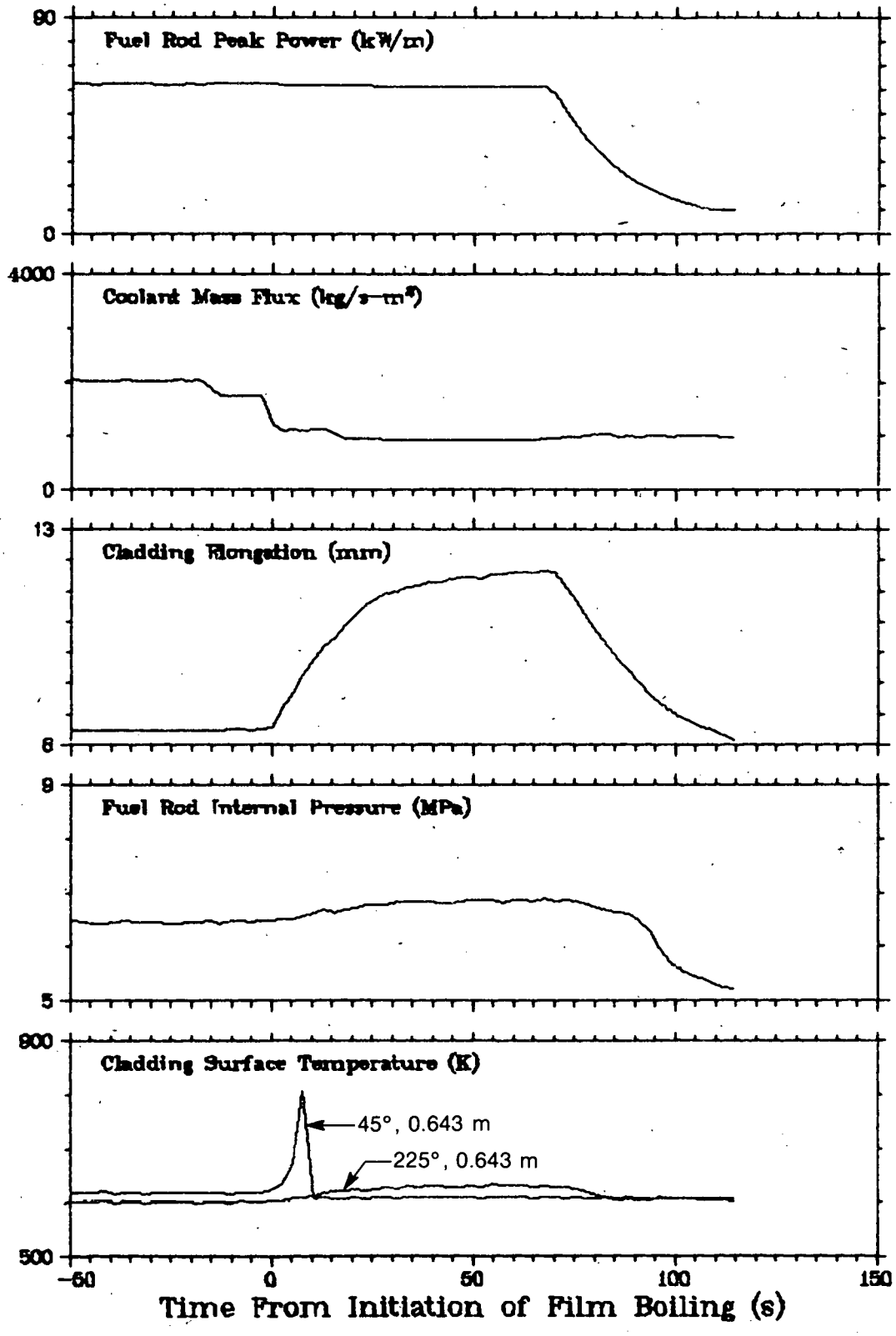

Fig. 15 Rod IE-021 behavior data during film boiling operation.

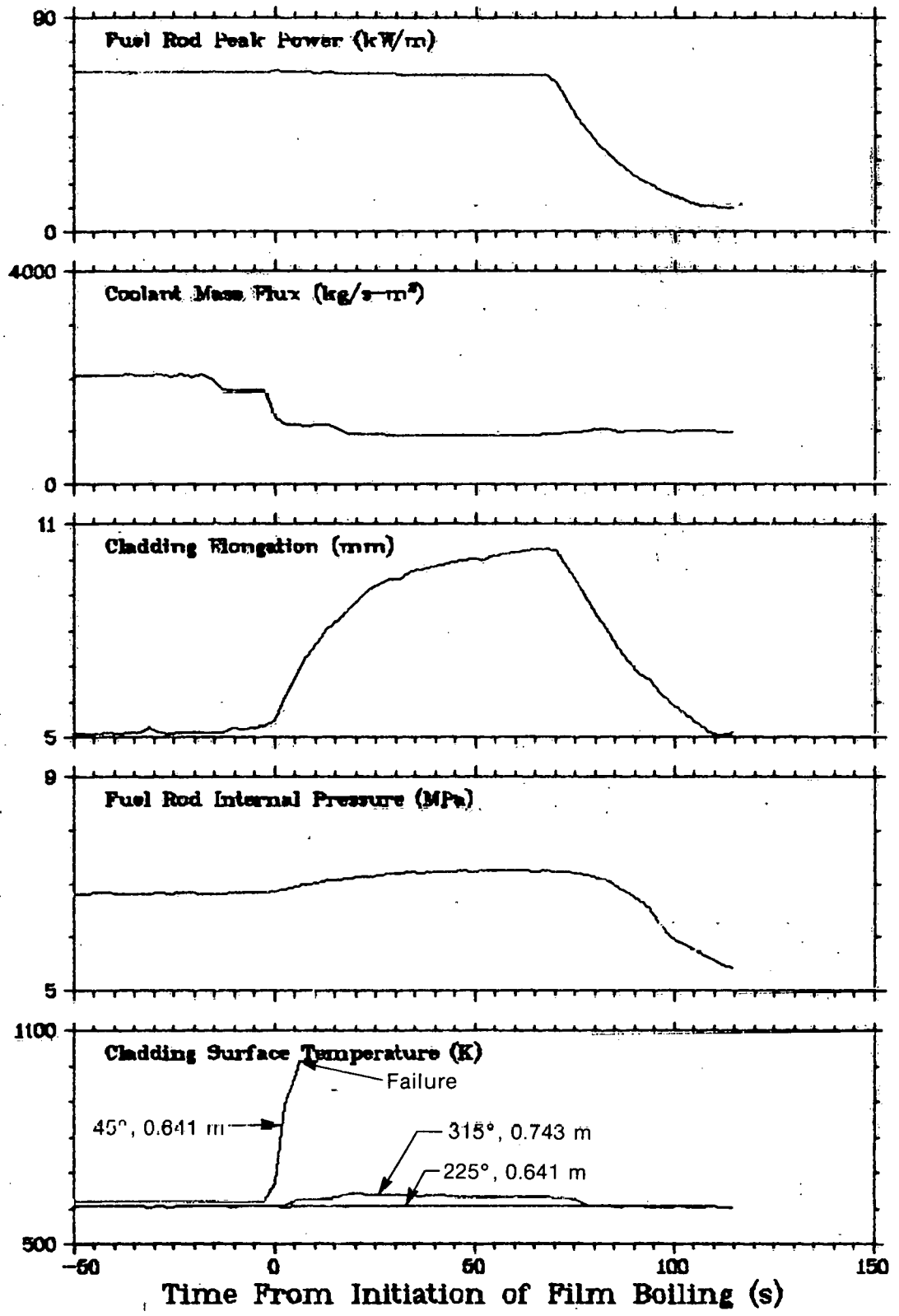

Fig. 16 Rod IE-022 behavior data during film boiling operation.

V. PRELIMINARY POSTIRRADIATION EXAMINATION RESULTS

A postirradiation examination (PIE) was performed to assess the posttest condition of the fuel rods and determine the lengths of the film boiling zones for input to a fuel rod behavior computer model. Visual observations and dimensional measurements and neutrographs made during that examination are reported in the following subsections. Results from a complete postirradiation examination to determine the microscopic fuel rod behavior will be published in a separate report.

1. VISUAL EXAMINATION

All four rods were intact following Test IE-5. Generally, the film boiling zones were visually distinguishable by cladding collapse into pellet-to-pellet interfaces or cladding oxidation and oxide spalling. Figure 17 shows the appearance of these oxide layers, typical of all the rods of Test IE-5.

1.1 Rod IE-019

Figure 18 shows the film boiling zone on Rod IE-019 at both the 0- and 180-degree orientations[a]. On the basis of the cladding diameter increase discussed in Section V.2, the film boiling zone was judged to extend approximately between the 0.450- and 0.860-m rod elevations. Oxide accumulation and associated spalling occurred at several locations within the film boiling zone. No cladding depressions or collapse into pellet interfaces (waisting) were observed on Rod IE-019 due to the high internal pressure. A pressure decrease indicated a loss of cladding integrity about 10 s after the onset of film boiling, however, the failure location was not visually discernable on this rod.

Rod IE-019 was initially pressurized to 8.3 MPa to induce ballooning during the film boiling phase of the test. An increase in rod diameter was measured over the film boiling zone, from the 0.450- to 0.860-m rod elevation, with maximum cladding swelling occurring between approximately the 0.630- and 0.650-m elevations (Figure 18). The cladding on Rod IE-019 was fractured at the 0.635-m elevation while the diametral measurements were being made. Figure 19, a side view of the fracture, shows prior molten fuel solidified on a pellet surface. Figure 20, an end view, shows fuel melting in 80 to 90% of the fuel pellet diameter. The ballooning was not uniform around the circumference, but was oriented in the plane of the cladding surface thermocouples (45 to 225 degrees).

Rod IE-019 displayed a smooth, cosine-shaped bow from approximately 0.47- to 0.70-m elevation. The estimated deflection from the 0- to 180-degree plane in the 270-degree direction was 5 mm.

---

[a] The 0-degree orientation of the fuel rod faces the centerline of the PBF in-pile tube.

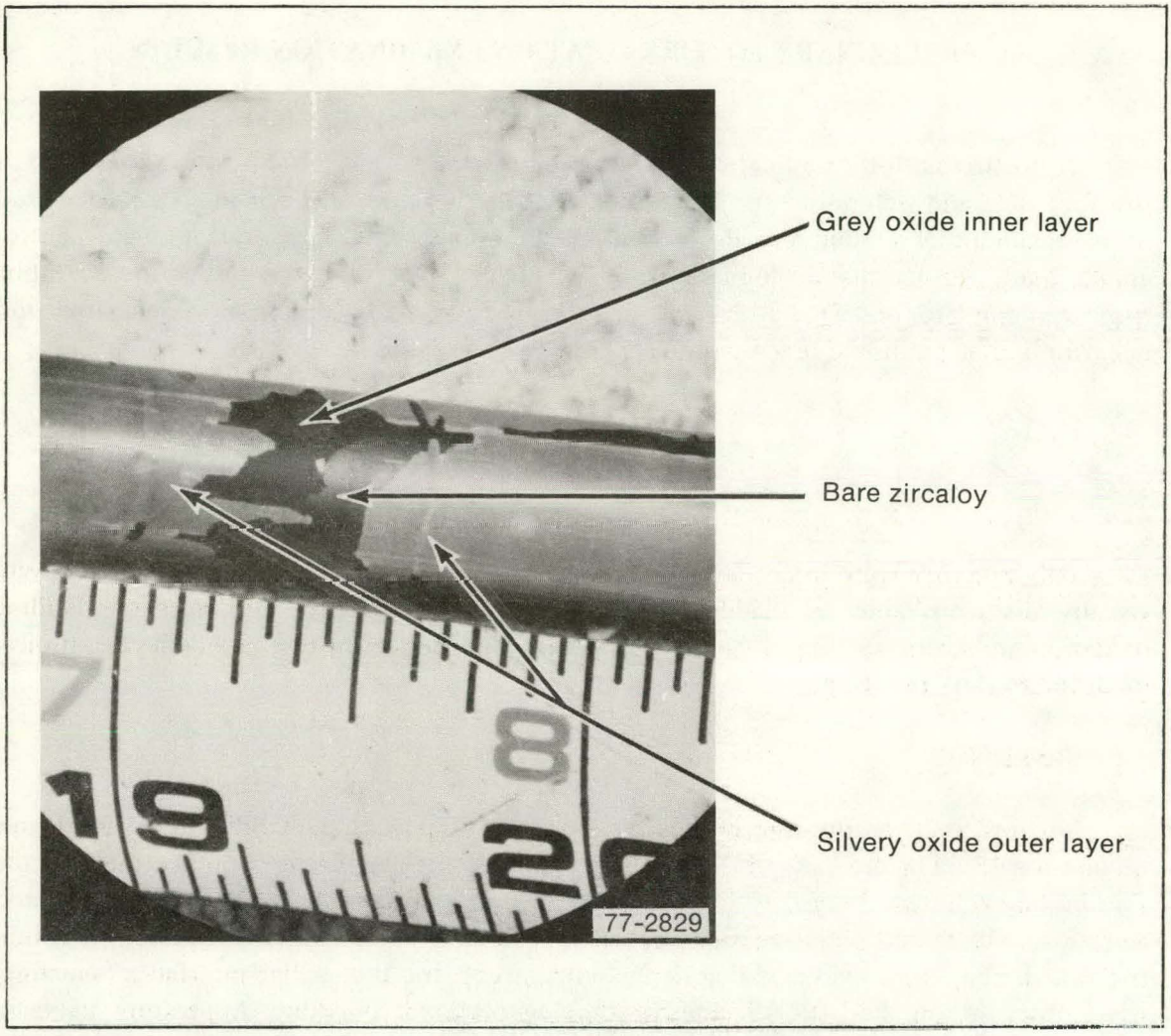

Fig. 17 Typical oxide appearances on rod surface in film boiling zone.

The two thermocouples brazed to the cladding surface at the 45- and 225-degree orientations and at approximately the 0.645-m elevation appeared to be in excellent condition and firmly attached to the rod. (Only the thermocouple at the 45-degree orientation responded to film boiling.) Small areas of light-grey discoloration, apparently resulting from the brazing process, were seen around each junction. The brazing process undoubtedly affected the cladding strength properties in the local region of the thermocouples since the braze temperature was near 1250 K.

Subsequent metallographic examination disclosed that the cladding failed in the α-phase in the region of maximum ballooning. The region surrounding the failure location was β-zircaloy. Although the brazing process may not have significantly affected the cladding properties at the actual failure location, the presence of the thermocouples and the brazing process did affect the properties near the failure location and may have contributed to the cladding ovality seen in Figure 20.

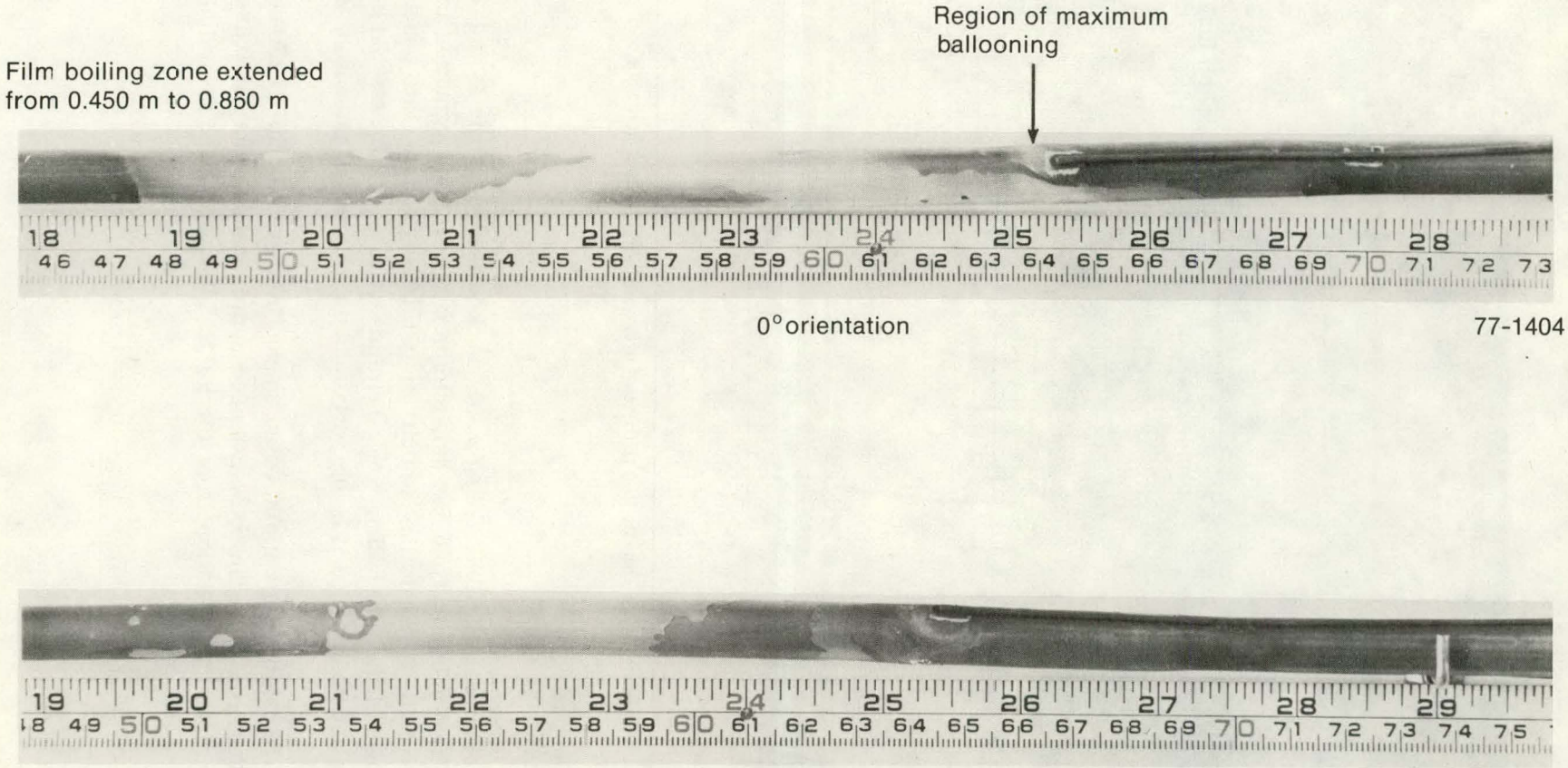

Fig. 18 Film boiling zone for Rod IE-019 at the 0 and 180° orientations.

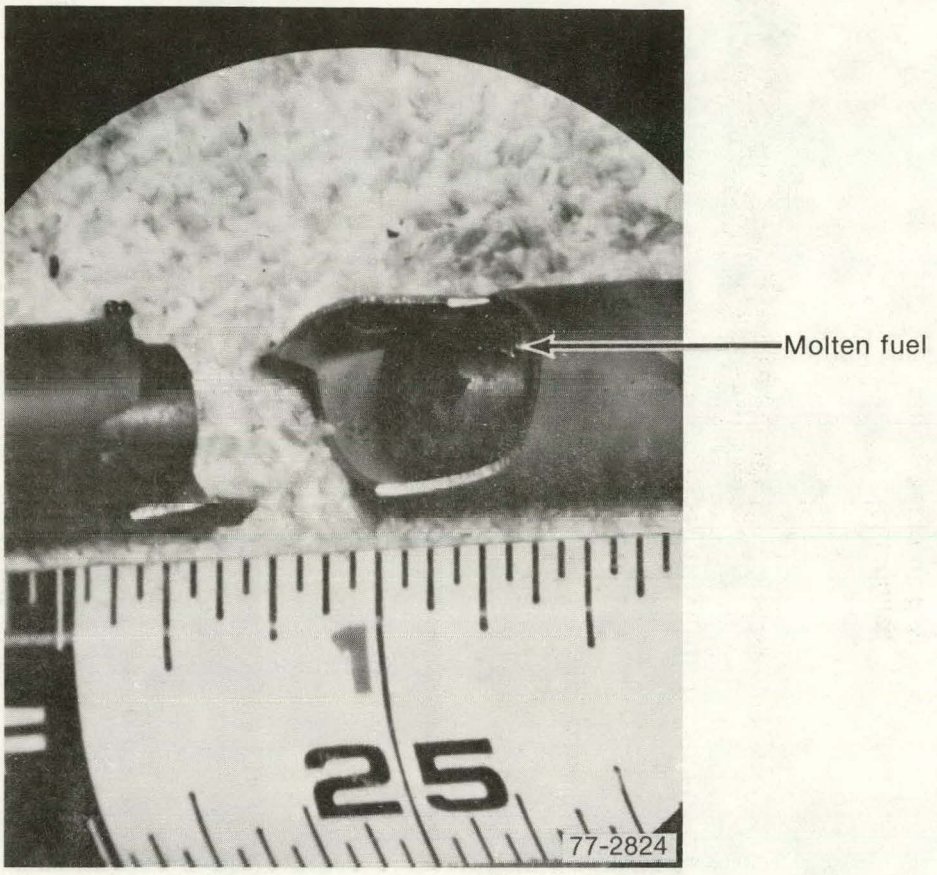

Fig. 19 Location of fracture on Rod IE-019 that occurred during handling in the hot cell.

1.2 Rod IE-020

Figure 21 shows the film boiling zone on Rod IE-020 at the 0- and 180-degree orientations. The film boiling zone, based on interpretation of oxide formation and spalling, was located from the 0.480- to 0.688-m elevation. Cladding collapse into pellet interfaces occurred throughout the film boiling zone. Instrumentation during the test did not indicate cladding failure and no evidence of failure was found during visual examination.

Rod IE-020 exhibited a smooth, cosine-shaped bow from the 90- to 270-degree plane in the 180-degree direction. This bow extended approximately from the 0.68- to 0.84-m elevation. The maximum deviation from the 90- to 270-degree plane was estimated to be 3 mm.

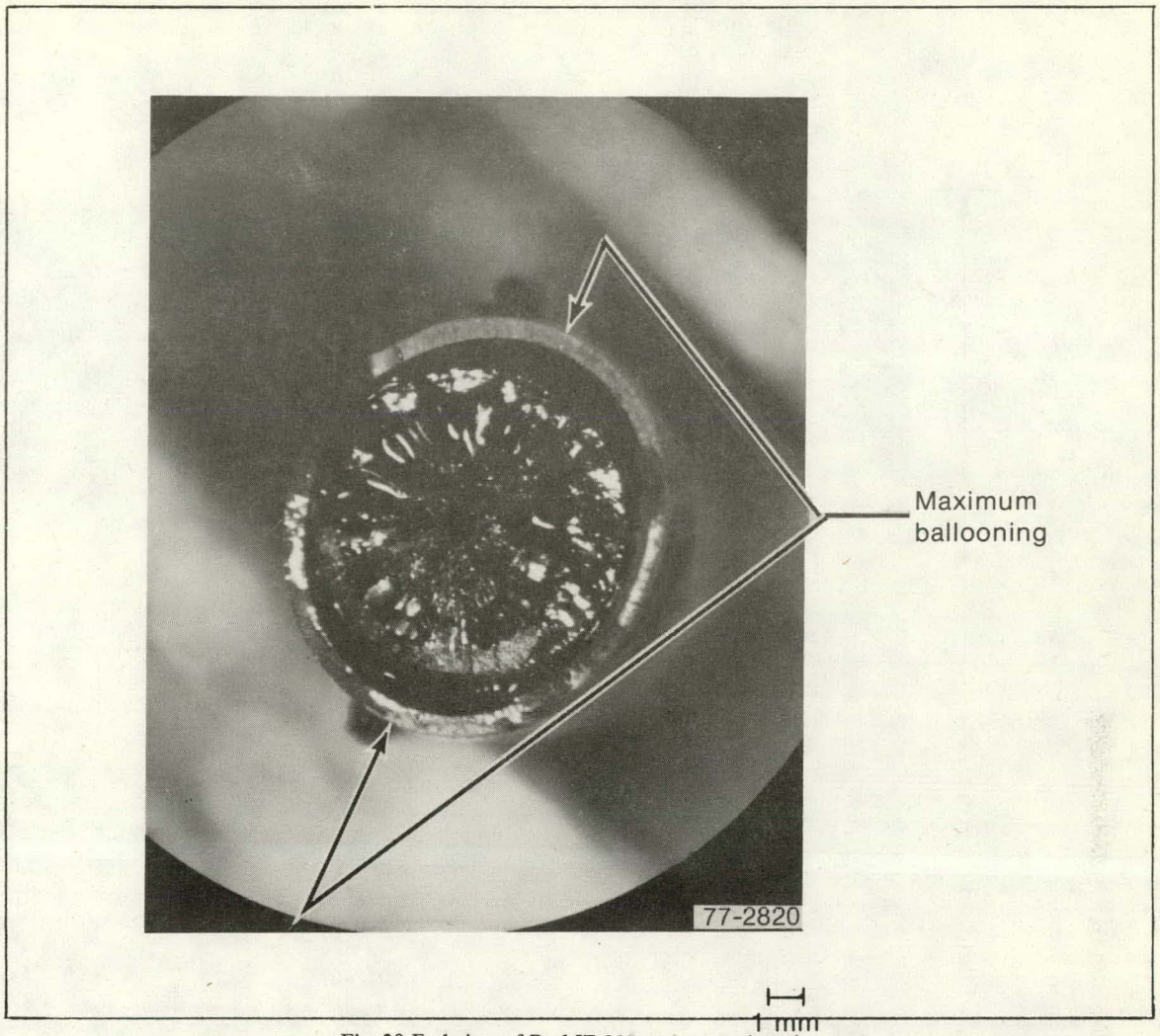

Fig. 20 End view of Rod IE-019 at fracture location.

1.3 Rod IE-021

Figure 22 shows the film boiling zone on Rod IE-021 at both the 0- and 180-degree orientations. On the basis of observations of oxide build-up and spalling, the film boiling zone was determined to extend from the 0.470- to 0.698-m elevation. Cladding waisting at pellet interfaces occurred throughout the film boiling zone. One circular cladding depression, indicative of a chipped pellet corner, was found at the 0.513-m elevation. There was no evidence of rod bowing or failure.

1.4 Rod IE-022

Figure 23 shows the film boiling zone on Rod IE-022 at both the 0- and 180-degree orientations. On the basis of oxide formation, spalling, and cladding collapse, the film boiling zone was determined to extend between the 0.450- to 0.710-m elevation. As with Rods IE-020 and IE-021, cladding waisting at pellet interfaces was found throughout the

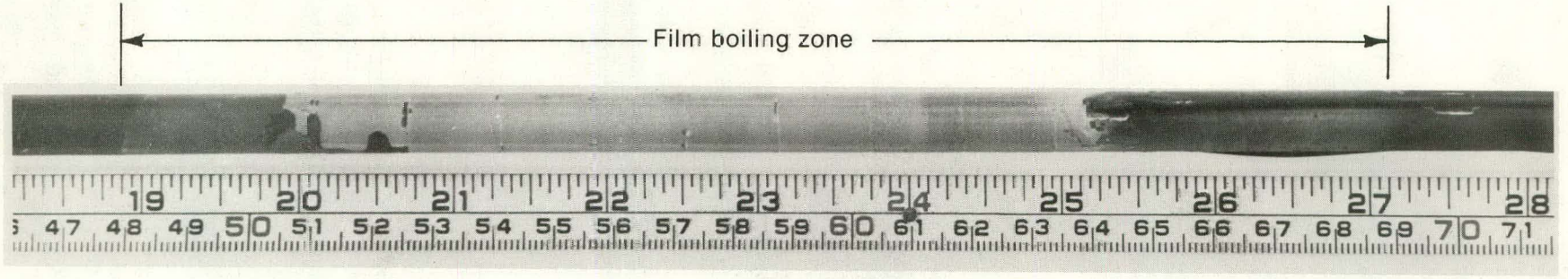

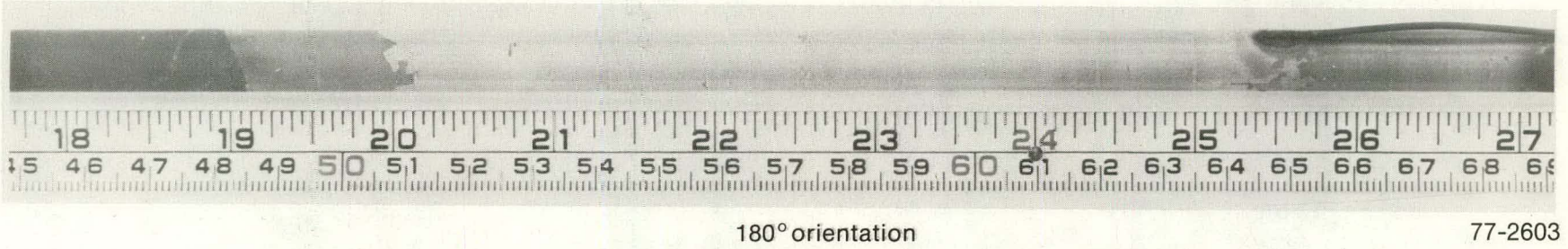

Fig. 21 Film boiling zone of Rod IE-020 at the 0 and 180° orientations.

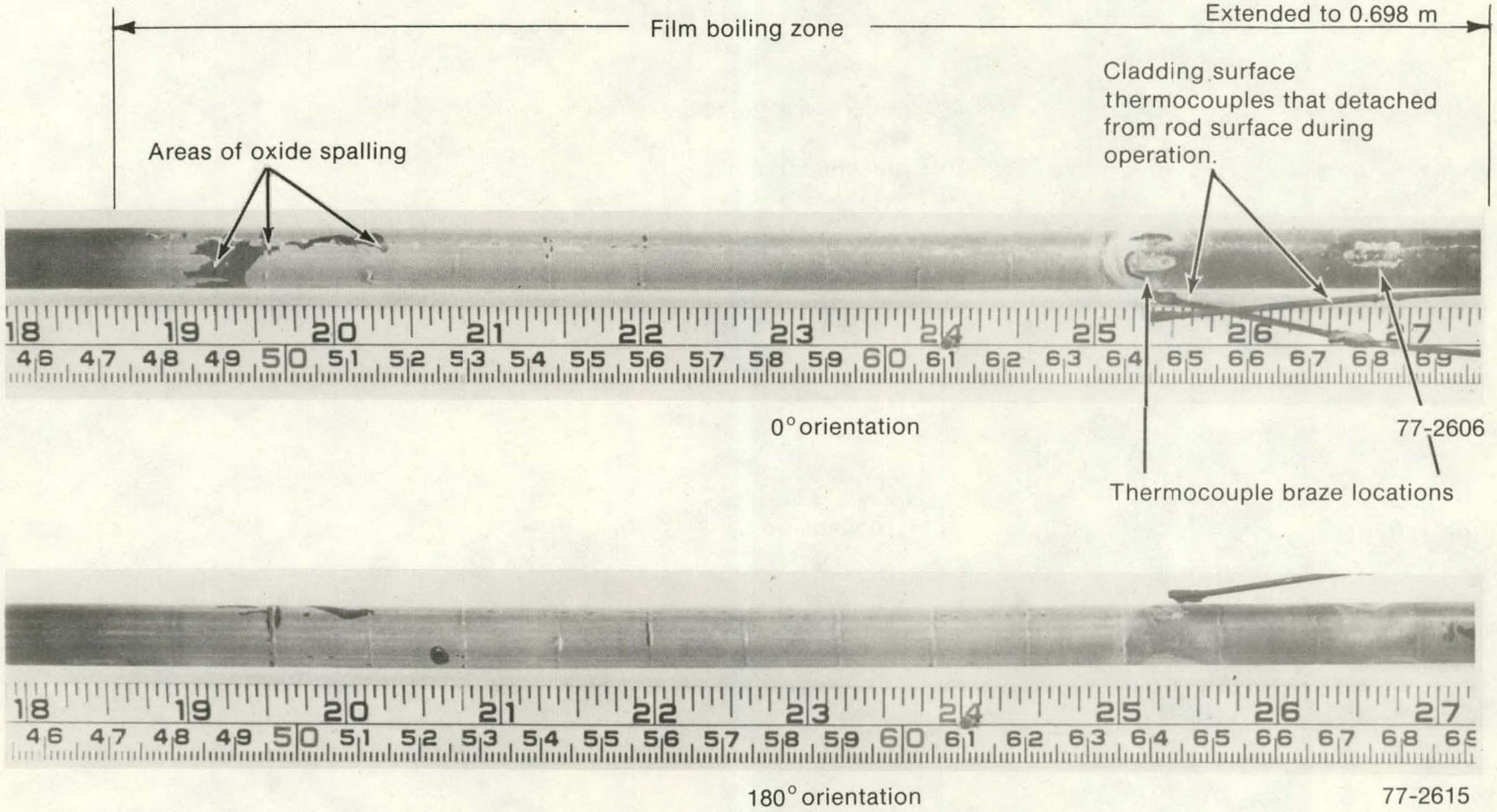

Fig. 22 Film boiling zone of Rod IE-021 at the 0 and 180° orientations.

Film boiling zone extended
from 0.450 m to 0.698 m

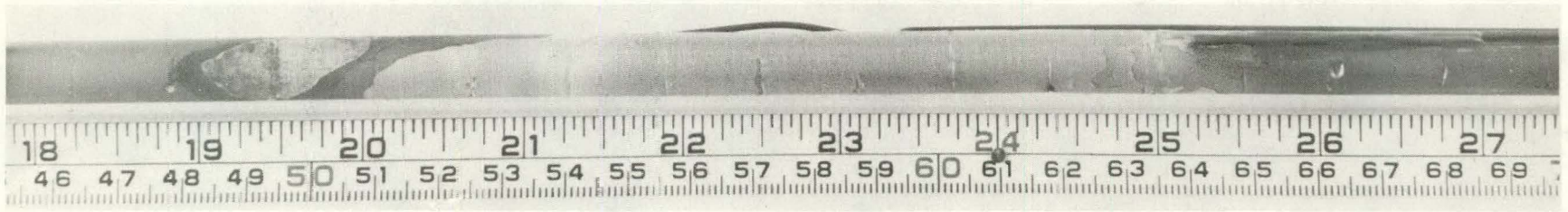

0° orientation 77-2616

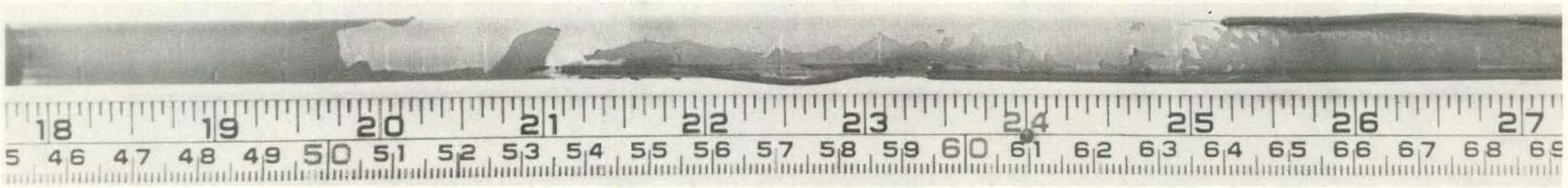

180° orientation 77-2614

Fig. 23 Film boiling zone of Rod IE-022 at the 0 and 180° orientations.

film boiling zone. Pronounced circular cladding depressions at pellet interfaces were noted at the 0.478-, 0.587-, 0.618-, 0.663-, and 0.694-m elevations. Although the internal pressure increased following the test, no failure location was evident. Bowing was not evident on this rod.

2. POSTTEST DIAMETER MEASUREMENT AND NEUTROGRAPHY

Cladding diameter measurements and neutron radiographs were obtained for each rod at two perpendicular orientations. Diameter measurements were made with a micrometer, at 50-mm increments outside the film boiling zones and at 12-mm increments within the zones. The neutrographs shown in the following figures are full scale, however, edge effects in the neutron radiographic process produce apparent gaps between pellets and decrease the image size of the pellet diameter.

Relative micrometer measurements on a given rod are accurate to within ±0.02 mm. Comparison of direct (pretest) and remote (in the hot cell) micrometer measurements indicated that the posttest measurements have a constant offset relative to the true diameter determined by pretest micrometer and pulsed-eddy-current[3] measurements. Since the cladding temperature below the film boiling zone remained less than 620 degrees K throughout the test, the cladding diameter in this region was assumed not to have been affected by operation in PBF. From this diameter measurement, the offset was determined to be approximately -0.12 mm.

2.1 Rod IE-019

Diameter increases occurred in the film boiling zone approximately between the 0.450- and 0.860-m elevation as shown in Figure 24. Additional measurements were obtained over the region of maximum ballooning (0.628- to 0.650-m elevation) with a calibrated Filar eyepiece. A maximum ballooning of approximately 24% occurred in the 45- to 225-degree plane at the 0.639 m elevation.

Figure 24 also contains the neutrograph of Rod IE-019 above the fracture location at the 0.635-m elevation (Section V.1.1). A large elongated central void, 2 to 4 mm in diameter, extended from the 0.641- to 0.692-m elevation. This void indicates that fuel melting occurred in this region of the rod. The drilled hole for the fuel centerline thermocouple may be seen in the upper four pellets shown in the neutrograph. The thermocouple junction is located at the 0.74-m elevation. Neutrographs of the bottom segment of Rod IE-019 indicated fuel cracking was not extensive.

2.2 Rod IE-020

Figure 25 contains the posttest cladding outside diameter measurements and the neutrograph of the film boiling zone. The holes in which simulated fission products were

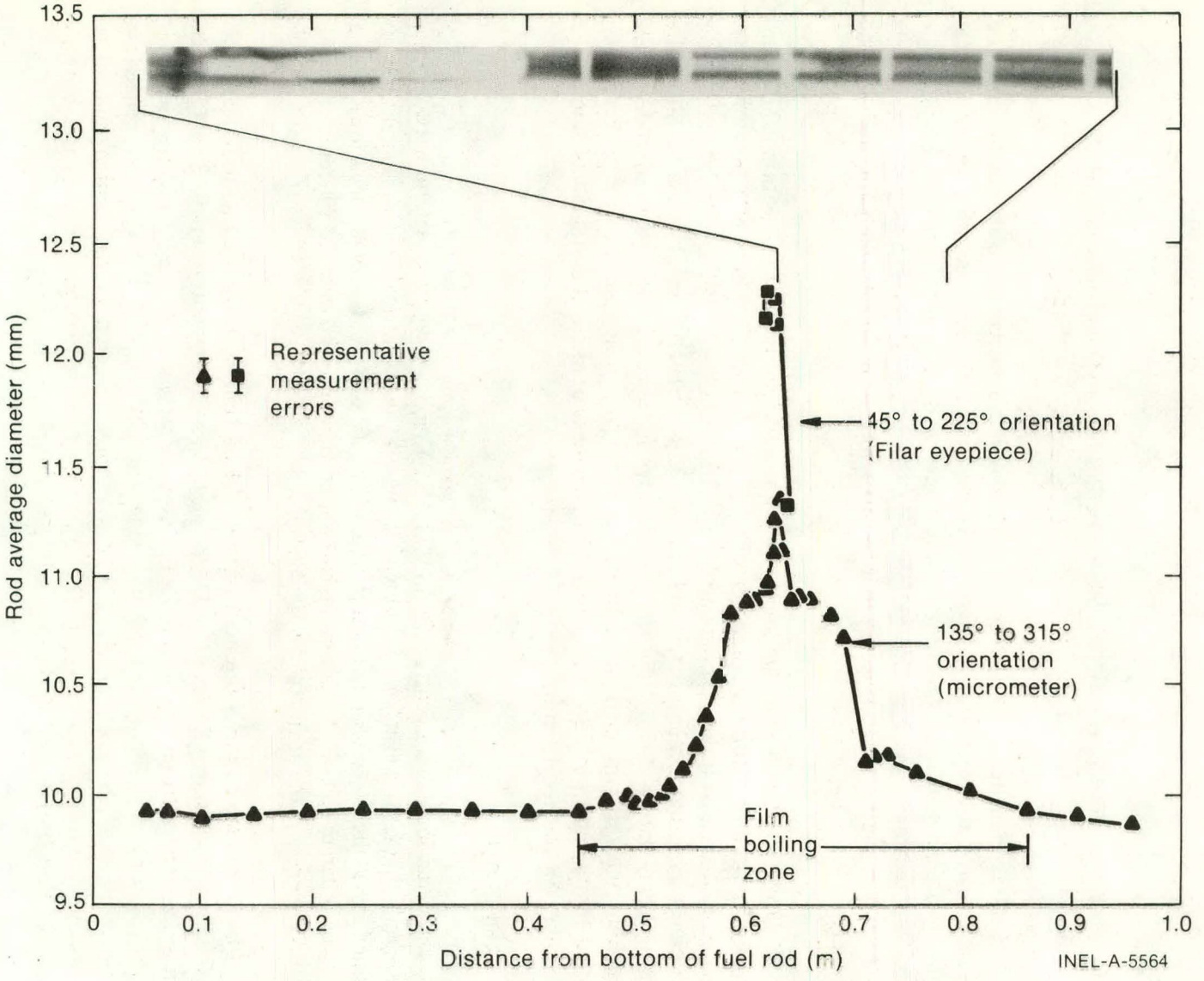

Fig. 24 Post-test diametral measurements and neutrograph of the film boiling zone of Rod IE-019.

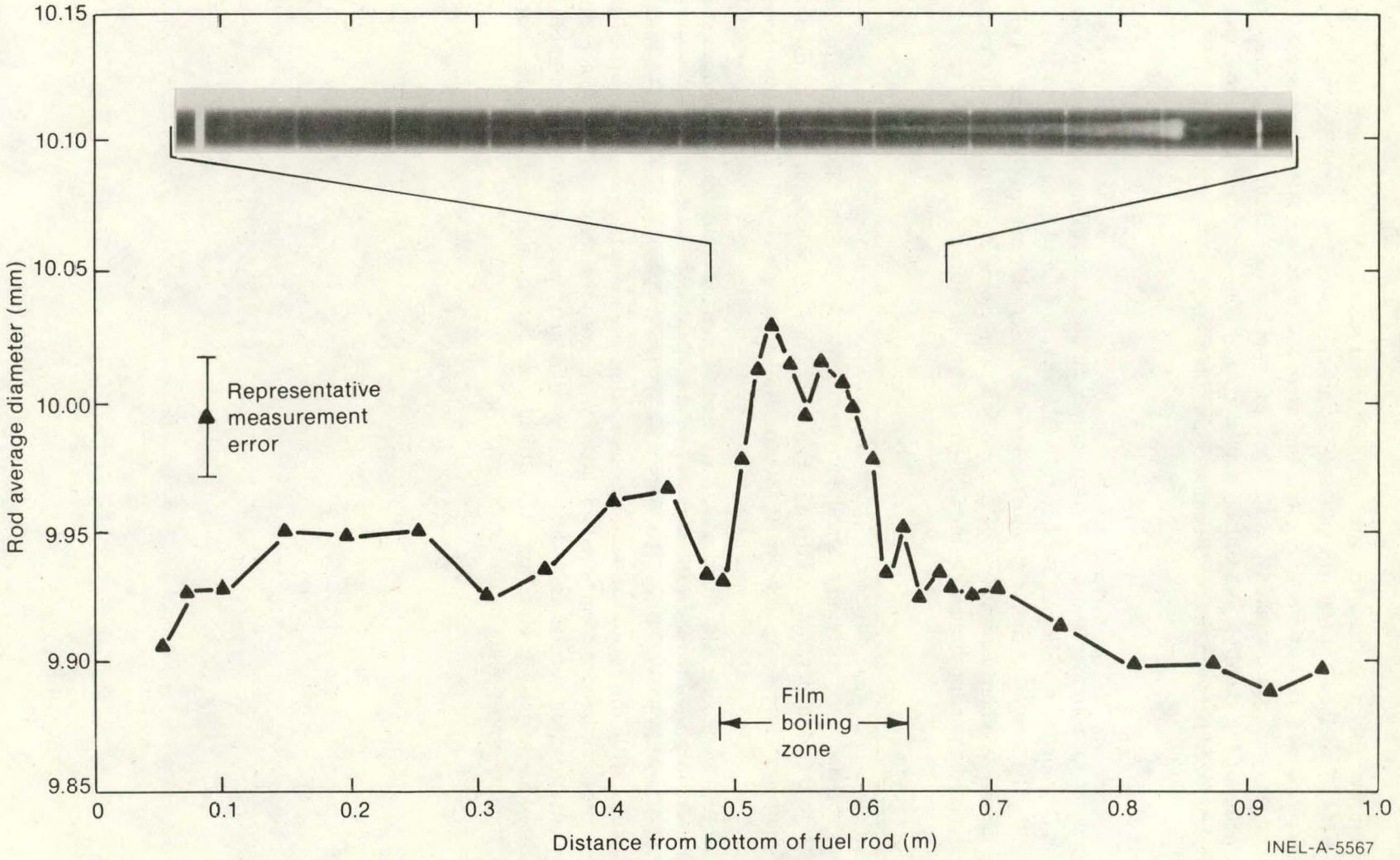

Fig. 25 Posttest diametral measurements and neutrograph of the film boiling zone of Rod IE-020.

placed were evident in the neutrographs of the entire rod, with the exception of a region from the 0.490- to 0.645-m elevation. (The holes are not visible in Figure 25). Significant pellet fracturing and indications of molten fuel were also noted in this same region. This region corresponds approximately with that of swelling observed in the diametral measurements of the cladding. A teardrop-shaped central void approximately 1 to 2 mm in diameter developed between the 0.580- and 0.645-m elevations.

2.3 Rod IE-021

Diameter measurements and the neutrograph of the film boiling zone are shown in Figure 26. The neutron radiographs of Rod IE-021 were similar in appearance to those of Rod IE-020. The simulated fission product holes were observable except from the 0.433- to 0.604-m elevation where indications of molten fuel were seen. A 2-mm-diameter central void was located from approximately the 0.55- to 0.59-m elevation.

2.4 Rod IE-022

This rod displayed a region of small diameter increase or swelling from approximately the 0.480- to 0.644-m elevation as shown in Figure 27. This region was surrounded by small areas of diameter decrease or collapse (0.460- to 0.480-m and 0.644- to 0.710-m elevations).

Fuel pellet cracking was more evident in the neutrographs than for the previous rods. Fuel fracturing occurred between the bottom of the fuel column and the 0.450-m elevation. Molten fuel was indicated from the 0.450- to 0.615-m elevation, which corresponds approximately with the region of swelling observed in the diametral measurements of the cladding. The simulated fission product holes were not observable within this region; however, an elongated central void, 1 to 2 mm in diameter, was measured from approximately the 0.55- to 0.61-m elevation. The drilled hole for the ultrasonic thermometer is visible in the uppermost pellet of the neutrograph.

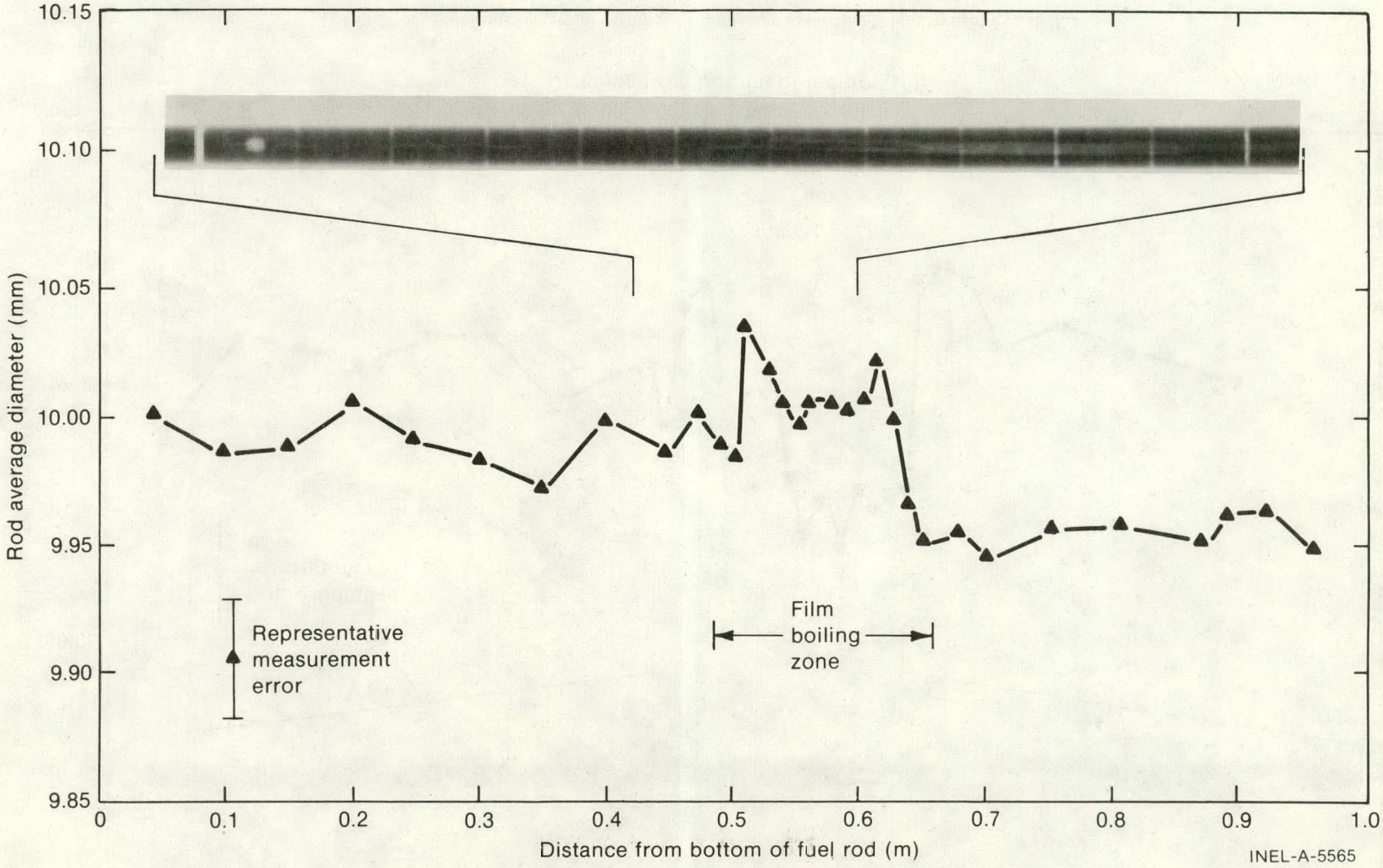

Fig. 26 Posttest diametral measurements and neutrograph of the film boiling zone of Rod IE-021.

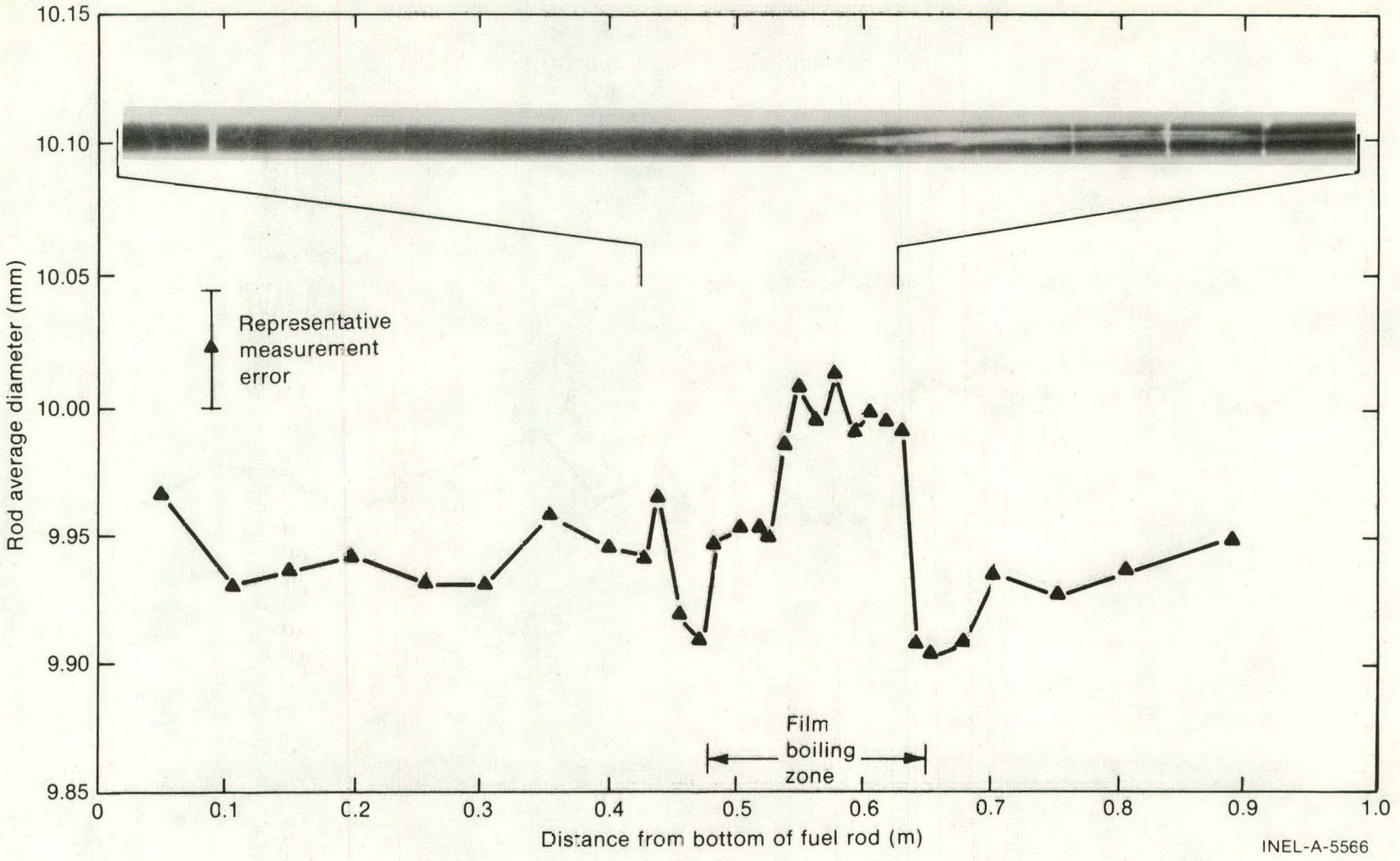

Fig. 27 Posttest diametra. measurements and neutrograph of the film boiling zone cf Rod IE-022.

VI. EXPERIMENTAL RESULTS AND COMPARISON OF MEASURED AND CALCULATED FUEL ROD BEHAVIOR

Test IE-5 data are presented and compared in this section with results calculated by FRAP-T4[a], a fuel rod behavior computer model. The information is divided into five categories: (a) cladding elongation, (b) cladding radial deformation, (c) fuel rod internal pressure, (d) fuel centerline temperature, and (e) cladding surface temperature. Data from the preconditioning phase, the high power steady state operation, and the flow reduction phase are presented in each category. The FRAP-T code is under continuing development incorporating improvements in fuel behavior models based on comparisons between measured data and calculated results similar to those presented in this section. A brief description of the FRAP-T4 analytical model and simulation of the experiment conduct is presented in Appendix E. Each of the following subsections presents test results pertinent to the test objectives. Section VII discusses the test objectives and supporting data. Steady state calculations were performed for various power levels to analyze the preconditioning and high-power steady state phases of the test. The flow reduction transient was analyzed by modeling the rod power and coolant mass flow reduction versus time for each rod. Calculations were performed for Rods IE-019, IE-020, and IE-021, but not for Rod IE-022, because the only difference between Rods IE-020 and IE-022 was the irradiation state of the cladding. Furthermore, the irradiation effects in the stress-strain relationship for the cladding would be annealed at cladding temperatures above about 925 K for the times involved in this test. FRAP-T4 calculations for Rod IE-020 are considered adequate to describe the behavior of Rod IE-022. The effects of internal pressure (high in Rod IE-019) and the addition of simulated fission products in Rod IE-020 were studied by modeling Rods IE-019 and IE-020. The effects of a difference of 0.05 mm in diametral gap was studied by modeling Rods IE-020 and IE-021.

1. CLADDING ELONGATION

Cladding elongation data for each rod during the preconditioning phase and the power ramp to a fuel rod average power of about 48 kW/m are presented in Figures 28 through 31. Cladding elongation data are presented in terms of a length change from a reference elongation at zero power and a temperature of 605 K at the start of the test. (Appendix C discusses the coordinate transformation and the reference elongation is shown in Table C-VI). PCI for all rods occurred at low power during the first power ramp of the preconditioning phase. As the fuel rods were subjected to additional preconditioning power cycles, cladding elongation as a function of fuel rod power approached equilibrium due to fuel cracking and relocation. Cladding elongation for Rods IE-019 and IE-022 reached

[a] FRAP-T4, a new unpublished version of FRAP-T2[4], is discussed in Appendix E.

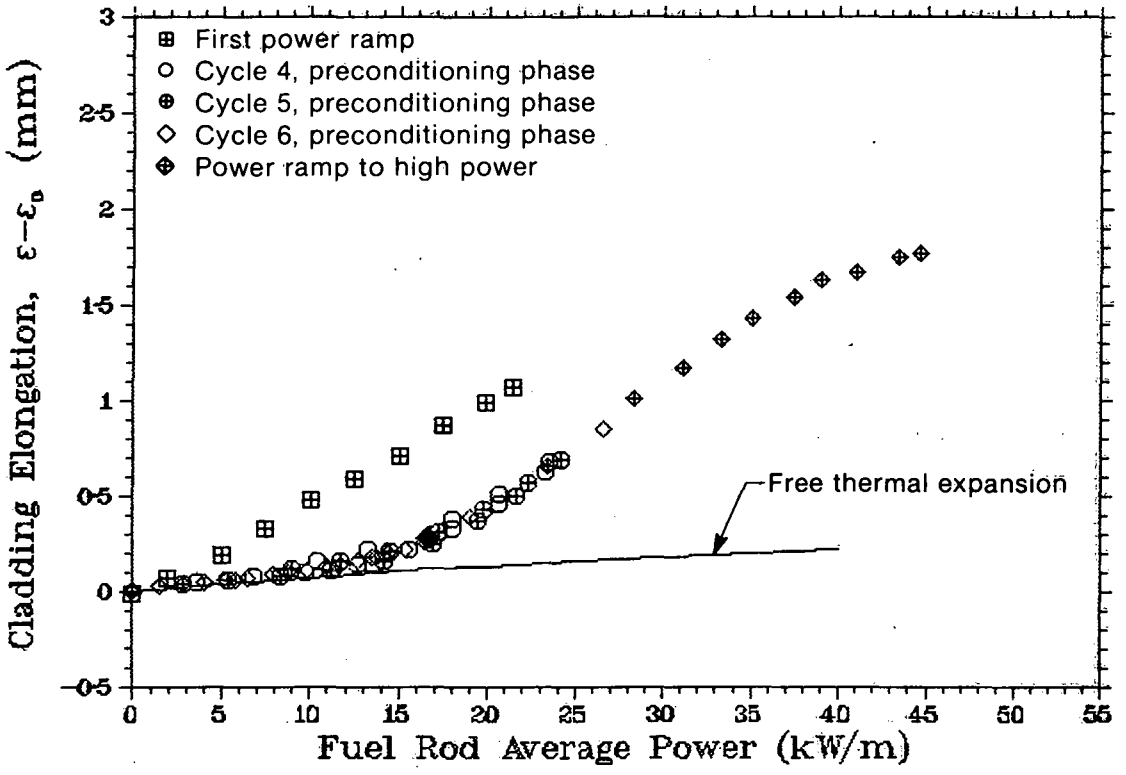

Fig. 28 Cladding elongation for Rod IE-019 during the preconditioning phase and rapid power ramp.

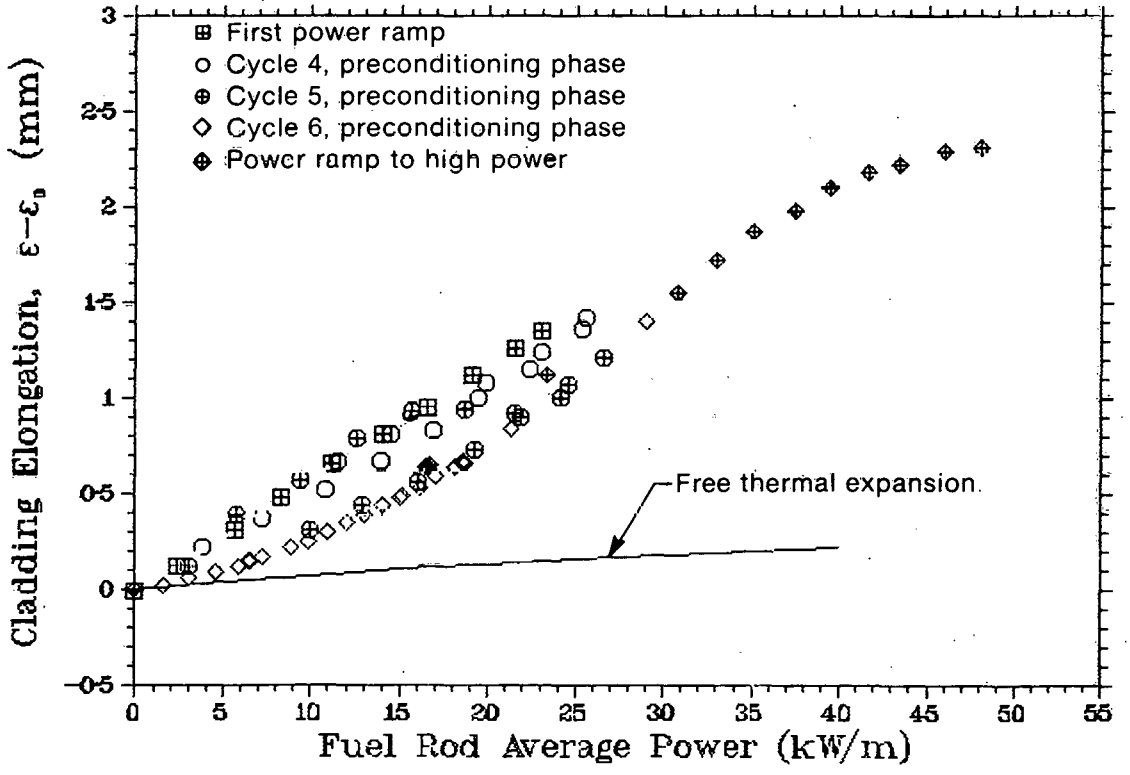

Fig. 29 Cladding elongation for Rod IE-020 during the preconditioning phase and rapid power ramp.

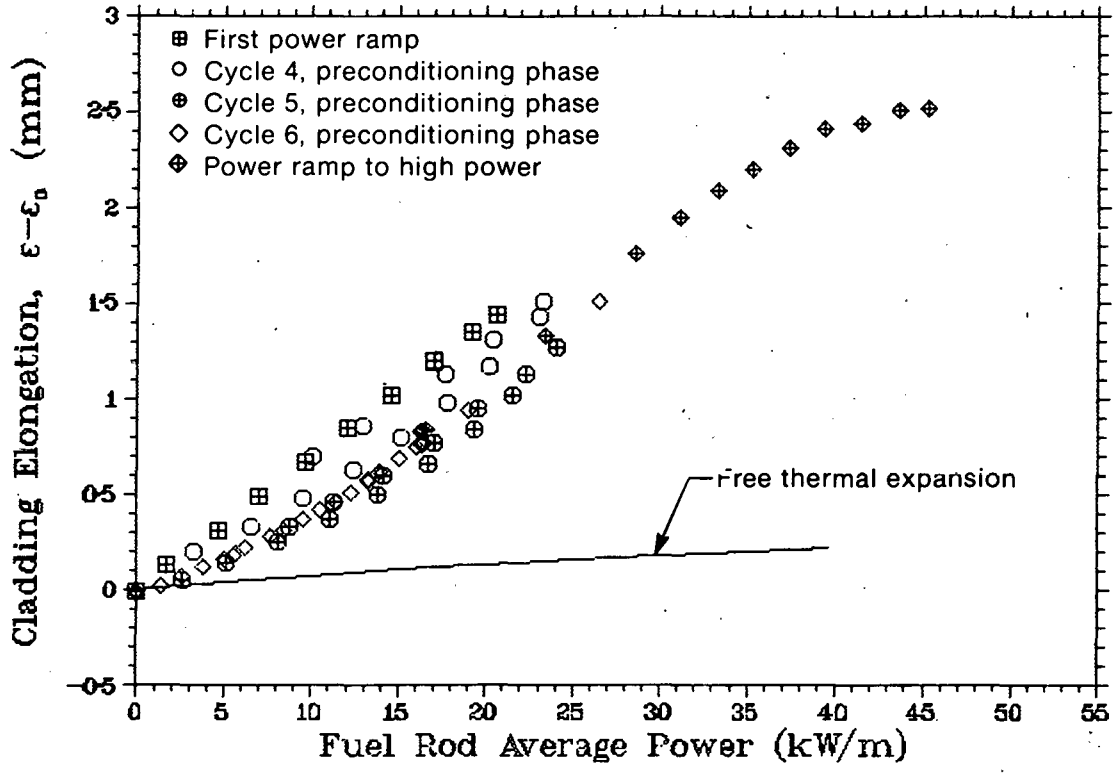

Fig. 30 Cladding elongation for Rod IE-021 during the preconditioning phase and rapid power ramp.

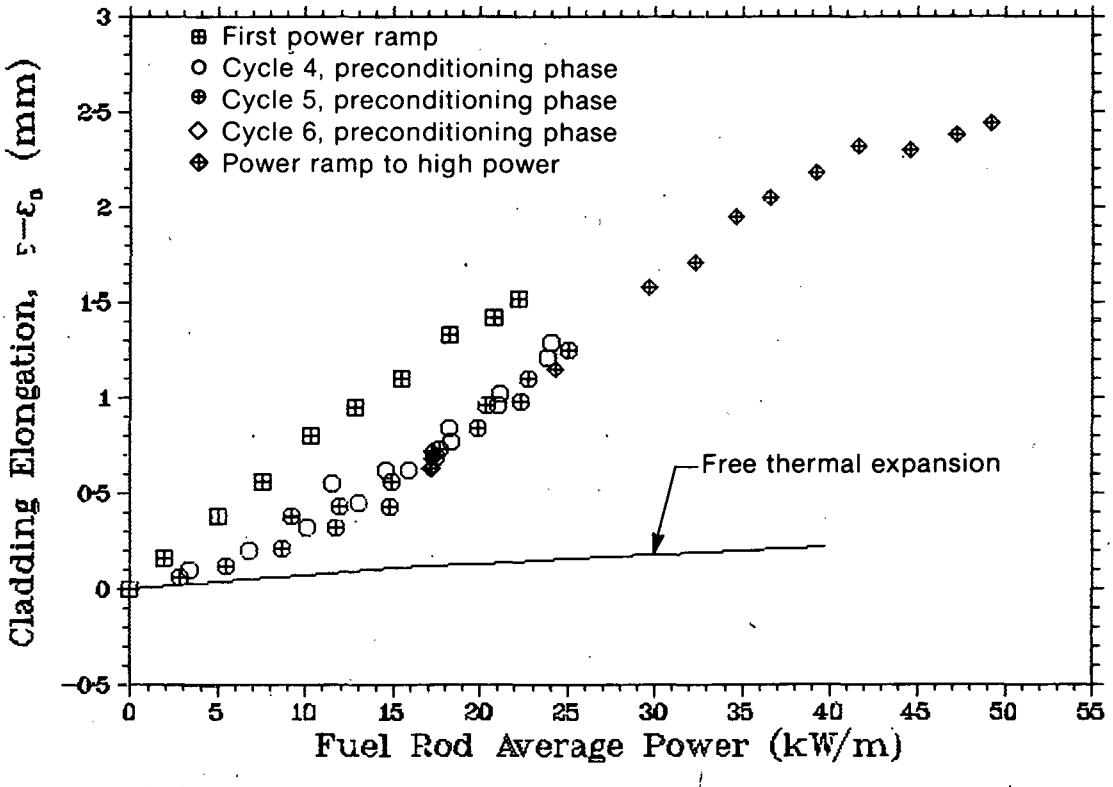

Fig. 31 Cladding elongation for Rod IE-022 during the preconditioning phase and rapid power ramp.

equilibrium conditions no later than the third power cycle. As shown in Figures 29 and 30, the two remaining rods required several power cycles before attaining equilibrium[a].

Due to assembly and handling of the fuel rods prior to the test, a nonuniform annular gap existed between the fuel pellets and the cladding. Off-center, skewed, and chipped pellets produce a random annular gap effectively smaller in local regions than the designed diametral gap. Since the designed gaps were only 0.09 to 0.14 mm, PCI was expected to occur at low power. Evidence exists that the heat from brazing the thermocouples to the cladding surface may crack the adjacent fuel pellets and produce points of fuel-cladding contact in these small gap rods. Rod IE-022 required disassembly and refabrication prior to the test. Fuel pellets were fractured and tended to adhere to the cladding in the regions of the brazed thermocouples. Therefore, initial PCI may have been enhanced in these four rods by the cladding thermocouple brazing process.

As the preconditioning phase continued, stresses between the cladding and the fuel column realigned the pellets and pellet fragments and produced an increased effective diametral gap. Once the fuel column became sufficiently relocated and the gap more uniform after two to five power cycles, differential fuel-cladding thermal expansion closed the diametral gap and caused PCI to occur in rod powers that were consistent from cycle to cycle. PCI occurred at the power level at which the cladding elongation data deviated from free thermal expansion of the cladding. Figures 28 through 31 indicate that PCI began at zero power during the first power ramp. Figure 28 indicates that PCI occurred on Rod IE-019 at a fuel rod average power of about 15 kW/m after a few cycles. PCI occurred on the remaining rods at average powers below 5 kW/m after several cycles as shown in Figures 29 through 31.

The equilibrium cladding elongation data from all four rods during the last preconditioning power cycle and the power ramp are compared with the elongation due to free thermal expansion in Figure 32. The initial high internal pressure (8.3 MPa) of Rod IE-019 is the only parameter distinguishing Rod IE-019 from Rod IE-020. PCI may have been caused at a higher power level by the rod internal pressure. Although the diametral gap of Rod IE-021 was 0.138 mm, the measured elongation was similar to that of Rods IE-020 and IE-022, which both had diametral gaps of 0.09 mm.

The two fuel deformation models specified in FRAP-T4 (Appendix E) assume radial cracks in the fuel extend from the fuel surface toward the centerline. The Standard Model uses the nominal design fuel-cladding gap, whereas the Coleman Fuel Relocation Model uses a reduced gap based on the nominal design that has been modified by an empirical relationship. Furthermore, the Coleman Model assumes that the gap is relocated into cracks of the fuel. Figures 33 through 35 compare the FRAP-T4 calculations using both the

[a] The elongation at zero power for Rods IE-019 and IE-020 drifted slightly negative during the test. Since no physical explanation of this behavior exists, the drift was attributed to a change in the calibration of the rod LVDTs. Figures 28 and 29 contain the corrected data.

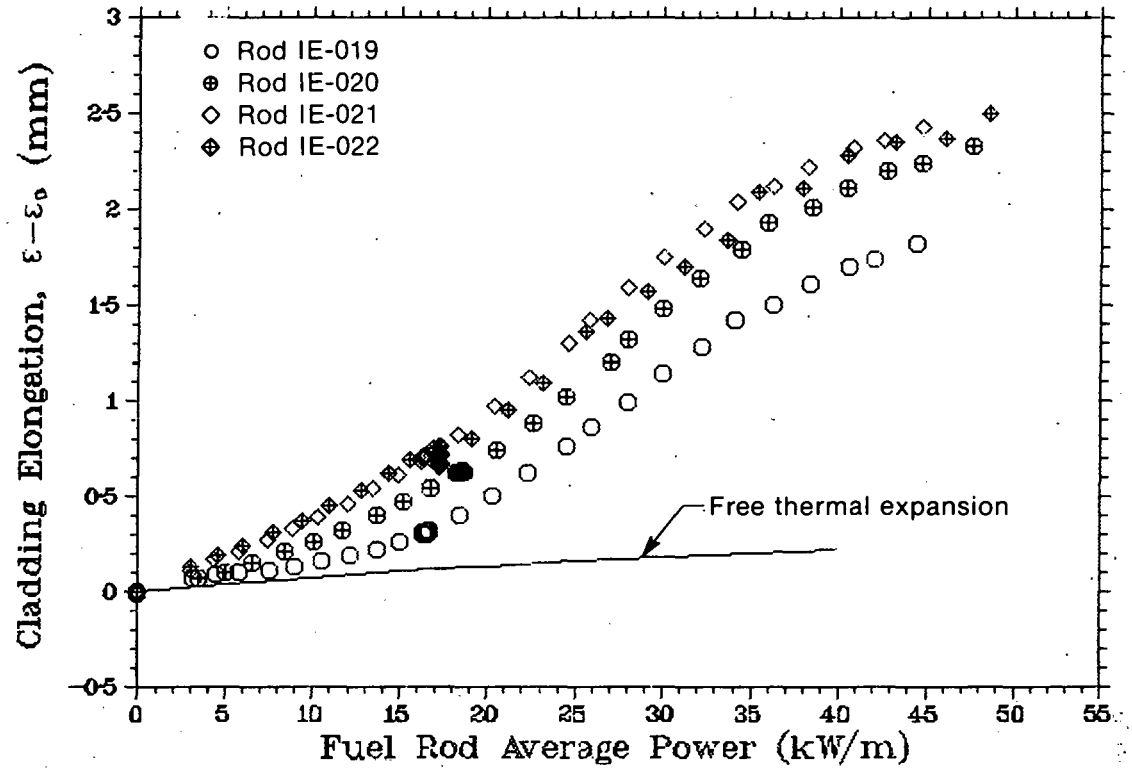

Fig. 32 Cladding elongation during the rapid power ramp for all four rods in Test IE-5.

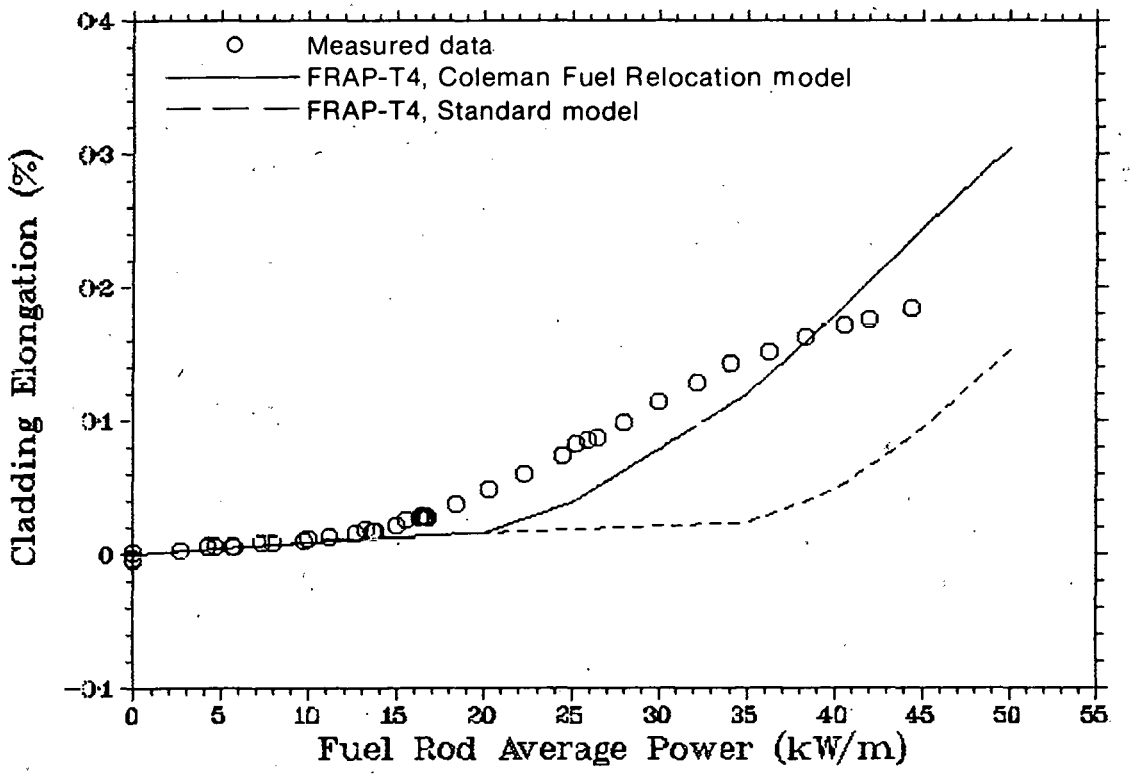

Fig. 33 Comparison of calculated with measured cladding elongation for Rod IE-019.

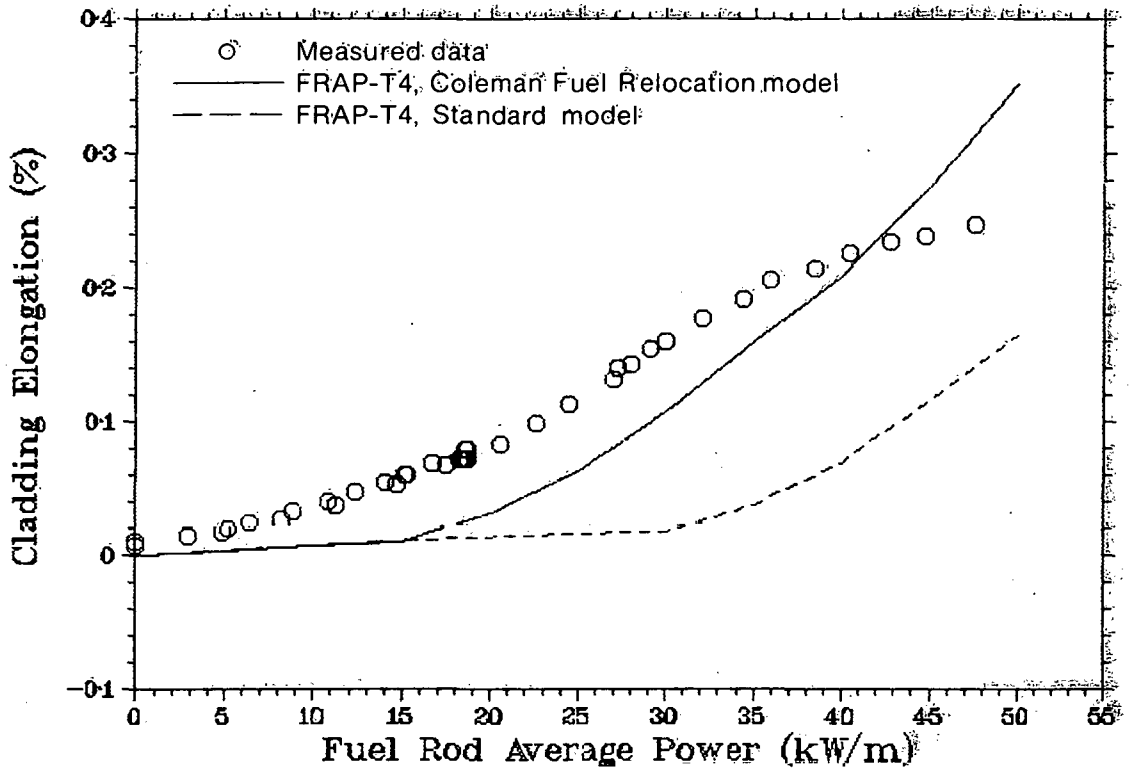

Fig. 34 Comparison of calculated with measured cladding elongation for Rod IE-020.

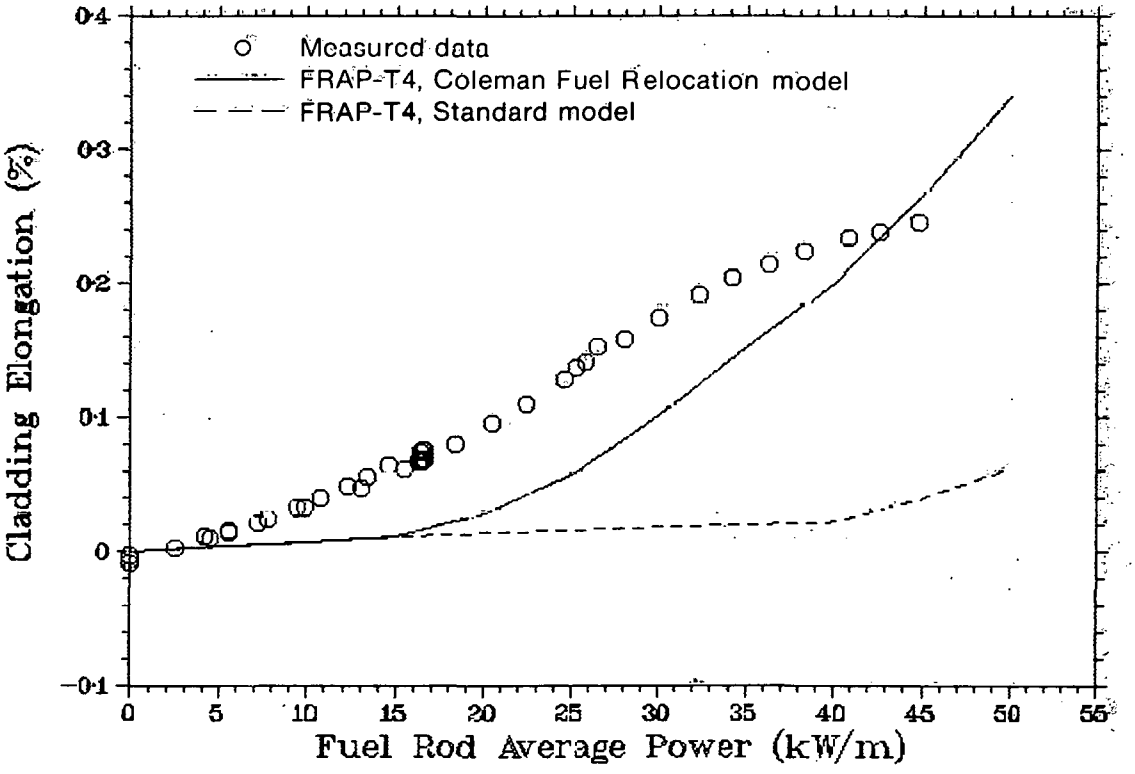

Fig. 35 Comparison of calculated with measured cladding elongation for Rod IE-021.

Standard Model and the Coleman Fuel Relocation Model with data from the last power cycle of the preconditioning phase and the rapid power ramp because FRAP-T4 does not model the power cycling effects of pellet cracking and relocation on pellet-cladding interaction. The plots show cladding elongation (in terms of percent of length change) as a function of fuel rod average power.

Comparison of results from both FRAP-T4 fuel deformation models with the experimental data shows that the Coleman Fuel Relocation Model best follows the trend of the data. Since this model reduces the effective size of the diametral gap, PCI was calculated at lower rod powers between 15 to 20 kW/m. Following PCI, the rate of increase in cladding elongation with average power calculated by this model corresponded well with measured data up to approximately 30 kW/m. The Standard Model calculated PCI between 30 and 40 kW/m, well above the measured data for all rods. Fuel creep or slippage between the fuel and cladding at power levels above approximately 35 kW/m reduced the rate of increase in measured cladding elongation. This behavior, not modeled in FRAP-T4, resulted in calculated strains higher than exhibited by the data. On the basis of FRAP-T4 results, the Coleman Fuel Relocation Model was used for the remainder of these analyses.

Figure 36 compares the measured and calculated cladding elongation of Rods IE-019 and IE-020. The higher internal pressure of Rod IE-019 produced a diametral gap larger (by 0.004 mm) than the gap of Rod IE-020 and this larger gap may have helped cause PCI at a power level higher than for Rod IE-020. Cladding elongation was approximately 20 to

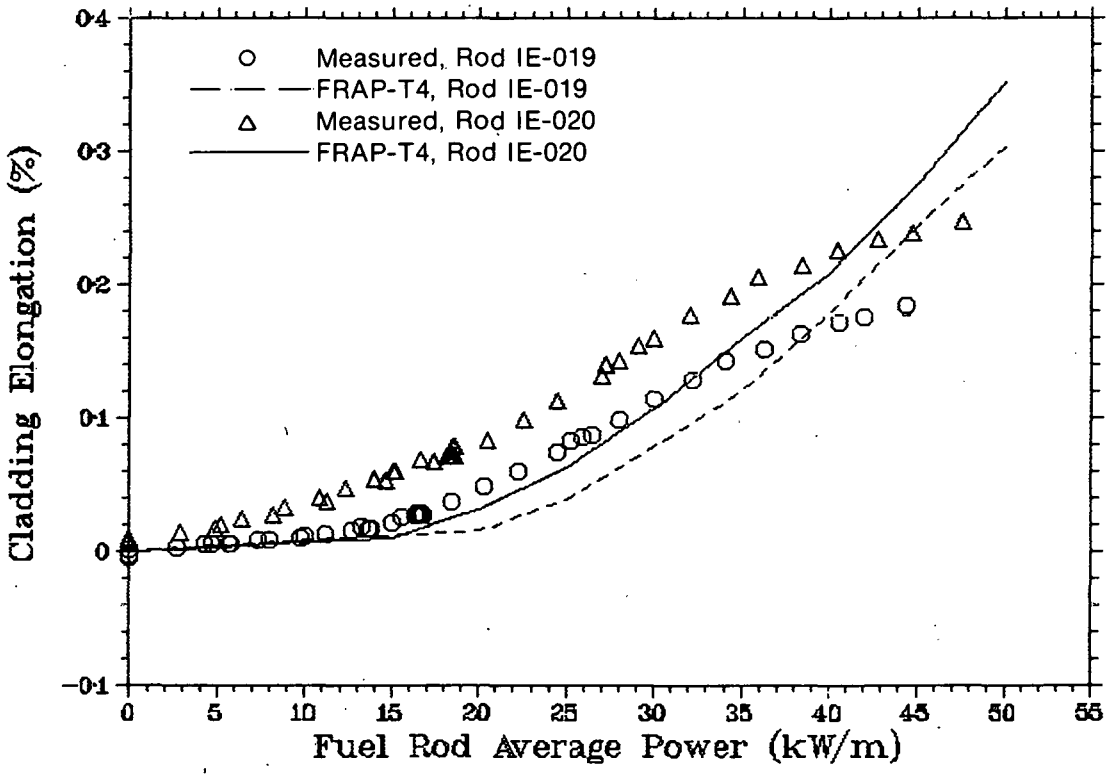

Fig. 36 Comparison of calculated and measured cladding elongation for Rods IE-019 and IE-020.

25% less for Rod IE-019 as demonstrated by both FRAP-T4 calculations and the experimental data. As shown later in Section VI.4, fuel centerline temperatures in Rod IE-019 were approximately 20 K higher than for Rod IE-020; therefore, the higher gap heat transfer (as a result of the high internal pressure) does not account for the behavior of Rod IE-019.

Figure 37 compares the calculations for Rods IE-021 and IE-020 with the measured cladding elongation of Rods IE-021 and IE-022, respectively. The difference in diametral gaps between Rods IE-021 and IE-022 is 0.05 mm. The similarity in the data and FRAP-T4 calculations shows little dependence on gap size in this range.

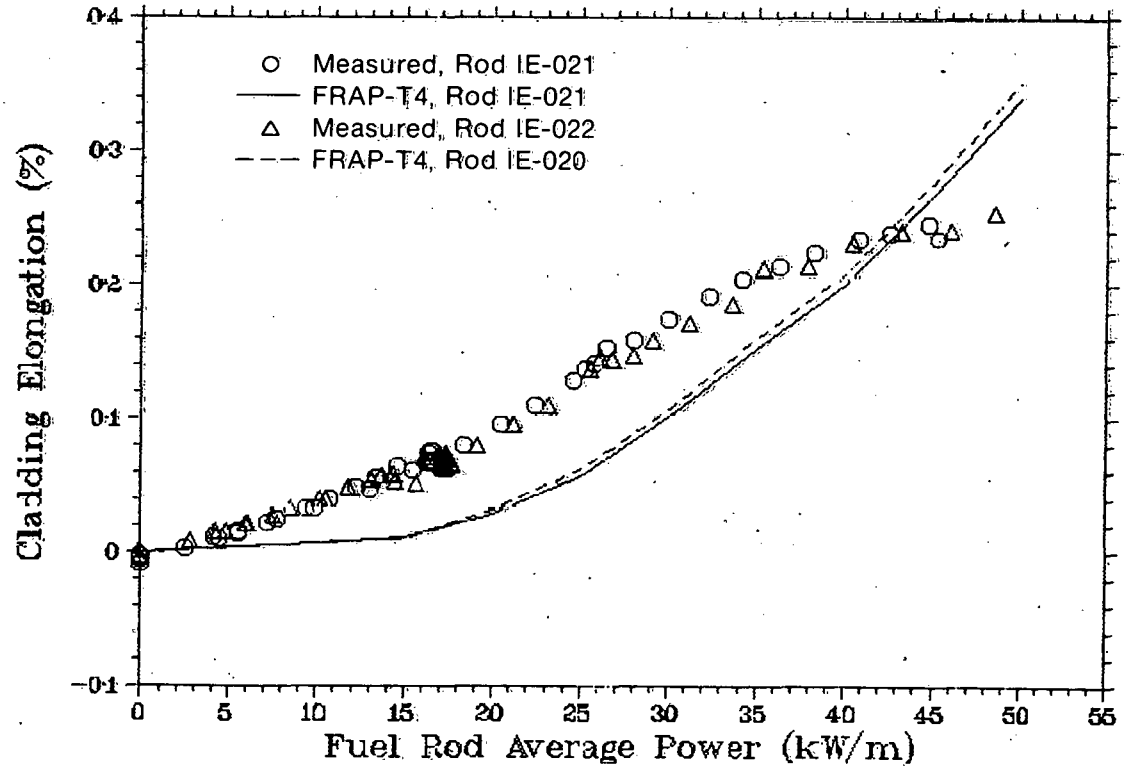

Fig. 37 Comparison of calculated cladding elongation for Rods IE-020 and IE-021 with the measured elongation for Rods IE-021 and IE-022, respectively.

Figure 38 shows the cladding elongation of all four rods during the power ramp and high power steady state operation. The data provide evidence of fuel creep at constant power during the steady state operation because the strain decreases in an exponential decay. Little difference in the nature of this decay was observed among the four rods. (Increases in elongation are due to slight increases in fuel rod power.) Fuel creep appeared to be independent of the variables of this test during the steady state operation.

Transient cladding axial displacements calculated by FRAP-T4 are compared with measurements for each rod in Figures 39 and 40. FRAP-T4 calculations agreed well with the measured cladding elongation associated with film boiling for Rods IE-020, IE-021, and

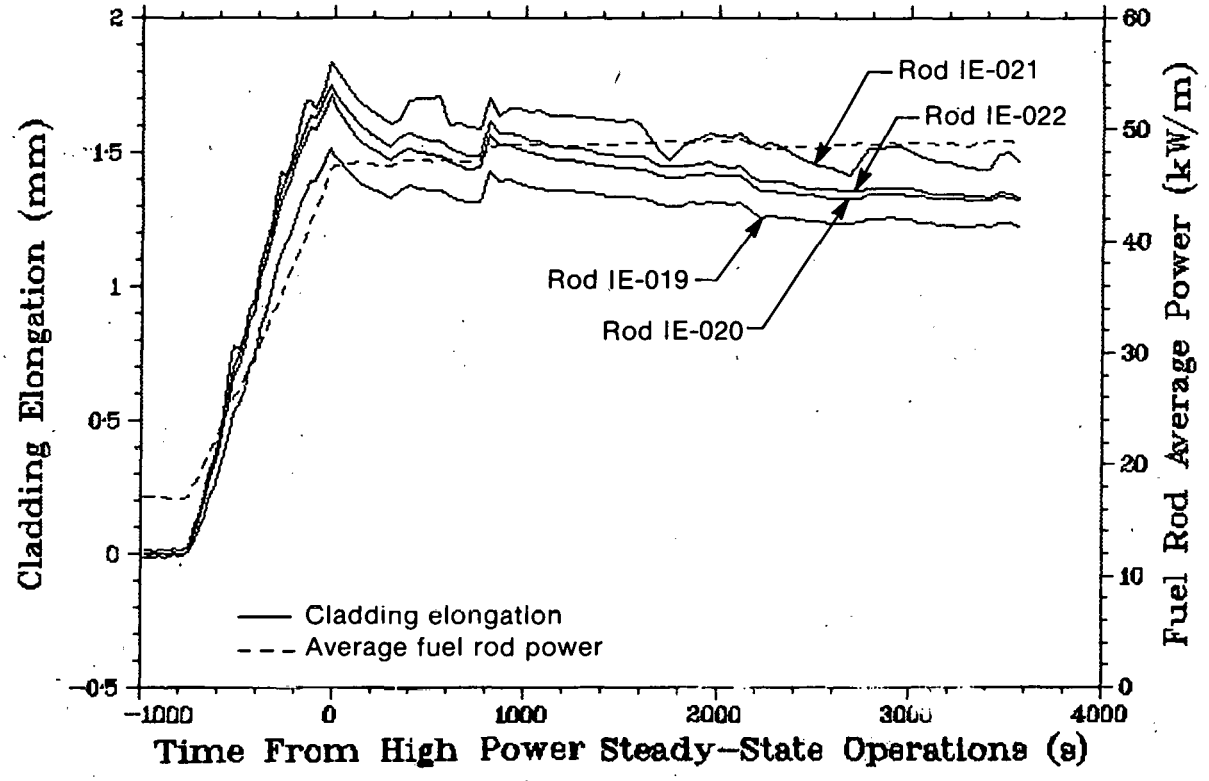

Fig. 38 Measured cladding elongation during the rapid power ramp and steady state operation for all four rods in Test IE-5.

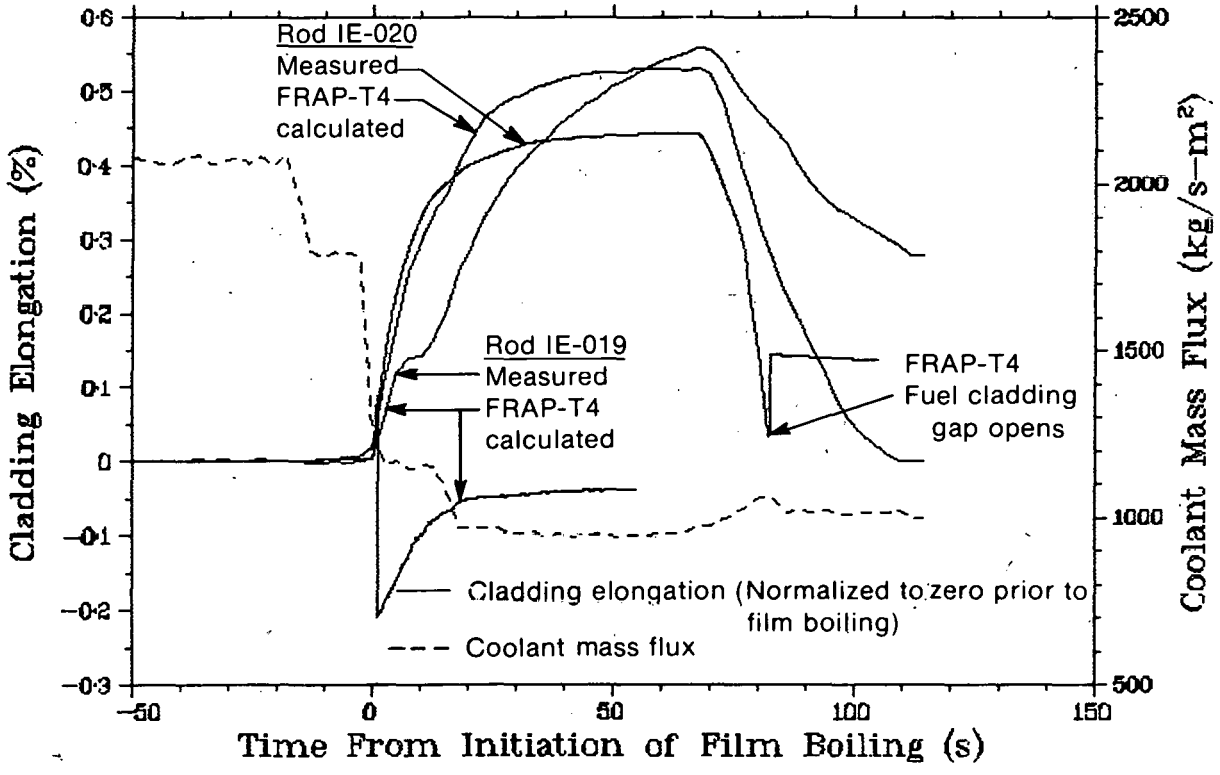

Fig. 39 Comparison of calculated and measured cladding elongation during film boiling for Rods IE-019 and IE-020.

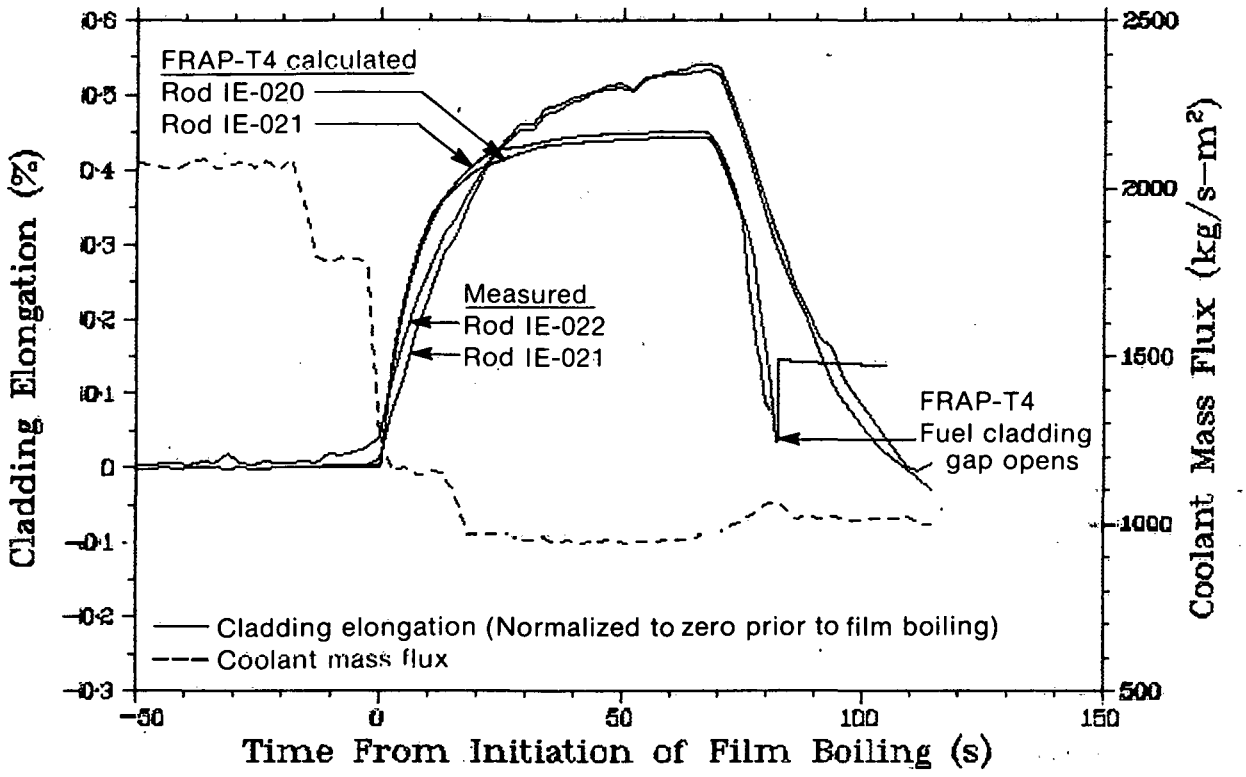

Fig. 40 Comparison of calculated cladding elongation for Rod IE-020 and IE-021 with measured elongation during film boiling for Rods IE-022 and IE-021, respectively.

IE-022. FRAP-T4 calculated cladding elongation increases that were approximately 18% below those measured for Rods IE-020 and IE-021. The film boiling region of each rod was modeled using a logic switch (discussed in Appendix E) that instantaneously forced the model into film boiling. Therefore, the rates of cladding length change are not comparable. Had FRAP-T4 been able to model the time dependent axial growth of the film boiling zone, the agreement between the calculated and measured elongation rate would have been better.

The cladding elongation for Rod IE-019 during film boiling was not well calculated by FRAP-T4. The test data indicated cladding failure 10 s after the initiation of film boiling. As shown in Figure 39, a 5-second period of negligible axial extension during cladding ballooning immediately preceded cladding failure. (Cladding failure was determined from the internal fuel rod pressure as was shown in Figure 13.) Subsequently, the elongation increased until reactor shutdown. FRAP-T4, although it did calculate failure 2 s after the onset of film boiling, indicated a reduction in cladding elongation; thus substantially underestimating the peak cladding elongation due to film boiling. The measured increase in cladding elongation after cladding failure is believed to have been caused by gap closure above the ballooned region and free thermal expansion due to film boiling.

The FRAP-T4 analysis for Rod IE-020 shown in Figures 39 and 40, was continued through the reactor shutdown period. FRAP-T4 calculated an abrupt increase in elongation followed by a constant strain during reactor shutdown. As the rod cooled, the fuel controlled the axial elongation and the rod strain rapidly decreased below the calculated

permanent axial strain (FRAP-T4 models no slippage between the fuel and cladding). FRAP-T4 then calculated complete opening of the fuel-cladding gap and the cladding returned to the level of calculated permanent axial strain. This behavior is not evident in the experimental data, because slippage between the fuel and cladding probably occurred.

FRAP-T4 calculated that Rods IE-020 and IE-021 would have closed gaps at a rod average power of 17 kW/m and would remain closed over the bulk of the rod prior to the flow reduction phase. If no slippage between the fuel and cladding occurred, the cladding would deform axially to accommodate the fuel expansion during film boiling. Unrestrained axial thermal expansion of the cladding due to an estimated average temperature during film boiling would result in a cladding elongation of approximately 3 mm. Unrestrained axial thermal expansion of the fuel for the corresponding average temperature would result in approximately 13 mm cladding elongation. FRAP-T4 calculated an axial displacement of 9.093 and 8.71 mm for Rods IE-020 and IE-021, respectively, between the range of free axial cladding elongation and free axial fuel elongation.

Posttest fuel rod lengths were not measured to determine permanent axial strain. However, in-reactor cladding elongation measurements were made approximately 10 minutes after reactor shutdown while the rods were at 605 K and zero power. They then were compared with the measured elongations at zero power prior to the high power ramp. The permanent axial strains measured in this manner were 0.41, 0.20, 0.14, and 0.24% for Rods IE-019 through IE-022, respectively. FRAP-T4 calculated permanent axial strains of -1.94, 0.13, and 0.12% for Rods IE-019, IE-020, and IE-021, respectively. Permanent axial strain of Rod IE-019, the high pressure rod that failed 10 s after the onset of the film boiling, was underestimated by FRAP-T4. The test data indicated that the rate of rod elongation was zero for 5 s immediately preceding failure and then continued to increase throughout film boiling operation. FRAP-T4 calculated rod failure at the onset of film boiling and a negative and permanent elongation unaffected by subsequent film boiling operation. FRAP-T4 also underestimated the measured growth in Rods IE-020 and IE-021. Again, FRAP-T4 results for Rod IE-020 can be compared with the data from Rod IE-022.

2. CLADDING RADIAL DEFORMATION

Permanent cladding radial deformation occurred during film boiling and may have occurred during the power ramp. Posttest cladding diameter measurements of all the rods reported in Section V.2 are compared with FRAP-T4 analyses in this subsection. The standard deviation of the strain shown in Figures 41 through 43 is estimated to be ±0.26%.

The percent diametral strain for Rod IE-019 calculated from pretest and posttest diameter measurements is shown in Figure 41. The initial high internal pressure produced ballooning of the cladding over the length of the film boiling zone. FRAP-T4 calculations are not shown in Figure 41 because failure was calculated to be immediately after the initiation of film boiling. As a result, constant strain of only 2% was calculated over the film boiling zone.

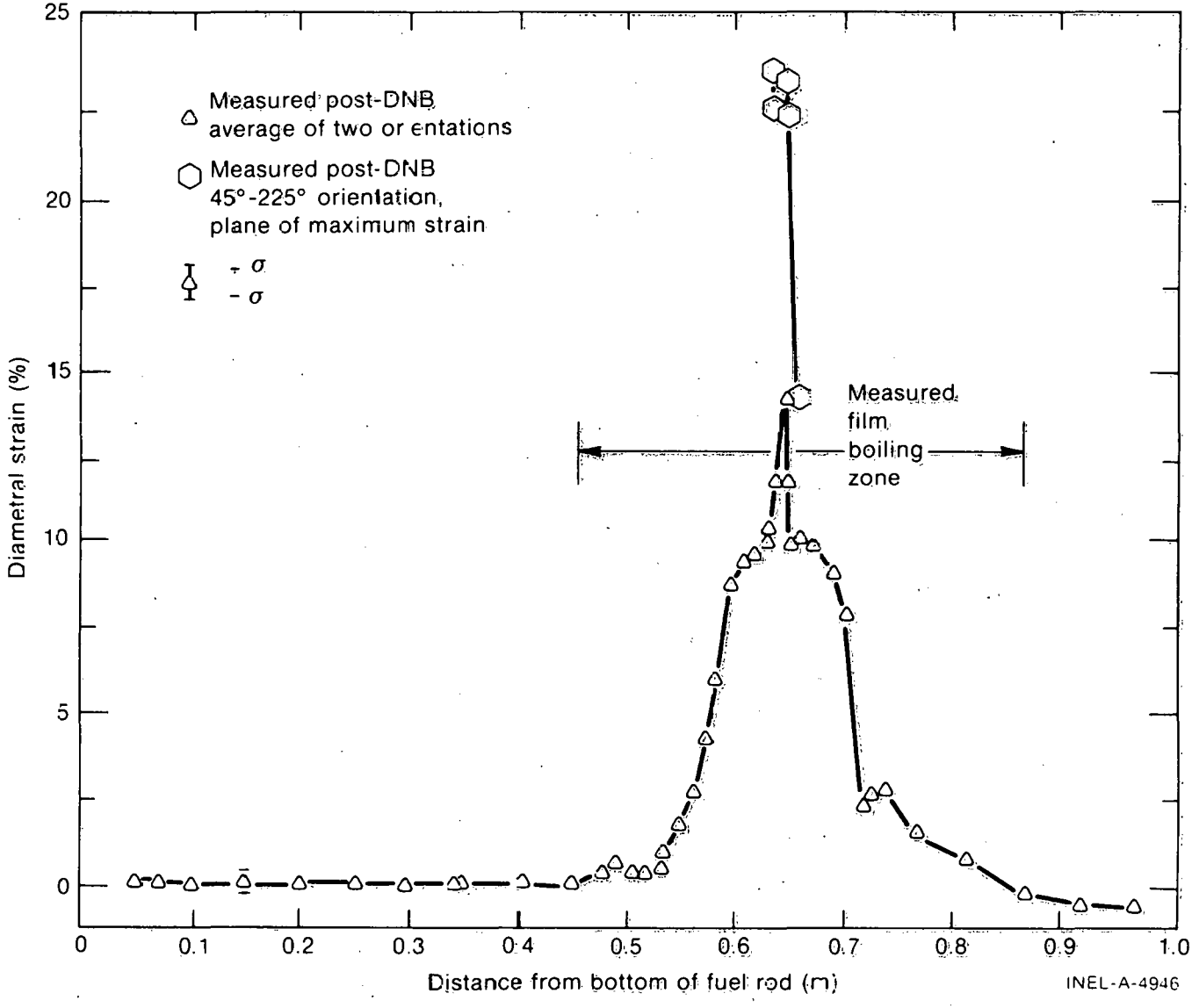

Fig. 41 Measured diametral strain for Rod IE-019.

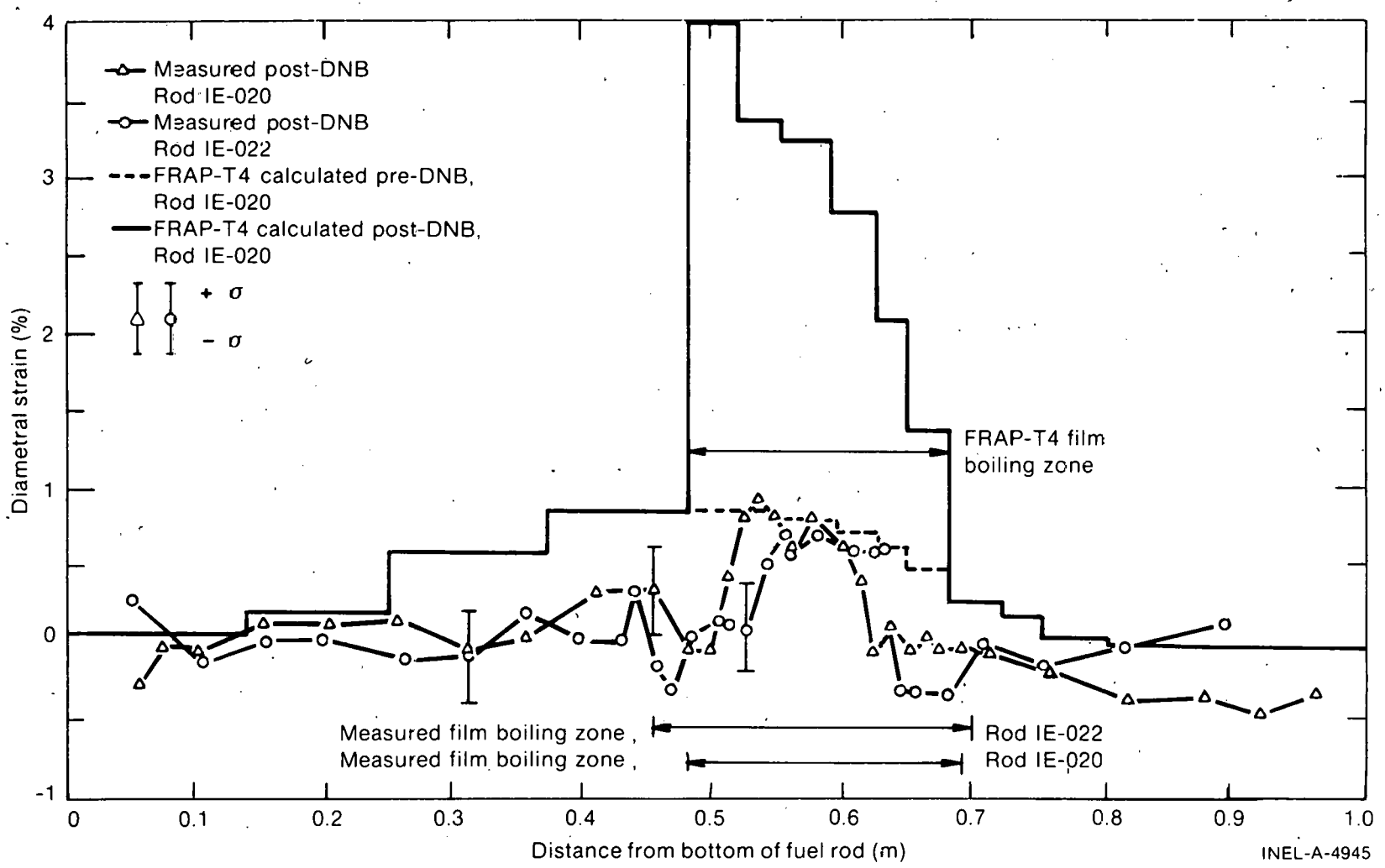

Fig. 42 Comparison of calculated diametral strain for Rod IE-020 with the measured diametral strains for Rods IE-020 and IE-022.

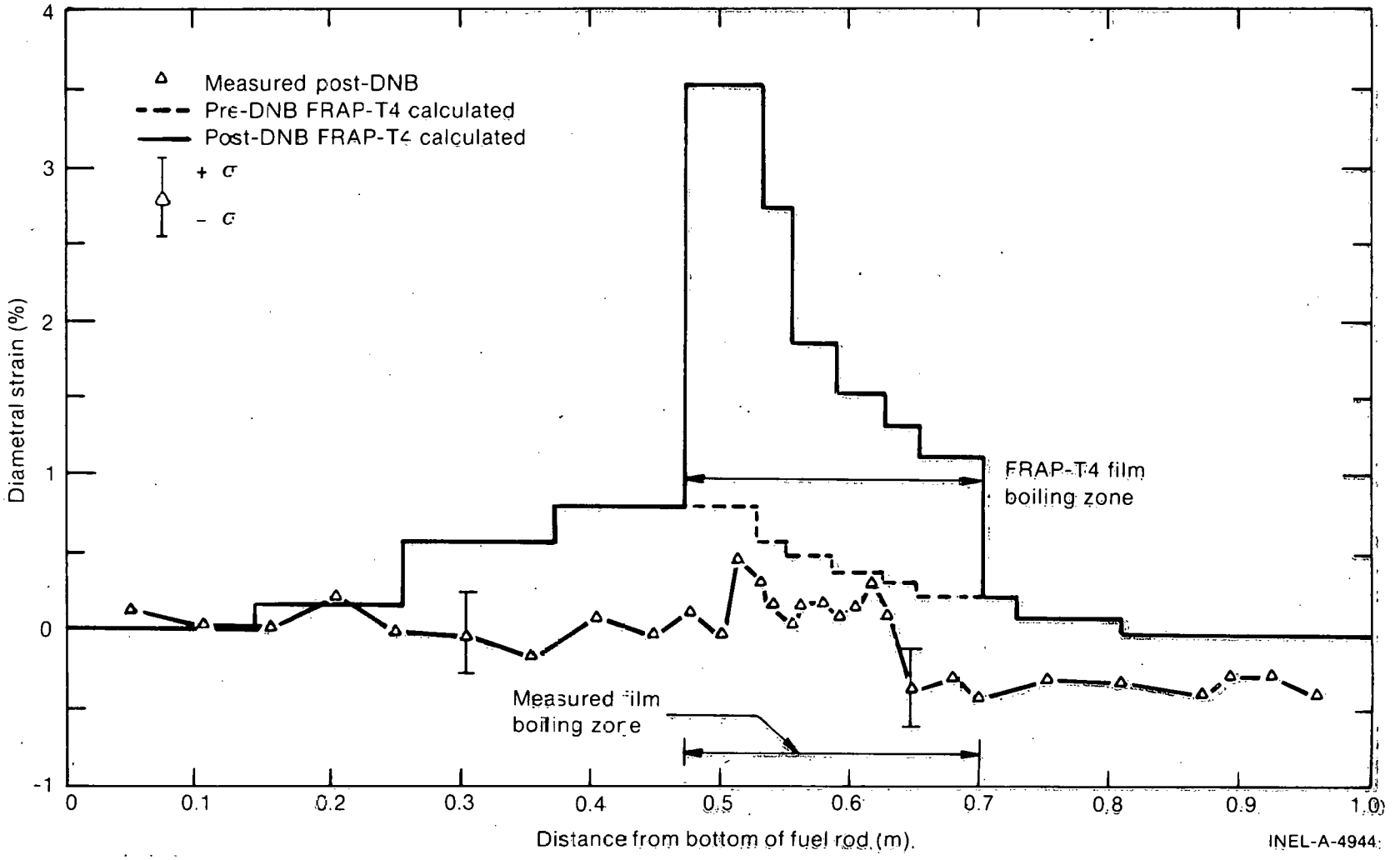

Fig. 43 Comparison of calculated and measured diametral strains for Rod IE-021.

Cladding diametral strains for Rods IE-020, IE-021, and IE-022 are compared with FRAP-T4 results for Rods IE-020 and IE-021 in Figures 42 and 43. Differential fuel-cladding thermal expansion and some molten fuel volume expansion contributed to produce the cladding growth. FRAP-T4 overestimated the cladding strain by a factor of three or four. These results are similar to those obtained in Test IE-2[5] in which FRAP-T3 overestimated the cladding growth of Rod IE-011 by a factor of three. Rod IE-011, having a 0.10-mm diametral gap and irradiated cladding experienced a maximum increase in diameter of 0.6%, slightly smaller than that for the rods in Test IE-5.

The radial strain data do not provide significant evidence of irradiation effects in the cladding. As previously discussed, Rods IE-019, IE-020, and IE-021 were fabricated from irradiated cladding. Rod IE-019 failed 10 s after the onset of film boiling. Rods IE-020 and IE-022 were similar except that the Rod IE-020 cladding was irradiated as a water tube without fuel and the Rod IE-022 cladding was unirradiated.

3. FUEL ROD INTERNAL PRESSURE

The fuel rod internal pressure data were corrected for large zero drifts due to decalibration of the pressure transducers (Appendix C). Rod internal pressure, P, is presented in terms of the fractional change in pressure,

$$\frac{P - P_o}{P_o}$$

where P_o is the rod internal pressure at the start of the test at 606 K after correction for decalibration of the pressure transducer (Table C-VI).

Internal pressure for all fuel rods during the preconditioning period is compared in Figure 44. The smaller scatter in the data indicate little dependence of rod pressure on the different power cycles during preconditioning. Rod IE-020 had a 20% greater pressure increase than the other rods. Rod IE-021, with a 50% larger diametral gap than the remaining rods, experienced the smallest pressure increase.

Figure 45 compares FRAP-T4 calculations of the fuel rod internal pressure with the data during the preconditioning phase for Rods IE-019 and IE-020. Pressures generally were underestimated. In Figure 45, the calculations demonstrate that Rod IE-019, with its high (16.6 MPa at 605 K) internal pressure at the start of the test, had a slightly greater increase in pressure than Rod IE-020. The high pressure results in a greater diametral gap which provides higher fuel and gas temperatures. This effect was not seen in the test data. In Figure 46, FRAP-T4 calculations and measured data demonstrate the small pressure differences between Rods IE-020 and IE-021, even though Rod IE-021 had a larger gap. No effects of power cycling on internal pressure were observed.

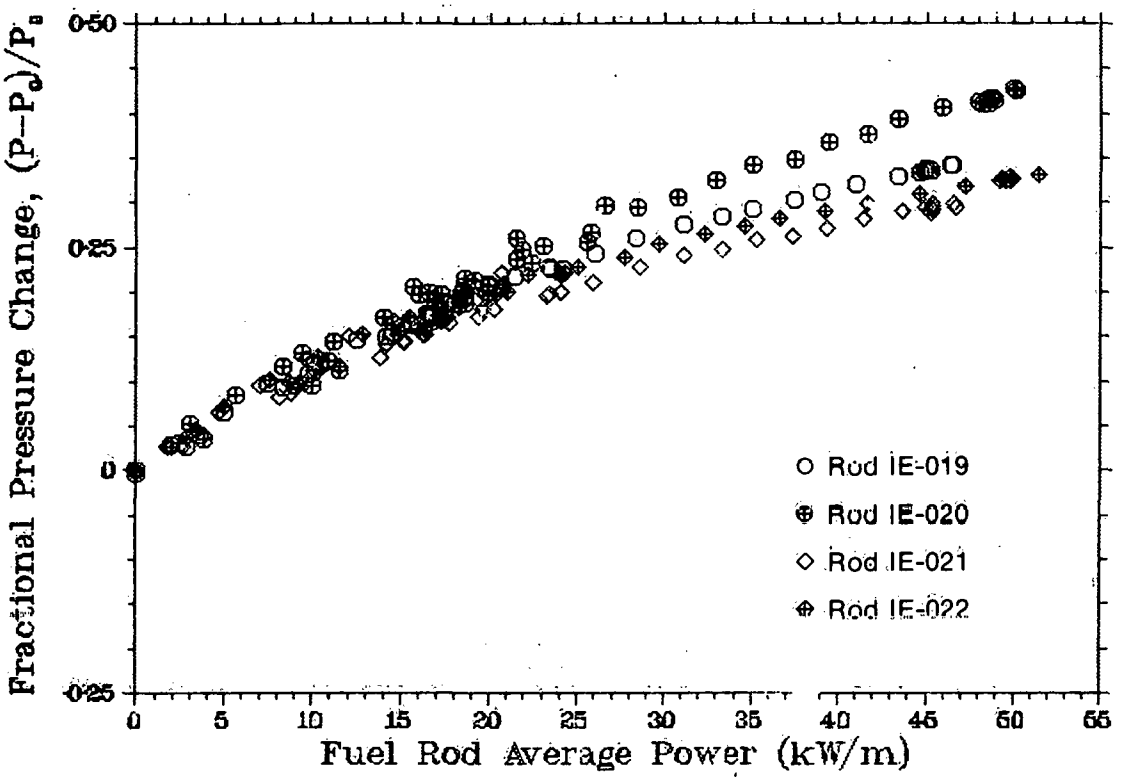

Fig. 44 Fuel rod internal pressure changes versus fuel rod average power during the preconditioning phase for all four fuel rods in Test IE-5.

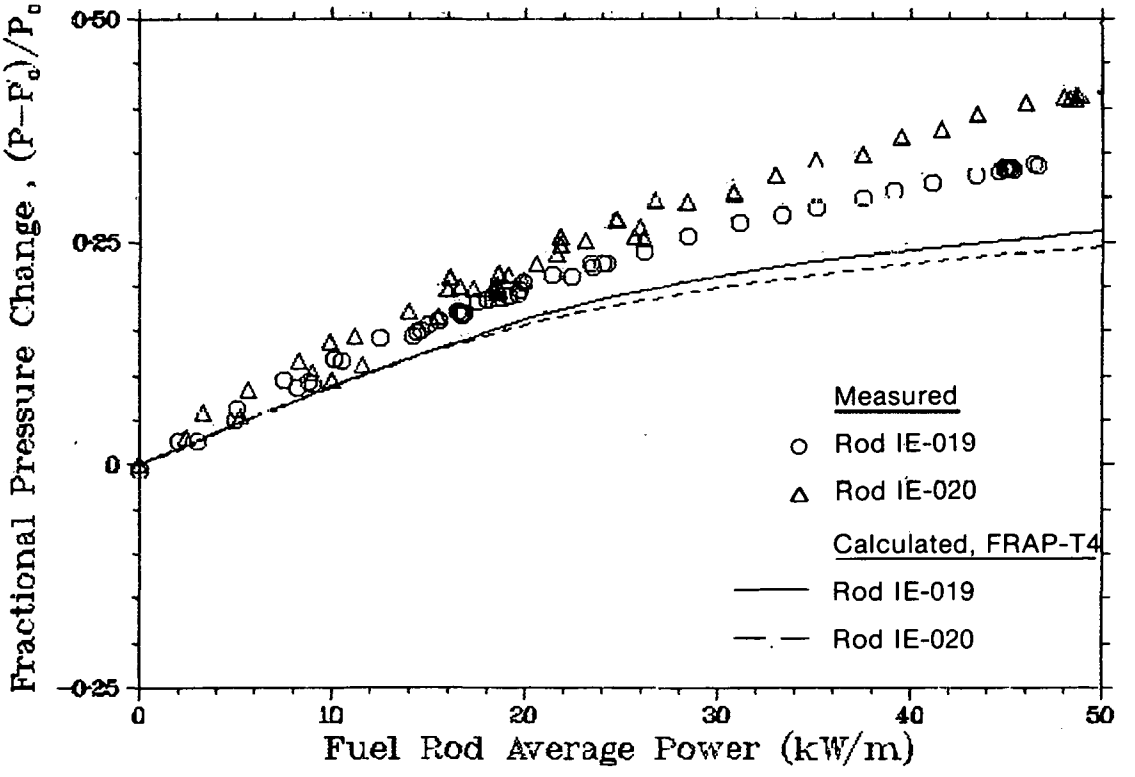

Fig. 45 Comparison of calculated and measured fuel rod internal pressure changes during the preconditioning phase for Rods IE-019 and IE-020.

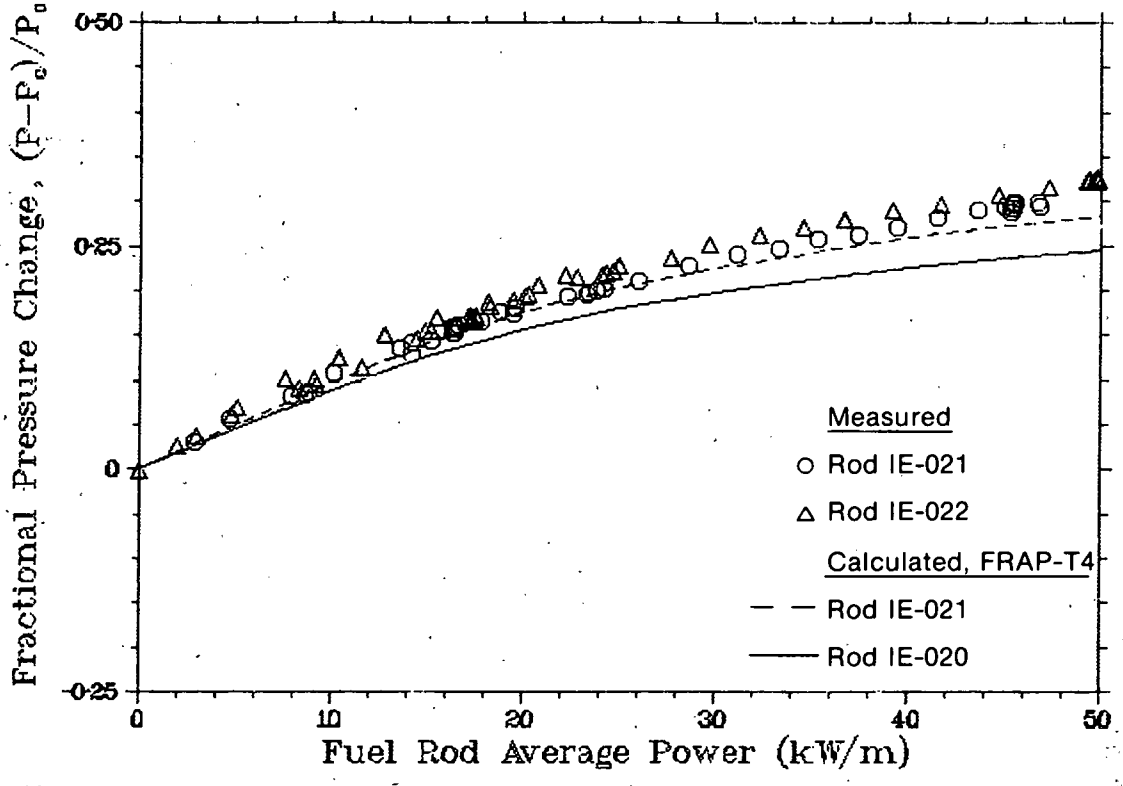

Fig. 46 Comparison of calculated fuel rod internal pressure changes for Rods IE-020 and IE-021 with the measured changes for Rods IE-022 and IE-021, respectively.

Pressure data for the power ramp and steady state operation are presented in Figure 47. The data show that pressure equilibrium conditions were attained before the flow reduction phase.

FRAP-T4 calculations of transient fuel rod internal pressure are compared with the data for Rods IE-019 and IE-020 in Figure 48 and are compared with the measurements for Rods IE-021 and IE-022, respectively, in Figure 49. All four transducers reponded to the occurrence of film boiling. FRAP-T4 calculated a closed fuel-cladding gap in the film boiling regions of Rods IE-019, IE-020, and IE-021. Therefore, no gap was modeled in these regions and no pressure increases during film boiling were calculated even though instantaneous pressure equilibrium between the fueled region and the plenum was assumed by FRAP-T4. Data from Rod IE-019 indicate that pressure communication exists between the fuel region and the plenum. The measured pressure increases are apparently due to gas in fuel cracks and pellet dishes.

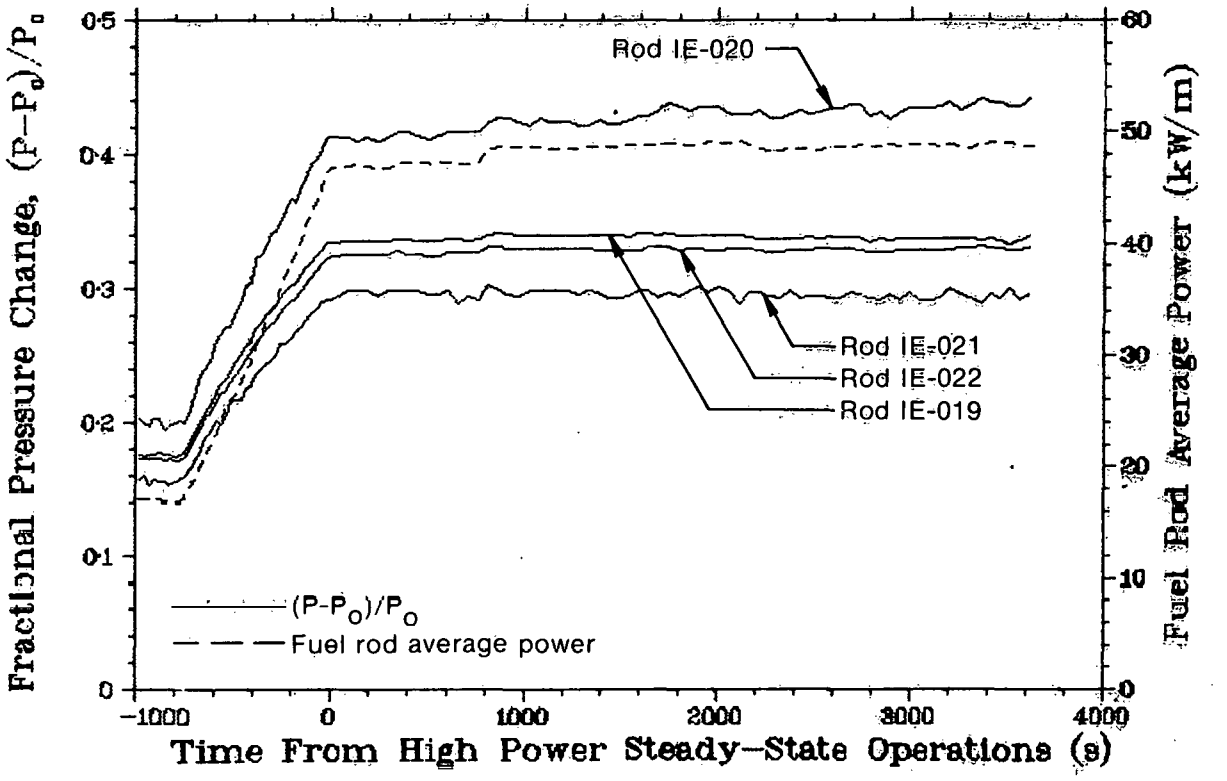

Fig. 47 Measured fuel rod internal pressure changes during the power ramp and steady state operation for all four rods in Test IE-5.

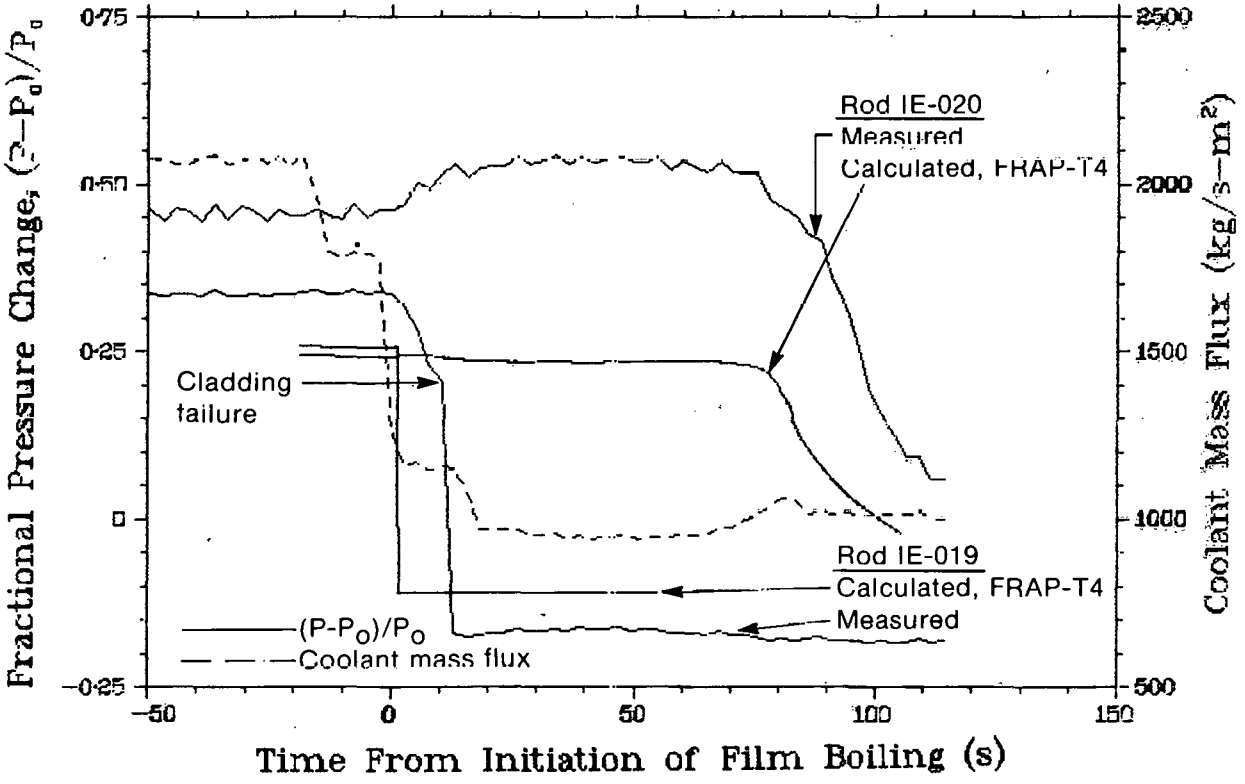

Fig. 48 Calculated and measured fuel rod internal pressure changes during film boiling on Rods IE-019 and IE-020.

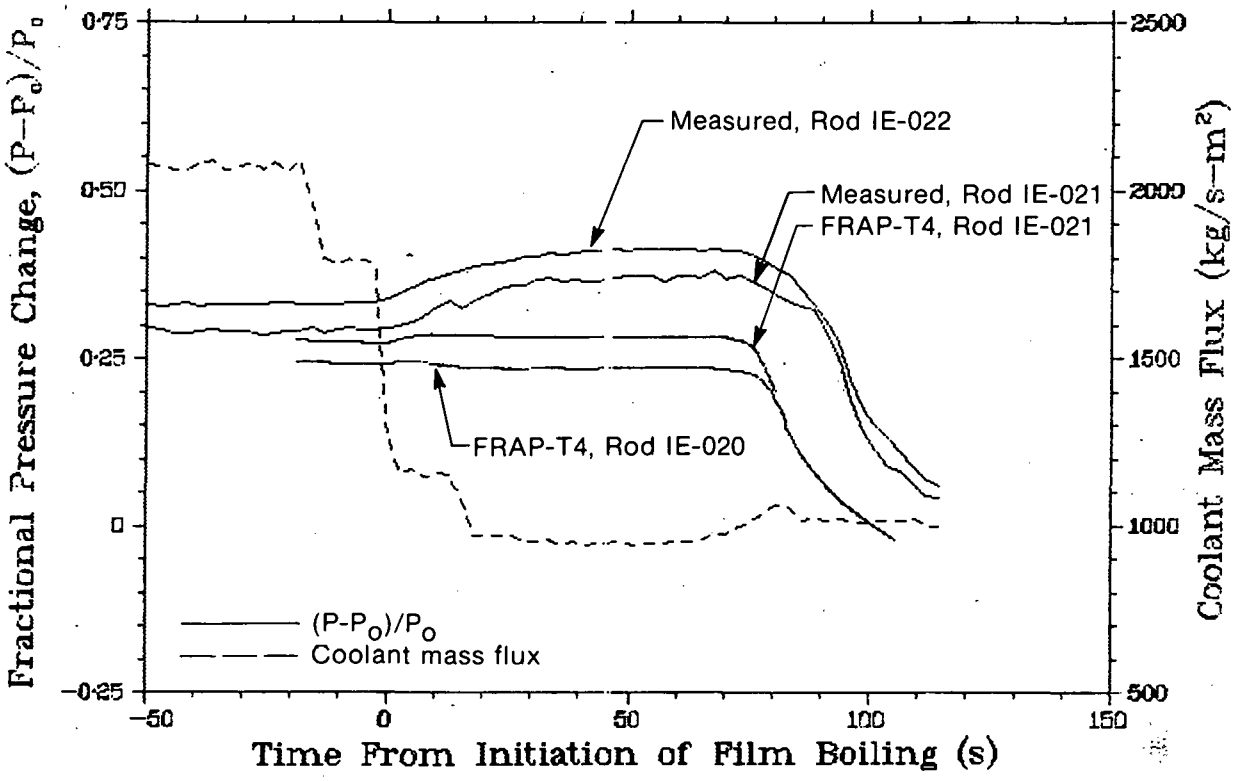

Fig. 49 Comparison of calculated fuel rod internal pressure changes during film boiling in Rods IE-020 and IE-021 with the measured pressure changes in Rods IE-022 and IE-021, respectively.

4. FUEL CENTERLINE TEMPERATURE

Centerline temperatures versus local fuel rod power for all fuel rods during the preconditioning phase are presented in Figure 50. No centerline temperature dependence on power cycling was observed.

Figures 51 to 53 compare FRAP-T4 calculations of the fuel centerline temperature for each rod with both fuel deformation models (the Coleman Fuel Relocation Model and the Standard Model) with the experimental data during the preconditioning phase. In all cases, the fuel centerline temperatures calculated with the Coleman Fuel Relocation Model more closely agreed with the test data than did those calculated with the Standard Model which generally overestimated fuel centerline temperatures by 100 to 200 K.

In Figure 54, the FRAP-T4 calculations of fuel centerline temperature are compared with the temperature data of Rod IE-019 and IE-020 during the preconditioning phase. Temperature data obtained from Rods IE-021 and IE-022 during the same period are compared with FRAP-T4 calculations in Figure 55. On the basis of the cladding elongation data in Section VI.1, the high internal pressure of Rod IE-019 increased the effective fuel-cladding gap, thereby reduced the gap conductance, and may account for the slightly higher temperatures ($\sim$20 K) over Rod IE-020 which had the same initial fuel-cladding gap.

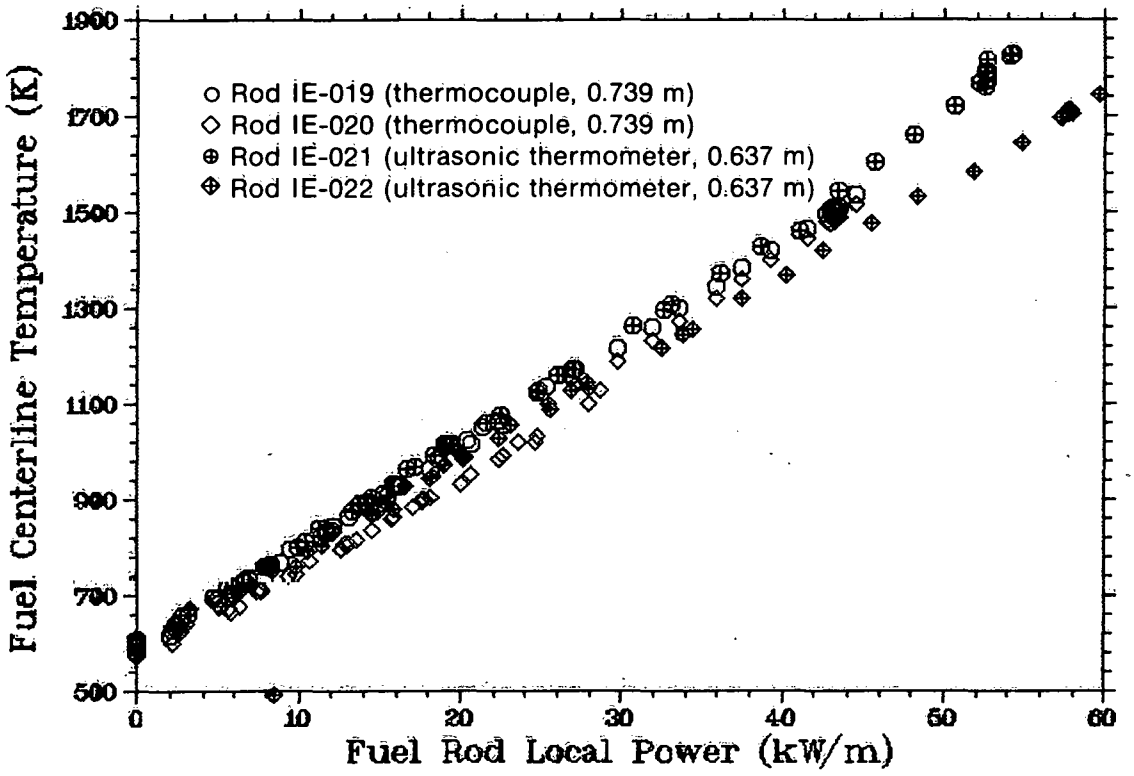

Fig. 50 Measured fuel centerline temperatures during the preconditioning phase for all four rods in Test IE-5.

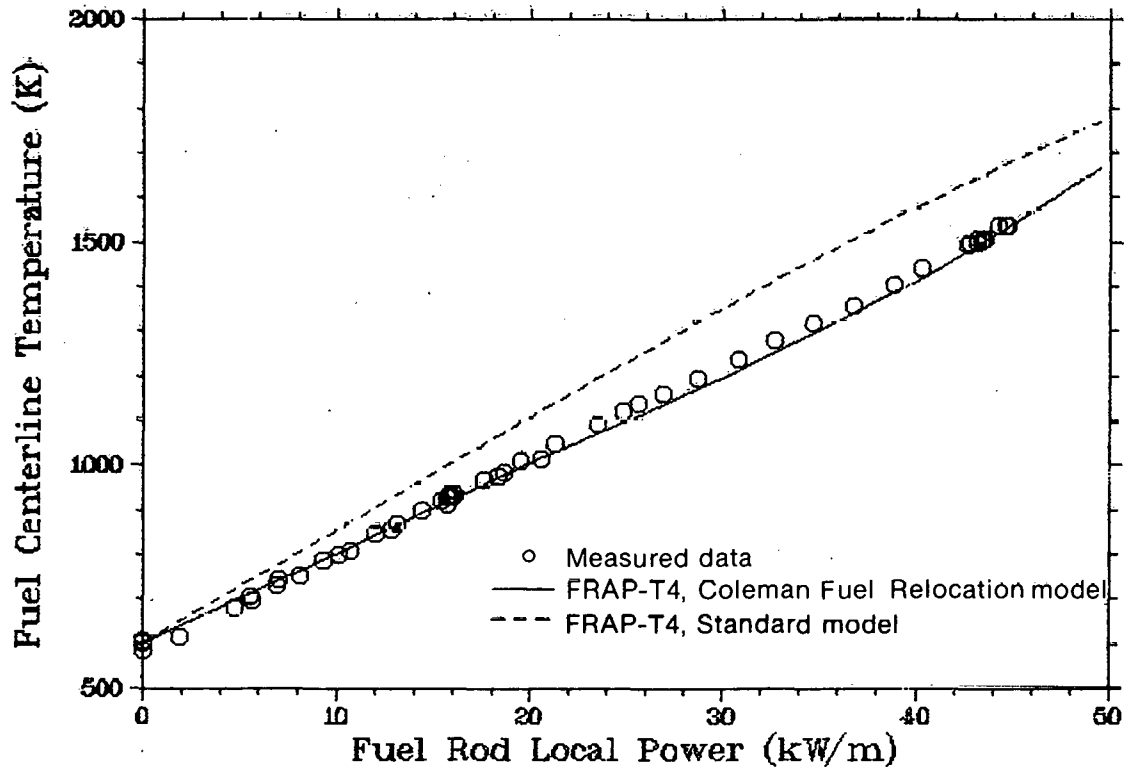

Fig. 51 Comparison of calculated with measured fuel centerline temperatures for Rod IE-019 at the 0.739-m elevation.

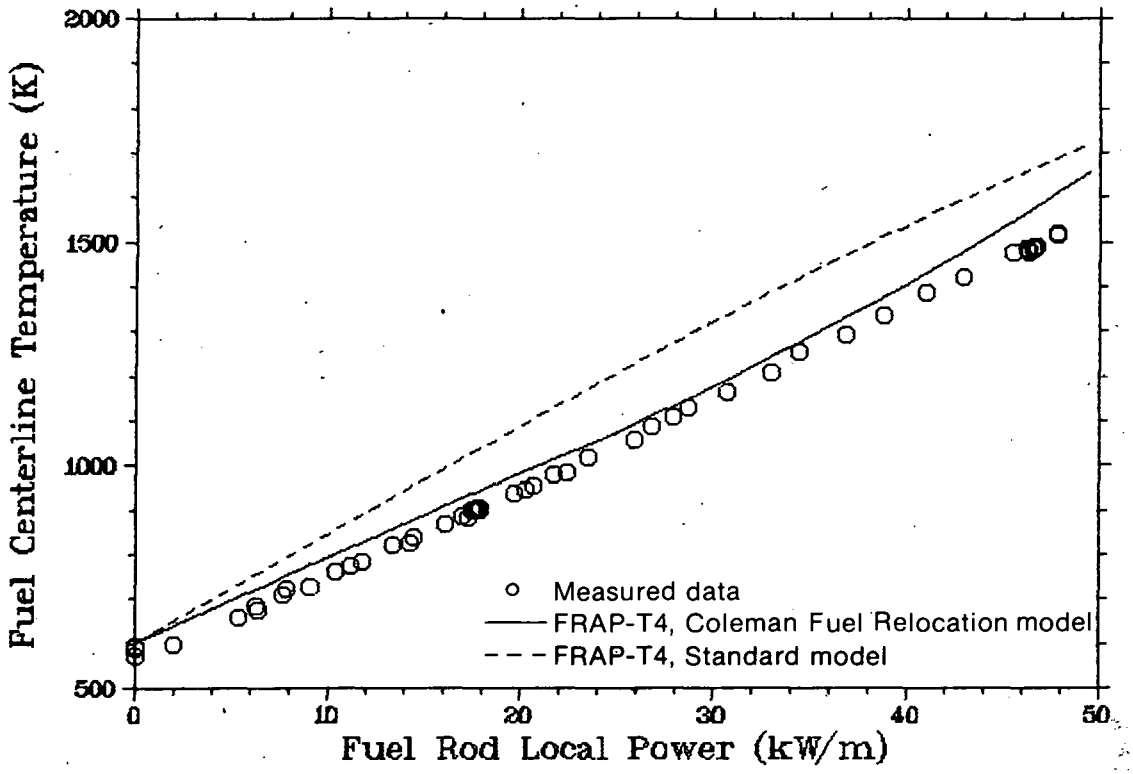

Fig. 52 Comparison of calculated with measured fuel centerline temperatures for Rod IE-020 at the 0.739-m elevation.

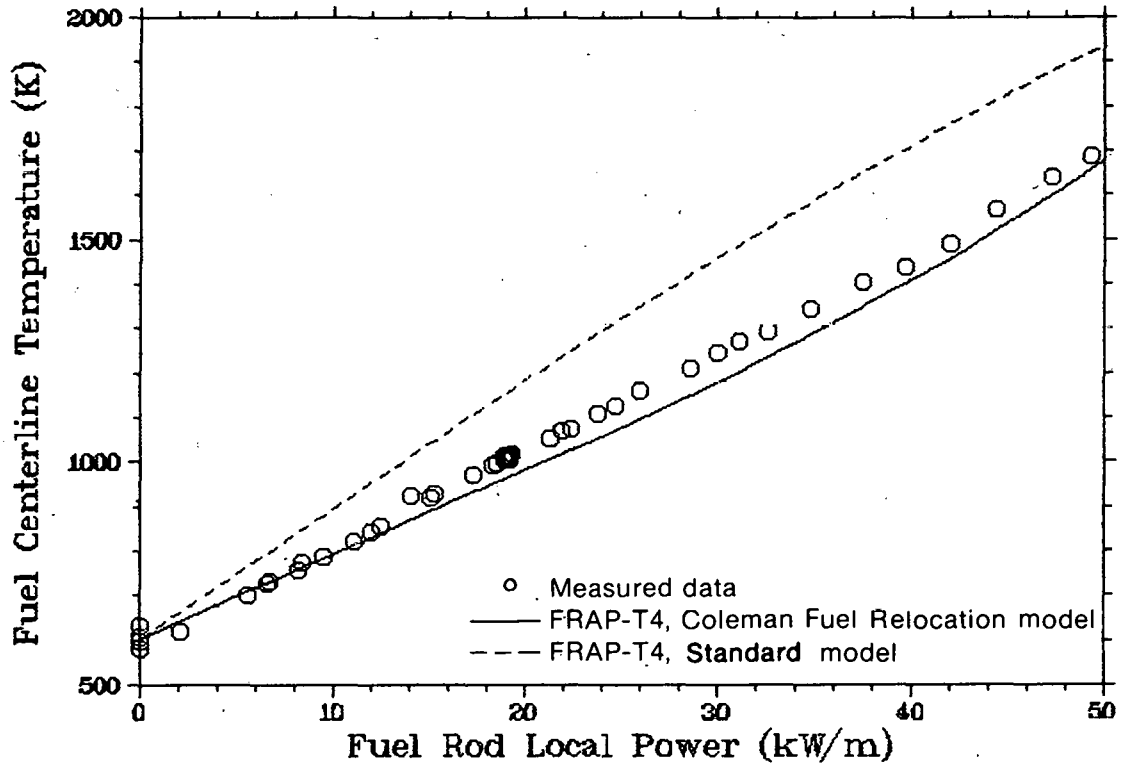

Fig. 53 Comparison of calculated with measured fuel centerline temperatures for Rod IE-021 at the 0.637-m elevation.

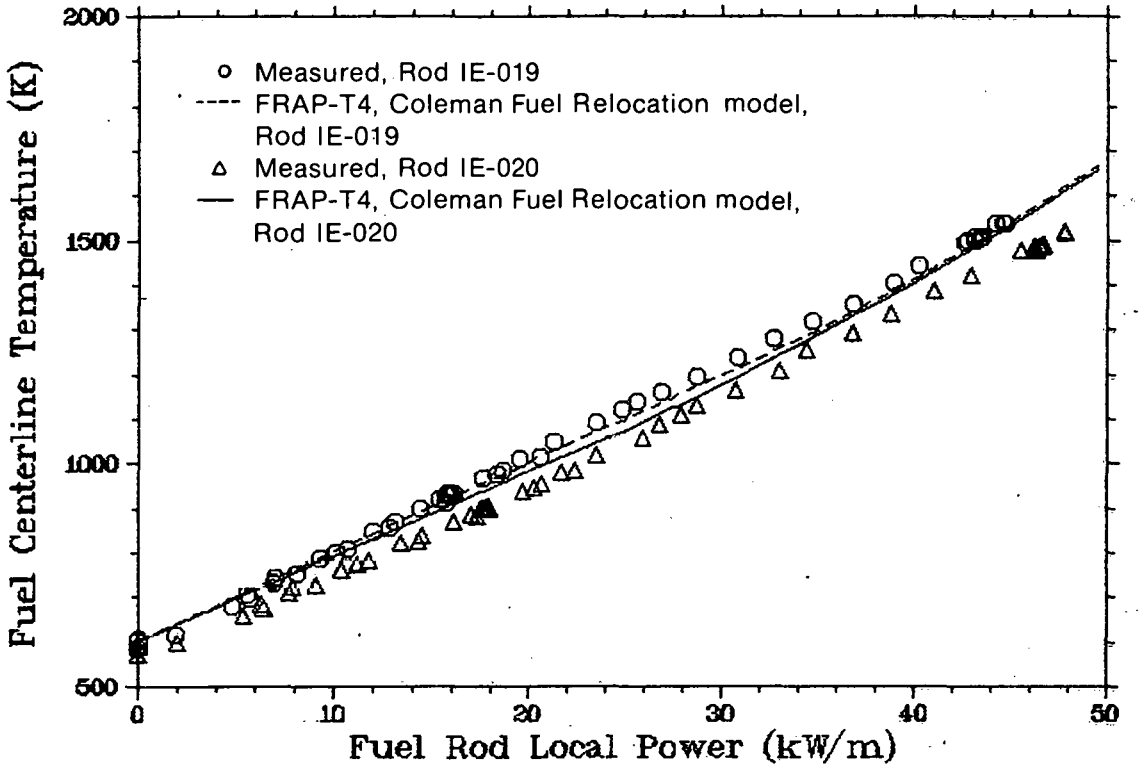

Fig. 54 Comparison of calculated and measured fuel centerline temperatures for Rods IE-019 and IE-020 at the 0.739-m elevation.

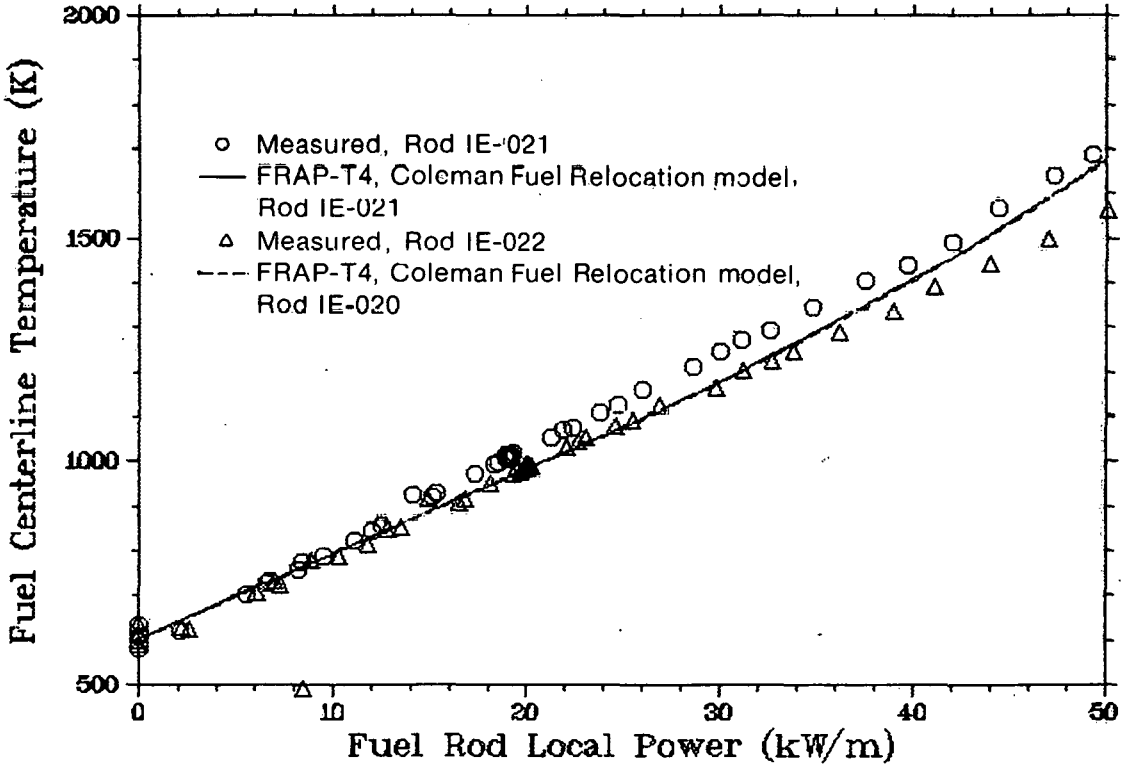

Fig. 55 Comparison of calculated fuel centerline temperatures for Rods IE-020 and IE-021 with measured temperatures for Rods IE-022 and IE-021, respectively, at the 0.637-m elevation.

The differences in fuel centerline temperature between Rods IE-021 and IE-022 (approximately 150 K at 50 kW/m) are attributed to the 0.05-mm larger fuel-cladding gap of Rod IE-021. No effects of power cycling on fuel centerline temperature were observed.

Fuel centerline temperature data during the power ramp and steady state operation are presented in Figure 56. The data indicate that fuel temperatures were stable and relatively constant prior to the flow reduction transient.

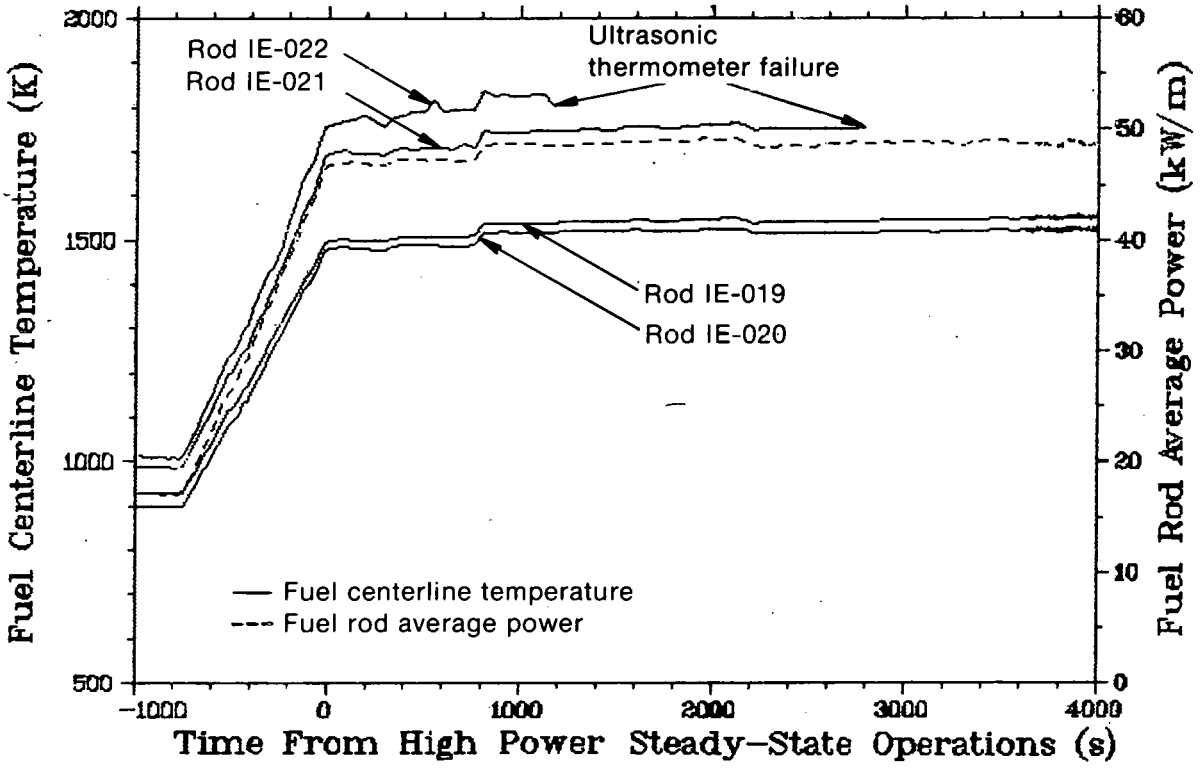

Fig. 56 Measured fuel centerline temperatures during the power ramp and steady state operation for all four rods in Test IE-5.

Figure 57 compares the fuel centerline temperatures measured at the 0.739-m elevation in Rods IE-019 and IE-020 with FRAP-T4 calculations during the flow reduction phase of the test. The erratic behavior of the Rod IE-019 fuel centerline temperatures demonstrates that the temperatures were well above the 2500 K limit of measurement for a refractory metal thermocouple. FRAP-T4 calculated a peak temperature of 2850 K. Metallographic examination disclosed that no fuel melting occurred in the region surrounding the 0.739-m elevation. An increase of approximately 750 K was experimentally observed in Rod IE-020, indicating that the 0.739-m elevation was probably within or near the film boiling zone during some portion of the test. Since the visual postirradiation examination determined that the top of the film boiling zone was 0.688 m above the bottom of the fuel rod, film boiling was not modeled at the thermocouple elevation of 0.739 m. Consequently, no calculations for Rod IE-020 are shown in Figure 57. FRAP-T4 calculated centerline temperatures above the fuel melting point at the 0.637-m elevation on Rods IE-021 and IE-022.

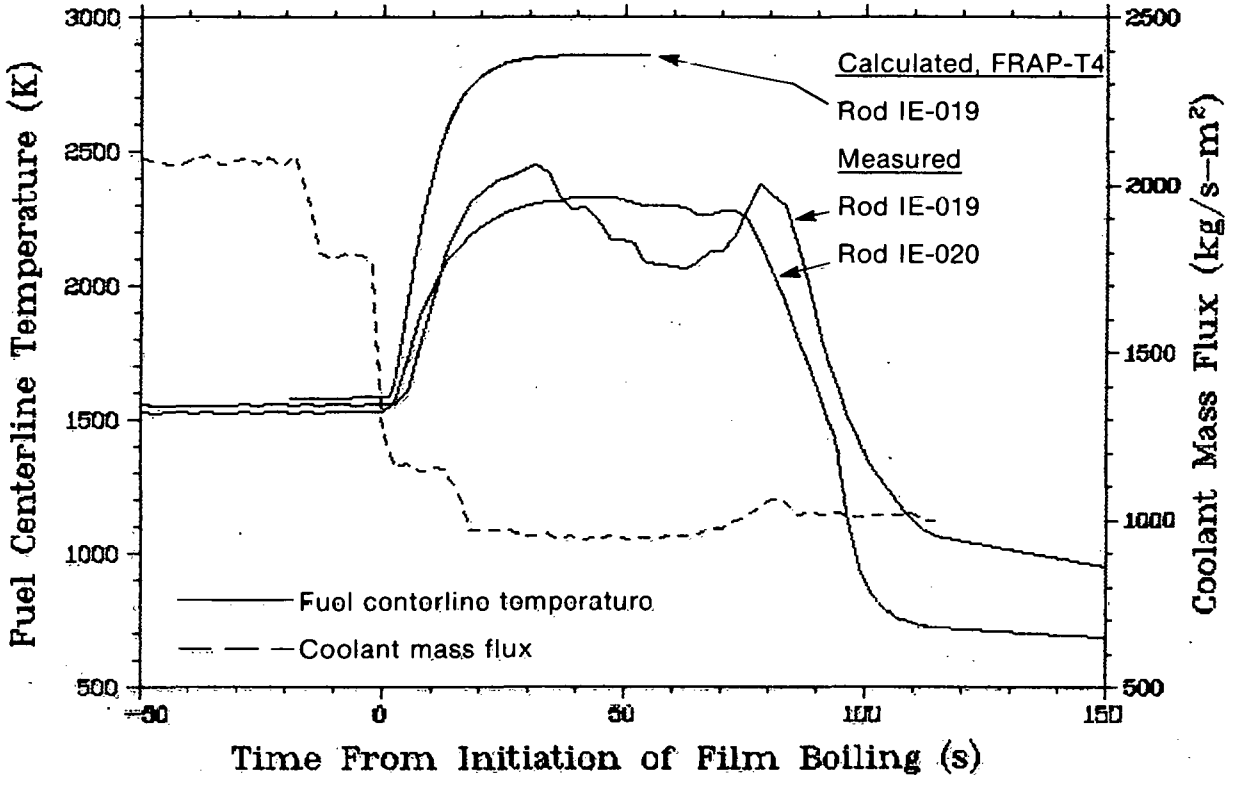

Fig. 57 Comparison of calculated fuel centerline temperatures in Rod IE-019 with measured temperatures in Rods IE-019 and IE-020 during film boiling operation at the 0.739-m elevation.

5. CLADDING SURFACE TEMPERATURE

Figure 58 compares cladding surface temperature data from the preconditioning phase for Rods IE-019, IE-020, and IE-021, at an average 0.643-m elevation, with steady state FRAP-T4 calculations. Figure 59 presents temperature data from the four thermocouples on Rod IE-022 for the same time period. Figures 60 to 62 present the cladding surface temperature data during film boiling for all rods. Film boiling was indicated at the 45-degree orientation on Rod IE-019. Film boiling occurred on Rod IE-020 at the 255-degree orientation, but was not indicated at the 45-degree position due to thermocouple failure and both thermocouples on Rod IE-021 indicated film boiling. The highest temperature, 975 K, was recorded on Rod IE-022 prior to failure of the thermocouple. In all cases, the cladding thermocouples indicated lower temperatures than expected in the region of film boiling.

FRAP-T4 results are compared with the cladding surface temperatures in Figures 63 and 64. Only data from thermocouples which responded to film boiling are compared with the calculations. Film boiling was not modeled in FRAP-T4 at the 0.72-m elevation on Rod IE-020 for comparison with the temperature data at the 0.743-m elevation from Rod IE-022. FRAP-T4 calculated surface temperatures on the order of 1600 K, substantially higher than the peak measured value of 800 K. In addition, cladding temperatures estimated from oxide layer thickness measurements during postirradiation examination indicated that the cladding probably reached the 1600 K calculated by FRAP-T4. The fin-cooling effect (Appendix B) associated with the thermocouple contributed to the low temperature measurement.

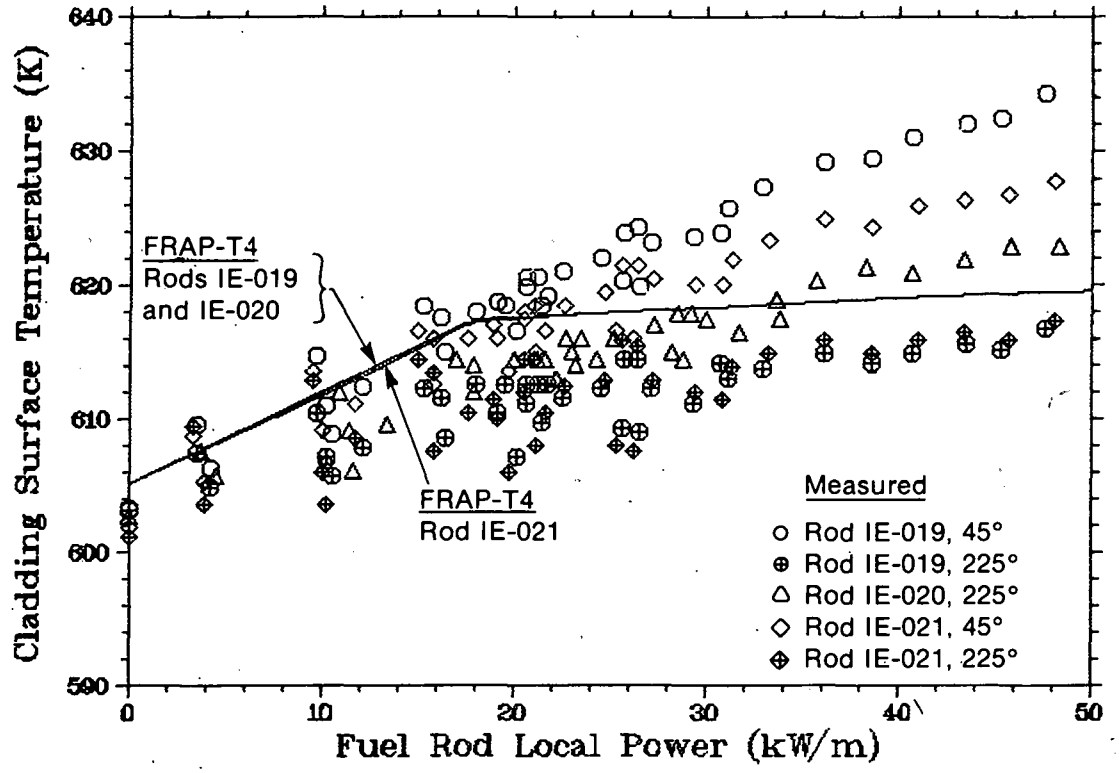

Fig. 58 Comparison of calculated cladding surface temperatures with measured temperatures during the preconditioning phase at approximately the 0.643-m elevation on Rods IE-019, IE-020, and IE-021.

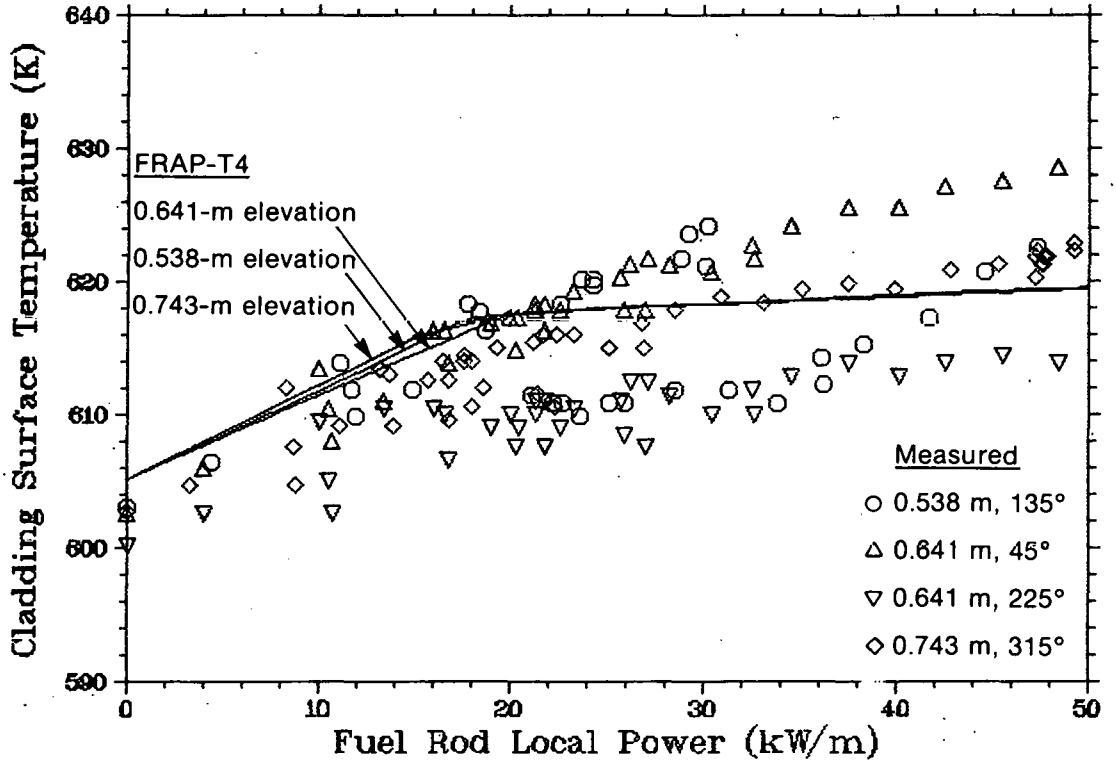

Fig. 59 Comparison of calculated and measured cladding surface temperatures on Rod IE-022.

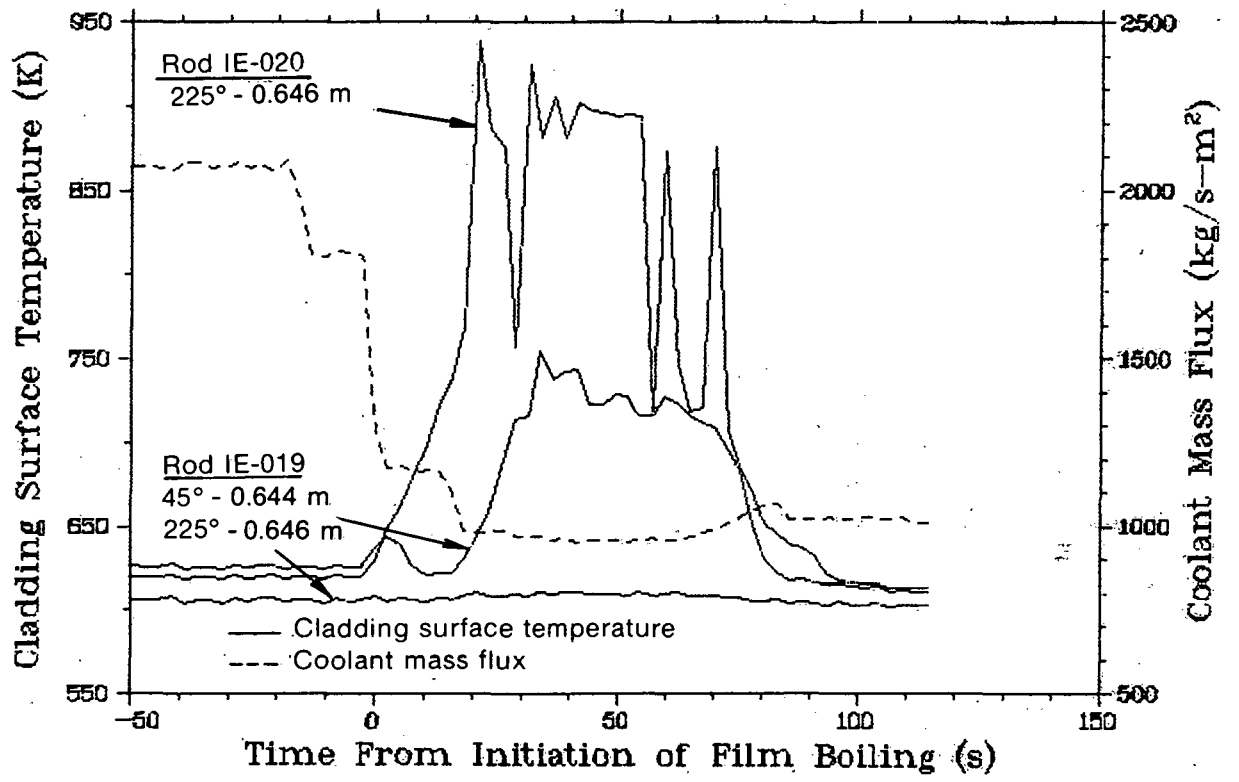

Fig. 60 Measured cladding surface temperatures on Rods IE-019 and IE-020 during film boiling.

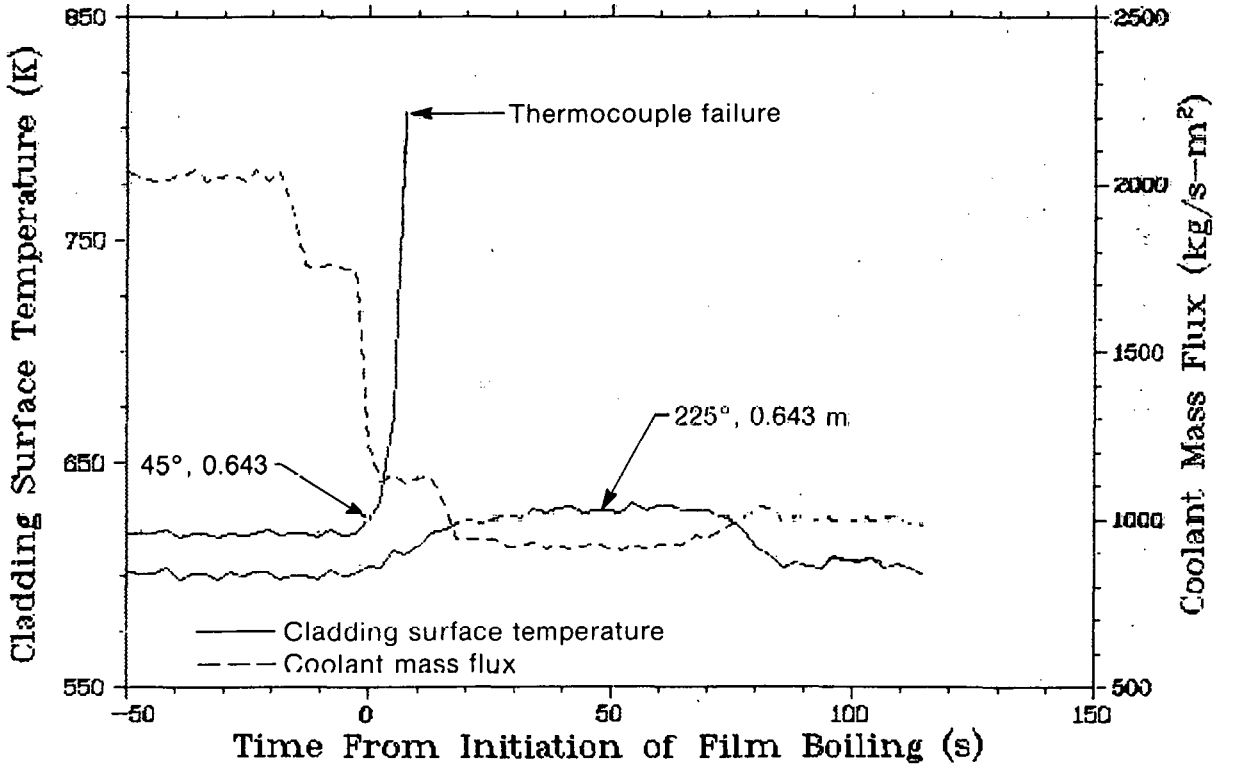

Fig. 61 Measured cladding surface temperatures on Rod IE-021 during film boiling.

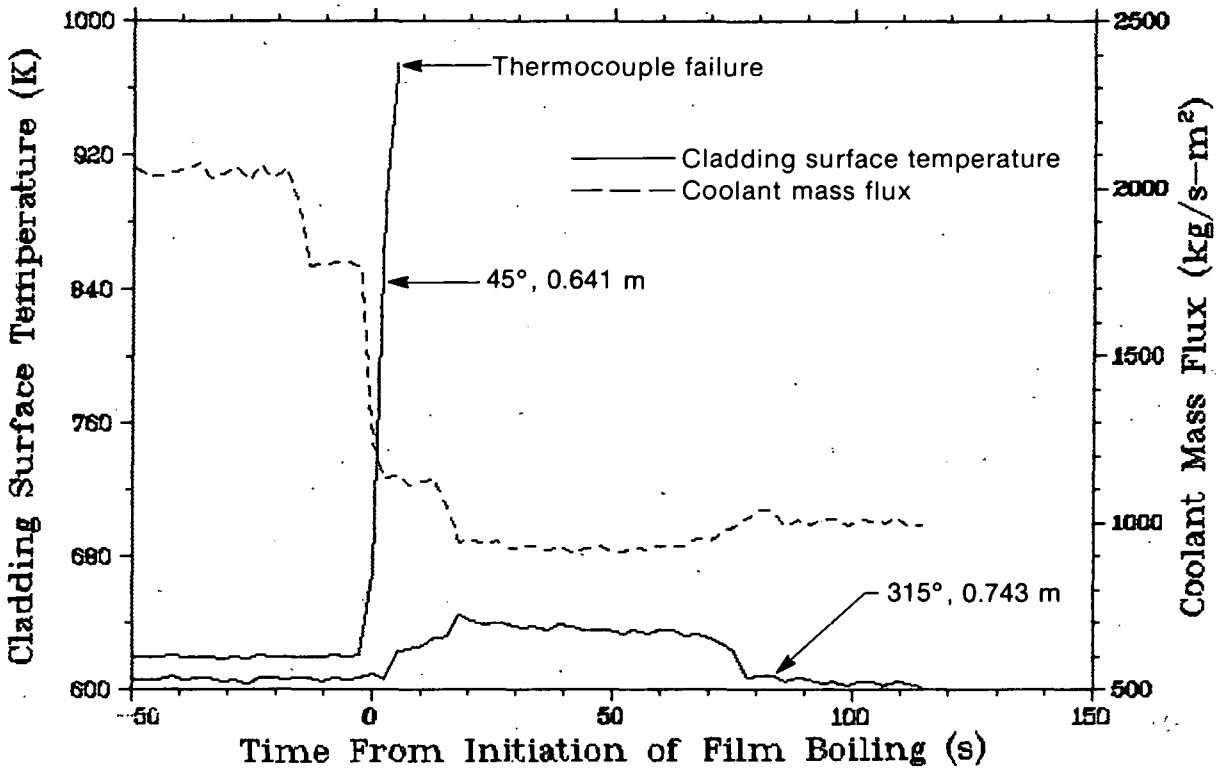

Fig. 62 Measured cladding surface temperatures on Rod IE-022 during film boiling.

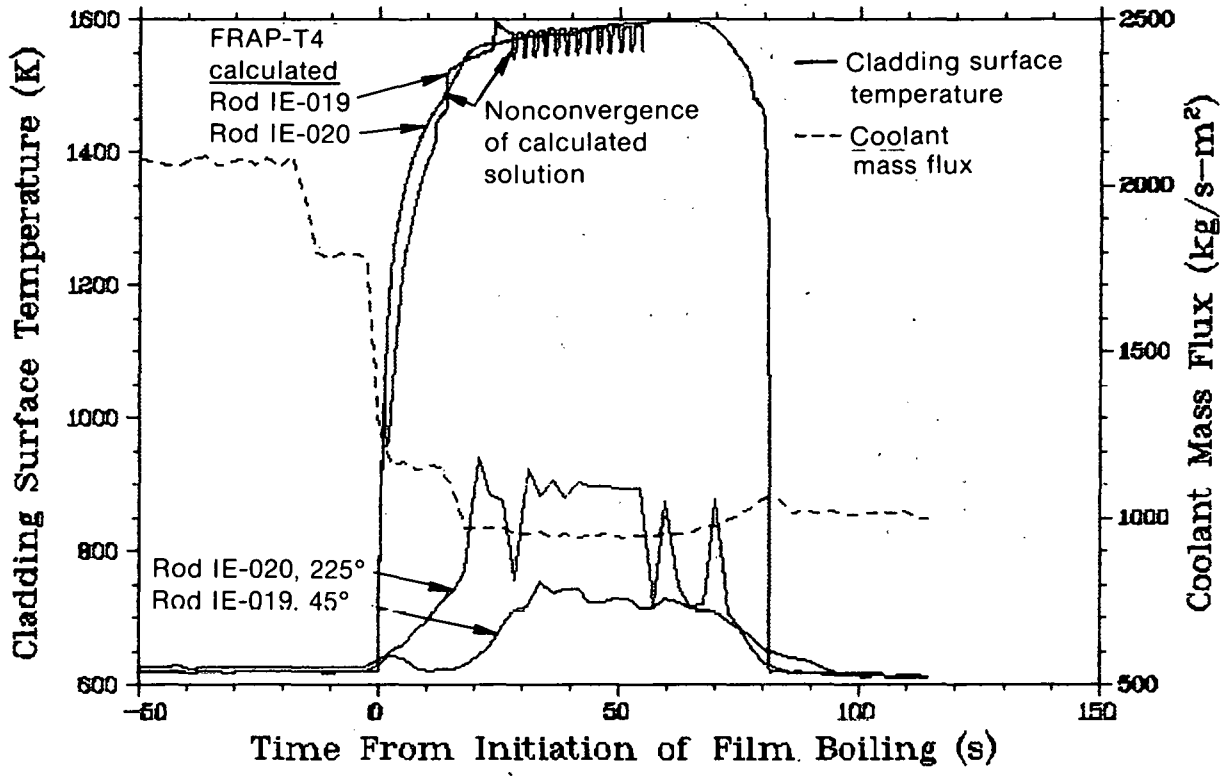

Fig. 63 Comparison of calculated and measured cladding surface temperatures at approximately the 0.643-m elevation on Rods IE-019 and IE-020.

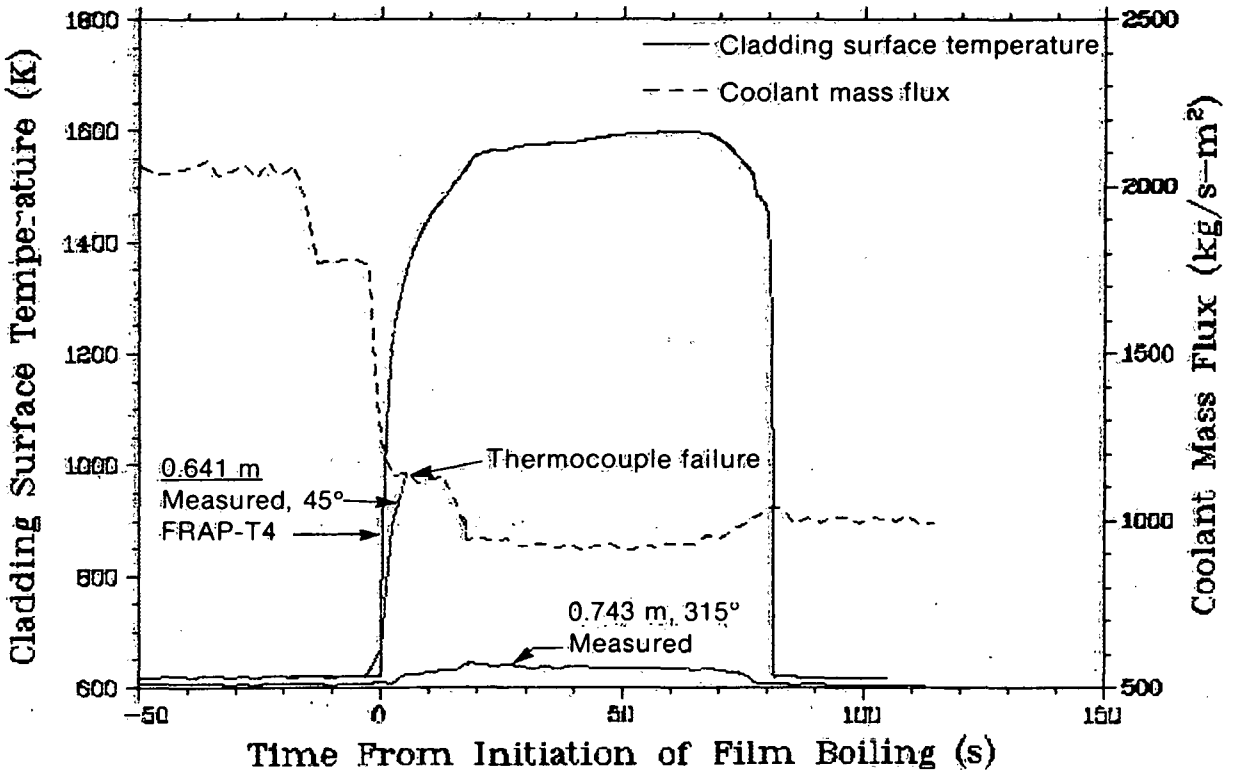

Fig. 64 Comparison of the calculated cladding surface temperature at the 0.641-m elevation on Rod IE-020 with the measured cladding surface temperatures at two locations on Rod IE-022.

VII. DISCUSSION

Test IE-5 was conducted to evaluate fuel rod behavior during abnormal and accident conditions. The objectives were to determine the influence of simulated fission products, cladding irradiation damage, and fuel rod internal pressure on pellet-cladding interaction during a power ramp and on fuel rod behavior during film boiling operation.

The data for all portions of Test IE-5 provided significant insight into fuel rod behavior for the parameters investigated. The FRAP-T4 calculations were generally in good agreement with the data and also augmented understanding of the data where instrumentation failed or provided questionable results. Table III provides a brief summary of the data and FRAP-T4 results. Fission product simulation, cladding irradiation damage, initial internal pressure, and fuel-cladding gap were variables in Test IE-5. Their effects on fuel rod behavior are discussed in the following subsections.

TABLE III

COMPARISON OF MEASURED AND CALCULATED FUEL ROD VARIABLES

	Steady State Pre-DNB		Peak During Film Boiling		Maximum Increase Due to Film Boiling	
	Data	FRAP-T4	Data	FRAP-T4	Data	FRAP-T4[b]
Cladding Elongation[a] (mm)						
IE-019	1.08	2.71	6.47	--	5.39	--
IE-020	1.57	3.43	6.66	7.79	5.09	4.27
IE-021	1.77	2.93	6.91	7.29	5.14	4.36
IE-022	1.88	[c]	6.92	[c]	5.04	[c]
Fuel Rod Internal Pressure (MPa)						
IE-019	22.34	22.09	[d]	[d]	-8.47[d]	-7.29[d]
IE-020	7.35	5.21	7.68	6.21	0.33	0
IE-021	6.48	6.38	6.90	6.41	0.42	0.04
IE-022	6.83	[c]	7.25	[c]	0.42	[c]
Fuel Centerline Temperature (K)						
0.739-m elevation						
IE-019	1556	1584	2450	2859[e]	894	1275
IE-020	1531	1662	2331	1634[e]	800	0
0.637-m elevation						
IE-021	1867	1870	[f]	2985	155	1115
IE-022	1807	[c]	[f]	[c]	265	[c]

TABLE III (continued)

	Steady State Pre-DNB		Peak During Film Boiling		Maximum Increase Due to Film Boiling	
	Data	FRAP-T4	Data	FRAP-T4	Data	FRAP-T4[b]
Cladding Surface Temperature (K)						
0.538-m elevation						
IE-022 (135°)	759.3	[c]	780	[c]	21	[c]
0.643-m elevation[g]						
IE-019 (45°)	627.0	619.8	755	1552	27	932
IE-019 (225°)	607.4	619.8	611	1552	4	932
IE-020 (45°)	[f]	620.0	[f]	1601	[f]	981
IE-020 (225°)	621.0	620.0	939	1601	318	981
IE-021 (45°)	620.2	619.7	807[h]	1552	187	932
IE-021 (225°)	602.4	619.7	632	1552	30	932
IE-022 (45°)	621.0	[c]	980[h]	[c]	359	[c]
IE-022 (225°)	607.3	[c]	609[h]	[c]	2	[c]
0.743-m elevation						
IE-022 (315°)	607.3	[c]	644	[c]	37	[c]

[a] Absolute values of cladding elongation are not directly comparable. The steady state measured elongation is a combination of the fuel rod expansion and the thermal expansion of the test train support hardware. FRAP-T4 calculates only the thermal expansion of the fuel rod.
[b] Coleman Fuel Relocation Model was used.
[c] FRAP-T4 analyses not done for Rod IE-022. FRAP-T4 analyses of Rod IE-020 should be compared with the data for Rod IE-022.
[d] Cladding failure occurred.
[e] Film boiling not modeled in FRAP-T4 at this elevation.
[f] Failed prior to the onset of film boiling.
[g] This is the average elevation for thermocouples at the 45- and 228-degree orientations.
[h] Failed during film boiling.

1. EFFECTS OF FISSION PRODUCT SIMULATION ON FUEL ROD BEHAVIOR

PCI as a result of a power increase (ramp) has caused cladding failures in boiling water reactors[6,7], CANDU reactors[8], and pressurized water reactors[9]. Roberts et al[9], and Penn et al[10], indicate that many of the observed features of power-ramp failures could be associated with iodine-induced stress-corrosion-cracking. Cesium iodide, cesium molybdate, and tellurium metal were added to the fuel stacks of Rods IE-020, IE-021, and IE-022 to simulate oxygen activity and accumulation of cesium, molybdenum, tellurium, and iodine fission products for the purpose of determining whether PCI stresses might be assisted by corrosive fission products and result in a stress-corrosion-cracking failure of the cladding. However, these chemical species apparently had no effect on fuel rod behavior under the power ramp, high power steady state, and film boiling operating conditions of this test. No PCI failures were observed during this test.

Not all fission products, but only cesium, iodine, molybdenum, and tellurium, were added to the fuel. Extensive out-of-pile experiments[11,12] have confirmed that zircaloy is susceptible to stress-corrosion-cracking in iodine environments. During this test, free iodine was produced by radiolytic dissociation of cesium iodide[13] and nuclear fission during the preconditioning phase. The 28-hour preconditioning phase was too short to obtain an equilibrium concentration of iodine representative of operating commercial reactors. Further, the iodine partial pressure from the preceding sources during the power ramp and high power steady state period of operation was apparently not high enough, so no failure occurred in either the unirradiated or irradiated cladding.

2. EFFECTS OF PRIOR CLADDING IRRADIATION ON FUEL ROD BEHAVIOR

Effects of irradiation would appear primarily in the stress-strain relationship of the cladding. Irradiation would increase the cladding strength and decrease the ductility. However, for the heating times during this test the irradiation damage anneals at temperatures above approximately 925 K, the α-zircaloy recrystalization temperature of zircaloy-4 cladding. Cladding irradiation effects would, therefore, be most evident during the preconditioning phase, the power ramp, and shortly after the onset of film boiling operation.

Cladding elongation measurements during the test did not identify any significant irradiation effects on fuel rod behavior. Rod IE-022 which had unirradiated cladding experienced only 0.03% (percent of the fueled length) greater elongation during the preconditioning and power ramp phases than Rod IE-020 which had irradiated cladding. The transient increase in elongation due to film boiling and the permanent axial strain as a result of the test were nearly identical for the two rods.

Effects of cladding irradiation were not evident from the radial strain produced during the film boiling operation. Rod IE-020 and IE-022 had similar radial deformations, even though the former was a water tube irradiated without fuel and the latter was unirradiated.

3. EFFECTS OF HIGH FUEL ROD INTERNAL PRESSURE ON FUEL ROD BEHAVIOR

Rod IE-019 was pressurized to 8.3 MPa prior to the test to investigate the effects of high internal pressure on fuel rod behavior during a power ramp and film boiling operation. Results for Rod IE-019 may be compared with those from Rods IE-020 and IE-022 which were initially pressurized to about 2.5 MPa.

The high internal pressure in Rod IE-019 apparently had an effect on the cladding elongation and possibly affected fuel centerline temperatures. The onset of PCI occurred at 15 kW/m rather than below 5 kW/m as it did in Rods IE-020 and IE-022 which had the same diametral gap as Rod IE-019. As a result, the cladding elongation during the preconditioning and power ramp phases was smallest for Rod IE-019. Fuel centerline temperatures at the same local power level were approximately 2% higher in Rod IE-019 than in Rods IE-020 and IE-022.

Rod IE-019 is the only rod to have been tested in the Irradiation Effects Test Series with an internal pressure higher than the coolant pressure. Prior to the onset of film boiling, Rod IE-019 had an internal pressure about 6 MPa higher than the coolant pressure. This greater pressure was sufficient to cause ballooning of the cladding within the film boiling zone and a loss of cladding integrity during film boiling. The proposed sequence of events is as follows:

(1) Immediately after the onset of film boiling, the cladding ballooned near the cladding surface thermocouple locations

(2) The cladding elongation and ballooning increased as the length of the film boiling zone increased

(3) The fuel-cladding gap opened at the upper film boiling zone boundary and slowed the increase in cladding elongation

(4) The cladding ruptured 10 s after the onset of film boiling

(5) The cladding continued to increase in length due to an additional flow reduction, growth of the film boiling zone, and closure of the fuel-cladding gap above the ballooned region of the cladding.

The process of brazing the thermocouples onto the cladding surface undoubtedly altered the irradiated state of the zircaloy. Additional postirradiation examination may quantify the amount of annealing and the effect of the presence of the thermocouples on cladding behavior.

Rods IE-020, IE-021, and IE-022, which were all pressurized to approximately 2.5 MPa, experienced cladding collapse at the onset of film boiling. Subsequent cladding diameter increases were probably due to differential fuel-cladding thermal expansion and the fuel volume change upon melting.

4. ADDITIONAL OBSERVATIONS

Additional observations on the effect of fuel-cladding diametral gap on fuel rod behavior and the FRAP-T4 results are discussed in the following subsections.

4.1 Effect of Fuel-Cladding Diametral Gap on Fuel Rod Behavior

The narrow range of gap sizes in Test IE-5 did not produce significant differences in fuel rod behavior. Although Rod IE-021 had a 0.05-mm larger gap than Rods IE-020 and IE-022, the elongation measured for Rod IE-021 during the preconditioning phase, the power ramp, and film boiling operation did not significantly differ from that of the other two rods, indicating gap closure at nominally the same axial elevation.

The peak cladding radial strains differed slightly among Rods IE-020, IE-021, and IE-022. Rods IE-020 and IE-022, which had 0.09-mm diametral gaps had peak radial strains of 1%; whereas Rod IE-021 which had an 0.138-mm diametral gap only had peak radial strains of 0.5%.

As a result of the 0.05-mm larger diametral gap, fuel centerline temperatures were 3 to 7% higher in Rod IE-021 than in the remaining rods.

4.2 Discussion of FRAP-T4 Results

FRAP-T4 steady state calculations and cladding elongation test data were in better agreement than achieved between earlier versions of FRAP-T and results from previous IE tests[5,14]. The Coleman Fuel Relocation Model calculated PCI at a lower power level than previous versions of FRAP-T, but still not at the power observed in the test. The fact that FRAP-T4 does not account for fuel or cladding creep and slippage, accounts for the deviation of calculated results for cladding elongation during the power ramp and steady state operation at rod average powers above 35 kW/m. FRAP-T4 underestimated the increase in cladding elongation due to film boiling by approximately 17% for Rods IE-020, IE-021, and IE-022 and by approximately 24% for Rod IE-019. Rod IE-019 failed soon after the onset of film boiling as calculated by FRAP-T4, but the trend in elongation shown by the data after rod failure was not calculated well.

Fuel centerline temperatures calculated using the Coleman Fuel Relocation Model option in FRAP-T4 agreed with the measured data during the preconditioning phase and power ramp. FRAP-T4 analyses of film boiling operation indicated that centerline

temperatures reached 2800 to 3400 K – beyond the measurement capabilities of the thermocouples. This result is consistent with the postirradiation neutrographs which indicated that fuel melting had occurred.

FRAP-T4 slightly underpredicted the pressures recorded during the preconditioning phase and the power ramp. FRAP-T4 also did not calculate a pressure increase during film boiling operation. The code calculated a closed fuel-cladding gap within the film boiling zone prior to film boiling; therefore, no gas except for gas in cracks and pellet dishes remained in that region to heat up during the transient. Furthermore, even though the gap is closed, the measured pressure increases inside Rods IE-020, IE-021, and IE-022 indicate that there is pressure communication from the fuel region to the plenum through cracks within the fuel.

VIII. CONCLUSIONS

Conclusions reached from Test IE-5 are:

(1) The simulated fission products did not cause a PCI induced failure and had no apparent effect on fuel rod behavior during film boiling

(2) A fuel rod internal pressure 6 MPa above the coolant pressure causes PCI to occur at a power level that is higher than the power level at which PCI occurred in low pressure rods and produces cladding ballooning and failure during film boiling operation

(3) Under the conditions of this test, no significant cladding irradiation effects were observed

(4) Fuel rods having small diametral gaps in the range of 0.09 to 0.14 mm behave similarly.

IX. REFERENCES

1. United States Nuclear Regulatory Commission, Reactor Safety Research Program, *A Description of Current and Planned Reactor Safety Research Sponsored by the Nuclear Regulatory Commission's Division of Reactor Safety Research,* NUREG-75/058 (June 1975).

2. G. W. Gibson et al, *Characteristics of UO_2-Zircaloy Fuel Rod Materials from the Saxton Reactor for Use in the Power Burst Facility,* ANCR-NUREG-1321 (September 1976).

3. M. E. Yancey et al, *Inspection System for Zircaloy Clad Fuel Rods,* ANCR-1259 (February 1976).

4.[a] J. A. Dearien et al, *FRAP-T2: A Computer Code for Transient Analysis of Oxide Fuel Rods,* TREE-NUREG-1040 (March 1977).

5. C. M. Allison et al, *Irradiation Effects Test Series, Test IE-2, Test Results Report,* TREE-NUREG-1074 (August 1977).

6. H. W. Williamson and R. A. Proebstle, "Results With BWR Fuel Improvements," *Proceedings of Joint ANS/CNA Topical Meeting on Commercial Nuclear Fuel Technology Today, Toronto, Canada, April 28-30, 1975,* p 1.38.

7. D. Cordall et al, "Fuel Failures in the Dodewaard Boiling Water Reactor," *Nuclear Technology, 34* (August 1977) pp 438-448.

8. J. A. L. Robertson, "Nuclear Fuel Failures, Their Causes and Remedies," *Proceedings of Joint ANS/CNA Topical Meeting on Commercial Nuclear Fuel Technology Today, Toronto Canada April 28-30, 1975,* p 2.2.

9. J. T. A. Roberts et al, "On The Pellet-Cladding Interaction Phenomenon," *Nuclear Technology, 35* (August 1977) pp 131-144.

10. W. J. Penn, R. K. Lo, and J. C. Wood, "CANDU Fuel-Power Ramp Performance Criteria," *Nuclear Technology, 34* (July 1977) pp 249-268.

11. J. C. Wood, "Interactions Between Stressed Zirconium Alloys and Iodine at 300°C", *Nuclear Technology, 23* (July1977) p 63.

---

[a] FRAP-T4 is the latest version of the FRAP-T fuel behavior code, however, it is unpublished for public review; therefore, FRAP-T2 is referenced.

12. A. Garlick, "Stress Corrosion Cracking of Zirconium Alloys in Iodine Vapor," *Proceedings of the British Nuclear Energy Society Conference on Effects of Environment on Material Properties in Nuclear Systems, London, July 1-2, 1971.*

13. D. Cubicciotti and J. H. Davies, "The Release of Iodine From Iodide Salts by Gamma Radiolysis," *Nuclear Science and Engineering, 60* (1976) pp 314-319.

14. W. J. Quapp et al, *Irradiation Effects Test Series, Test IE-1, Test Results Report,* TREE-NUREG-1046 (March 1977).

APPENDIX A

FUEL ROD CHARACTERIZATION DATA

THIS PAGE

WAS INTENTIONALLY

LEFT BLANK

APPENDIX A

FUEL ROD CHARACTERIZATION DATA

The pretest fuel rod characterization data for Test IE-5 are presented in this appendix. The characterization data available are different for each fuel rod and all measurements, except mass and volume, were obtained in U.S. Customary units and converted to SI units.

Rod IE-019 was constructed from irradiated water tube W06, an unfueled zircaloy tube used to fill the open lattice locations in the extended burnup tests in the Saxton reactor[a]. The estimated peak fluence received by the tube was 9.9×10^{20} neutrons/cm^2 greater than 1 MeV. Fresh 12.4 wt% $^{235}UO_2$ fuel was placed inside the irradiated tube at the Idaho National Engineering Laboratory. An instrumented end cap sealed the upper end of the rod. The rod was pressurized to 8.3 MPa at room temperature in order to study the cladding ballooning phenomenon. Characterization data for Rod IE-019 are presented in Table A-I.

The 95% population loaded value in the table refers to the dimensional range of a parameter within which 95% of the measurements were found. The void volume measurement, accurate to ±0.2 cm^3, includes the void found in the fueled region, the plenum, and the instrumented end cap. The cladding mechanical properties are typical of water tube cladding prior to irradiation in the Saxton reactor. Table A-II contains characterization data for the fresh fuel pellets inserted into Rod IE-019. Pellet length measurements were obtained by measuring the length between the upper and lower dish shoulder of each pellet. Both the diameter and length measurements were performed using a Bausch and Lomb optical gauge, Model BR-25. The measurements are accurate to ±0.005 mm. An analytical balance, accurate to ±1 mg, was used to weigh the pellets. Table A-III contains cladding dimensions for Rod IE-019. An air gauge was used to obtain measurements of the cladding inside diameter (ID) for the length of the rod. The accuracy of these measurements is estimated to be ±0.005 mm. Figure A-1 combines the fuel pellet outside diameter and cladding inner diameter measurements to illustrate the diametral gap as a function of axial position.

Rod IE-020 was similar to Rod IE-019. Water tube W08, irradiated in the Saxton reactor to an estimated peak fluence of 9.3×10^{20} neutrons/cm^2 greater than 1 MeV, was filled with 12.4 wt% $^{235}UO_2$ fuel which had simulated fission products. The rod was fitted with an instrumented end cap and backfilled to a pressure of 2.5 MPa, a factor of three less than Rod IE-019. Characterization data for the fuel rod and fuel pellets are contained in Tables A-IV and A-V, respectively. Measured cladding dimensions are presented in Table A-VI. Figure A-2 illustrates the diametral gap versus axial position for Rod IE-020.

---

[a] The Saxton reactor was designed by Westinghouse Electric Corporation for the USAEC. The reactor was a small, prototypic, pressurized water reactor.

TABLE A-I

OVERALL PRETEST FUEL AND CLADDING DATA FOR ROD IE-019

Finished Tube Data:	
Mean Outside Diameter[a]	9.931 mm
Mean Inside Diameter	8.724 mm
Ovality (Max ID/Min ID)	1.012
Cladding Length	0.9483 m
Mechanical Properties of Unirradiated Fuel Rod Cladding[b]:	
Yield Tensile Strength	
At Room Temperature	524.0 MPa
At 658 K	324.1 MPa
Utlimate Tensile Strength	
At Room Temperature	703.3 MPa
At 658 K	380.9 MPa
Fuel Data:	
Enrichment	12.38%
Mean Geometric Density	10.4211 g/cm^3
95% Population Loaded	10.4211 (+ 0.0004, - 0.0012) g/cm^3
Mean Diameter	8.633 mm
95% Population Loaded	8.6330 (+ 0.0010, - 0.0030) mm
Stack Mass	521.2177 g
Measured Stack Length	878.764 mm
Dish Dimensions	
Dish Chord	6.604 mm
Dish Depth	0.343 mm
Grain Diameter	$2.25 \pm 0.65 \times 10^{-2}$ mm
Center Hole Length	198.45 mm
Mean Fuel-cladding Gap	0.091 mm
Measured Void Volume	6.5 ml
Fill Gas Data:	
Pressure	8.30 MPa
Composition	77.7% He, 22.3% Ar

[a] Nominal dimension, not measured after irradiation in the Saxton reactor.

[b] Data supplied by Westinghouse Electric Corporation.

TABLE A-II

FUEL PELLET CHARACTERIZATION DATA FOR ROD IE-019

Pellet[a] Number	Diameter (mm)				Length (mm)			Weight (Grams)	Geometric Density (g/cm^3)	Immersion Density (g/cm^3)	Centerline Hole Diameter (mm)	
	Top	Center	Bottom	Average	0°	90°	Average				Top	Bottom
1	8.6360	8.6360	8.6360	8.6360	9.9289	10.0127	9.9708	5.9787	10.4477	0.0	0.0	0.0
2	8.6309	8.6309	8.6309	8.6309	15.2044	15.2375	15.2209	9.0931	10.3480	0.0	0.0	0.0
3	8.6335	8.6335	8.6335	8.6335	15.2552	15.3035	15.2794	9.1972	10.4197	0.0	0.0	0.0
4	8.6360	8.6360	8.6360	8.6360	15.2146	15.2883	15.2514	9.1941	10.4293	0.0	0.0	0.0
5	8.6335	8.6360	8.6360	8.6351	15.1943	15.2552	15.2248	9.1754	10.4286	10.4783	0.0	0.0
6	8.6335	8.6335	8.6335	8.6335	15.0851	15.1460	15.1155	9.0169	10.3276	0.0	0.0	0.0
7	8.6335	8.6335	8.6309	8.6326	15.2679	15.2984	15.2832	9.0782	10.2843	0.0	0.0	0.0
8	8.6309	9.6309	8.6309	8.6309	14.3238	15.3746	15.3492	9.2286	10.4132	0.0	0.0	0.0
9	8.6335	8.6335	8.6335	8.6335	15.2095	15.2781	15.2438	9.1700	10.4134	0.0	0.0	0.0
10	8.6335	8.6335	8.6360	8.6343	15.3111	15.3645	15.3378	9.2187	10.4016	10.4133	0.0	0.0
11	8.6335	8.6335	8.6335	8.6335	15.1892	15.2273	15.2082	9.1814	10.4510	0.0	0.0	0.0
12	8.6335	8.6335	8.6335	8.6335	15.2121	15.2298	15.2209	9.1490	10.4054	0.0	0.0	0.0
13	8.6360	8.6360	8.6360	8.6360	15.2629	15.3035	15.2832	9.0778	10.2757	0.0	0.0	0.0
14	8.6385	8.6360	8.6360	8.6368	15.1232	15.2222	15.1727	9.1236	10.4017	0.0	0.0	0.0
15	8.6309	8.6309	8.6284	8.6301	15.2933	15.3391	15.3162	9.1609	10.3615	10.4260	0.0	0.0
16	8.6309	8.6309	8.6335	8.6318	15.2730	15.3670	15.3200	9.1980	10.3967	0.0	0.0	0.0
17	8.6309	8.6309	8.6335	8.6318	15.3086	15.3518	15.3302	9.1719	10.3602	0.0	0.0	0.0
18	8.6335	8.6335	8.6360	8.6343	15.3772	15.4305	15.4038	9.1440	10.2725	0.0	0.0	0.0
19	8.6335	8.6335	8.6335	8.6335	15.0165	15.0800	15.0482	9.0440	10.4056	0.0	0.0	0.0
20	8.6385	8.6385	8.6385	8.6385	15.2070	15.2273	15.2171	9.0504	10.2836	10.3676	0.0	0.0
21	8.6360	8.6360	8.6360	8.6360	15.1308	15.1867	15.1587	9.0985	10.3848	0.0	0.0	0.0
22	8.6360	8.6360	8.6360	8.6360	15.2197	15.2679	15.2438	9.1649	10.4014	0.0	0.0	0.0
23	8.6309	8.6309	8.6284	8.6301	15.2273	15.2857	15.2565	9.1700	10.4129	0.0	0.0	0.0
24	8.6335	8.6335	8.6335	8.6335	15.0673	15.1282	15.0977	9.0694	10.4001	0.0	0.0	0.0
25	8.6385	8.6385	8.6335	8.6368	15.1740	15.2095	15.1917	9.1203	10.3847	10.4070	0.0	0.0

TABLE A-II (continued)

Pellet[a] Number	Diameter (mm)				Length (mm)			Weight (Grams)	Geometric Density (g/cm^3)	Immersion Density (g/cm^3)	Centerline Hole Diameter (mm)	
	Top	Center	Bottom	Average	0°	90°	Average				Top	Bottom
26	8.6335	8.6335	8.6335	8.6335	15.2095	15.2476	15.2286	9.1410	10.3910	0.0	0.0	0.0
27	8.6436	8.6436	8.6436	8.6436	15.2324	15.2603	15.2463	9.0809	10.2859	0.0	0.0	0.0
28	8.6335	8.6335	8.6335	8.6335	15.1282	15.2222	15.1752	9.1119	10.3948	0.0	0.0	0.0
29	8.6385	8.6360	8.6335	8.6360	15.1968	15.2756	15.2362	9.1019	10.3351	0.0	0.0	0.0
30	8.6360	8.6360	8.6360	8.6360	15.1130	15.1562	15.1346	9.0103	10.3007	10.3252	0.0	0.0
31	8.6335	8.6335	8.6309	8.6326	14.9962	15.0495	15.0228	9.0492	10.4315	0.0	0.0	0.0
32	8.6335	8.6335	8.6309	8.6326	15.1460	15.1765	15.1612	9.0799	10.3700	0.0	0.0	0.0
33	8.6360	8.6360	8.6360	8.6360	15.2603	15.2730	15.2667	9.0638	10.2767	0.0	0.0	0.0
34	8.6309	8.6309	8.6335	8.6318	15.2502	15.2959	15.2730	9.0710	10.2851	0.0	0.0	0.0
35	8.6335	8.6335	8.6284	8.6318	15.3619	15.4508	15.4064	9.2494	10.3954	10.4315	0.0	0.0
36	8.6335	8.6335	8.6335	8.6335	15.1638	15.1714	15.1676	9.1056	10.3929	0.0	0.0	0.0
37	8.6335	8.6335	8.6335	8.6335	15.0597	15.1130	15.0863	9.0573	10.3942	0.0	0.0	0.0
38	8.6335	8.6335	8.6335	8.6335	15.4127	15.5169	15.4648	9.1952	10.2908	0.0	0.0	0.0
39	8.6335	8.6335	8.6309	8.6326	15.1816	15.2324	15.2070	9.1352	10.4014	0.0	0.0	0.0
40	8.6385	8.6385	8.6335	8.6368	15.1562	15.2248	15.1905	9.1152	10.3797	10.4215	0.0	0.0
41	8.6360	8.6360	8.6385	8.6368	15.2197	15.3162	15.2679	9.1730	10.3919	0.0	0.0	0.0
42	8.6335	8.6335	8.6360	8.6343	15.3111	15.3949	15.3530	9.2515	10.4281	0.0	0.0	0.0
43	8.6335	9.6335	9.6335	9.6335	14.9327	15.0292	14.9809	9.0067	10.4099	0.0	0.0	0.0
44	8.6335	8.6335	8.6335	8.6335	15.1816	15.2019	15.1917	9.0737	10.3398	0.0	0.0	0.0
45	8.5987	8.6030	8.6081	8.6030	15.0927	15.1435	15.1181	9.0271	10.4050	10.4347	0.0	0.0
46	8.6335	8.6335	8.6360	8.6343	14.2832	15.3568	15.3200	8.8146	10.4434	10.5128	1.8796	1.8542
47	8.6360	8.6360	8.6335	8.6351	15.3086	15.3746	15.3416	8.8149	10.4336	10.4631	1.8796	1.8795
48	8.6360	8.6360	8.6385	8.6368	15.1867	15.2248	15.2057	8.6737	10.3977	10.3845	1.9558	1.9558
49	8.6436	8.6436	8.6436	8.6436	15.4127	15.4534	15.4330	8.9272	10.4742	0.0	1.8796	1.8796
50	8.6360	8.6360	8.6360	8.6360	15.2476	15.3391	15.2933	8.7780	10.4210	10.3958	1.8796	1.8796
51	8.6360	8.6385	8.6385	8.6377	15.2832	15.3568	15.3200	8.7822	10.4033	0.0	1.8796	1.8796
52	8.6360	8.6360	8.6335	8.6351	15.0139	15.0800	15.0470	8.6132	10.4112	10.3907	1.9050	1.9050
53	8.6360	8.6360	8.6385	8.6368	15.0774	15.1232	15.1003	8.6751	10.4337	0.0	1.8796	1.8796
54	8.6360	8.6360	8.6385	8.6368	15.2502	15.3137	15.2819	8.7664	10.4129	10.4303	1.8796	1.8796
55	8.6436	8.6411	8.6411	8.6419	15.2730	15.3086	15.2908	8.7841	10.4148	0.0	1.8796	1.8796

TABLE A-II (continued)

Pellet[a] Number	Diameter (mm)				Length (mm)			Weight (Grams)	Geometric Density (g/cm^3)	Immersion Density (g/cm^3)	Centerline Hole Diameter (mm)	
	Top	Center	Bottom	Average	0°	90°	Average				Top	Bottom
56	8.6385	8.6385	8.6385	8.6385	15.0774	15.1435	15.1105	8.7163	10.4611	10.4518	1.8796	1.8542
57	8.6385	8.6385	8.6360	8.6377	15.3848	15.4203	15.4025	8.8284	10.4082	0.0	1.9050	1.8796
58	8.6284	8.6335	8.6335	8.6318	15.1486	15.1841	15.1663	8.6728	10.4083	10.4216	1.9050	1.9050

[a] Pellets are numbered from bottom of fuel column.

TABLE A-III

AIR GAUGE MEASUREMENTS OF FUEL ROD
IE-019 CLADDING INSIDE DIAMETER

Elevation[a] (mm)	0° (mm)	45° (mm)	90° (mm)
50.8	8.720	8.716	8.718
76.2	8.717	8.717	8.713
101.6	8.723	8.713	8.711
127.0	8.713	8.724	8.723
152.4	8.715	8.720	8.724
177.8	8.710	8.723	8.725
203.2	8.709	8.719	8.724
228.6	8.720	8.718	8.717
254.0	8.724	8.714	8.711
279.4	8.720	8.712	8.710
304.8	8.717	8.716	8.714
330.2	8.709	8.722	8.728
355.6	8.716	8.716	8.716
381.0	8.715	8.720	8.723
406.4	8.717	8.719	8.724
431.8	8.718	8.718	8.723
457.2	8.712	8.723	8.725
482.6	8.714	8.726	8.725
508.0	8.716	8.724	8.719
533.4	8.719	8.718	8.716
558.8	8.725	8.710	8.708
584.2	8.731	8.709	8.702
609.6	8.719	8.715	8.715
635.0	8.718	8.716	8.718
660.4	8.714	8.718	8.720
685.8	8.715	8.715	8.721
711.2	8.713	8.717	8.724
736.6	8.715	8.718	8.722
762.0	8.718	8.719	8.718
787.4	8.716	8.720	8.722
812.8	8.713	8.721	8.722
838.2	8.713	8.721	8.721
863.6	8.721	8.724	8.713
889.0	8.721	7.719	8.715

[a] Distance from bottom of fuel rod.

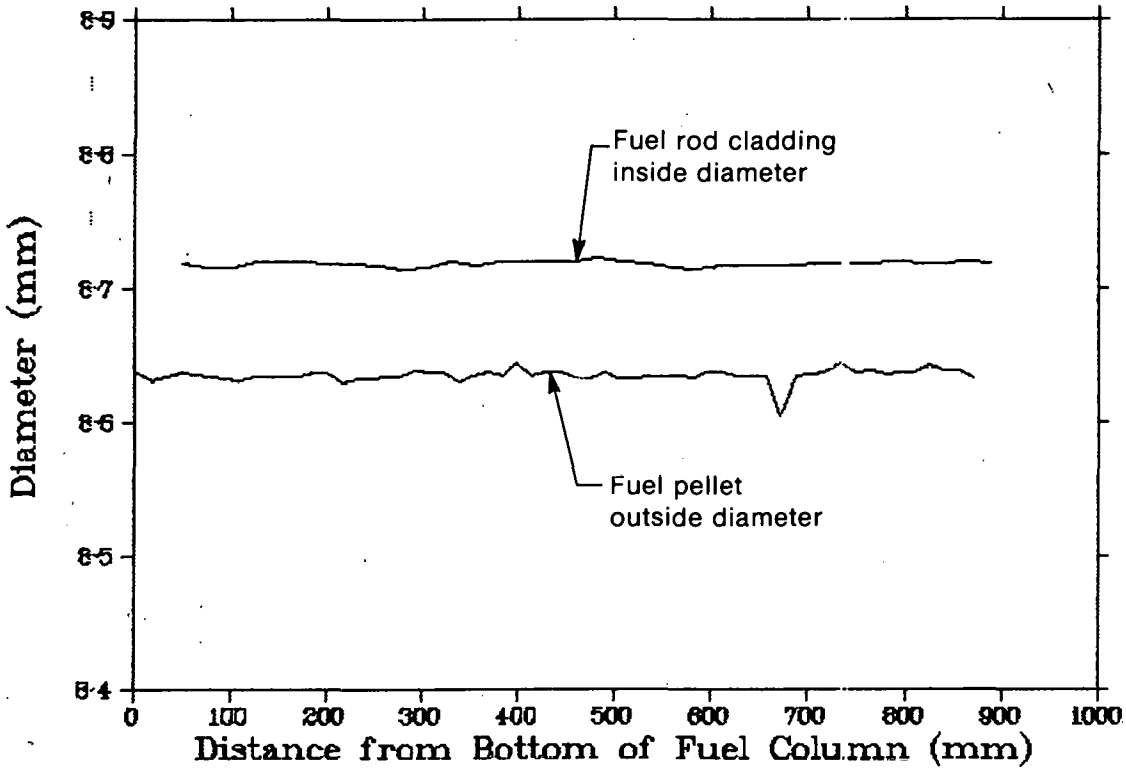

Fig. A-1 Cladding inside diameter and fuel pellet diameter versus axial position for Rod IE-019.

Rod IE-021 was constructed from MAPI[a] fuel rod M-23 irradiated in the Saxton reactor to an approximate burnup of 3.78 MWd/kgU. Based on gamma scans and burnup information reported in Reference A-1, the peak fluence received by this cladding is estimated to be 3.5×10^{20} neutrons/cm^2 greater than 1 MeV. The irradiated fuel within the rod was replaced by fresh 12.4 wt% $^{235}UO_2$ fuel which had simulated fission products. Characterization data for the fuel rod and fuel pellets are presented in Tables A-VII and A-VIII, respectively. The cladding, for which dimensions are presented in Table A-IX, has a 0.046-mm larger inside diameter than the remaining rods. The resulting fuel-cladding diametral gap of 0.138 mm is 50% larger than the remaining rods and is illustrated as a function of axial position in Figure A-3.

Rod IE-022 was manufactured with cladding from unirradiated Saxton fuel Rod 930. Fresh 12.4 wt% $^{235}UO_2$ fuel pellets which had simulated fission products were used. Tables A-X, A-XI, and A-XII, respectively, contain characterization data for the fuel rod, fuel pellets, and cladding. Fuel pellet outside diameter and cladding inside diameter measurements are shown in Figure A-4 to illustrate the axial profile of the diametral gap.

Chemical compounds simulating fission products were added to Rods IE-020, IE-021, and IE-022 to determine whether stresses due to fuel-cladding mechanical interactions in a

[a] Mitsubishi Atomic Power Industries of Japan.

TABLE A-IV

OVERALL PRETEST FUEL AND CLADDING DATA FOR ROD IE-020

Finished Tube Data:	
Mean Outside Diameter[a]	9.931 mm
Mean Inside Diameter	8.731 mm
Ovality (Max ID/Min ID)	1.012
Cladding Length	0.9481 m
Mechanical Properties of Unirradiated Fuel Rod Cladding[b]:	
Yield Tensile Strength	
At Room Temperature	524.0 MPa
At 658 K	324.1 MPa
Ultimate Tensile Strength	
At Room Temperature	703.3 MPa
At 658 K	380.9 MPa
Fuel Data:	
Enrichment	12.38%
Mean Geometric Density	10.3979 g/cm^3
95% Population Loaded	10.3979 (+ 0.1339, - 0.0948) g/cm^3
Mean Diameter	8.639 mm
95% Population Loaded	8.6390 (+ 0.0076, - 0.0152) mm
Stack Mass	518.8778 g
Measured Stack Length	878.535 mm
Dish Dimensions	
Dish Chord	6.604 mm
Dish Depth	0.343 mm
Grain Diameter	$2.25 \pm 0.65 \times 10^{-2}$ mm
Center Hole Length	197.637 mm
Mean Fuel-cladding Gap	0.092 mm
Measured Void Volume	6.7 ml
Fill Gas Data:	
Pressure	2.50 MPa
Composition	77.7% He, 22.3% Ar

[a] Nominal dimension, not measured after irradiation in the Saxton reactor.

[b] Data supplied by Westinghouse Electric Corporation.

TABLE A-V

FUEL PELLET CHARACTERIZATION DATA FOR ROD IE-020

Pellet[a] Number	Diameter (mm)				Length (mm)			Weight (Grams)	Geometric Density (g/cm^3)	Immersion Density (g/cm^3)	Centerline Hole Diameter (mm)	
	Top	Center	Bottom	Average	0°	90°	Average				Top	Bottom
1	8.6411	8.6411	8.6411	8.6411	10.6731	10.8280	10.7505	6.4569	10.4368	0.0	0.0	0.0
2	8.6258	8.6258	8.6258	8.6258	15.1968	15.2425	15.2197	9.1157	10.3869	0.0	0.0	0.0
3	8.6131	8.6335	8.6335	8.6267	15.1333	15.1790	15.1562	9.0093	10.3072	0.0	0.0	0.0
4	8.6309	8.6335	8.6335	8.6326	15.2451	15.2756	15.2603	9.0240	10.2384	10.3031	0.0	0.0
5	8.6385	8.6385	8.6411	8.6394	15.2603	15.3822	15.3213	9.1662	10.3413	10.4631	0.0	0.0
6	8.6411	8.6411	8.6385	8.6402	15.1155	15.1613	15.1384	9.1157	10.4082	0.0	0.0	0.0
7	8.6360	8.6360	8.6360	8.6360	15.3949	15.4508	15.4229	9.1254	10.2347	0.0	0.0	0.0
8	8.6360	8.6360	8.6360	8.6360	15.3695	15.4178	15.3937	9.1782	10.3137	0.0	0.0	0.0
9	8.6360	8.6360	8.6385	8.6368	15.0266	15.0825	15.0546	9.0646	10.4166	0.0	0.0	0.0
10	8.6335	8.6360	8.6335	8.6343	15.3492	15.3975	15.3733	9.1075	10.2521	10.3111	0.0	0.0
11	8.6360	8.6360	8.6335	8.6351	15.3314	15.4203	15.3759	9.1182	10.2604	0.0	0.0	0.0
12	8.6360	8.6360	8.6360	8.6360	14.2222	15.2832	15.2527	9.1541	10.3830	0.0	0.0	0.0
13	8.6360	8.6385	8.6411	9.6385	15.0749	15.1536	15.1143	8.8048	10.0735	0.0	0.0	0.0
14	8.6436	8.6436	8.6462	8.6445	15.0876	15.1232	15.1054	9.0480	10.3435	0.0	0.0	0.0
15	8.6436	8.6436	8.6436	8.6436	15.1257	15.1663	15.1460	9.0220	10.2878	10.3573	0.0	0.0
16	8.6335	8.6335	8.6335	8.6335	15.2578	15.2959	15.2768	8.9703	10.1643	10.2700	0.0	0.0
17	8.6360	8.6360	8.6360	8.6360	15.1130	15.1689	15.1409	9.1179	10.4193	0.0	0.0	0.0
18	8.6385	8.6385	8.6385	8.6385	15.3670	15.4076	15.3873	9.1390	10.2679	0.0	0.0	0.0
19	8.6284	8.6309	8.6335	8.6309	15.2629	15.2908	15.2768	9.0614	10.2736	0.0	0.0	0.0
20	8.6411	8.6385	8.6385	8.6394	15.1359	15.2171	15.1765	9.0507	10.3098	10.4218	0.0	0.0
21	8.6385	8.6385	8.6385	8.6385	15.0216	15.0901	15.0558	9.0396	10.3828	0.0	0.0	0.0
22	8.6309	8.6335	8.6360	8.6334	15.3873	15.4381	15.4127	9.0848	10.2021	10.3076	0.0	0.0
23	8.6385	8.6385	8.6385	8.6385	15.1308	15.2476	15.1892	9.0869	10.3443	0.0	0.0	0.0
24	8.6360	8.6360	8.6360	8.6360	15.1155	15.1587	15.1371	9.0411	10.3342	0.0	0.0	0.0
25	8.6309	8.6335	8.6335	8.6326	15.1181	15.1968	15.1574	8.9677	10.2445	10.3430	0.0	0.0

TABLE A-V (continued)

Pellet[a] Number	Diameter (mm)				Length (mm)			Weight (Grams)	Geometric Density (g/cm^3)	Immersion Density (g/cm^3)	Centerline Hole Diameter (mm)	
	Top	Center	Bottom	Average	0°	90°	Average				Top	Bottom
26	8.6462	8.6462	8.6462	8.6462	15.3619	15.3975	15.3797	9.2965	10.4314	0.0	0.0	0.0
27	8.6411	8.6411	8.6411	8.6411	15.0673	15.1028	15.0851	9.0458	10.3634	0.0	0.0	0.0
28	8.6335	8.6335	8.6335	8.6335	14.9631	15.0317	14.9974	8.8804	10.2524	10.3475	0.0	0.0
29	8.6462	8.6462	8.6462	8.6462	15.1460	15.1816	15.1638	9.1668	10.4343	0.0	0.0	0.0
30	8.6411	8.6411	8.6411	8.6411	15.3416	15.3975	15.3695	9.2320	10.3783	10.4509	0.0	0.0
31	8.6385	8.6411	8.6411	8.6402	15.1460	15.1867	15.1663	8.9429	10.1919	0.0	0.0	0.0
32	8.6385	8.6385	8.6385	8.6385	15.2425	15.2806	15.2616	9.1730	10.3921	0.0	0.0	0.0
33	8.6385	8.6385	8.6385	8.6385	15.2324	15.2578	15.2451	9.0637	10.2795	0.0	0.0	0.0
34	8.6335	8.6360	8.6360	8.6351	15.0698	15.0901	15.0800	8.9471	10.2681	10.3696	0.0	0.0
35	8.6385	8.6385	8.6385	8.6385	15.1435	15.1790	15.1613	9.0403	10.3104	10.3751	0.0	0.0
36	8.6335	8.6335	8.6335	8.6335	15.2705	15.3645	15.3175	9.1762	10.3697	0.0	0.0	0.0
37	8.6335	8.6385	8.6385	8.6368	15.3010	15.3772	15.3391	9.0721	10.2293	0.0	0.0	0.0
38	8.6411	8.6436	8.6436	8.6428	15.0825	15.1638	15.1232	9.1057	10.4012	0.0	0.0	0.0
39	8.6385	8.6385	8.6360	8.6377	15.1308	15.2476	15.1892	9.0868	10.3462	0.0	0.0	0.0
40	8.6335	8.6360	8.6360	8.6351	15.1460	15.2273	15.1867	8.9621	10.2121	10.3389	0.0	0.0
41	8.6411	8.6411	8.6411	8.6411	15.1714	15.2984	15.2349	9.1635	10.3936	0.0	0.0	0.0
42	8.6385	8.6385	8.6385	8.6385	15.2121	15.2324	15.2222	9.1462	10.3889	0.0	0.0	0.0
43	8.6284	8.6309	8.6335	8.6309	15.2324	15.2705	15.2514	9.0222	10.2465	0.0	0.0	0.0
44	8.6360	8.6360	8.6360	8.6360	15.3162	15.3645	15.3403	9.1311	10.2970	0.0	0.0	0.0
45	8.6411	8.6436	8.6436	8.6428	15.2908	15.3568	15.3238	9.1725	10.3385	10.4607	0.0	0.0
46	8.6385	8.6385	8.6385	8.6385	15.2476	15.3289	15.2883	8.7857	10.4271	10.5034	1.8796	1.8796
47	8.6411	8.6436	8.6436	8.6428	15.0673	15.1181	15.0927	8.6850	10.4183	10.4860	1.8542	1.8542
48	8.6411	8.6436	8.6436	8.6428	15.3086	15.3314	15.3200	8.8039	10.4021	10.4575	1.8542	1.8542
49	8.6335	8.6335	8.6335	8.6335	15.1460	15.1917	15.1689	8.5912	10.2634	10.3690	1.8288	1.8288
50	8.6411	8.6411	8.6411	8.6411	15.3619	15.4000	15.3810	8.8443	10.4123	10.5318	1.8542	1.8542
51	8.6335	8.6360	8.6385	8.6360	15.0927	15.1105	15.1016	8.6554	10.3803	0.0	1.8288	1.8288
52	8.6233	8.6258	8.6233	8.6241	14.0190	15.0927	15.0558	8.4961	10.2639	10.3760	1.8542	1.8542
53	8.6335	8.6360	8.6360	8.6351	15.0520	15.1232	15.0876	8.6692	10.4088	0.0	1.8288	1.8288
54	8.6360	8.6385	8.6385	8.6377	15.3594	15.4305	15.3949	8.8128	10.3743	10.4531	1.8542	1.8542
55	8.6309	8.6335	8.6335	8.6326	15.0190	15.0673	15.0431	8.5340	10.2835	0.0	1.8288	1.8288

TABLE A-V (continued)

Pellet[a] Number	Diameter (mm)				Length (mm)			Weight (Grams)	Geometric Density (g/cm^3)	Immersion Density (g/cm^3)	Centerline Hole Diameter (mm)	
	Top	Center	Bottom	Average	0°	90°	Average				Top	Bottom
56	8.6360	8.6385	8.6385	8.6377	15.1638	15.2552	15.2095	8.7127	10.3831	10.5163	1.8542	1.8542
57	8.6411	8.6411	8.6411	8.6411	15.0571	15.1130	15.0851	8.6904	10.4344	0.0	1.8542	1.8542
58	8.6309	8.6335	8.6360	8.6334	15.3441	15.3873	15.3657	8.6902	10.2536	10.3384	1.8542	1.8288

[a] Pellets are numbered from bottom of fuel column.

TABLE A-VI

AIR GAUGE MEASUREMENTS OF FUEL ROD
IE-020 CLADDING INSIDE DIAMETER

Elevation[a] (mm)	0° (mm)	45° (mm)	90° (mm)
25.4	8.735	8.731	8.722
50.8	8.729	8.722	8.726
76.2	8.725	8.729	8.723
101.6	8.729	8.728	8.720
127.0	8.729	8.724	8.720
152.4	8.725	8.724	8.724
177.8	8.722	8.722	8.723
203.2	8.722	8.725	8.721
228.6	8.725	8.728	8.718
254.0	8.726	8.728	8.719
279.4	8.727	8.725	8.721
304.8	8.727	8.708	8.732
330.2	8.719	8.729	8.722
355.6	8.726	8.729	8.721
381.0	8.726	8.727	8.721
406.4	8.726	8.726	8.723
431.8	8.725	8.728	8.720
457.2	8.724	8.729	8.720
482.6	8.725	8.728	8.723
508.0	8.727	8.727	8.726
533.4	8.725	8.727	8.729
558.8	8.722	8.724	8.716
584.2	8.725	8.718	8.722
609.6	8.735	8.739	8.722
635.0	8.726	8.729	8.722
660.4	8.726	8.729	8.722
685.8	8.727	8.727	8.721
711.2	8.729	8.727	8.722
736.6	8.728	8.727	8.724
762.0	8.727	8.727	8.725
787.4	8.727	8.780	8.724
812.8	8.728	8.730	8.723
838.2	8.727	8.726	8.725
863.6	8.724	8.725	8.725
889.0	8.725	8.715	8.804

[a] Distance from bottom of fuel rod.

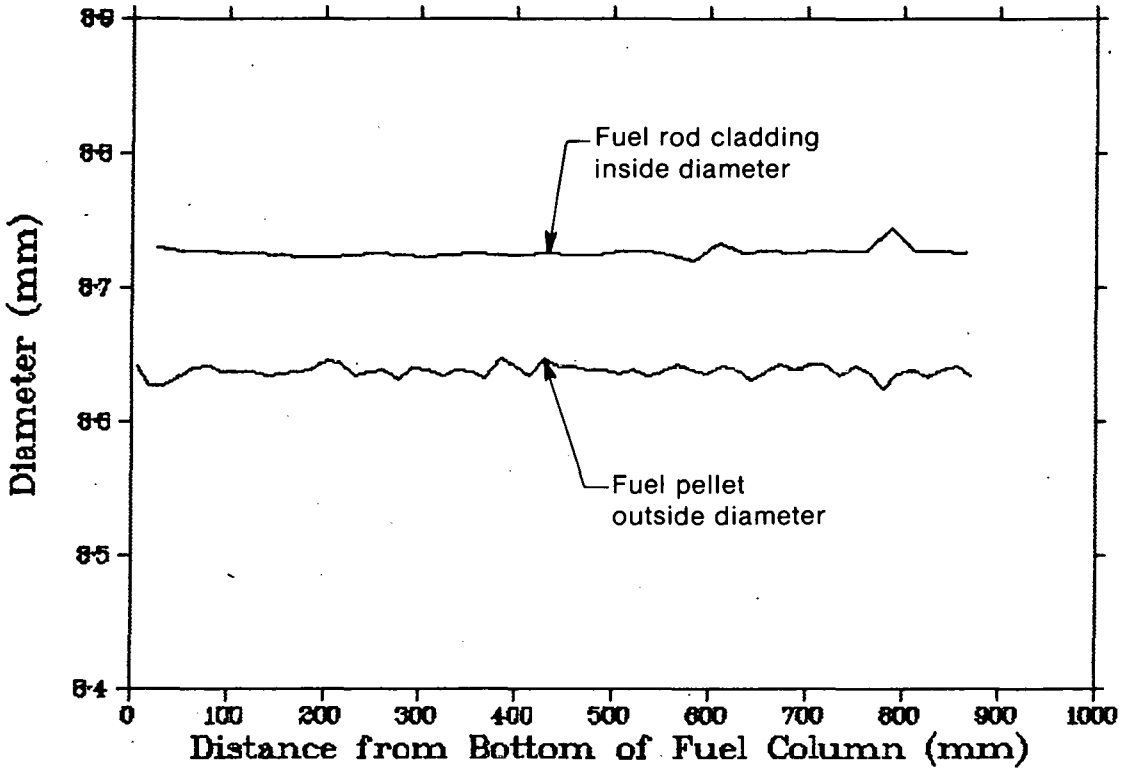

Fig. A-2 Cladding inside diameter and fuel pellet diameter versus axial position for Rod IE-020.

corrosive atmosphere of fission products might lead to stress-corrosion-cracking of the cladding. The fission products of cesium, iodine, tellurium, and molybdenum were in the form of cesium iodide, tellurium metal, and cesium molybdate. Table A-XIII contains the quantities of each compound included in the three fuel rods. Some thermophysical properties of these compounds are contained in Table II of Section II. The fuel stack composition is summarized in Table A-XIV. The geometry of the cored pellets is shown in Figure 5 of Section II.

A detailed characterization of these and other fuel rods used in the IE Test Series can be found in Reference A-1.

TABLE A-VII

OVERALL PRETEST FUEL AND CLADDING
DATA FOR ROD IE-021

Finished Tube Data:	
Mean Outside Diameter[a]	9.995 mm
Mean Inside Diameter	8.777 mm
Ovality (Max ID/Min ID)	1.010
Cladding Length	0.9695 m
Mechanical Properties of Unirradiated Fuel Rod Cladding[b]:	
Yield Tensile Strength	
At Room Temperature	568.7 MPa
At 658 K	320.3 MPa
Ultimate Tensile Strength	
At Room Temperature	749.1 MPa
At 658 K	423.0 MPa
Fuel Data:	
Enrichment	12.38%
Mean Geometric Density	10.3698 g/cm^3
95% Population Loaded	10.3698 (+ 0.1411, - 0.2739) g/cm^3
Mean Diameter	8.639 mm
95% Population Loaded	8.6390 ($\pm$ 0.0076) mm
Stack Mass	515.2823 g
Measured Stack Length	878.622 mm
Dish Chord	6.604 mm
Dish Depth	0.343 mm
Grain Diameter	2.25 $\pm$ 0.65 x 10^{-2} mm
Center Hole Length	351.612 mm
Mean Fuel-cladding Gap	0.138 mm
Measured Void Volume	[c]
Fill Gas Data:	
Pressure	2.50 MPa
Composition	77.7% He, 22.3% Ar

[a] Nominal dimension, not measured after irradiation in the Saxton reactor.
[b] Data supplied by Westinghouse Electric Corporation.
[c] Not measured for this rod.

TABLE A-VIII

FUEL PELLET CHARACTERIZATION DATA FOR ROD IE-021

Pellet[a] Number	Diameter (mm)				Length (mm)			Weight (Grams)	Geometric Density (g/cm^3)	Immersion Density (g/cm^3)	Centerline Hole Diameter (mm)	
	Top	Center	Bottom	Average	0°	90°	Average				Top	Bottom
1	8.6335	8.6335	8.6335	8.6335	8.8748	8.9916	8.9332	5.3322	10.4314	0.0	0.0	0.0
2	8.6411	8.6411	8.6411	8.6411	15.1079	15.1892	15.1486	9.0167	10.2862	0.0	0.0	0.0
3	8.6284	8.6309	8.6309	8.6301	15.1638	15.2273	15.1955	8.9460	10.1998	10.3011	0.0	0.0
4	8.6385	8.6360	8.6360	8.6368	15.1968	15.2324	15.2146	9.0934	10.3383	0.0	0.0	0.0
5	8.6360	8.6360	8.6360	8.6360	15.0952	15.1511	15.1232	9.1089	10.4214	10.4645	0.0	0.0
6	8.6309	8.6309	8.6309	8.6309	15.1333	15.1765	15.1549	8.9512	10.2315	0.0	0.0	0.0
7	8.6385	8.6385	8.6385	8.6385	15.1435	15.1943	15.1689	9.0924	10.3646	0.0	0.0	0.0
8	8.6385	8.6385	8.6360	8.6377	15.1867	15.2197	15.2032	9.0445	10.2885	0.0	0.0	0.0
9	8.6360	8.6360	8.6360	8.6360	15.0952	15.1409	15.1181	8.8892	10.1735	10.0959	0.0	0.0
10	8.6385	8.6385	8.6385	8.6385	15.0825	15.1333	15.1079	9.1201	10.4387	10.4581	0.0	0.0
11	8.6385	8.6385	8.6385	8.6385	15.1943	15.2578	15.2260	9.1140	10.3497	0.0	0.0	0.0
12	8.6335	8.6360	8.6360	8.6351	15.1765	15.2451	15.2108	9.0058	10.2454	0.0	0.0	0.0
13	8.6385	8.6385	8.6385	8.6385	15.2730	15.3314	15.3022	9.2061	10.4015	0.0	0.0	0.0
14	8.6385	8.6385	8.6385	8.6385	15.1028	15.2248	15.1638	9.0789	10.3527	0.0	0.0	0.0
15	8.6360	8.6385	8.6385	8.6377	15.3670	15.3975	15.3822	9.0555	10.1795	10.2452	0.0	0.0
16	8.6436	8.6436	8.6436	8.6436	15.1409	15.1765	15.1587	9.1568	10.4327	0.0	0.0	0.0
17	8.6385	8.6385	8.6385	8.6385	15.1689	15.2070	15.1879	9.0783	10.3354	0.0	0.0	0.0
18	8.6335	8.6335	8.6335	8.6335	15.1943	15.2603	15.2273	8.9824	10.2116	0.0	0.0	0.0
19	8.6385	8.6385	8.6385	8.6385	15.2959	15.3289	15.3124	9.1430	10.3233	0.0	0.0	0.0
20	8.6360	8.6360	8.6360	8.6360	15.1155	15.1511	15.1333	9.1237	10.4313	10.4467	0.0	0.0
21	8.6309	8.6335	8.6360	8.6334	15.2095	15.2654	15.2374	8.9772	10.1988	10.2907	0.0	0.0
22	8.6360	8.6360	8.6360	8.6360	15.5575	15.5804	15.5689	9.2499	10.2758	0.0	0.0	0.0
23	8.6360	8.6360	8.6360	8.6360	15.5804	15.6362	15.6083	9.3160	10.3228	0.0	0.0	0.0
24	8.6360	8.6360	8.6360	8.6360	15.1968	15.2730	15.2349	9.0453	10.2717	0.0	0.0	0.0
25	8.6360	8.6360	8.6360	8.6360	15.3238	15.3619	15.3429	9.1404	10.3057	10.3647	0.0	0.0

TABLE A-VIII (continued)

Pellet[a] Number	Diameter (mm)				Length (mm)			Weight (Grams)	Geometric Density (g/cm^3)	Immersion Density (g/cm^3)	Centerline Hole Diameter (mm)	
	Top	Center	Bottom	Average	0°	90°	Average				Top	Bottom
26	8.6385	8.6385	8.6385	8.6385	15.0546	15.0927	15.0736	9.0739	10.4097	0.0	0.0	0.0
27	8.6335	8.6335	8.6335	8.6335	15.2298	15.2705	15.2502	8.9515	10.1610	10.2861	0.0	0.0
28	8.6411	8.6411	8.6411	8.6411	15.1359	15.1435	15.1397	9.1051	10.3932	0.0	0.0	0.0
29	8.6385	8.6385	8.6385	8.6385	15.2044	15.2806	15.2425	9.1453	10.3744	0.0	0.0	0.0
30	8.6360	8.6385	8.6385	8.6377	15.3264	15.3543	15.3403	9.0097	10.1560	10.2386	0.0	0.0
31	8.6335	8.6335	8.6360	8.6343	15.3035	15.3391	15.3213	9.1662	10.3575	0.0	0.0	0.0
32	8.6385	8.6385	8.6385	8.6385	15.3010	15.3568	15.3289	9.1999	10.3762	0.0	0.0	0.0
33	8.6360	8.6360	8.6360	8.6360	15.0114	15.0876	15.0495	8.9499	10.2903	10.3582	0.0	0.0
34	8.6411	8.6411	8.6411	8.6411	15.3111	15.3822	15.3467	9.2238	10.3848	0.0	0.0	0.0
35	8.6335	8.6335	8.6360	8.6343	15.0393	15.1054	15.0723	9.0892	10.4386	10.5109	0.0	0.0
36	8.6309	8.6335	8.6528	8.6301	15.3848	15.4102	15.3975	8.7180	10.3078	10.2406	1.9050	1.9050
37	8.6411	8.6411	8.6436	8.6419	15.1562	15.2248	15.1905	8.7510	10.4380	10.4837	1.8796	1.8542
38	8.6436	8.6436	8.6436	8.6436	15.2197	15.2883	15.2540	8.7515	10.3972	10.4780	1.8796	1.8796
39	8.6360	8.6360	8.6360	8.6360	15.1867	15.2400	15.2133	8.7177	10.4046	10.4677	1.8796	1.8796
40	8.6411	8.6411	8.6411	8.6411	15.1765	15.1816	15.1790	8.6957	10.3891	10.3714	1.8796	1.8796
41	8.6436	8.6436	8.6411	8.6428	15.3187	15.3594	15.3391	8.8017	10.4002	10.3726	1.8796	1.8796
42	8.6385	8.6385	8.6385	8.6385	15.2451	15.2959	15.2705	8.7708	10.4148	10.3742	1.8542	1.8796
43	8.6411	8.6411	8.6411	8.6411	15.3645	15.4051	15.3848	8.8070	10.3795	0.0	1.8796	1.8796
44	8.6436	8.6436	8.6436	8.6436	15.1282	15.1511	15.1397	8.6604	10.3746	10.3777	1.8796	1.9050
45	8.6309	8.6335	8.6335	8.6326	15.3340	15.3594	15.3467	8.6902	10.3029	0.0	1.9050	1.9050
46	8.6436	8.6436	8.6436	8.6436	15.3467	15.4000	15.3733	8.8314	10.4026	10.3929	1.8796	1.8542
47	8.6436	8.6462	8.6462	8.6453	15.2654	15.3238	15.2946	8.8082	10.4251	0.0	1.8542	1.8796
48	8.6335	8.6335	8.6335	8.6335	15.3492	15.4051	15.3772	8.6918	10.2681	10.2564	1.8796	1.8796
49	8.6436	8.6436	8.6462	8.6445	15.1232	15.1638	15.1435	8.7157	10.4431	0.0	1.9050	1.9050
50	8.6436	8.6436	8.6436	8.6436	15.3518	15.3924	15.3721	8.8010	10.3746	10.4371	1.8796	1.8796
51	8.6411	8.6436	8.6436	8.6428	15.0952	15.1308	15.1130	8.5543	10.2611	0.0	1.8796	1.8796
52	8.6462	8.6462	8.6436	8.6453	14.4864	15.5321	15.5092	8.9093	10.4039	10.4464	1.8796	1.8796
53	8.6411	8.6411	8.6411	8.6411	15.1740	15.2908	15.2324	8.7533	10.4278	0.0	1.8796	1.9050
54	8.6385	8.6385	8.6411	8.6394	15.3772	15.3848	15.3810	8.6335	10.2929	10.3595	1.8796	1.8542
55	8.6436	8.6436	8.6436	8.6436	14.9708	15.0241	14.9974	8.7387	10.4341	0.0	1.8542	1.8796

TABLE A-VIII (continued)

Pellet[a] Number	Diameter (mm)				Length (mm)			Weight (Grams)	Geometric Density (g/cm^3)	Immersion Density (g/cm^3)	Centerline Hole Diameter (mm)	
	Top	Center	Bottom	Average	0°	90°	Average				Top	Bottom
56	8.6436	8.6436	8.6436	8.6436	15.2375	15.2806	15.2590	8.7860	10.4346	10.4891	1.8796	1.8796
57	8.6360	8.6411	8.6411	8.6394	15.2806	15.3314	15.3060	8.6717	10.2707	0.0	1.8542	1.8796
58	8.6436	8.6436	8.6436	8.6436	15.3822	15.4813	15.4318	8.8405	10.3803	10.3779	1.8796	1.8796

[a] Fuel pellets are numbered from bottom of fuel column.

TABLE A-IX

AIR GAUGE MEASUREMENTS OF FUEL ROD
IE-021 CLADDING INSIDE DIAMETER

Elevation[a] (mm)	0° (mm)	45° (mm)	90° (mm)
0	8.730	8.814	8.746
25.4	8.757	8.780	8.752
50.8	8.769	8.764	8.749
76.2	8.769	8.759	8.756
101.6	8.760	8.758	8.789
127.0	8.736	8.759	8.760
152.4	8.766	8.780	8.753
177.8	8.780	8.764	8.757
203.2	8.782	8.757	8.764
228.6	8.780	8.762	8.777
254.0	8.771	8.769	8.769
279.4	8.784	8.781	8.786
304.8	8.774	8.770	8.778
330.2	8.777	8.786	8.777
355.6	8.777	8.791	8.802
381.0	8.754	8.787	8.796
406.4	8.781	8.797	8.791
431.8	8.769	8.793	8.796
457.2	8.781	8.795	8.789
482.6	8.787	8.801	8.796
508.0	8.780	8.793	8.775
533.4	8.798	8.798	8.763
558.8	8.808	8.785	8.770
584.2	8.796	8.781	8.744
609.6	8.799	8.777	8.788
635.0	8.781	8.769	8.762
660.4	8.815	8.793	8.796
685.8	8.782	8.771	8.792
711.2	8.774	8.804	8.794
736.6	8.776	8.788	8.760
762.0	8.786	8.798	8.781
787.4	8.778	8.763	8.784
812.8	8.786	8.785	8.795
838.2	8.761	8.794	8.753
863.6	8.768	8.795	8.770
889.0	8.765	8.756	8.757
914.4	8.763	8.771	8.761
939.8	8.750	8.761	8.753
965.2	8.748	8.764	8.754
990.6	8.746	8.758	8.754

[a] Distance from bottom of fuel rod.

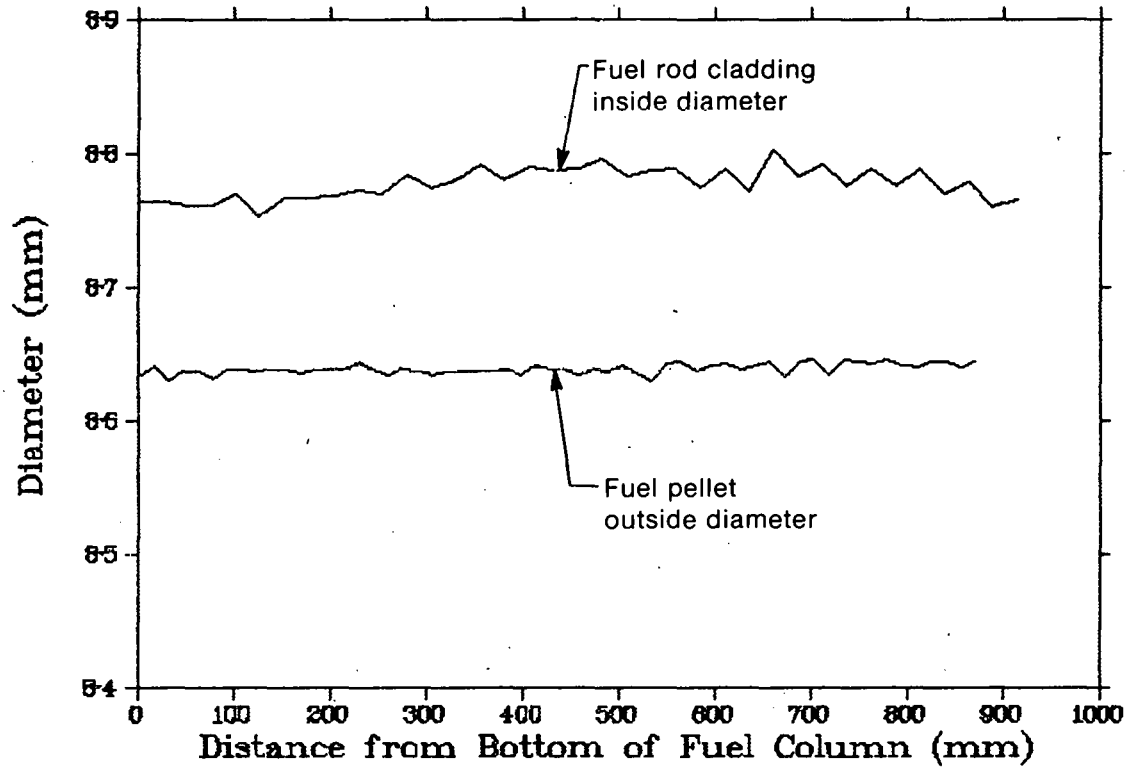

Fig. A-3 Cladding inside diameter and fuel pellet diameter versus axial position for Rod IE-021.

TABLE A-X

OVERALL PRETEST FUEL AND CLADDING
DATA FOR ROD IE-022

Finished Tube Data:	
Mean Outside Diameter	9.933 mm
Mean Inside Diameter	8.731 mm
Ovality (Max ID/Min ID)	1.002
Cladding Length	0.9694 m
Mechanical Properties of Unirradiated Fuel Rod Cladding[a]:	
Yield Tensile Strength	
At Room Temperature	571.4 MPa
At 658 K	388.9 MPa
Ultimate Tensile Strength	
At Room Temperature	772.8 MPa
At 658 K	489.5 MPa
Fuel Data:	
Enrichment	12.38%
Mean Geometric Density	10.4036 g/cm^3
95% Population Loaded	10.4036 (+ 0.137, - 0.168) g/cm^3
Mean Diameter	8.639 mm
95% Population Loaded	8.6390 (+ 0.0076, - 0.0102) mm
Stack Mass	515.4343 g
Measured Stack Length	878.408 mm
Dish Dimensions	
Dish Chord	6.604 mm
Dish Depth	0.343 mm
Grain Diameter	$2.25 \pm 0.65 \times 10^{-2}$ mm
Center Hole Length	351.587 mm
Mean Fuel-cladding Gap	0.092 mm
Measured Void Volume	7.88 ml
Fill Gas Data:	
Pressure	2.56 MPa
Composition	77.7% He, 22.3% Ar

[a] Data supplied by Westinghouse Electric Corporation.

TABLE A-XI

FUEL PELLET CHARACTERIZATION DATA FOR ROD IE-022

Pellet[a] Number	Diameter (mm)				Length (mm)			Weight (Grams)	Geometric Density (g/cm^3)	Immersion Density (g/cm^3)	Centerline Hole Diameter (mm)	
	Top	Center	Bottom	Average	0°	90°	Average				Top	Bottom
1	8.6360	8.5360	8.6360	8.6360	7.6886	7.7673	7.7279	4.5919	10.4153	0.0	0.0	0.0
2	8.6335	8.5335	8.6335	8.6335	15.3467	15.3746	15.3606	9.1037	10.2584	0.0	0.0	0.0
3	8.6360	8.5360	8.6360	8.6360	15.1765	15.2222	15.1993	8.9768	10.2181	10.3366	0.0	0.0
4	8.6411	8.6411	8.6411	8.6411	15.3695	15.4254	15.3975	9.2892	10.4234	0.0	0.0	0.0
5	8.6284	8.6309	8.6309	8.6301	15.1384	15.1562	15.1473	9.0048	10.3000	10.3976	0.0	0.0
6	8.6335	8.6360	8.6360	9.6351	15.2298	15.2629	16.2463	9.0343	10.2535	0.0	0.0	0.0
7	8.6335	8.6335	8.6335	8.6335	15.5016	15.5524	15.5270	9.3348	10.4046	0.0	0.0	0.0
8	8.6335	8.6335	8.6335	8.6335	15.2883	15.3949	15.3416	9.1967	10.3763	0.0	0.0	0.0
9	8.6360	8.6360	8.6360	8.6360	15.2502	15.2984	15.2743	9.0795	10.2836	10.3782	0.0	0.0
10	8.6385	8.6385	8.6385	8.6385	15.2019	15.2349	15.2184	9.1154	10.3565	10.4120	0.0	0.0
11	8.6360	8.6335	8.6309	8.6334	15.1892	15.2273	15.2082	9.1289	10.3913	0.0	0.0	0.0
12	8.6385	8.6385	8.6385	8.6385	15.3695	15.4203	15.3949	9.1576	10.2836	0.0	0.0	0.0
13	8.6411	8.6411	8.6436	8.6419	15.1841	15.2248	15.2044	9.1497	10.3969	0.0	0.0	0.0
14	8.6360	8.6360	8.6360	8.6360	15.3695	15.4153	15.3924	9.2133	10.3541	0.0	0.0	0.0
15	8.6385	8.6385	8.6385	8.6385	15.0724	15.1105	15.0914	8.8515	10.1425	10.3018	0.0	0.0
16	8.6360	8.6360	8.6360	8.6360	15.2375	15.3213	15.2794	9.0315	10.2258	0.0	0.0	0.0
17	8.6360	8.6360	8.6360	8.6360	15.2908	15.3086	15.2997	9.1436	10.3388	0.0	0.0	0.0
18	8.6360	8.6385	8.6385	8.6377	15.1613	15.2019	15.1816	8.9995	10.2520	0.0	0.0	0.0
19	8.6309	8.6335	8.6335	8.6326	15.3670	15.4280	15.3975	9.2182	10.3643	0.0	0.0	0.0
20	8.6335	8.6335	8.6360	8.6343	15.2222	15.2527	15.2374	9.1304	10.3707	10.4054	0.0	0.0
21	8.6385	8.6385	8.6385	8.6385	15.1867	15.2679	15.2273	9.0438	10.2691	10.3885	0.0	0.0
22	8.6411	8.6411	8.6411	8.6411	15.3467	15.3772	15.3619	9.2130	10.3622	0.0	0.0	0.0
23	8.6284	8.6284	8.6284	8.6284	15.0901	15.1511	15.1206	9.0287	10.3499	0.0	0.0	0.0
24	8.6360	8.6360	8.6360	8.6360	15.0952	15.1333	15.1143	8.9635	10.2612	0.0	0.0	0.0
25	8.6335	8.6360	8.6385	8.6360	15.1714	15.2400	15.2057	9.1304	10.3886	10.4173	0.0	0.0

TABLE A-XI (continued)

Pellet[a] Number	Diameter (mm)				Length (mm)			Weight (Grams)	Geometric Density (g/cm^3)	Immersion Density (g/cm^3)	Centerline Hole Diameter (mm)	
	Top	Center	Bottom	Average	0°	90°	Average				Top	Bottom
26	8.6436	8.6436	8.6436	8.6436	15.3086	15.3594	15.3340	9.1731	10.3302	0.0	0.0	0.0
27	8.6335	8.6360	8.6360	8.6351	15.1435	15.2070	15.1752	8.9186	10.1703	10.2601	0.0	0.0
28	8.6411	8.6411	8.6411	8.6411	15.2984	15.3441	15.3213	9.1732	10.3451	0.0	0.0	0.0
29	8.6385	8.6411	8.6411	8.6402	14.9174	14.9657	14.9415	8.9617	10.3690	0.0	0.0	0.0
30	8.6360	8.6360	8.6360	8.6360	15.2425	15.2679	15.2552	8.9343	10.1320	10.2356	0.0	0.0
31	8.6411	8.6411	8.6411	8.6411	15.3899	15.4330	15.4114	9.2424	10.3614	0.0	0.0	0.0
32	8.6411	8.6411	8.6411	8.6411	15.2527	15.2933	15.2730	9.1766	10.3821	0.0	0.0	0.0
33	8.6360	8.6385	8.6385	8.6377	15.1308	15.2019	15.1663	8.9970	10.2596	10.3693	0.0	0.0
34	8.6385	8.6385	8.6385	8.6385	15.3137	15.3645	15.3391	9.1870	10.8815	0.0	1.9050	1.9050
35	8.6360	8.6360	8.6385	8.6368	15.0724	15.1054	15.0889	9.0335	10.8840	0.0	1.9050	1.9050
36	8.6335	8.6360	8.6360	8.6351	15.1714	15.2527	15.2121	8.6128	9.4679	10.3838	1.8542	1.8542
37	8.6385	8.6385	8.6385	8.6385	15.2857	15.3391	15.3124	8.7946	10.4072	10.4142	1.8542	1.8542
38	8.6385	8.6385	8.6385	8.6385	15.2121	15.2705	15.2413	8.7815	10.4688	10.3838	1.9050	1.9050
39	8.6385	8.6411	8.6411	8.6402	15.3035	15.4483	15.3759	8.8097	10.3636	10.4693	1.8288	1.8288
40	8.6411	8.6436	8.6436	8.6428	15.1689	15.2019	15.1854	8.7328	10.4108	10.4640	1.8542	1.8542
41	8.6411	8.6411	8.6411	8.6411	15.2044	15.2375	15.2209	8.7299	10.4148	10.2175	1.9050	1.9050
42	8.6385	8.6385	8.6385	8.6385	15.1765	15.2324	15.2044	8.6409	10.3264	10.4439	1.9050	1.9050
43	8.6335	8.6360	8.6360	8.6351	15.3416	15.3721	15.3568	8.8293	10.4543	10.5114	1.9050	1.9050
44	8.6411	8.6411	8.6411	8.6411	15.2959	15.3264	15.3111	8.8154	10.4400	10.4088	1.8796	1.8796
45	8.6335	8.6335	8.6284	8.6318	15.2857	15.3340	15.3098	8.6815	10.2788	0.0	1.8288	1.8288
46	8.6360	8.6385	8.6385	8.6377	15.1562	15.1917	15.1740	8.6819	10.3987	10.4684	1.9050	1.9050
47	8.6411	8.6411	8.6411	9.6411	15.2298	15.2959	15.2628	8.7551	10.4158	10.5185	1.9050	1.9050
48	8.6309	8.6309	9.6309	8.6309	15.1409	15.1841	15.1625	8.5706	10.2905	10.3504	1.9050	1.9050
49	8.6411	8.6411	8.6411	8.6411	15.2171	15.2527	15.2349	8.7759	10.4321	0.0	1.8542	1.8542
50	8.6385	8.6385	8.6385	8.6385	15.3035	15.3518	15.3276	8.7820	10.3683	10.4663	1.8288	1.8288
51	8.6436	8.6462	8.6462	8.6453	15.3314	15.3746	15.3530	8.7087	10.2608	0.0	1.8542	1.8542
52	8.6411	8.6411	8.6411	8.6411	15.2298	15.3518	15.2908	8.7401	10.3579	10.3411	1.8796	1.8542
53	8.6284	8.6309	8.6335	8.6309	15.1841	15.2121	15.1981	8.7097	10.3911	0.0	1.8288	1.8288
54	8.6335	8.6360	8.6360	8.6351	15.2578	15.3264	15.2921	8.6549	10.2642	10.3235	1.8542	1.8542
55	8.6385	8.6385	8.6411	8.6394	15.3645	15.4356	15.4000	8.8816	10.4270	0.0	1.8288	1.8034

TABLE A-XI (continued)

Pellet[a] Number	Diameter (mm)				Length (mm)			Weight (Grams)	Geometric Density (g/cm^3)	Immersion Density (g/cm^3)	Centerline Hole Diameter (mm)	
	Top	Center	Bottom	Average	0°	90°	Average				Top	Bottom
56	8.6385	8.6385	8.6385	8.6385	15.3086	15.3594	15.3340	8.8054	10.3915	10.4842	1.8288	1.8288
57	8.6258	8.6309	8.6335	8.6301	15.2375	15.2806	15.2590	8.6530	10.4434	0.0	1.8288	1.8288
58	8.6411	8.6411	8.6411	8.6411	15.3721	15.4584	15.4153	8.8908	10.4434	10.5406	1.8542	1.8542

[a] Fuel pellets are numbered from bottom of fuel column.

TABLE A-XII

CLADDING DIMENSIONS FOR ROD IE-022

Tube Inside Diameter Measurements

Elevation[a] (mm)	Inside Diameter (mm) 0°	90°
25.4	8.735	8.738
50.8	8.731	8.729
76.2	8.729	8.729
101.6	8.733	8.728
127.0	8.731	8.732
152.4	8.736	8.732
177.8	8.734	8.733
203.2	8.738	8.729
228.6	8.740	8.735
254.0	8.734	8.737
279.4	8.733	8.739
304.8	8.727	8.731
330.2	8.728	8.728
355.6	8.724	8.726
381.0	8.730	8.731
406.4	8.733	8.729
431.8	8.736	8.736
457.2	8.733	8.737
482.6	8.735	8.736
508.0	8.735	8.736
533.4	8.729	8.734
558.8	8.723	8.733
584.2	8.726	8.728
609.6	8.727	8.725
635.0	8.729	8.732
660.4	8.732	8.735
685.8	8.737	8.734
711.2	8.738	8.735
736.6	8.732	8.739
762.0	8.731	8.735
787.4	8.725	8.731
812.8	8.725	8.729
838.2	8.721	8.729
863.6	8.724	8.724
884.0	8.732	8.722
914.4	8.731	8.725
939.8	8.732	8.726
965.2	8.731	8.735

Tube Outside Diameter Measurements

Elevation[a] (mm)	Outside Diameter (mm) 0°	90°
25.4	9.931	9.931
304.8	9.919	9.944
609.6	9.931	9.931
914.4	9.944	9.931

[a] Distance from bottom of fuel rod.

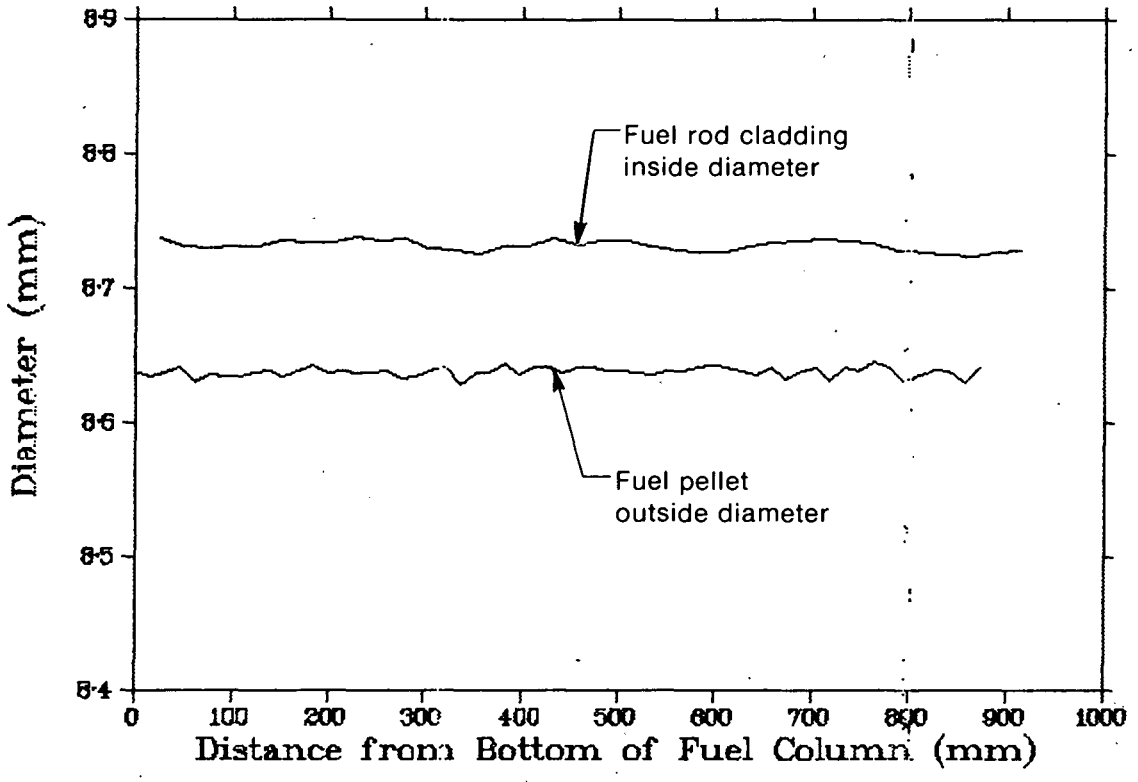

Fig. A-4 Cladding inside diameter and fuel pellet diameter versus axial position for Rod IE-022.

TABLE A-XIII

QUANTITIES OF SIMULATED FISSION PRODUCTS PER FUEL STACK

Rod	Cesium Iodide (CsI) (mg)	Cesium Molybdate (Cs_2MoO_4) (mg)	Tellurium (Te_2) (mg)
IE-020	34 ± 1	457 ± 1	39 ± 1
IE-021	33 ± 1	451 ± 1	35 ± 1
IE-022	35 ± 1	450 ± 1	37 ± 1

TABLE A-XIV

COMPOSITION OF TEST IE-5 FUEL STACKS

	Number of Fuel Pellets in Fuel Stack			
	Without Holes for Fission Products		With Holes for Fission Products	
Rod	Solid	Cored[a]	Solid	Cored[a]
IE-020	31	9	14	4
IE-021	24	17	11	6
IE-022	23	18	11	6

[a] Centerline hole drilled for instrumentation.

REFERENCE

A-1. G. W. Gibson et al, *Characteristics of UO_2-Zircaloy Fuel Rod Materials from the Saxton Reactor for Use in the Power Burst Facility*, ANCR-NUREG-1321 (September 1976).

APPENDIX B

INSTRUMENTATION AND DATA ACQUISITION SYSTEM UNCERTAINTIES

THIS PAGE

WAS INTENTIONALLY

LEFT BLANK

APPENDIX B

INSTRUMENTATION AND DATA ACQUISITION SYSTEM UNCERTAINTIES

The calibration equations that were used to convert the transducer output to engineering units during the data reduction process for Test IE-5 are presented in this appendix.

Data obtained during the conduct of the test are subjected to three significant sources of error: (a) instrument calibration error, (b) data system acquisition error, and (c) measurement error. Estimates of both the instrument calibration error and data system acquisition error are provided in this appendix. The systematic measurement error is a consequence of the transducer design and installation. To quantify the effect of the measurement error it would be necessary, either by analysis or experiment, to simulate the in-use configuration of the transducer. Since this effort has not been made, an estimate of the measurement error is not available. This type of measurement error is not judged to be significant, and the measurements provided by the instruments should reflect values of the physical parameter measured within the error estimates specified in this appendix (cladding surface temperature measurements had the most significant systematic error primarily due to a fin-cooling effect). Also, this statement is made assuming that the instruments do not decalibrate prior to or during the experiment, however, posttest calibrations were not performed on the test instrumentation to verify the assumption due to the difficulties involved in handling irradiated components. As indicated by the test data for rod internal pressure, significant errors due to decalibration can occur. Data corrections or coordinate transformations were used to minimize these errors (Appendix C).

Calibration equations for each instrument are presented in a tabular form in Table B-I. Included in the table is the 95% confidence interval estimate for each equation. The data system error and the quadratic sum of the data system and calibration instrument errors are also provided.

The criterion for the 95% confidence interval estimate for those transducers that had a linear calibration equation was established using the following relation:

$$L_i = Y_i \pm t(1-\alpha/2)\ S_{y \cdot x} \left[\frac{1}{n} + 1 + \frac{n(x_i - \bar{x})^2}{n\Sigma x^2 - (\Sigma x)^2} \right]^{1/2} \qquad \text{(B-1)}$$

TABLE B-I

SUMMARY OF CALIBRATION EQUATIONS AND UNCERTAINTIES IN EXPERIMENTAL MEASUREMENTS FOR TEST IE-5

Measurements	Transducer (Serial Number)	Fuel Rod Number	Calibration Equation	Output (% of Range)	Output	Data System Error	Calibration Error	Total Error
					(MPa)	(MPa)	(MPa)	(MPa)
System Pressure	0- to 69-MPa Strain Post (SN 158)	[a]	MPa = -12.03 + 4.495 (mV) +0.0144 (T)	0	0	0.22	0.58	0.62
				25	9.3	0.27	0.43	0.51
				50	18.6	0.35	0.33	0.48
				75	27.9	0.46	0.45	0.64
				100	37.2	0.58	0.63	0.86
System Pressure	0- to 21-MPa Strain Post (SN 309)	[a]	MPa = -3.29 + 0.591 (mV)[b]	0	0	0.11	0.07	0.13
				25	5.2	0.13	0.05	0.14
				50	10.3	0.17	0.04	0.17
				75	15.5	0.23	0.05	0.24
				100	20.7	0.29	0.07	0.30
					(K)	(K)	(K)	(K)
Coolant Inlet and Outlet Temperature	Chromel-Alumel Thermocouple (All Devices)	[a]	K = 343.6 + 24.05 (mV)	0	540	0.3	1.0	1.0
				25	568	0.3	1.1	1.1
				50	595	0.4	1.2	1.3
				75	623	0.5	1.3	1.4
				100	650	0.7	1.4	1.6
Coolant Temperature Differential	Copper-Constantan Thermocouple (Type T)	[a]	K = 0.0250 + 16.971 (mV)[c]	0	0	0.12	0.010	0.12
				25	5.6	0.11	0.015	0.14
				50	11.2	0.19	0.034	0.19
				75	16.8	0.25	0.053	0.26
				100	22.4	0.31	0.076	0.32
					(cm^3/s)	(cm^3/s)	(cm^3/s)	(cm^3/s)
Coolant Flow	Turbine Flowmeter (SN 104)	IE-019	cm^3/s = -0.250 + 0.485 (HZ)	0	0	6.8	[d]	[d]
				25	315.8	8.1	0.75	8.1
				50	631.7	10.6	1.05	10.6
				75	947.5	14.1	1.8	14.2
				100	1263.3	17.7	[d]	[d]
Coolant Flow	Turbine Flowmeter (SN 102)	IE-020	cm^3/s = 0.634 + 0.476 (HZ)	0	0	6.8	[e]	[e]
				25	317.8	8.1	0.70	8.1
				50	635.6	10.6	0.95	10.6
				75	953.5	14.1	1.7	14.2
				100	1271.3	17.7	[d]	[d]

TABLE B-I (continued)

Measurements	Transducer (Serial Number)	Fuel Rod Number	Calibration Equation	Output (% of Range)	Output (cm^3/s)	Data System Error (cm^3/s)	Calibration Error (cm^3/s)	Total Error (cm^3/s)
Coolant Flow	Turbine Flowmeter (SN 101)	IE-021	$cm^3/s = 0.111 + 0.481$ (HZ)	0	0	6.8	[d]	[d]
				25	315.5	8.1	0.1	8.1
				50	630.9	10.6	0.1	10.6
				75	946.4	14.1	0.15	14.1
				100	1261.8	17.1	[d]	[d]
Coolant Flow	Turbine Flowmeter (SN 103)	IE-022	$cm^3/s = 0.601 + 0.481$ (HZ)	0	0	6.8	[d]	[d]
				25	315.5	8.1	0.55	8.1
				50	630.9	10.6	0.75	10.6
				75	946.4	14.1	1.85	14.2
				100	1261.8	17.7	[d]	[d]
					(mm)	(mm)	(mm)	(mm)
Cladding Elongation	LVDT (SN 427)	IE-019	$mm = 0.07725 + 0.8475$ (mV) $+1.5963$ (mV^2)[b]	0	0	0.07	0.14	0.16
				25	3.2	0.08	0.08	0.11
				50	6.4	0.11	0.08	0.14
				75	9.5	0.14	0.07	0.16
				100	12.7	0.18	0.13	0.22
Cladding Elongation	LVDT (SN 428)	IE-020	$mm = 0.03647 + 9.83606$ (mV) $+0.6272$ (mV^2)[b]	0	0	0.07	0.07	0.10
				25	3.2	0.08	0.04	0.09
				50	6.4	0.11	0.04	0.12
				75	9.5	0.14	0.04	0.15
				100	12.7	0.18	0.07	0.19
Cladding Elongation	LVDT (SN 429)	IE-021	$mm = 0.03767 + 9.7842$ (mV) $+0.7076$ (mV^2)[b]	0	0	0.07	0.06	0.09
				25	3.2	0.08	0.04	0.09
				50	6.4	0.11	0.04	0.12
				75	9.5	0.14	0.03	0.18
				100	12.7	0.18	0.06	0.19
Cladding Elongation	LVDT (SN 431)	IE-022	$mm = -0.05457 + 9.1959$ (mV) $+1.1767$ (mV^2)[b]	0	0	0.07	0.10	0.12
				25	3.2	0.08	0.06	0.10
				50	6.4	0.11	0.06	0.12
				75	9.5	0.14	0.06	0.15
				100	12.7	0.18	0.10	0.21

TABLE B-I (continued)

Measurements	Transducer (Serial Number)	Fuel Rod Number	Calibration Equation	Output (% of Range)	Output	Data System Error	Calibration Error	Total Error
					(MPa)	(MPa)	(MPa)	(MPa)
Fuel Rod Pressure	21-MPa Strain Post (SN 531)	IE-019	MPa = -6.451 + 3.798 (mV) $+4.922 \times 10^{-2}(mV)^2$ $+0.8717$ (T)	0	0	0.11	0.11	0.16
				25	5.2	0.13	0.08	0.15
				50	10.4	0.15	0.08	0.17
				75	15.6	0.17	0.08	0.19
				100	20.7	0.20	0.10	0.22
Fuel Rod Pressure	17-MPa Strain Post (SN 527)	IE-020	MPa = -6.427 + 3.958 (mV) $+1.257 \times 10^{-3}(mV)^2$ -1.754×10^{-2}(T)	0	0	0.11	0.12	0.16
				25	4.3	0.13	0.09	0.16
				50	8.6	0.15	0.09	0.17
				75	12.9	0.17	0.08	0.19
				100	17.2	0.20	0.14	0.24
Fuel Rod Pressure	17-MPa Strain Post (SN 528)	IE-021	MPa = -0.743 + 3.163 (mV) $-1.630 \times 10^{-3}(mV)^2$ $+5.735 \times 10^{-3}$(T)	0	0	0.11	0.24	0.26
				25	4.3	0.13	0.48	0.50
				50	8.6	0.15	0.50	0.52
				75	12.9	0.17	0.50	0.53
				100	17.2	0.20	0.74	0.77
Fuel Rod Pressure	17-MPa Strain Post (SN 420)	IE-022	MPa = -2.491 + 1.068 (mV) -4.401×10^{-3}(T)	0	0	0.11	0.18	0.21
				25	4.3	0.13	0.14	0.19
				50	8.6	0.15	0.13	0.20
				75	12.9	0.17	0.14	0.22
				100	17.2	0.20	0.18	0.27
					(K)	(K)	(K)	(K)
Fuel Centerline Temperature	W5%Re/W26%Re Thermocouple (SN 578)	IE-019	K = 391.4 - 49.55 (mV) $+0.2209$ $(mV)^2$	0	340	14	[e]	[e]
				25	880	16	[e]	[e]
				50	1420	19	[e]	[e]
				75	1960	23	[e]	[e]
				100	2500	28	[e]	[e]
Fuel Centerline Temperature	W5%Re/W26%Re Thermocouple (SN 579)	IE-020	K = 383.4 - 47.62 (mV) $+0.2709$ $(mV)^2$	0	350	14	[e]	[e]
				25	910	16	[e]	[e]
				50	1470	19	[e]	[e]
				75	2030	23	[e]	[e]
				100	2590	28	[e]	[e]

TABLE B-I (continued)

Measurements	Transducer (Serial Number)	Fuel Rod Number	Calibration Equation	Output (% of Range)	Output (K)	Data System Error (K)	Calibration Error (K)	Total Error (K)
Fuel Centerline Temperature	Ultrasonic Thermometer (SN 588)	IE-021	$K = -2480.3 + 693.31\ (mV) - 15.979\ (mV)^2 - 0.7566\ (mV)^3$	0	300	11	17	20
				25	750	13	18	22
				50	1200	18	17	25
				75	1650	24	19	31
				100	2100	29	23	37
Fuel Centerline Temperature	Ultrasonic Thermometer (SN 589)	IE-022	$K = -2057.7 + 814.19\ (mV) - 45.867\ (mV)^2 + 0.7937\ (mV)^3$	0	300	12	30	32
				25	800	15	28	32
				50	1300	19	27	33
				75	1800	26	28	38
				100	2300	32	43	54
Cladding Surface Temperature	Chromel-Alumel (Type K) Thermocouple	IE-019	[f] $K = 365.4 + 21.10\ (mV) + 5.7099 \times 10^{-2} (mV)^2$	0	500	9	4	10
				25	788	11	6	13
				50	1075	14	8	16
				75	1363	18	10	21
				100	1650	23	12	26
Cladding Surface Temperature	Platinum/Platinum-10% Rhodium (Type S) Thermocouple	IE-020 IE-021 IE-022	[f] $K = 381.2 + 103.7\ (mV) - 0.7667\ (mV)^2$	0	500	11	4	12
				25	882	13	7	15
				50	1230	17	9	19
				75	1580	23	12	26
				100	2030	28	15	32

[a] Calibrations are not unique to a particular fuel rod.
[b] This equation is applicable to a coolant inlet temperature of 589 K.
[c] This equation is applicable to a coolant inlet temperature of 606 K.
[d] Output outside expected range of use so device not calibrated for these flow rates.
[e] Undefined, see Appendix A discussion.
[f] See Appendix A discussion for high and low range accuracy.

where

L_i	=	the confidence interval estimate
Y_i	=	calculated value of the dependent variable from the regression equation
$t(1-\alpha/2)$	=	value from a t distribution for n-2 degrees of freedom
α	=	level of confidence (0.95 was used here)
$S_{y \cdot x}$	=	standard error of the regression of y on x
n	=	number of points
x	=	independent variable
$\bar{x}$	=	mean value of the independent variable
x_i	=	value of the independent variable for which error estimate applies.

The evaluation for L_i for several x_i values established the 95% confidence interval estimate.

For those transducers that had nonlinear or more multivariate functional relationships the 95% confidence interval estimate is given by:

$$L_i = Y_i \pm t(1 - \alpha/2)E \qquad \text{(B-2)}$$

where E is the standard error for the multivariate or polynominal relationship, and the other terms are as defined previously. The standard error term contains cross terms of the coefficients and independent variables. The above procedures were extracted from Reference B-1.

For those transducers that were not calibrated, the 95% confidence interval estimate was assumed to be specified by the accuracy limits as established by a manufacturer or an ANSI standard. The type of error estimate for each transducer is specified below.

1. TEST TRAIN INSTRUMENTATION

1.1 System Pressure

One 0- to 69-MPa and one 0- to 21-MPa strain post type pressure transducer were used to monitor the coolant pressure.

1.2 Coolant Inlet Temperature

Two Chromel-Alumel (Type K) thermocouples, used to measure the coolant inlet temperature, were not calibrated. The 95% confidence interval estimate was 0.375% of the reading as stated by the manufacturer when using the standard calibration tables.

1.3 Coolant Outlet Temperature

One Chromel-Alumel (Type K) thermocouple measured the coolant outlet temperature of each fuel rod. Again, these devices were not calibrated, and the error estimate for these devices was the same as the inlet temperature thermocouples, 0.375% of the reading as stated by the manufacturer.

1.4 Coolant Temperature Rise

One copper-constantan differential temperature measurement thermocouple pair was positioned in each flow shroud. Calibrations were obtained for the thermocouple pair from standard calibration tables. Inlet temperatures of 555, 583, and 606 K with a 20 K temperature rise were used in generating the thermocouple functions. The total estimated error is the square root of the sum of the squares of the calibrated error, data system error, and 0.375% of the thermocouple differential. The calibration error shown in Table B-1 is at a coolant inlet temperature of 606 K.

1.5 Coolant Flow

Four flowmeters with graphite journal bearings were used to measure the coolant flow rate through each flow shroud. These flowmeters were calibrated by the manufacturer (Flow Technology Incorporated). Although the calibrations were conducted with a slightly different inlet and outlet flow geometry than was used during the test, it was established that these deviations did not affect the measured coolant flow accuracy.

1.6 Cladding Elongation

A linear variable differential transformer (LVDT) was used on each fuel rod to measure the cladding elongation. The output of each LVDT is sensitive to the transducer temperature, the lead wire resistance, and the electronic settings on the signal conditioner used. The transducers used for this experiment were not calibrated at the temperature and with the same lead wire and electronic settings that were used during the test. The procedure followed in determining a calibration function for the LVDTs was briefly described in the IE-1 Test Results Report[B-2]. It was estimated that this method resulted in a calibration function that was within 2% of the actual calibration.

2. FUEL ROD INSTRUMENTATION

2.1 Fuel Rod Internal Pressure

One 0- to 21-MPa strain post type pressure transducer was attached to Rod IE-019 to measure the fuel rod internal pressure. The remaining three rods each had one 0- to 17-MPa pressure transducer. The error estimates provided in this appendix represent the uncertainty associated with a multivariate (transducer case temperature and diaphragm pressure) fit to the calibration data. The design of these devices is such that they are occasionally subject to zero offsets between repeated pressure increase and decrease cycles. Sometimes this drift is excessive. A review of calibration data for several of these pressure transducers has shown that the calibration of the transducer generally does not shift during a pressure increase cycle but instead, the shift usually occurs during the pressure decrease portion of a cycle. Consequently, the pressure differentials indicated during power increases are likely to be an accurate measure of the fuel rod internal pressure. The reason for the zero shift is not fully understood, but it was probably due to the strain gauges not being integrally attached to the strain post in the pressure transducer.

2.2 Fuel Centerline Temperature

Tungsten-rhenium thermocouples were used to measure the fuel centerline temperature in Rods IE-019 and IE-020. The thermocouples consisted of a short, high temperature section spliced to a long lead-out cable. The lead-out cable was insulated with magnesium oxide, a stainless steel sheath, and wires (405/426 Hoskins alloys). These alloys match the standard calibration for W5%Re/W26%Re thermocouples. The high temperature zone had a tantalum sheath, berrylium oxide insulation, and stranded W5%Re/W26%Re wires. The result was a thermocouple with a dual calibration which responded differently to temperature gradients along different parts of its length. This problem is discussed in IE Scoping Test 2 Test Results Report[B-3]. The estimated uncertainty for these two thermocouples was ±25 K over the range from 600 to 2500 K.

Ultrasonic thermometers (UT) were used to measure the fuel centerline temperature in Rods IE-021 and IE-022. The sheathed UTs were calibrated up to 2800 K using a combination of an optical pyrometer and a tungsten-rhenium thermocouple. The calibration is in the form of microsecond (μs) response versus temperature. The thermometer output was converted to millivolts during the test. The instrumentation for this device was set up such that a change of output range occurred during the film boiling portion of the test at approximately 2200 K. Both devices failed during the high power steady state operation so only the low range calibration is presented. The UTs were expected to be accurate within ±5%.

2.3 Cladding Surface Temperature

Uncalibrated Chromel-Alumel (Type K) thermocouples were used to measure the cladding surface temperature on Rods IE-019. The 95% confidence interval estimate was

0.375% of the reading, as stated by the manufacturer when using the standard calibration tables. Type S thermocouples were used on the remaining rods. Again, standard calibration tables were used to convert these data.

Table B-I contains calibration equations for cladding surface thermocouples in the range of 500 to 2000 K. Not included are separate equations developed for cladding temperatures between 540 and 640 K. The calibration error of the narrow range equations is negligible compared to the equations shown in Table B-I. The narrow range equations were applied during the power calibration and preconditioning portions of the test. The wide range equations in Table B-I were employed during the power ramp and high power steady state operation.

Although use of the wide range equations contributed to the uncertainty associated with the cladding thermocouples, the accuracy was governed by the data system error and the systematic error of the thermocouples. During the power calibration portion of the test the data system was set to record cladding temperatures between 500 and 700 K. However, amplifier gains were altered for times subsequent to the power calibration period to record temperatures between 300 and 1800 K. This action decreased the accuracy of the recorded data and increased scatter in the cladding surface temperature data. The systematic error of the thermocouples is briefly discussed in Appendix A of Reference B-4.

3. DATA ACQUISITION SYSTEM

A summary of the data recording system errors associated with decalibration and drift of the electronics used to record and reduce the data are given for each transducer in Table B-I. A thorough discussion of the source of these errors is given in Appendix B of the IE Scoping Test 1 Report[B-5].

The data system amplification, gain, and offset are such that the input signal (transducer output) and the output signal (recorded data signal) are related by the equation:

$$V_o = (V_i - V_z)G \tag{B-3}$$

where

V_o = recorded data signal (volts)

V_i = transducer output signal (volts)

V_z = offset (volts)

G = gain.

The standard deviation of the recorded data signal, S_{V_o}, can then be determined

$$S_{V_o} = \left[\left(\frac{V_o}{G} \right)^2 S_G^2 + G^2 S_{V_z}^2 + G^2 V_i \right]^{1/2} . \quad \text{(B-4)}$$

For the calibration, S_{V_i}, can be considered to be zero such that

$$S_{V_o} = \left[\left(\frac{V_o}{G} \right)^2 S_G^2 + G^2 S_{V_z}^2 \right]^{1/2} . \quad \text{(B-5)}$$

A test performed to evaluate the data system resulted in values of $\frac{S_G}{G}$ and GS_{V_z} to be 0.65% and 2.7 millivolts, respectively.

For a total span ($Y_{max} - Y_{min}$) of 1000 millivolts on the recording channel, Equation (B-5) can be simplified to

$$\frac{S_Y}{Y_{max} - Y_{min}} \% = \left[\left(\frac{Y - Y_{min}}{Y_{max} - Y_{min}} \right)^2 (0.65\%)^2 + (0.27\%)^2 \right]^{1/2} \quad \text{(B-6)}$$

where

Y	=	measured signal in engineering units
S_Y	=	standard deviation of Y
Y_{max}	=	maximum output signal
Y_{min}	=	minimum output signal
Y_{max}-Y_{min}	=	span of output signal.

The total transducer measurement uncertainty, excluding the systematic measurement error, can be estimated by combining the uncertainty in the calibration and the uncertainty associated with the data acquisition system. The "total error" is given to be the square root of the sum of the squares of these two errors. Table B-I summarizes the data system error, calibration error, and the resultant total error for each of the transducers that functioned during the test.

4. REFERENCES

B-1. M. G. Natrella, *Experimental Statistics National Bureau of Standards Handbook 91*, U.S. Government Printing Office, 1963.

B-2. W. J. Quapp et al, *Irradiation Effects Test Series Test IE-1 Test Results Report*, TREE-NUREG-1046 (March 1977).

B-3. W. J. Quapp et al, *Irradiation Effects Test Series Scoping Test 2 Test Results Report*, TREE-NUREG-1044 (September 1977).

B-4. L. C. Farrar et al, *Irradiation Effects Test Series Test IE-3 Test Results Report*, TREE-NUREG-1106 (September 1977).

B-5. W. J. Quapp et al, *Irradiation Effects Test Series Scoping Test 1 Test Results Report*, TREE-NUREG-1066 (September 1977).

THIS PAGE

WAS INTENTIONALLY

LEFT BLANK

APPENDIX C

DATA REDUCTION AND EVALUATION

THIS PAGE

WAS INTENTIONALLY

LEFT BLANK

APPENDIX C

DATA REDUCTION AND EVALUATION

All data for Test IE-5 were recorded on the PBF Surveillance System[a] in an analog format and then were digitized by the PBF PDP-15 data reduction facility. The resulting digital data were processed on an IBM 360, using the MAC/RAN Time Series Analysis Program[C-2], and permanently stored on seven-track magnetic tapes in the MAC/RAN SIDU (Standard Input Data Unit) format.

During the processing on the IBM 360, several data reductions steps were completed:

(1) Data were converted from data system volts to engineering units (SI) using the calibration presented in Appendix A

(2) Any wild points were removed

(3) Zero power offsets due to data system drift were removed from coolant ΔT data channels

(4) SPND data were converted from detector nanoamps to neutron flux

(5) Rod internal pressure data were corrected for large drifts due to instrument decalibration.

1. REDUCED DATA FORMAT

Three separate sets of data are stored on tape in the form of:

(1) Data system volts

(2) Engineering units (SI) obtained by applying calibration equations tabulated in Appendix B

(3) A set reduced from (2) with calculated parameters added for additional calculations and plotting.

---

[a] The Surveillance System is an FM mulitplexed data recording system that records channels of analog data plus a standard time code (IRIG-A) on magnetic tape[C-1].

Each data channel of the first two sets contains approximately 25,000 data values with variable digitizing intervals ranging from 10 s down to 0.2 s[a]. Table C-I shows the digitizing intervals used.

TABLE C-I

DIGITIZING INTERVALS USED FOR DATA REDUCTION IN TEST IE-5

Time Period[a] (s)	Phase Test	Digitizing Interval (s)
0-109,520	Preconditioning	10.0
119,350-144,490	Power Ramp	2.0
144,520-148,060	Steady State Operation at 65 kW/m	4.0
148,107-148,840	Flow Reduction	0.2
148,870-166,610	After Shutdown	10.0

[a] The time corresponds to time on Figure 7 where time of zero designates the beginning of the first power increase.

The third data set was numerically filtered and reduced by a factor of 13 to give approximately 2000 points per channel. Several calculated parameters were added to the original data channels including:

(1) Results from SPND data: (a) axial local power, (b) average neutron flux, (c) peak elevation, and (d) peak to average (see Appendix D)

(2) Average rod power for each rod, calculated from thermal-hydraulic data (Appendix D)

(3) Coolant mass flux for each rod, calculated using ASTEM[C-3] water properties and inlet temperatures,

[a] As the data were digitized, they were filtered with a low pass filter whose cutoff frequency corresponds to the Nyquist frequency ($1/2\Delta T$).

In the SIDU format, each data channel has a unique number and eight character names. All of the data channels available are listed in Table C-II. The data channels are shown in Figures C-1 through C-11.

TABLE C-II

DATA CHANNEL FORMAT FOR TEST IE-5

Comments	Transducer Name	Rod Number	Elevation (m)	Serial Number	Azimuthal Orientation (Degrees)	Data System Channel Number	Reduced Tape Number	Channel ID	Units
Corrected for zero shift	Fuel Rod PxD	IE-019	--	531	--	9-3	34	RODPRS11	MPA
	Centerline Thermocouple	IE-019	0.739	578		10-3	38	FULTMP11	K
	Cladding Thermocouple	IE-019	0.644	07-07	45°	11-3	42	CLDTMP11	K
	Cladding Thermocouple	IE-019	0.646	07-09	225°	11-4	43	CLDTMP12	K
Corrected for zero shift	Coolant Δ T	IE-019	--	452	--	6-1	20	DELTMP11	K
	Flowmeter	IE-019	--	10104	--	7-1	24	FLORAT11	cm^3/s
	LVDT	IE-019	--	427	--	8-1	28	CLDDSP11	mm
Corrected for zero shift	Fuel Rod PxD	IE-020	--	527	--	9-4	35	RODPRS21	MPa
	Centerline Thermocouple	IE-020	0.739	579	--	10-4	39	FULTMP21	K
Failed during preconditioning	Cladding Thermocouple	IE-020	0.641	117607	45°	13-1	44	CLDTMP21	K
	Cladding Thermocouple	IE-020	0.646	117606	225°	13-2	45	CLDTMP22	K

TABLE C-II (continued)

Comments	Transducer Name	Rod Number	Elevation (m)	Serial Number	Azimuthal Orientation (Degrees)	Data System Channel Number	Reduced Tape Number	Channel ID	Units
Corrected for zero shift	Coolant Δ T	IE-020	--	453	--	6-2	21	DELTMP21	K
	Flowmeter	IE-020	--	10102	--	7-2	25	FLORAT21	cm^3/s
	LVDT	IE-020	--	428	--	8-2	29	CLDDSP21	mm
Corrected for zero shift	Fuel Rod PxD	IE-021	--	528	--	10-1	36	RODPRS31	MPa
Failed during high power steady state operation	Centerline Ultrasonic Thermometer	IE-021	0.637	588	--	11-1	40	FULTMP31	K
	Cladding Thermocouple	IE-021	0.643	117604	45°	13-3	46	CLDTMP31	K
	Cladding Thermocouple	IE-021	0.643	117609	225°	13-4	47	CLDTMP32	K
Corrected for zero shift	Coolent Δ T	IE-021	--	454	--	6-3	22	DELTMP31	K
	Flowmeter	IE-021	--	10101	--	7-3	26	FLORAT31	cm^3/s
	LVDT	IE-021	--	429	--	8-3	30	CLDOSP31	mm
Corrected for zero shift	Fuel Rod PxD	IE-022	--	420	--	10-2	37	RODPRS41	MPa
Failed during high power steady state operation	Centerline Ultrasonic Thermometer	IE-022	0.637	489	--	11-2	41	FULTMP41	K

TABLE C-II (continued)

Comments	Transducer Name	Rod Number	Elevation (m)	Serial Number	Azimuthal Orientation (Degrees)	Data System Channel Number	Reduced Tape Number	Channel ID	Units
Failed during preconditioning	Cladding Thermocouple	IE-022	0.538	117617	135°	14-1	48	CLDTMP41	K
	Cladding Thermocouple	IE-022	0.641	117618	45°	14-2	49	CLDTMP42	K
	Cladding Thermocouple	IE-022	0.641	117615	225°	14-3	50	CLDTMP43	K
	Cladding Thermocouple	IE-022	0.743	117616	315°	14-4	51	CLDTMP44	K
Corrected for zero shift	Coolant Δ T	IE-022	--	455	--	6-4	23	DELTMP41	K
	Flowmeter	IE-022	--	10103	--	7-4	27	FLORAT41	cm^3/s
	LVDT	IE-022	--	431	--	8-4	31	CLDDSP41	mm
	SPND 1	--	0.1588	55209	--	3-2	9	NTFLUX01	neutrons/cm^2·s
	SPND 2	--	0.3152	55206	--	3-3	10	NTFLUX02	neutrons/cm^2·s
	SPND 3	--	0.4717	55208	--	3-4	11	NTFLUX03	neutrons/cm^2·s
	SPND 4	--	0.6281	55204	--	4-1	12	NTFLUX04	neutrons/cm^2·s
	SPND 5	--	0.7846	56082	--	4-2	13	NTFLUX05	neutrons/cm^2·s
	SPND 6	--	0.1588	53964	--	4-3	14	NTFLUX06	neutrons/cm^2·s
	SPND 7	--	0.3152	53979	--	4-4	15	NTFLUX07	neutrons/cm^2·s
	SPND 8	--	0.4717	53968	--	5-1	16	NTFLUX08	neutrons/cm^2·s

TABLE C-II (continued)

Comments	Transducer Name	Rod Number	Elevation (m)	Serial Number	Azimuthal Orientation (Degrees)	Data System Channel Number	Reduced Tape Number	Channel ID	Units
Corrected for zero shift	SPND 9	--	0.6281	52721	--	5-2	17	NTFLUX09	neutrons/cm^2·s
	SPND 10	--	0.7846	52768	--	5-3	18	NTFLUX10	neutrons/cm^2·s
	Loop Flowmeter	--	--	--	--	2-3	6	LOPFLO01	cm^3/s
	SLP-1	--	--	--	--	1-4	3	RECPOW01	MW
	Fission Break	--	--	--	--	3-1	8	FISREL01	Log_{10}(R/hr)
	Monitor								
	PPS #1	--	--	--	--	1-3	2	RECPOW02	MW
	PPS #2	--	--	--	--	2-1	4	RECPOW03	MW
0-1.67 x 10^5	(Time)	--	--	--	--	12-1 thru 12-4	1	TIME	s
Decalibrated	Coolant Pressure	--	--	158	--	5-4	19	SYSPRS01	MPa
Decalibrated	Loop IPT Inlet Pressure	--	--	--	--	2-4	7	LØPPRS01	MPa
	Inlet Thermocouple	--	--	450	--	9-1	32	INTEMP01	K
	Inlet Thermocouple	--	--	451	--	9-2	33	INTEMP02	K
	IPT Pressure	--	--	--	--	2-2	5	IPT-DP01	--

TABLE C-II (continued)

Comments	Transducer Name	Rod Number	Elevation (m)	Serial Number	Azimuthal Orientation (Degrees)	Data System Channel Number	Reduced Tape Number	Channel ID	Units
Decalibrated (continued)	(Local Peaking Factor)	--	0.013	--	--	--	52	AXFLUX01	--
	(Local Peaking Factor)	--	0.159	--	--	--	53	AXFLUX02	--
	(Local Peaking Factor)	--	0.306	--	--	--	54	AXFLUX03	--
	(Local Peaking Factor)	--	0.452	--	--	--	55	AXFLUX04	--
	(Local Peaking Factor)	--	0.521	--	--	--	56	AXFLUX05	--
	(Local Peaking Factor)	--	0.599	--	--	--	57	AXFLUX06	--
	(Local Peaking Factor)	--	0.662	--	--	--	58	AXFLUX07	--
	(Local Peaking Factor)	--	0.724	--	--	--	59	AXFLUX08	--
	(Local Peaking Factor)	--	0.745	--	--	--	60	AXFLUX09	--
	(Local Peaking Factor	--	0.892	--	--	--	61	AXFLUX10	--
	(Average Neutron Flux)	--	--	--	--	--	52	FLUXAVER	neutrons/$cm^2 \cdot s$

TABLE C-II (continued)

Comments	Transducer Name	Rod Number	Elevation (m)	Serial Number	Azimuthal Orientation (degrees)	Data System Channel Number	Reduced Tape Number	Channed ID	Units
Decalibrated (continued)	(Elevation or Peak)	--	--	--	--	--	63	FLXMXELV	m
	(Peak to Average)	--	--	--	--	--	64	FLUXMAX	--
Peak = 1.338 Average	(Average Rod Power)	IE-019	--	--	--	--	65	RODWR01	kW/m
	(Average Rod Power)	IE-020	--	--	--	--	66	RODPWR02	kW/m
	(Average Rod Power)	IE-021	--	--	--	--	67	RODPWR03	kW/m
	(Average Rod Power)	IE-022	--	--	--	--	68	RODPWR04	kW/m
(Average of all four rods)	(Average Rod Power)	--	--	--	--	--	69	RODPWRAV	kW/m
	(Standard deviation of rod power)	--	--	--	--	--	70	RODPWRSD	kW/m
	(Mass flux)	IE-019	--	--	--	--	71	MASFLX01	$kg/s \cdot m^2$
	(Mass flux)	IE-020	--	--	--	--	72	MASFLX02	$kg/s \cdot m^2$
	(Mass flux)	IE-021	--	--	--	--	73	MASFLX03	$kg/s \cdot m^2$
	(Mass flux)	IE-022	--	--	--	--	74	MASFLX04	$kg/s \cdot m^2$
(Average of all four rods)	(Mass flux)	--	--	--	--	--	75	MASFLXAV	$kg/s \cdot m^2$

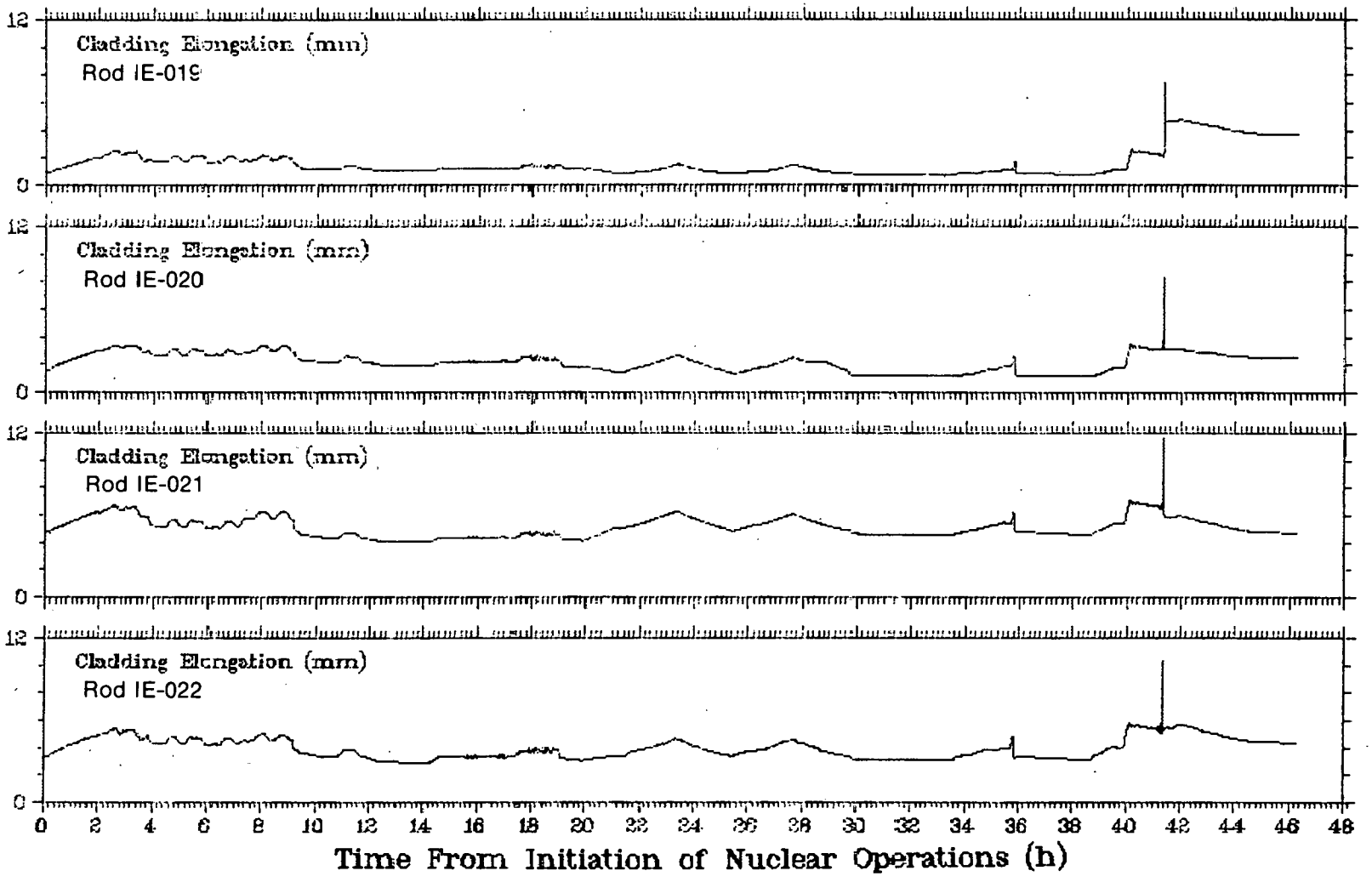

Fig. C-1 Cladding elongation for all four rods during Test IE-5.

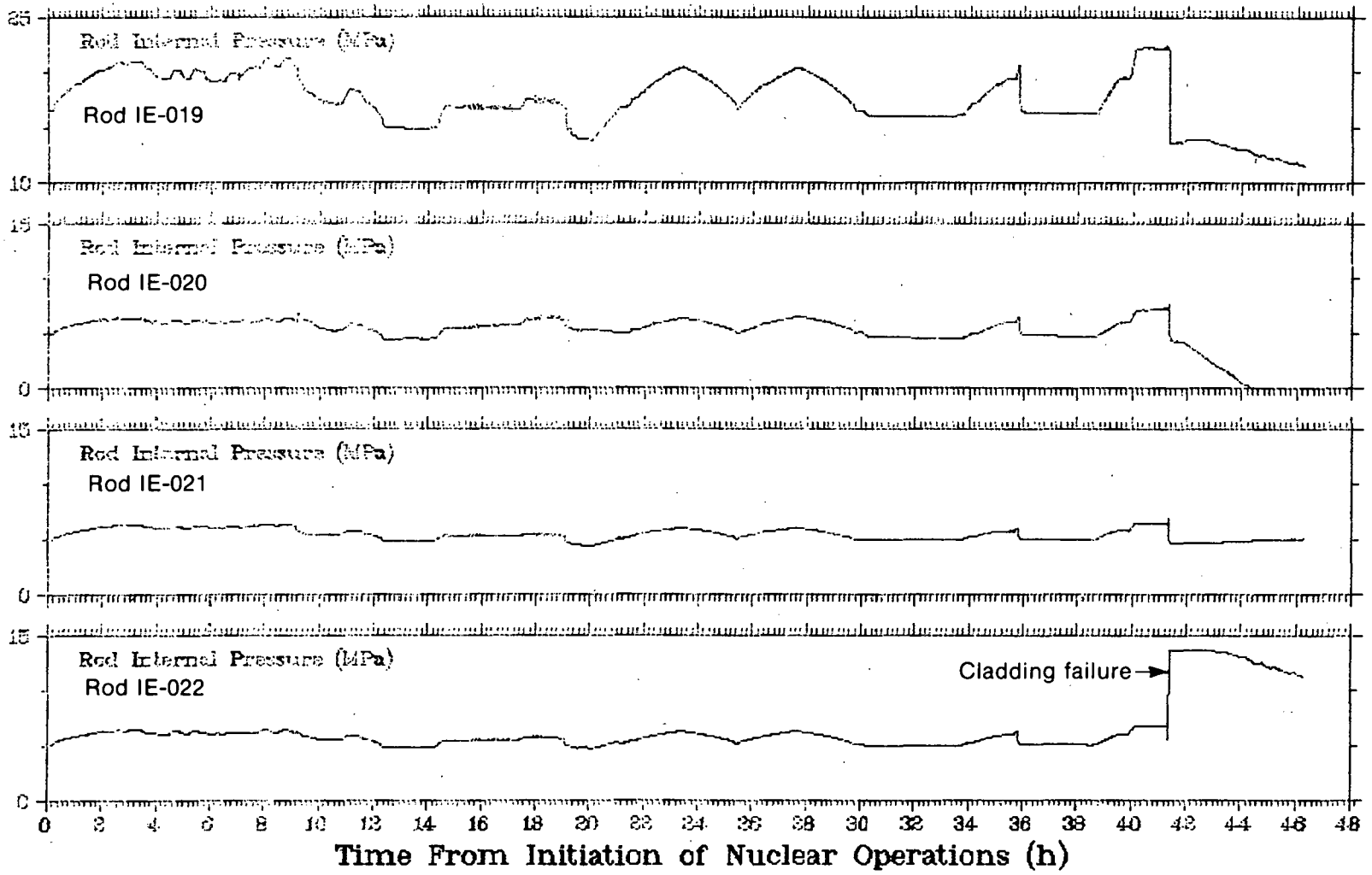

Fig. C-2 Fuel rod internal pressure for all four rods during Test IE-5.

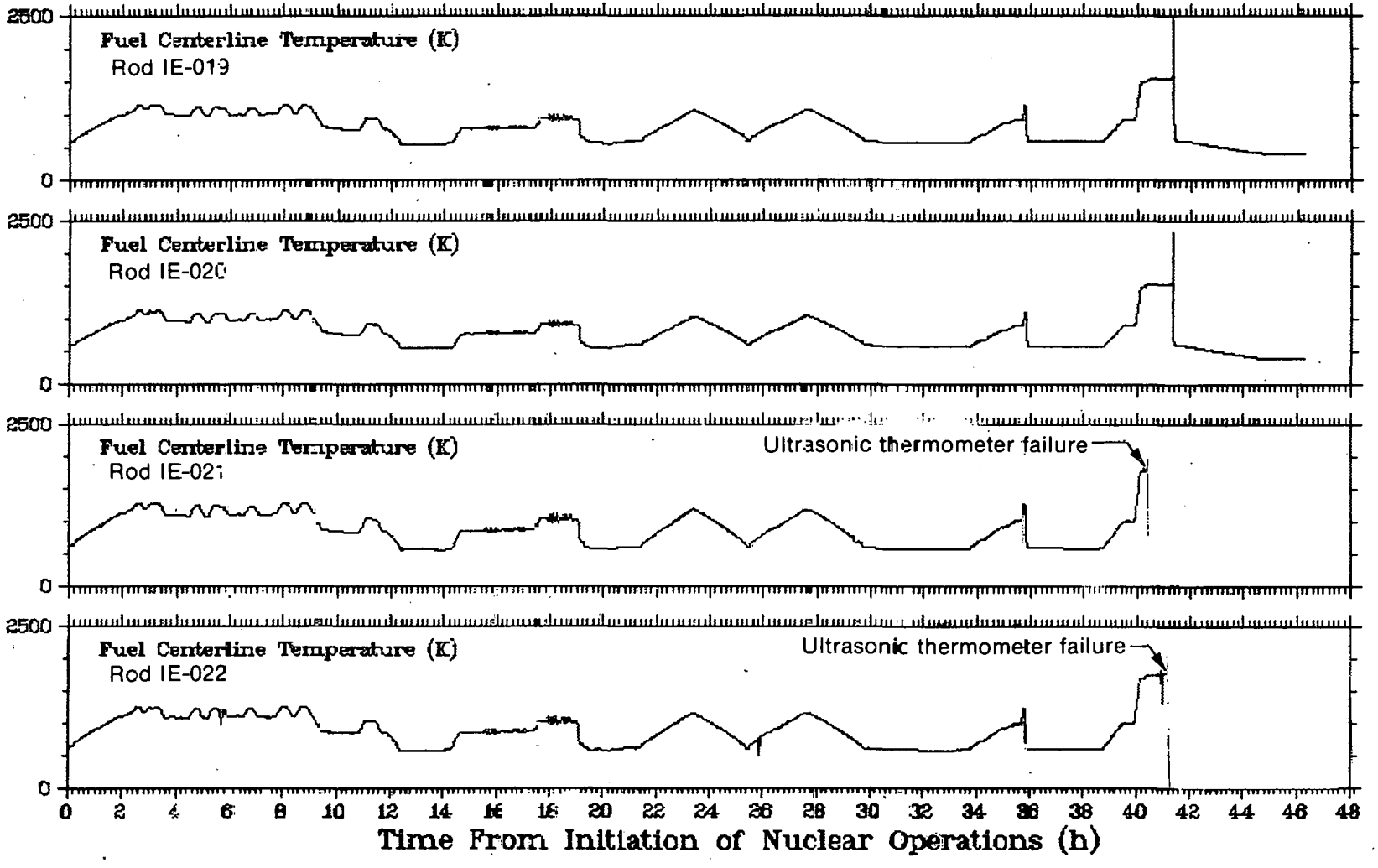

Fig. C-3 Fuel centerline temperature for all four rods during Test IE-5.

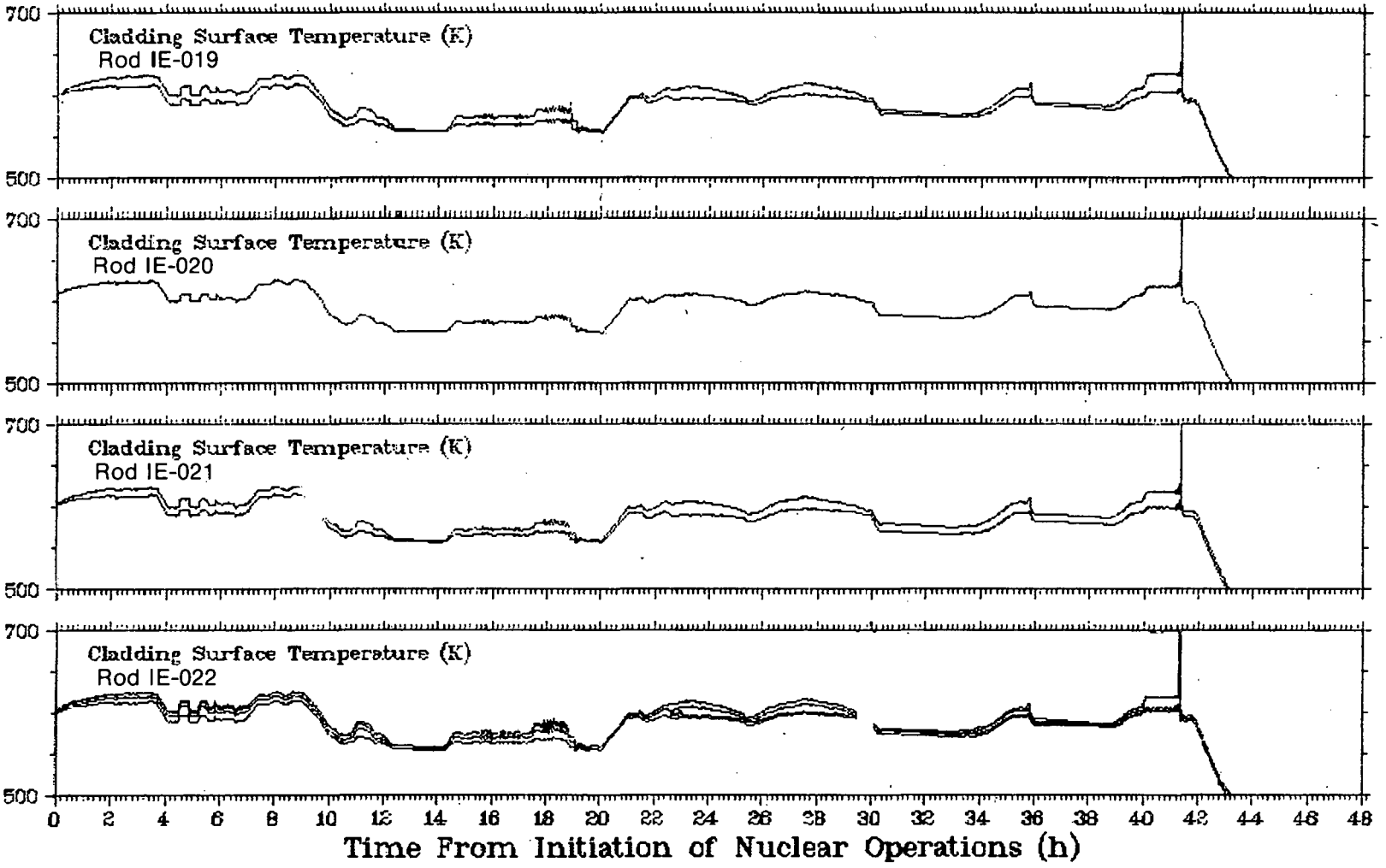

Fig. C-4 Cladding surface temperature for all four rods during Test IE-5.

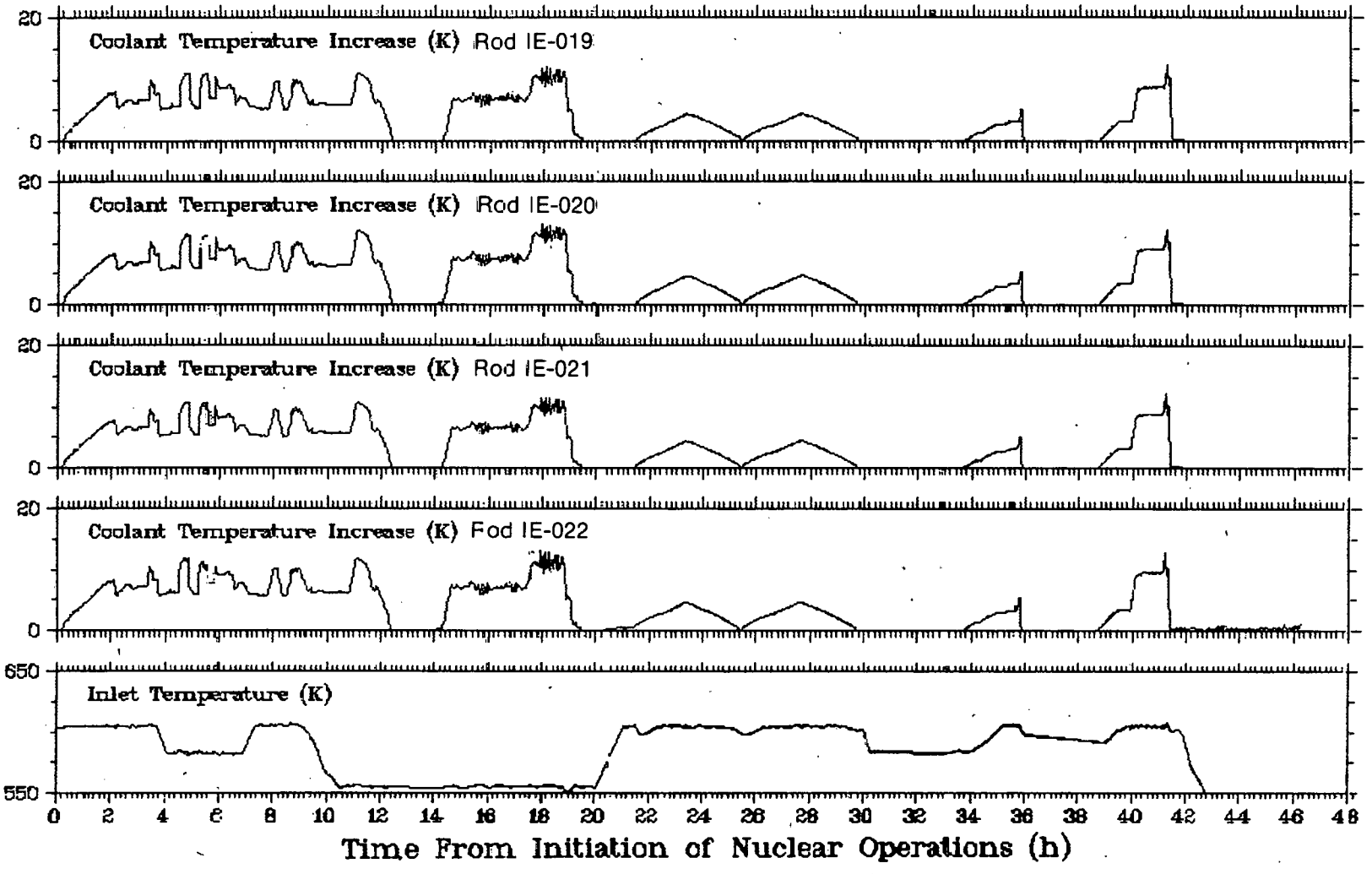

Fig. C-5 Coolant inlet temperature and coolant temperature increase for all four rods during Test IE-5.

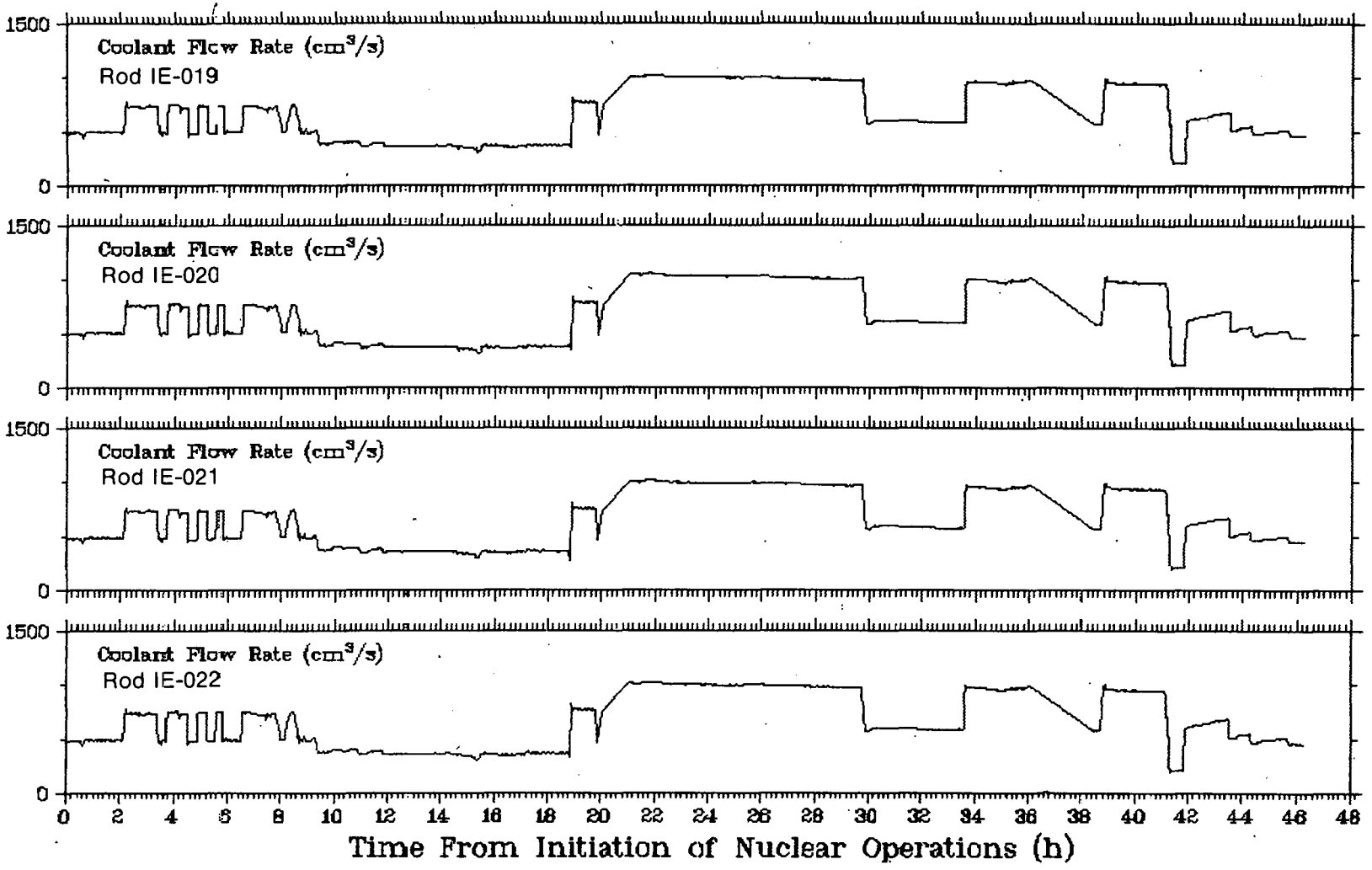

Fig. C-6 Coolant flow rate for all four rods during Test IE-5.

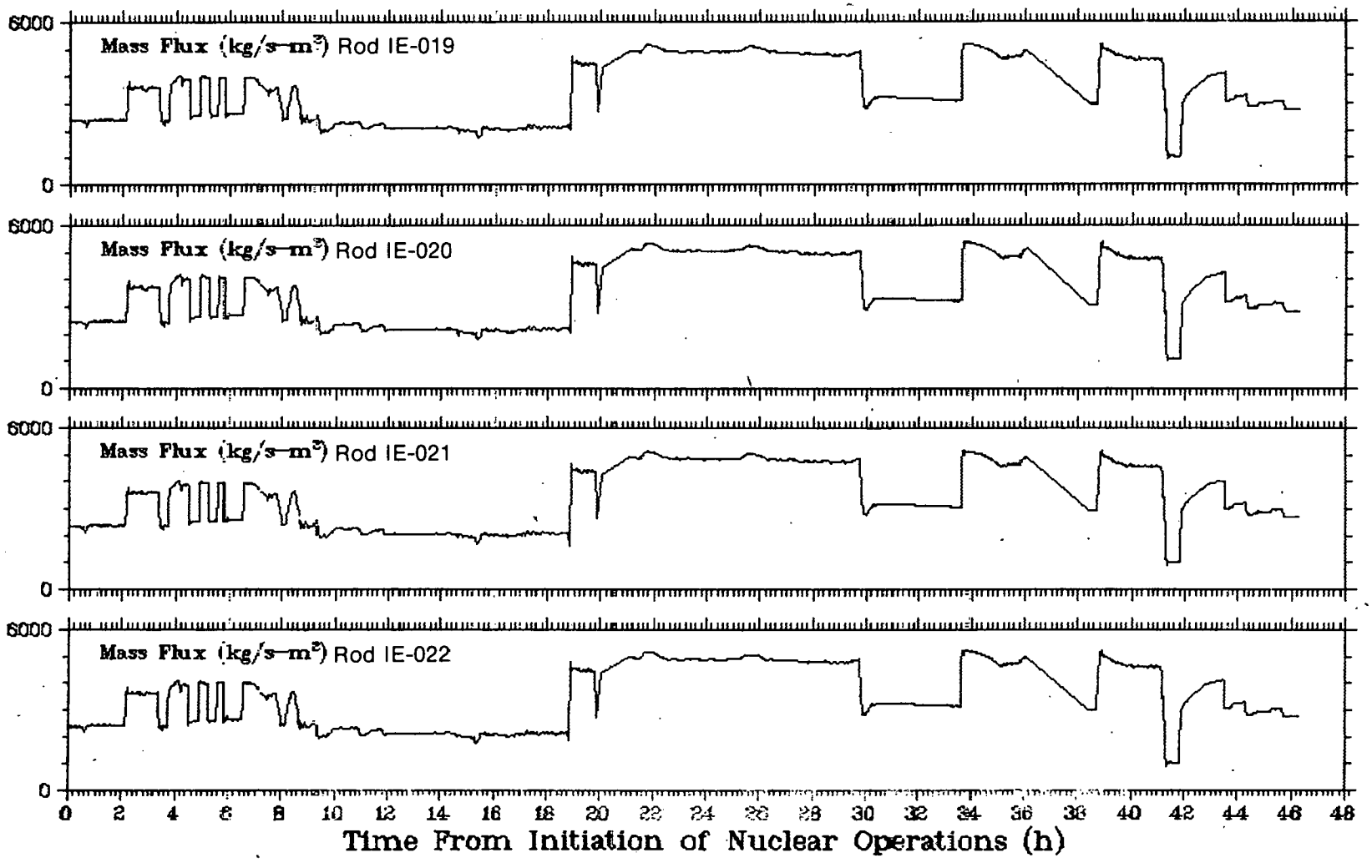

Fig. C-7 Coolant mass flux for all four rods during Test IE-5.

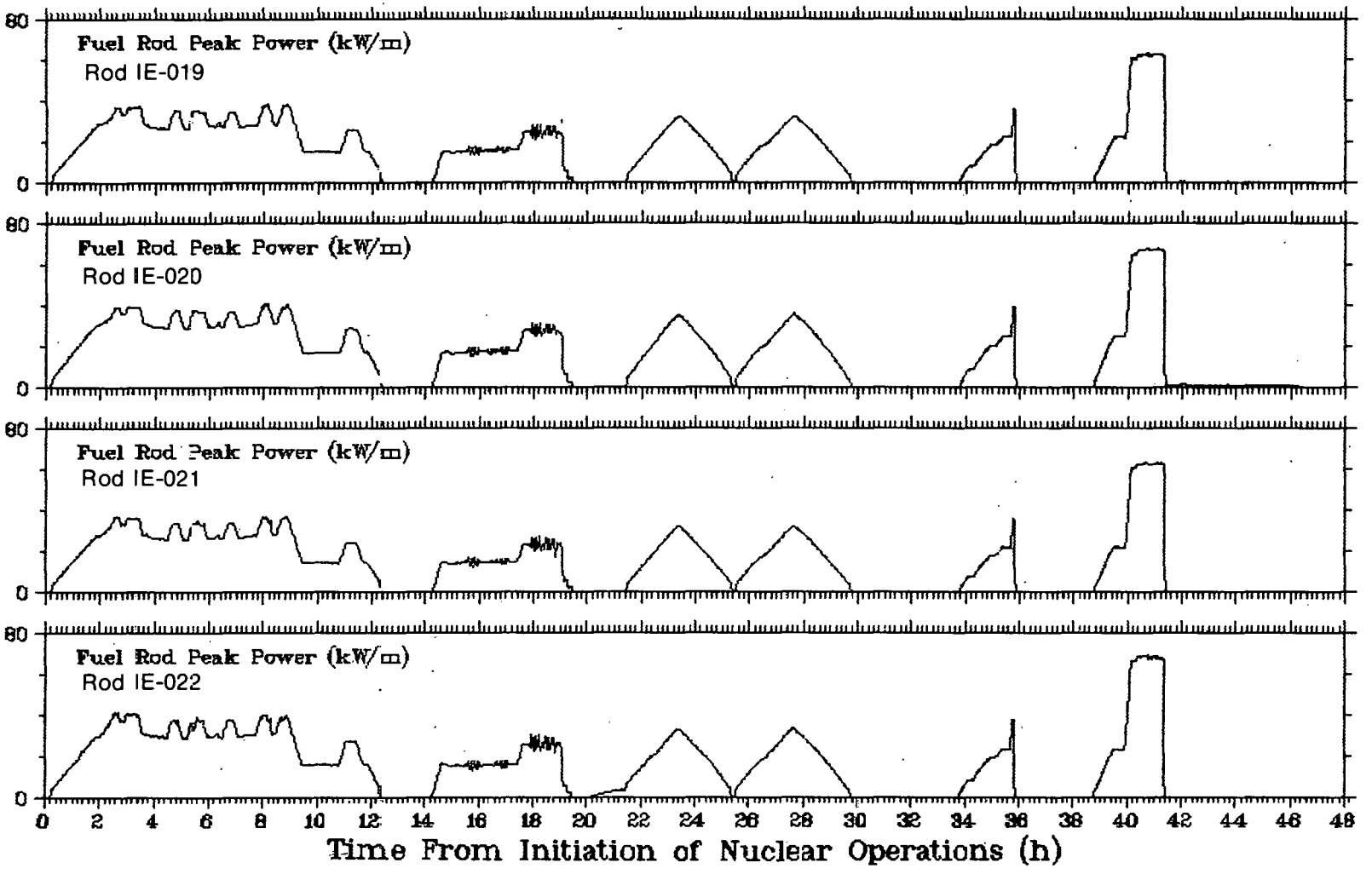

Fig. C-8 Fuel rod peak power for all four rods during Test IE-5.

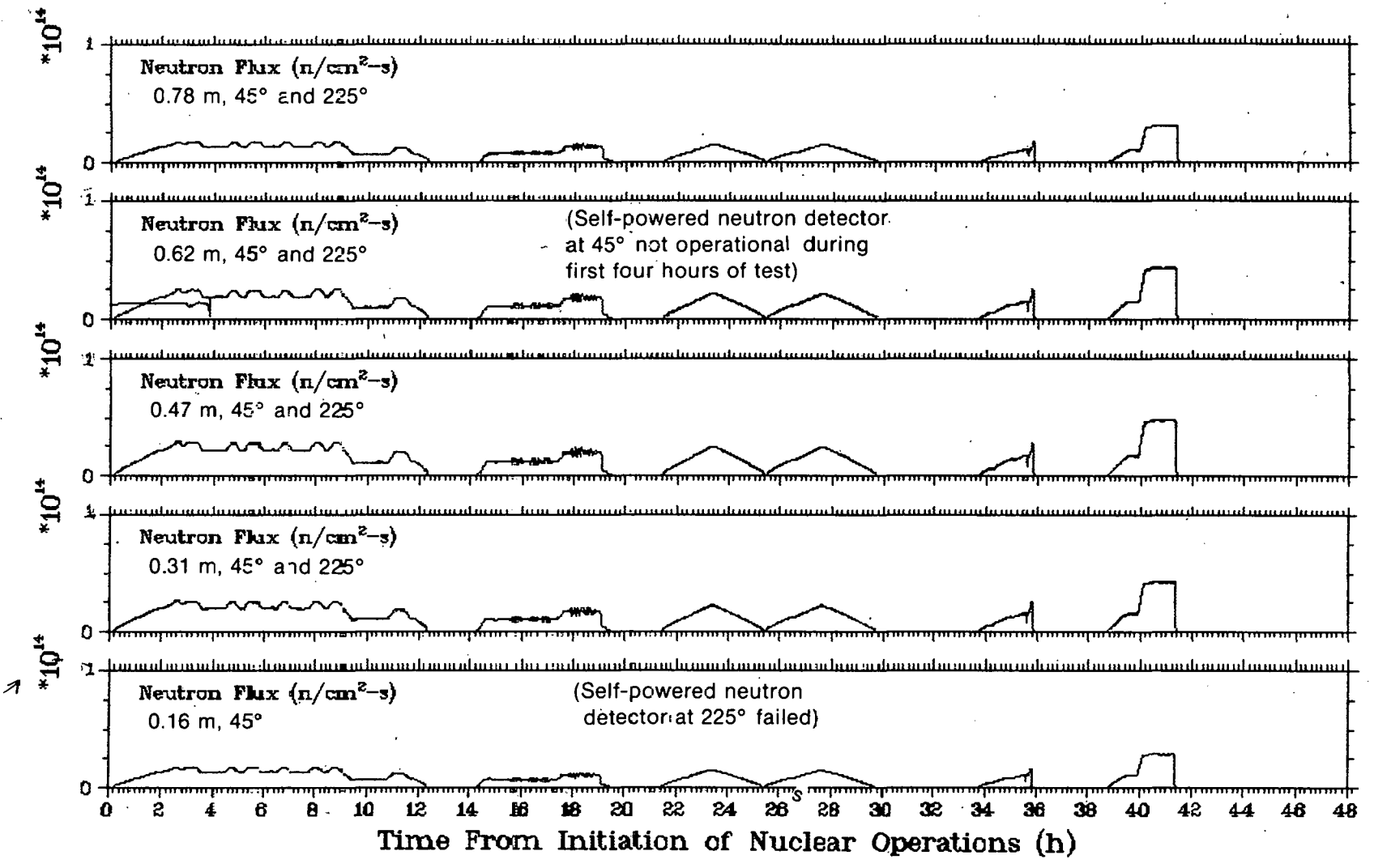

Fig. C-9 Neutron flux at several axial locations during Test IE-5.

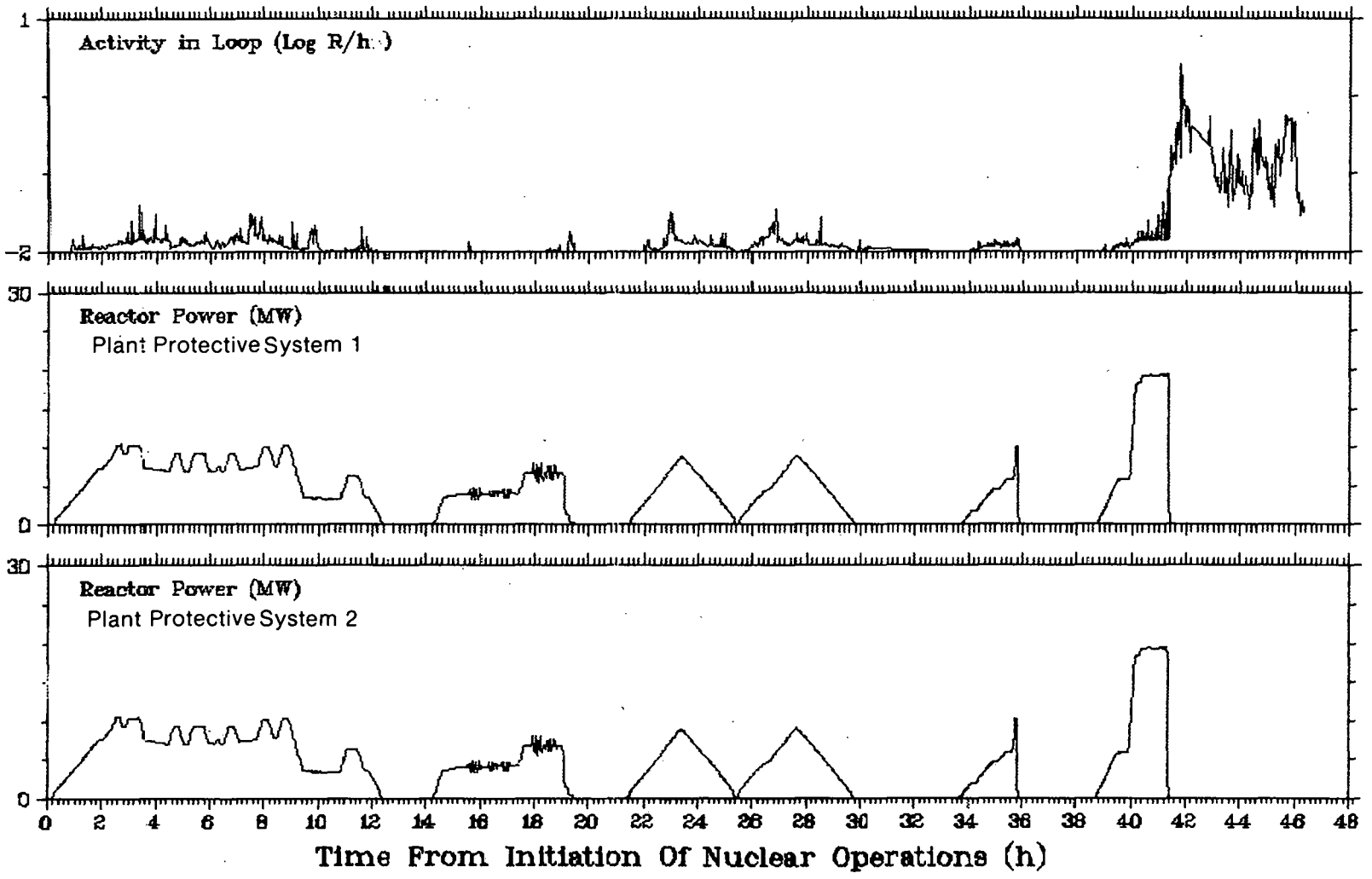

Fig. C-10 Reactor power and loop fission activity during Test IE-5.

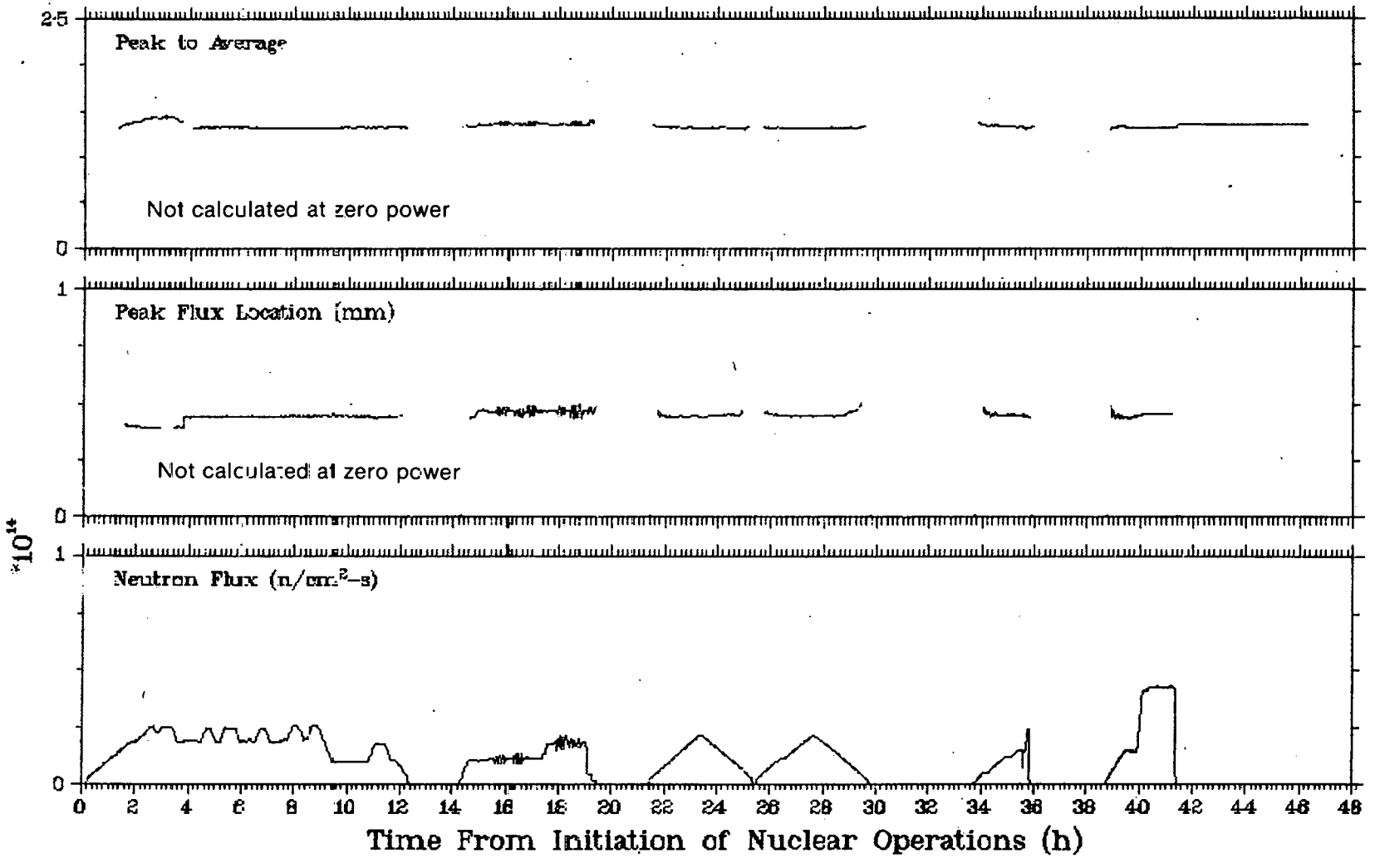

Fig. C-11 Peak to average, peak elevation, and average neutron flux during Test IE-5.

2. DATA REDUCTION

Corrections were applied to some of the channels to eliminate obvious errors in the data. Each of the corrections are discussed below. The first correction was wild point removal. During the digitizing process, particularly at the beginning or end of an analog tape, wild points were sometimes introduced into the data. Most of these points were removed using the MAC/RAN processor following conversion to engineering units.

The second step was elimination of zero power offsets in coolant ΔT data. These transducers have a very small output. Therefore, the signals must be recorded through high gain amplifiers. For this reason, these transducers are subject to small electronic zero drifts. This zero shift was corrected by adding an offset to the data so that the temperature rise is zero at zero reactor power. The constants that were applied are shown in Table C-III.

TABLE C-III

ZERO POWER OFFSET CORRECTIONS APPLIED TO DIFFERENTIAL THERMOCOUPLE CHANNELS FOR FIRST AND SECOND HALVES OF TEST IE-5

		Corrections[a]	
Instrument	Rod	0-75600 s	75600-166610 s
SN 452	IE-019	-0.4	-0.4
SN 453	IE-020	-0.122	-0.122
SN 454	IE-021	-0.38	-0.6
SN 455	IE-022	-0.35	-0.6

[a] These corrections were added to the data so that the average instrument signals at zero power were zero.

The SPND data were then converted from detector nanoamps to neutron flux. The conversion factors were determined from comparisons of the SPNDs and a cobalt wire mounted in the Test IE-5 hardware. The fluence was then determined from a gamma scan of the cobalt wire. Neutron flux was calculated by dividing the fluence by the time at power. A conversion between individual SPND output and neutron flux was found by dividing the neutron flux at each SPND elevation by a corresponding SPND current. The conversion factors are tabulated in Table C-IV.

TABLE C-IV

CONVERSION FACTORS RELATING SPND CURRENT AND NEUTRON FLUX IN TEST IE-5

Instrument	Conversion Factor[a] (10^{20} neutrons/cm^2·s per ampere)
SPND 1	3.473
SPND 2	3.712
SPND 3	3.862
SPND 4	4.002
SPND 5	4.194
SPND 6	Failed
SPND 7	3.457
SPND 8	3.714
SPND 9	3.905
SPND 10	3.996

[a] The SPND data were multiplied by this constant to produce neutron flux.

Rod internal pressure data were also corrected for zero shifts due to decalibration of the pressure transducers. The correction was determined using the results of a multiple regression analysis of the data. The model chosen for the regression was determined as follows.

The pressure of the fill gas should be described fairly well using the perfect gas equation,

$$P = \rho RT \qquad \text{(C-1)}$$

where

P = gas pressure (MPa)

ρ = gas density (kg/m^3)

R = gas constant (m^3/kg·K)

T = temperature (K).

The measured pressure (P_m) was assumed to be

$$P_m = P + bt + b_1 t^2 + C \quad \text{(C-2a)}$$

or

$$P_m = \rho RT + bt + b_1 t^2 + C \quad \text{(C-2b)}$$

where

b and b_1 = quadratic time drift coefficients

t = time from start of test (s)

C = zero shift from the time of pressurization of the rod to the start of the test.

Since the average temperature of the gas cannot be measured, it has been assumed to be a quadratic function of average fuel rod power as

$$T = T_{in} + d\,\Phi + d_1\,\Phi^2 \quad \text{(C-3)}$$

where

Φ = average fuel rod power (kW/m)

d and d_1 = quadratic power coefficients

T_{in} = inlet temperature (K).

When Equation (C-3) is substituted into (C-2b) and a general set of coefficients applied, the measured pressure is

$$P_m = a_o + a_1\,\Phi + a_2\,\Phi^2 + a_3 T_{in} + a_4 t + a_5 t^2 \quad \text{(C-4)}$$

where

a_o = C

a_1 = ρRd

a_2 = ρRd

$a_3 = \rho R$

$a_4 = b$

$a_5 = b_1$

The first coefficient, a_o, was determined by using the cold (300 K) fill pressure adjusted to hot (606 K) conditions at the start of the test, i.e.

$$a_o = P_m - P = P_m - P_{cold}\left(\frac{606}{300}\right). \quad \text{(C-5)}$$

A multiple regression analysis was then used to determine the remainder of the coefficients. The analysis was made using data from the first power ramp and the last two cycles of the preconditioning phase. This was done to avoid highly transient data such as the gap conductance segment and the power ramp. The results of this analysis are given in Table C-V.

The corrected pressure (P) was then calculated for the entire test using

$$P = P_m - a_o - a_4 t - a_5 t^2. \quad \text{(C-6)}$$

The corrected pressure is presented in the text.

TABLE C-V

MULTIPLE REGRESSION ANALYSIS RESULTS FOR TEST IE-5 FUEL ROD INTERNAL PRESSURE

	Regression Equation Coefficients[a]					
Rod	a_0	a_1	a_2	a_3	a_4	a_5
IE-019	2.60 2.69	0.198	-0.171×10^{-2}	0.282×10^{-1}	0.944×10^{-4}	-0.337×10^{-10}
IE-020	1.30 2.13	0.601×10^{-1}	-0.386×10^{-3}	0.264×10^{-1}	-0.211×10^{-5}	0.338×10^{-10}
IE-021	0.70 0.04	0.555×10^{-1}	-0.530×10^{-3}	0.110×10^{-2}	0.335×10^{-6}	-0.920×10^{-11}
IE-022	0.64 0.79	0.586×10^{-1}	-0.517	0.836	-0.799	0.873

[a] The regression analysis model was $P_m = a_1 \Phi + a_2 \Phi^2 + a_3 T_{in} + a_3 T_{in} + a_4{}^t + a_5 t^5$ where a_o was determined using cold fill pressure.

3. COORDINATE TRANSFORMATION

Coordinate transformations were used in some of the cladding elongation and rod internal pressure plots. These were not data corrections because no changes were made to the data. They were made, particularly in the case of comparisons with FRAP-T4[C-4] results, to minimize the effects of small uncertainties in transducer output or to eliminate the effect of heating the fuel rods to test conditions prior to nuclear operation.

For the pressure transducer, the transformations minimize the uncertainties in transducer zero shift prior to the test [a_o in Equation (C-4)] and to minimize the slight differences in fill gas pressure between the rods. The first transformation was applied as follows. At operating temperatures, prior to an increase in fuel rod power (at time = 0), the corrected pressure is

$$P_o = \rho_o R T_o + a_o^* - a_o \qquad \text{(C-7)}$$

where

P_o = corrected pressure at zero power under hot conditions at start of the test (MPa)

ρ_o = initial gas density (kg/m^3)

T_o = rod temperature at the start of the test (605 K)

a_o^* = actual difference between measured and hot pressure.

The quantity $a_o^* - a_o$ should be zero if the hot pressure is determined exactly in Equation (C-5). If pressure data is presented in terms of pressure differences, ie.

$$P - P_o = \rho R T - \rho_o R T_o \qquad \text{(C-8)}$$

the offset prior to the test ($a_o^* - a_o$) is eliminated. Therefore, the difference in corrected pressure is equal to the difference in actual pressure. Of course, if there were no uncertainties involved in calculating in Equation (C-5), this would be unnecessary since P_m in Equation (C-6) would equal the actual pressure. However, with this transformation all the pressure differences are equal,

$$P_m - P_o(\text{measured}) = P\ (\text{actual}) - P_o(\text{actual}) \doteq P - P_o\ . \qquad \text{(C-9)}$$

The second transformation minimizes the effects of slight differences in the initial fill gas pressure of the rods. If Equation (C-8) is divided by P_o, the following is obtained when $a_o^* - a_o$ is zero

$$\frac{P - P_o}{P_o} = \frac{\rho T}{\rho_o T_o} - 1 . \qquad \text{(C-10a)}$$

If written in terms of void volume (V_o) and change in void volume (ΔV_o), it is

$$\frac{P - P_o}{P_o} = \frac{V_o}{V_o + \Delta V_o} \left(\frac{T}{T_o}\right) - 1 . \qquad \text{(10b)}$$

Therefore, if the void volume or initial fill gas pressure is slightly different for each rod (P_o and V_o for each rod) that difference is minimized. Using the coordinate transformation of Equation (C-10b), only the changes in gas temperature and void volume are important. The P_o's for each rod are given in Table C-VI.

TABLE C-VI

TEST IE-5 REFERENCE INITIAL CLADDING STRAINS AND ROD INTERNAL PRESSURES[a]

Rod	Initial Pressure (P_o) (MPa)	Initial Elongation (ΔL_o) (mm)	Initial Cladding Strain, ε_o (10^{-3} mm/mm)
IE-019	16.60	0.806	0.83
IE-020	5.00	1.130	1.16
IE-021	5.00	4.740	4.89
IE-022	5.12	3.330	3.43
IE-019 (FRAP-T4)[b]	16.84	1.418	1.46
IE-020 (FRAP-T4)	5.00	1.418	1.46
IE-021 (FRAP-T4)	5.00	1.418	1.46

[a] 605 K, zero power.

[b] See Appendix E for a discussion of the fuel rod behavior model FRAP-T4.

A transformation was also applied to the cladding elongation data. Cladding thermal strain, referenced to the cold rod temperatures, can be written

$$\epsilon = \alpha\ (T-T_{in}) + \alpha_o\ (T_{in}-T_{cold}) \qquad \text{(C-11)}$$

where

ϵ = strain = cladding elongation divided by initial cladding length

α = expansion coefficient of the cladding during the test (during PCI it will be a combination of both the fuel expansion and cladding expansion coefficients)

α_o = expansion coefficient of the cladding during heat up and changes in inlet temperature

T = temperature of the cladding

T_{in} = inlet temperature

T_{cold} = cold temperature (300 K).

Defining an initial strain at the start of the test,

$$\epsilon_o = \alpha_o\ (T_o - T_{cold}) \qquad \text{(C-12)}$$

the difference is

$$\epsilon - \epsilon_o = \alpha\ (T - T_{in}) + \alpha_o\ (T_{in} - T_o)\ . \qquad \text{(C-13)}$$

In this form, effects of growth during heatup have been eliminated and the effects of changes in inlet temperature [$\alpha_o (T_{in} - T_o)$] have been isolated. For actual cladding growth, α_o is the expansion coefficient for the cladding, but for the measured growth it is not. The LVDTs are mounted in the test assembly which also grows during heatup and inlet temperature increases. The hardware is mostly zircaloy so that the measured growth is approximately zero. Thus, for the measured values of strain, α_o is approximately zero. If it is not exactly zero, expressing cladding strain in terms of Equation (C-13) minimizes the effect of hardware growth, since ($T_{in} - T_o$) is small (<10 K), except for the gap conductance testing. This is particularly important in the case of comparisons with FRAP-T4 since α_o is not zero in the calculations. The test assembly is not modeled in FRAP so the α_o used in the calculations is the actual expansion coefficient.

Cladding elongation data are presented in terms of a length change, $\Delta L - \Delta L_0$ (in mm), and a change in strain (in %) given by

$$\epsilon - \epsilon_o = \frac{\Delta L - \Delta L_o}{L} \qquad \text{(C-14)}$$

where

ϵ = cladding strain

ϵ_o = cladding strain at the start of the nuclear portion of the test shown in Table C-VI

ΔL = cladding elongation

ΔL_o = cladding elongation at the start of the test

L = cladding cold length (970 mm).

4. REFERENCES

C-1. W. J. Quapp et al, *Irradiation Effects Test Series Scoping Test 1 Test Results Report*, TREE-NUREG-1066 (September 1977).

C-2. R. K. Otnes (ed.), *References Manual: MAC/RAN III-Time Series Data Analysis System*, Agababian Associates (1973).

C-3. K. W. Moore, *ASTEM – A Collection of FORTRAN Subroutines to Evaluate the 1967 ASME Equations of State for Water/Steam and Derivatives of these Equations*, ANCR-1026 (October 1971).

C-4.[a] J. A. Dearien et al, *FRAP-T2: A Computer Code for the Transient Analysis of Oxide Fuel Rods*, TREE-NUREG-1040 (March 1977).

[a] FRAP-T4 is the latest version of the FRAP-T fuel behavior code; however, it is unpublished for public review; therefore, FRAP-T2 is referenced (see Appendix E).

THIS PAGE

WAS INTENTIONALLY

LEFT BLANK

APPENDIX D

POWER CALIBRATION RESULTS

THIS PAGE

WAS INTENTIONALLY

LEFT BLANK

APPENDIX D

POWER CALIBRATION RESULTS

Fuel rod power was calculated using a combination of several techniques. During the test, except for the flow reduction phase, fuel rod average power was calculated from a thermal balance. During the flow reduction phase, average power was determined from SPND 9 current using a linear regression equation relating the two variables. Local rod powers were determined from both cobalt flux wires and SPNDs.

1. FUEL ROD AVERAGE POWER

Each of the four fuel rods were instrumented for a thermal balance. Each fuel rod was surrounded by an individual flow shroud which was instrumented with a differential thermocouple pair and a flowmeter. The test assembly was instrumented for coolant inlet temperature and pressure. All of these instruments were available throughout the test except for the system pressure transducers. No usable pressure data was recorded. A constant pressure of 14.8 MPa was assumed based on PBF plant instrumentation.

Fuel rod average power was calculated from the thermal balance using a computer program which incorporates the equations presented in Reference D-1 and water properties determined from the ASTEM subroutines[D-2]. The computer program used the decimated data (Appendix C) for the preceding instruments and generated individual fuel rod average power, average fuel rod average power, and individual flow shroud coolant mass fluxes.

During the flow reduction phase of the test, saturated conditions existed at the outlets of the flow shrouds preventing valid thermal balances. A set of linear regression equations relating SPND 9 current and individual fuel rod average powers were generated using the data from the previous parts of the test. These equations, given in Table D-I, were used to calculate fuel rod average powers during the flow reduction.

Since individual fuel rod power data were available throughout the test, a comparison of the power in each rod was made. This was done to check for any unexpected variations in power due to instrument drift or asymmetry in the neutron flux due to control rod changes; there were none. The ratios of individual fuel rod power to average rod power, shown in Table D-II, remained constant within the listed uncertainties.

The uncertainties in rod power for Rods IE-019 through IE-022 were calculated using both instrument calibration errors and data acquisition errors. These results are shown in Table D-III.

TABLE D-I

LINEAR REGRESSION EQUATIONS RELATING NEUTRON FLUX MEASURED BY SPND 9 AND AVERAGE FUEL ROD POWER

Rod Number	Test[a] Phase	Regression[b] Equation	95% Confidence Interval (kW/m)
IE-019	Preconditioning	$y = 8.980\ x + 0.40$	$\pm$ 0.40
	Power Ramp, Steady State Operation and Flow Reduction	$y = 8.723\ x + 0.43$	$\pm$ 0.49
IE-020	Preconditioning	$y = 9.877\ x + 0.46$	$\pm$ 0.58
	Power Ramp, Steady State Operation and Flow Reduction	$y = 9.374\ x + 0.80$	$\pm$ 0.98
IE-021	Preconditioning	$y = 8.941\ x + 0.25$	$\pm$ 0.37
	Power Ramp, Steady State Operation and Flow Reduction	$y = 8.800\ x + 0.28$	$\pm$ 0.36
IE-022	Preconditioning	$y = 8.901\ x + 1.07$	$\pm$ 1.23
	Power Ramp, Steady State Operation and Flow Reduction	$y = 9.622\ x - 0.76$	$\pm$ 0.84
Average	Preconditioning	$y = 9.175\ x + 0.54$	$\pm$0.47
	Power Ramp, Steady State Operation and Flow Reduction	$y = 9.130\ x + 0.36$	$\pm$0.44

[a] The gap conductance data was not included in the "Preconditioning Phase" regression.

[b] y = Average fuel rod power (kW/m)

x = Neutron flux neutrons/cm^2·s measured by SPND 9 divided by 10^{14}.

TABLE D-II

RATIOS OF INDIVIDUAL FUEL ROD POWER TO AVERAGE FUEL ROD POWER

Power Ratios	Mean	95% Confidence Interval
Rod IE-019/Average	0.967	±0.020
Rod IE-020/Average	1.065	±0.037
Rod IE-021/Average	0.947	±0.026
Rod IE-022/Average	1.022	±0.050

TABLE D-III

UNCERTAINTIES IN FUEL ROD POWER[a]

Average Fuel Rod Power (kW/m)	95% Confidence Level (kW/m)
0.0	± 1.47
29.2	± 1.53
60.7	± 1.68

[a] At system conditions of: pressure, 14.8 MPa; inlet temperature, 600 K; and flow rate, 1000 cm^3/s. The tabulated results for fuel rod power and total error are for the average coolant differential temperature and total error presented in Appendix A. The variation of the error between the rods was insignificant.

[b] Total error is based on uncertainties in transducer calibration, data acquisition, and a propagation of these uncertainties in the thermal balance.

2. LOCAL POWER

A local power profile (power as a function of the elevation above the bottom of the rod) was obtained using the data from SPNDs and cobalt flux wires. The SPND results were used to determine the instantaneous peaking factors which were then multiplied by average fuel rod power to obtain an instantaneous local power. The instantaneous peaking factors were calculated by fitting a sine function to the output from each column of SPNDs. The

sine function was then divided by the integral average of the fit over the length of the fuel to normalize the profile (see Reference D-1 for a discussion of the techniques).

Analysis of the two instantaneous profiles as a function of power indicated that any appreciable skewing in local power, due to change in control rod position, was limited to a rod less than 10 kW/m. Above that level, any change in local power was minor. In going from a fuel rod power of less than 30 kW/m, the ratio of the peak to average changed less than 0.5%. Even this change is limited to the lower half of the rod; so that the normalized local power on the upper half of the rod remained fixed.

As shown in Table D-IV, the uncertainties in the normalized local power as determined from the SPNDs in the vertical column of 225° are extremely high. The exact cause for this problem is not fully understood, but is a consequence of the delay of two weeks between the first half and the second half of the test. For the first half of the test, the peak to average was approximately 1.30 while the peak to average for the second half was 1.35. The data for the second half are more noisy, so a degradation of one of the SPND amplifiers is suspected as the cause of this shift. This problem was not seen in the SPNDs at 45°. Therefore, instantaneous local power was determined from the SPND column at 45° only.

A comparison of the local power profiles from the two columns of SPNDs and the four cobalt wires extending the length of the fuel rods indicated that the azimuthal flux profile did not show any measureable asymmetry or tilting with change in power. Each cobalt wire mounted on the flow shroud of Rods IE-019, IE-020, IE-021, and IE-022 at the same radial distance from the centerline of the test assembly as the centerline of the fuel rods, gave nearly identical average neutron fluences (the deviation was less than 2.3%, well within the uncertainties of the measured fluences).

Local power profiles versus axial elevation from both SPNDs and average of the four wires are shown in Figure D-1 and tabulated in Table D-IV.

TABLE D-IV

LOCAL POWER PROFILE WITH UNCERTAINTIES

Instantaneous Local Power From SPNDs					Integrated Profile	
	Column at 45°[a]		Column at 225°[b]		From an Average of Flux Wires[c]	
Elevation[d]	Normalized Local Power	95% Confidence Intervals	Normalized Local Power	95% Confidence Intervals	Normalized Local Power	95% Confidence Intervals
0.013	0.34C	0.475	0.503	2.103	--	--
0.159	0.82E	0.045	0.869	0.939	0.824	0.017
0.306	1.201	0.047	1.177	0.576	1.208	0.031
0.452	1.331	0.051	1.300	0.890	1.328	0.034
0.521	1.32C	0.135	1.275	0.671	1.301	0.024
0.599	1.24E	0.330	1.187	0.361	1.190	0.036
0.662	1.137	0.365	1.077	0.181	1.098	0.024
0.724	0.981	0.226	0.943	0.125	0.954	0.060
0.745	0.92C	0.144	0.894	0.129	0.902	0.059
0.892	0.453	0.535	0.517	0.201	0.504	0.124

[a] Average Peak Elevation: 0.432 ± 0.050 m
Average Peak to Average: 1.323 ± 0.064

[b] Average Peak Elevation: 0.411 ± 0.024 m
Average Peak to Average: 1.428 ± 0.175

[c] Average of the four wires
Average Peak Elevation: 0.456 ± 0.069 m
Average Peak to Average: 1.338 ± 0.0557

[d] Measured from the bottom of the fuel rod.

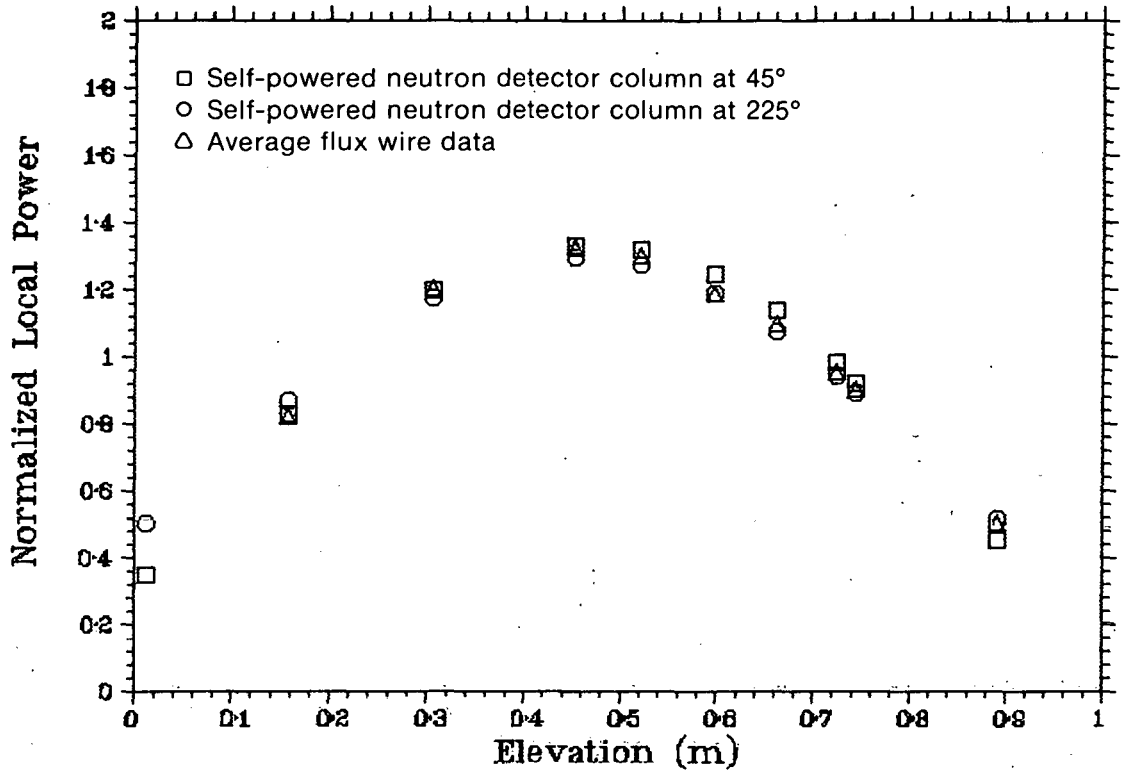

Fig. D-1 Normalized local fuel rod power for fuel rod average powers above 10 kW/m determined from self-powered neutron detectors and cobalt flux wires versus axial elevation.

3. REFERENCES

D-1. W. J. Quapp et al, *Irradiation Effects Test Series Scoping Test 1 Test Results Report*, TREE-NUREG-1066 (September 1977).

D-2. K. V. Moore, *ASTEM – A Collection of FORTRAN Subroutines to Evaluate the 1967 ASME Equations of State for Water/Steam and Derivations of these Equations*, ANCR-1026 (October 1971).

APPENDIX E

FRAP-T4 COMPUTER CODE MODEL DESCRIPTION

THIS PAGE

WAS INTENTIONALLY

LEFT BLANK

APPENDIX E

FRAP-T4 COMPUTER CODE MODEL DESCRIPTION

Calculational results for Rods IE-019, IE-020, and IE-021 were obtained using FRAP-T4, a fuel rod behavior code. FRAP-T[E-1] is a FORTRAN IV computer code developed to describe the transient behavior of nuclear fuel rods. The version used in this report[a] is the fourth in a series of fuel codes with each succeeding version incorporating the most recent advances made in fuel rod response analysis.

The FRAP-T4 computer code is a composite of various subcodes that are used to predict zircaloy oxidation and the thermal and mechanical response of a fuel rod to input power and flow conditons. The code is designed to allow the user to specify a few fuel behavior submodels, heat transfer correlations, axial and radial power distributions, and the physical characteristics of the fuel rod (e.g. dimensions, fuel-cladding gap, etc.). The FRAP-T4 code differs from the FRAP-T2[E-1] code in the following areas important for analysis of Test IE-5: (a) the time at which film boiling initiates and the length of the film boiling zone may be prescribed by the user, (b) a central void in the fuel may be modeled, and (c) stress induced fuel deformation, fuel relaxation, and cladding creep are considered in FRAP-T4.

1. FUEL ROD MODEL

For this analysis, the fuel rods were modeled using 11 radial and 16 axial nodes. FRAP-T4 input included the nominal measured conditions of coolant flow, coolant inlet temperature, coolant pressure, fuel rod average power, and axial flux profile. The Westinghouse W-3[E-3] critical heat flux (CHF) correlation (with the cold wall factor) and the Groeneveld tubes and annulus film boiling heat transfer correlation (Version 5.9)[E-4] were used. A void at the fuel centerline for a centerline thermocouple or ultrasonic thermometer was modeled for all rods. The Ross and Stoute[E-5] gap conductance model was selected. Gas within the rod was assumed to be in instant pressure equilibrium throughout the rod.

Two fuel deformation models are available in FRAP-T4. Both models assume radial cracks in the fuel extend from the fuel surface to the fuel centerline. The standard model employs the nominal cold fuel-cladding gap in calculating mechanical and thermal behavior. The second model is an option in FRAP-T4 called the Coleman Fuel Relocation Model which was developed empirically from steady state fuel rod data. It assumes that fuel pellet cracking produces radial relocation of the pellet pieces and reduces the nominal gap to an

[a] FRAP-T4, MOD004, Version 05/10 on Tape T9V720 was used in conjunction with MATPRO MOD008[E-2].

effective gap which describes the observed fuel rod thermal and mechanical behavior. The nominal gap is reduced by increasing the effective fuel pellet diameter. The increase in diameter of the fuel pellet, ΔD, is given by

$$\Delta D = G - 0.005 (D) \quad \text{(E-1)}$$

where

G = nominal cold fuel-cladding diametral gap (mm)

D = nominal cold fuel pellet diameter (mm).

The steady state calculations of each model compared with centerline temperature and fuel rod elongation data at various power levels during the preconditioning period of the test are given in Section VI.

Fuel rod average power was calculated from the experimental data using steady state coolant flow and coolant temperature rise measurements. The axial and radial power profiles used in the calculations are shown in Tables E-I and E-II. The radial profile was obtained from neutron transport calculations. The axial flux profile was determined by averaging results from a gamma scan of four cobalt wires that were positioned in the reactor test space during the test. Evaluation of the axially distributed self-powered neutron detector data and the flux wire data showed that the axial flux profile was not effected significantly by changes in the reactor power level. Consequently, the flux wire data, although they represent an integral of the power profile, were the best available measure of the rod axial power distribution (see Appendix D).

FRAP-T4 input to model the fuel rods, summarized in Table E-III, included the fresh fuel pellet nominal dimensions and cladding inside and outside diameter measurements taken prior to testing in the PBF reactor. These data are summarized in Section II, Table I, and in Appendix A.

TABLE E-I

AXIAL POWER PROFILE FOR TEST IE-5 FRAP-T4 CALCULATIONS

Elevation (m above bottom of fuel rod)	Local Power/Average Power
0.0	0.0
0.0276	0.0
0.0277	0.477
0.0576	0.523
0.1076	0.641
0.1576	0.783
0.2076	0.929
0.2576	0.062
0.3076	1.171
0.3576	1.251
0.4076	1.301
0.4276	1.312
0.4476	1.318
0.4676	1.319
0.4876	1.316
0.5076	1.308
0.5099	1.296
0.5476	1.280
0.5676	1.260
0.6076	1.209
0.6576	1.127
0.7076	1.029
0.7576	0.915
0.8076	0.789
0.9062	0.505

TABLE E-II

RADIAL POWER PROFILE FOR TEST IE-5 FRAP-T4 CALCULATIONS

Radial Location (mm from fuel centerline)	Local Power/Average Power
0.0 - 0.6178	0.870
0.6178 - 1.2355	0.880
1.2355 - 1.8533	0.896
1.8533 - 2.4711	0.928
2.4711 - 3.0888	0.970
3.0888 - 3.7066	1.030
3.7066 - 4.3243	1.130
3.7066 - 4.3243	1.130

TABLE E-III

FRAP-T4 CODE INPUT FOR TEST IE-5 POSTTEST ANALYSIS

	Fuel Rod		
	IE-019	IE-020	IE-021
Fuel Region			
Active length (m)	0.8786	0.8786	0.8786
Material	UO_2	UO_2	UO_2
Pellet height (mm)	15.240	15.240	15.240
Pellet diameter (mm)	9.931	9.931	9.995
Pellet shoulder radius (mm)	3.302	3.302	3.302
Dish depth (mm)	0.343	0.343	0.342
Density (10^{-3} kg/m^3)	10.4211	10.3679	10.3698
Theoretical density (%)	94.0	94.0	94.0
Roughness (μm)	2.16	2.16	2.16
Cladding Region			
Material	Zircaloy-4	Zircaloy-4	Zircaloy-4
Cladding ID (mm)	8.748	8.748	8.751
Cladding OD (mm)	9.931	9.931	9.995
Roughness (μm)	1.14	1.14	1.14
Plenum Region			
Gas quantity (moles)	0.0215	0.006366	0.006775
Plenum volume (ml)	5.37	5.37	5.37
Gas pressure (MPa)	8.3	2.5	2.5
Spring length (mm)	57.20	57.20	57.20
Spring coil OD (mm)	8.72	8.72	8.72
Spring wire diameter (mm)	1.72	1.72	1.72
Number of spring coils	15	15	15
Flow Shroud			
Coolant flow area (mm^2)	131.2	131.2	130.2
Hydraulic diameter (mm)	6.368	6.368	6.305
Equivalent heated diameter (mm)	16.82	16.82	16.587
Steady State Operation Conditions			
Coolant inlet temperature (K)	605.0	605.0	605.0
Coolant pressure (MPa)	14.8	14.8	14.8
Coolant mass flux (kg/s·m^2)	4880	5050	4832

2. EXPERIMENT CONDUCT MODEL

Steady state analyses using FRAP-T4 were made using incremental steps in fuel rod average power of 5 kW/m, from zero to a maximum of 50 kW/m. At each step, steady state fuel rod parameters were calculated. These parameters (cladding surface temperatures, cladding elongation, etc.) at each 5 kW/m power step were used to generate the data for the steady state comparisons. The data were compared to measurements during the first power cycle, the last two cycles of the preconditioning phase, and the ramp to a rod peak power of 50 kW/m.

To model the transient fuel rod behavior during the flow reduction, the experimentally determined fuel rod average power, coolant pressure, coolant inlet temperature, and coolant flow history during the flow reduction steps were used. Experimentally, the onset of film boiling occurred for Rods IE-019, IE-020, and IE-021 at mass flow rates of 1275 ± 30, 1315 ± 30, and 1210 ± 30 kg/s-m^2, respectively. FRAP-T4 using the W-3 correlation with the cold wall factor predicted that the onset of CHF would occur at 2775, 2813, and 2260 kg/s-m^2, respectively.

To improve the analysis of fuel behavior during film boiling, the FRAP-T4 code was modified to use the film boiling heat transfer coefficients only after the time DNB was measured to occur during the experiment. At the flow rate where DNB occurred during the experiment, a logic switch was used in FRAP-T4 to force specific axial locations along the fuel rod into film boiling. The transition to film boiling cannot be modeled by this method, but equilibrium conditions during film boiling should be more correctly calculated. Postirradiation examination of the fuel rods provided measurements of the axial extent of the film boiling zones for input to the FRAP-T4 code. The film boiling zones for Rods IE-019, IE-020, and IE-021 were modeled exactly in FRAP-T4 by selecting the node structure to coincide approximately with measured film boiling zones[a]. The time dependent coolant flow, inlet enthalpy, and fuel rod power that occurred in the test were used as input to FRAP-T4. Figures E-1 and E-2 compare the coolant mass fluxes and fuel rod peak powers for Rods IE-019, IE-020, and IE-021 during the flow reduction to the same quantities input to FRAP-T4.

[a] Rod IE-022 can be compared with Rod IE-020 by noting that Rod IE-022 had a film boiling zone that was 8.8% longer than Rod IE-020.

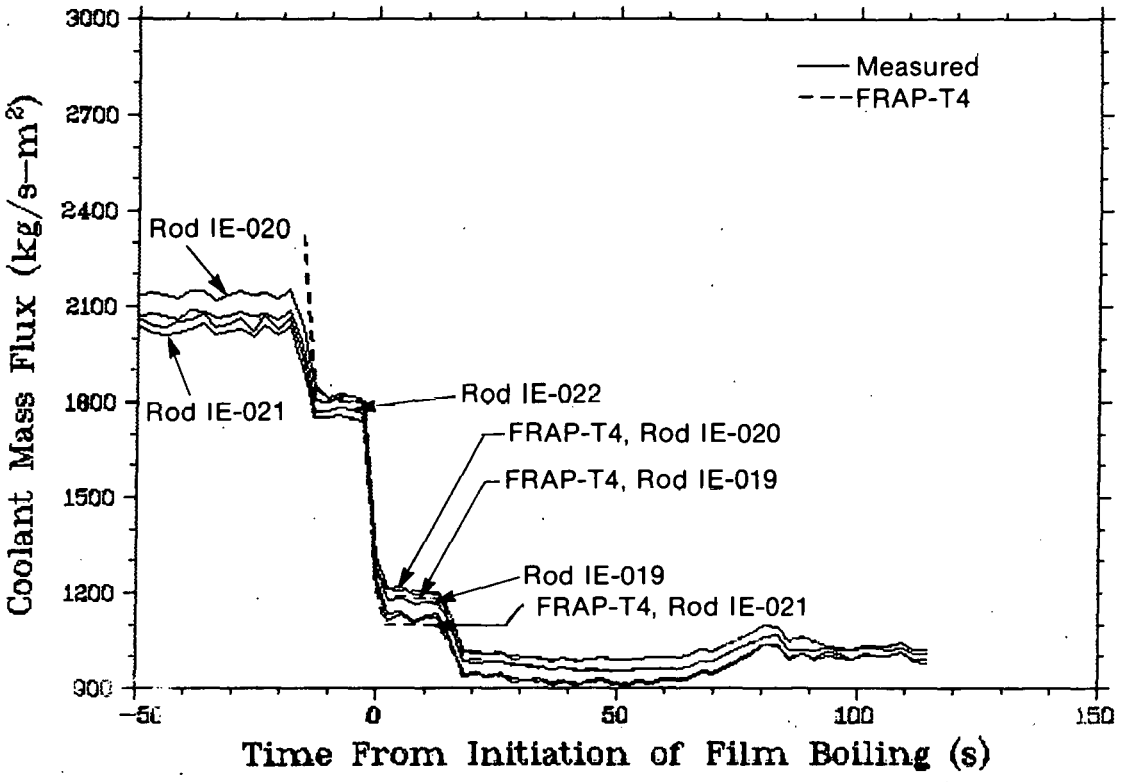

Fig. E-1 Coolant mass fluxes during the flow reduction phase of Test IE-5.

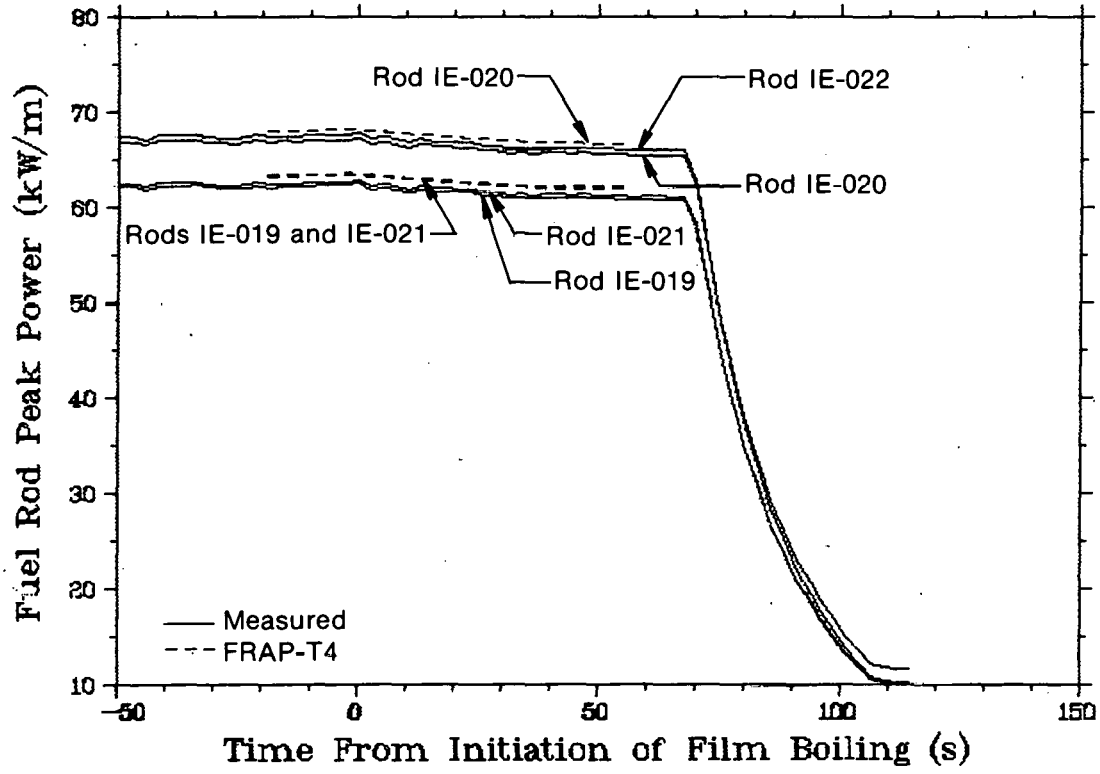

Fig. E-2 Fuel rod peak powers during the flow reduction phase of Test IE-5.

3. REFERENCES

E-1.[a] J. A. Dearien et al, *FRAP-T2: A Computer Code for the Transient Analysis of Oxide Fuel Rods,* TREE-NUREG-1040 (March 1977).

E-2.[b] P. E. MacDonald and L. B. Thompson (eds.), *MATPRO Version 09 – A Handbook of Materials Properties for Use in the Analysis of Light Water Reactor Fuel Rod Behavior,* TREE-NUREG-1005 (December 1976).

E-3. L. S. Tong, *Boiling Crisis and Critical Heat Flux, AEC Critical Review Series,* TID-25887 (1972).

E-4. D. C. Groeneveld, *An Investigation of Heat Transfer in the Liquid Deficient Regime,* AECL-3281 (December 1968, Revised August 1969).

E-5. A. M. Ross and R. L. Stoute, *Heat Transfer Coefficient Between UO_2 and Zircaloy-2,* AECL-1552 (June 1962).

---

[a] FRAP-T4 is the latest version of the FRAP-T fuel behavior code; however, it is unpublished for public review; therefore, FRAP-T2 is referenced.

[b] MATPRO, Version 08, is an unpublished version of MATPRO. MATPRO, Version 08, does not contain updated models of cladding specific heat, cladding thermal expansion, cladding strain-to-failure, fuel swelling, and fuel densification that are in MATPRO, Version 09. Therefore, MATPRO, Version 09, is referenced.

DISTRIBUTION RECORD FOR TREE-NUREG-1130

Internal Distribution

1 - Chicago Patent Group-DOE
9800 South Cass Avenue
Argonne, Illinois 60439

2 - C. A. Benson
Idaho Operations Office-DOE
Idaho Falls, ID 83401

3 - R. J. Beers, ID

4 - P. E. Litteneker, ID

5 - R. E. Tiller, ID

6 - R. E. Wood, ID

7 - H. P. Pearson, Supervisor
Information Management

8-17 - INEL Technical Library

18-38 - Authors

38-117 - Special Internal

External Distribution

118-119 - Saul Levine, Director
Office of Nuclear Regulatory Research, NRC
Washington, D. C. 20555

120-439 - Distribution under NRC-3, Water Reactor Safety Research
Fuel Behavior